

**FABRICATION, MODELING, AND ACTUATION OF  
SOFT BIOINSPIRED MICROROBOTS**

*Zihan Wang*





university of  
 groningen

# Fabrication, modeling, and actuation of soft bioinspired microrobots

PhD thesis

to obtain the degree of PhD at the  
 University of Groningen  
 on the authority of the  
 Rector Magnificus Prof. J.M.A. Scherpen  
 and in accordance with  
 the decision by the College of Deans.

This thesis will be defended in public on  
 Wednesday 12 March 2025 at 12.45 hours

by

**Zihan Wang**

born on 23 July 1998  
 in Hubei, China

## **Supervisors**

Prof. S. Misra

Dr. I. S. M. Khalil

## **Assessment Committee**

Assoc. Prof. U K. Cheang

Prof. R. Schirhagl

Prof. P. R. Onck

This work is part of the research project MAESTRO.



This work was supported by the European Research Council (ERC) under the European Union's Horizon 2020 Research and Innovation programme under grant 866494 project-MAESTRO, and financial support from the China Scholarship Council (CSC No. 202006120058) is acknowledged.



European  
Research  
Council



This dissertation has been approved by:

**Prof. Dr. Sarthak Misra**

**Dr. Islam S. M. Khalil**

Cover design: Zihan Wang

Lay-out: Chuang Li

Printed by: Ipskamp

©2025 Zihan Wang, The Netherlands. All rights reserved. No parts of this thesis may be reproduced, stored in a retrieval system or transmitted in any form or by any means without permission of the author. Alle rechten voorbehouden. Niets uit deze uitgave mag worden vermenigvuldigd, in enige vorm of op enige wijze, zonder voorafgaande schriftelijke toestemming van de auteur.

*Dedicated to my family*



# Samenvatting

Zachte bio-geïnspireerde microrobots hebben uitgebreide belangstelling gekregen in biomedische toepassingen vanwege hun flexibiliteit, wendbaarheid en miniaturisatie. Deze kenmerken stellen hen in staat om zich door beperkte ruimtes in het menselijk lichaam te bewegen. De microrobots gebruiken synthetische flagellen en bootsen zo de voortstuwing van biologische organismen na. Naast de bewegelijkheid is een andere essentiële eigenschap die zachte bio-geïnspireerde microrobots proberen na te bootsen de opmerkelijke aanpassingsvermogen van biologische organismen aan complexe omgevingen. Het begrijpen van deze 2 mechanismen stelt ons in staat om zachte microrobots te ontwerpen en te fabriceren die nauwkeurig hun biologische tegenhangers nabootsen. Echter, er blijft een aanzienlijke kloof bestaan tussen synthetische microrobots en biologische organismen. Het overbruggen van deze kloof vereist verder onderzoek, met name in het begrijpen van hoe biologische organismen zich aanpassen aan externe verstoringen en het verbeteren van de bewegelijkheid van synthetische microrobots.

Het doel van dit doctoraal onderzoek is om de kloof te verkleinen tussen biologische organismen en zachte bio-geïnspireerde microrobots en deze microrobots verder te ontwikkelen zodat ze meer op hun biologische tegenhangers gaan lijken. **Hoofdstuk 1** introduceert de ontwikkeling van microrobotica, de oorsprong van microfabricage en de fabricagemethoden van bio-geïnspireerde microrobots. **Hoofdstuk 2** richt de focus op zachte bio-geïnspireerde microrobots en geeft een overzicht van hun ontwerpbegin-selen, aansturingsmecanismes en biomedische toepassingen. Hoewel de zachte bio-geïnspireerde microrobots veelbelovend zijn gebleken in verschillende biomedische taken, zoals gerichte vracht-/geneesmiddelafgifte, biopsie en biofilmuitroeiing, is de volgende fase van het onderzoek gericht op het verbeteren van hun bewegelijkheid efficiëntie en het vergroten van hun gelijkenis met de organismen die hun ontwerp inspireerden. Daartoe verdiepen we ons in de aanpassingsvermogen van natuurlijke zaadcellen via experimentele observatie en theoretische validatie. **Hoofdstuk 3** onderzoekt de flagellaire voortstuwing van zaadcellen onder externe krachten en stelt een elastohydrodynamisch model voor om dit proces te bestuderen. Ons model voorspelt dat zowel de gemiddelde flagellaire kromming als de buigingsam-

plitude van de golfpatronen afnemen na blootstelling aan externe kracht, wat consistent is met onze experimentele waarneming. Bovendien biedt dit model een theoretische basis voor het verkennen van de invloed van andere interacties op flagellaire voortstuwing en voor het verbeteren van de voortstuwings efficiëntie van synthetische microrobots met behulp van voortbewegende golven.

De onderzoeksfocus verschuift dan naar zachte microrobots geïnspireerd door zaadcellen en kikkervisjes die voortstuwing verkrijgen door met hun zachte staart golfbewegingen te maken. De principes van elastohydrodynamica die worden gebruikt om de flagellaire voortstuwing van zaadcellen te bestuderen, zijn ook toepasbaar op deze zachte bio-geïnspireerde microrobots. In het bijzonder is de stap-uitfrequentie een cruciale maatstaf voor het evalueren van de bewegelijkheid efficiëntie van magnetische microrobots. Boven deze frequentie loopt de microrobot achter op externe magnetische velden, waardoor zijn snelheid afneemt. Om verder in te gaan op de stap-uit frequentie, introduceert **Hoofdstuk 4** een analytische vergelijking die elastohydrodynamica en magnetisme combineert. Deze vergelijking legt een kwantitatieve relatie vast tussen de stap-uit frequentie van zachte bio-geïnspireerde microrobots a hun magnetische eigenschappen, geometrie, golfpatronen en de viscositeit van het omringende medium. Validatie van deze vergelijking houdt in dat de zwemcapaciteit van elektrogewonnen sperma-achtige microrobots in media met verschillende viscositeiten wordt onderzocht. Ons theoretische model geeft aan dat de stap-uit frequentie afhangt van de golfpatronen van de zaadcelachtige microrobot. De stap-uit frequentie kan nauwkeurig worden voorspeld door kleine veranderingen in golfpatronen te analyseren die worden waargenomen zonder de stap-uitdrempel te overschrijden. Ons voorgestelde model biedt inzicht in de bewegelijkheid-efficiëntie van zachte bio-geïnspireerde microrobots en kan gebruikt worden voor het verbeteren van de experimentele aanpasbaarheid van zachte bio-geïnspireerde microrobots. Resultaat van deze aanpassingen zijn zachte bio-geïnspireerde microrobots met verbeterde bewegelijkheid efficiëntie en aanpassingsvermogen een aanzienlijk potentieel voor praktische toepassingen. Vervolgens richten we onze aandacht op proof-of-concept studies die microrobotsystemen verkennen. **Hoofdstuk 5** stelt een microrobotsysteem voor met efficiënte bewegelijkheid, dubbele bewegingsmogelijkheden en biologisch afbreekbaarheid. Magnetische alginaatmicrorobots, waaronder druppel- en kikkervisvormen, worden vervaardigd met behulp

van een aanpasbare centrifugale stroom. De rollende beweging van de druppelvormige microrobots en de stick-slip beweging van de kikkervisvormige microrobots worden gedemonstreerd onder roterende en oscillerende velden. Deze dual-motion functie stelt hen in staat zich aan te passen aan verschillende omgevingen, zoals het oversteken van obstakels en navigeren in krappe ruimtes. Ten slotte zetten we een echografie-imaging systeem in om hun beweging en afbraak te observeren, waarbij we hun potentieel voor gerichte medicijnafgifte in toekomstige klinische proeven benadrukken.

**Hoofdstuk 6** sluit dit doctoraatsproefschrift af door onze bevindingen uit **Hoofdstukken 3-5** over biologische organismen en synthetische microrobots samen te vatten. Het presenteert ook een visie voor toekomstig onderzoek om zachte bio-geïnspireerde microrobots te ontwikkelen die biologische organismen nauwkeuriger nabootsen. Hoewel dit doctoraal onderzoek voornamelijk gericht is op laboratoriumuitdagingen bij zachte bio-geïnspireerde microrobots, legt het de basis voor toekomstige innovaties in medische microrobots.



# Summary

Soft bioinspired microrobots have gained extensive interest in biomedical applications due to their flexibility, maneuverability, and miniaturization. These characteristics enable them to navigate confined spaces within the human body. By emulating the locomotion of biological organisms, these microrobots can use their synthetic flagella to achieve flagellar propulsion. In addition to locomotion ability, another essential feature that soft bioinspired microrobots aim to replicate is the remarkable adaptability of biological organisms to complex environments. Understanding the underlying mechanisms of locomotion and adaptability enables us to design and fabricate soft microrobots that closely mimic their biological counterparts. However, there remains a significant gap between synthetic microrobots and biological organisms. Bridging this gap necessitates further research, particularly in understanding how biological organisms adapt to external disturbances and enhancing the locomotion capabilities of synthetic microrobots.

The objective of this doctoral research is to bridge the gap between biological organisms and soft bioinspired microrobots, advancing these microrobots to resemble their biological counterparts more closely. **Chapter 1** introduces the development of microrobotics, the origin of microfabrication, and the fabrication methods of bioinspired microrobots. **Chapter 2** narrows the focus to soft bioinspired microrobots and presents an overview of their design principles, actuation methods, and biomedical applications. While the soft bioinspired microrobots have shown promise in various biomedical tasks, such as targeted cargo/drug delivery, biopsy, and biofilm eradication, the next phase of research aims to enhance their locomotion efficiency and improve their resemblance to the organisms that inspired their design. To this end, we delve into the environmental adaptability of natural sperm cells via experimental observation and theoretical validation. **Chapter 3** investigates the flagellar propulsion of sperm cells under external forces and proposes an elastohydrodynamic model to study this process. Our model predicts that both the mean flagellar curvature and the bending amplitude of the wave patterns reduce after experiencing external force, which is consistent with our experimental observation.

Furthermore, this model provides a theoretical basis for exploring other interactions' influence on flagellar propulsion and for improving the locomotion efficiency of synthetic microrobots using traveling waves.

The research focus then shifts to soft microrobots inspired by sperm cells and tadpoles, which acquire propulsion by undulating their soft and flexible tail. The principles of elasto-hydrodynamics used to study the flagellar propulsion of sperm cells are also applicable to these soft bioinspired microrobots. In particular, step-out frequency is a crucial metric for evaluating the locomotion efficiency of magnetic microrobots. Beyond this frequency, the microrobot lags behind external magnetic fields, thus reducing its velocity. To elaborate on the step-out frequency, **Chapter 4** introduces an analytic equation combining elasto-hydrodynamics and magnetism. This equation establishes a quantitative relationship between the step-out frequency of soft bioinspired microrobots and their magnetic properties, geometry, wave patterns, and the viscosity of the surrounding medium. Validation of this equation involves investigating the swimming performance of electrospun sperm-like microrobots in mediums with varying viscosities. Our theoretical model indicates that the step-out frequency depends on the wave patterns of the sperm-like microrobot. However, it can be accurately predicted by analyzing wave patterns observed without exceeding the step-out threshold. This is due to the slight variations in wave patterns, unlike those observed in natural sperm cells. Our proposed model provides insights into the locomotion efficiency of soft bioinspired microrobots. It has implications for enhancing the experimental adaptability of soft bioinspired microrobots, as the high locomotion efficiency allows these microrobots to overcome external disturbance. As a result, soft bioinspired microrobots with improved locomotion efficiency and adaptability have significant potential for practical applications. Next, we shift our attention to proof-of-concept studies that explore microrobotic systems. **Chapter 5** proposes a microrobotic system with efficient locomotion, dual-motion capabilities, and biodegradability. Magnetic alginate microrobots, including teardrop and tadpole shapes, are fabricated by adjusting centrifugally driven flow. The rolling motion of the teardrop-like microrobots and the stick-slip motion of the tadpole-like microrobots are demonstrated under rotating and oscillating fields, respectively. This dual-motion capability enables them to adapt to different environments, such as obstacle crossing and navigation in confined spaces. Finally, we deploy an ultrasound imaging system

to observe their motion and degradation, highlighting their potential for targeted drug delivery in future clinical trials.

**Chapter 6** concludes this doctoral thesis by summarizing our findings from **Chapters 3-5** on biological organisms and synthetic microrobots. It also presents a vision for future research to develop soft bioinspired microrobots that mimic biological organisms more closely. While this doctoral research primarily addresses laboratory-level challenges in soft bioinspired microrobots, it lays the groundwork for future innovations in medical microrobots.



# Contents

<b>1</b>	<b>Introduction</b>	<b>1</b>
1.1	Evolution of Microrobotics . . . . .	1
1.1.1	From Micro-Electro-Mechanical Systems (MEMS) Technology to Microrobots . . . . .	2
1.1.2	Locomotion at Low-Reynold-Fluid Regimes . . . . .	4
1.1.3	Bioinspired Microrobots . . . . .	6
1.2	Research Objectives . . . . .	8
1.3	Outline of the Thesis . . . . .	11
1.4	Research Framework Funding . . . . .	13
1.5	Scientific Output . . . . .	13
1.5.1	Peer-Reviewed Journal Articles . . . . .	13
1.5.2	Abstract . . . . .	14
<b>2</b>	<b>Soft Bio-Microrobots: Toward Biomedical Applications</b>	<b>15</b>
2.1	Introduction . . . . .	16
2.2	Design Principles of Soft Bio-Microrobots . . . . .	19
2.2.1	Biologically Inspired Microrobots . . . . .	20
2.2.2	Microrobots with Joints . . . . .	20
2.2.2.1	Microrobots with Soft Segments . . . . .	22
2.2.2.2	Microrobots with Soft and Continuous Bodies . . . . .	24
2.3	Biohybrid Microrobots . . . . .	27
2.3.1	Sperm-Based Microrobots . . . . .	28
2.3.2	Bacteria-Driven Microrobots . . . . .	30
2.3.3	Algal Microrobots . . . . .	33
2.4	Energy Sources for Soft Bio-Microrobots . . . . .	34
2.4.1	Magnetic Actuation . . . . .	35
2.4.2	Acoustic Actuation . . . . .	36
2.4.3	Optical Actuation . . . . .	37
2.4.4	Self-Propulsion . . . . .	38
2.5	Biomedical Applications of Soft Bio-Microrobots . . . . .	40
2.5.1	Targeted Delivery . . . . .	41
2.5.2	Surgery . . . . .	45

2.5.2.1	Biopsy . . . . .	46
2.5.2.2	Biofilm Eradiction . . . . .	46
2.6	Challenges . . . . .	48
2.7	Conclusions . . . . .	52
<b>3</b>	<b>Flagellar Propulsion of Sperm Cells Against a Time-Periodic Interaction Force</b>	<b>53</b>
3.1	Introduction . . . . .	54
3.2	Actively Propagated Waves along Two Collinear Flagella . . . . .	56
3.2.1	Cell-to-Cell Interactions . . . . .	56
3.2.2	The Elasto-Hydrodynamic Flagellum . . . . .	58
3.2.3	Kinematics of Sperm Bundles . . . . .	61
3.2.4	Numerical Results . . . . .	62
3.2.4.1	The Formation of Collinear Bundles . . . . .	62
3.2.4.2	The Influence of a Time-Periodic force . . . . .	64
3.3	Experimental results . . . . .	71
3.3.1	Sperm Cells under Time-Periodic Interaction . . . . .	71
3.3.2	Flow Field and Bending Moment . . . . .	76
3.4	Discussion . . . . .	78
3.5	Conclusions . . . . .	81
3.6	Experimental Section . . . . .	82
3.6.1	Sperm Cell Video Microscopy . . . . .	82
3.6.2	Fourier Analysis of Wave-Pattern . . . . .	83
3.6.3	Calculation of the Drag-Based Thrust . . . . .	83
3.6.4	Calculation of the Fluid Response . . . . .	84
3.6.5	Bending Moment of the Flagellum . . . . .	84
3.6.6	Statistical Analysis . . . . .	84
3.7	Supplementary Video . . . . .	85
<b>4</b>	<b>Magnetic Control of Soft Microrobots Near Step-Out Frequency: Characterization and Analysis</b>	<b>87</b>
4.1	Introduction . . . . .	88
4.2	Results and Discussion . . . . .	91
4.2.1	Fabrication and Magnetic Actuation of Soft Sperm-Like Microrobots . . . . .	91
4.2.2	Geometric, Chemical, and Magnetization Characterization . . . . .	93

4.2.3	Nondimensional Analysis . . . . .	95
4.2.4	Derivation of the Equation for Step-Out Frequency and Velocity at Step-Out Frequency . . . . .	97
4.2.5	Wave Pattern Analysis at the Step-Out Frequency . . . . .	98
4.2.6	Analysis of Wave Patterns Observed without Exceeding Step-Out Frequency . . . . .	101
4.2.7	Model Validation and Guidance . . . . .	105
4.3	Conclusion . . . . .	107
4.4	Materials and Methods . . . . .	109
4.4.1	Preparation of Polymer Solution for Electrospinning . . . . .	109
4.4.2	Fabrication of Soft Sperm-Like Microrobots . . . . .	109
4.4.3	SEM Characterization . . . . .	109
4.4.4	Magnetization Measurements . . . . .	110
4.4.5	Preparation of Methyl Cellulose (MC) Solutions . . . . .	110
4.4.6	Viscosity Measurements . . . . .	110
4.4.7	Magnetic Actuation and Microscopic Observation Setup . . . . .	110
4.4.8	Position Acquisition of Wave Patterns . . . . .	111
4.5	Supplementary Figure . . . . .	112
4.6	Supplementary Table . . . . .	113
4.7	Supplementary Movie . . . . .	114

## **5 Magnetic Alginate Microrobots with Dual-Motion Patterns through Centrifugally Driven Flow Control 115**

5.1	Introduction . . . . .	116
5.2	Results and Discussion . . . . .	119
5.2.1	Fabrication of Magnetic Alginate Microrobots . . . . .	119
5.2.2	Characterization and Formation Simulations of Magnetic Alginate Microrobots . . . . .	119
5.2.3	Size Scalability of Magnetic Alginate Microrobots . . . . .	124
5.2.4	Locomotion and Dual Motion Capability of Magnetic Alginate Microrobots . . . . .	128
5.2.5	Ultrasound Imaging of Magnetic Alginate Microrobots' Locomotion and Degradation . . . . .	133
5.3	Conclusion . . . . .	135
5.4	Materials and Methods . . . . .	136
5.4.1	Preparation and Gelation of Magnetic Alginate Solution . . . . .	136

5.4.2	Viscosity and Oscillatory Shear Rheology Measurement	137
5.4.3	Pendant Drop Method . . . . .	137
5.4.4	SEM Characterization . . . . .	138
5.4.5	Experimental Setup . . . . .	138
5.4.6	Finite Element Analysis . . . . .	139
5.5	Supplementary Figures . . . . .	140
5.6	Supplementary Tables . . . . .	148
5.7	Supplementary Movies . . . . .	150
<b>6</b>	<b>Conclusions</b>	<b>151</b>
6.1	Biological Organisms . . . . .	152
6.2	Synthetic Microrobots . . . . .	153
6.3	Outlook . . . . .	154
6.3.1	Stimuli-Responsive Capability . . . . .	155
6.3.2	Optimizing Actuation . . . . .	157
6.3.3	Challenges for Clinical Translation . . . . .	158
	<b>References</b>	<b>195</b>
	<b>Acknowledgements</b>	<b>197</b>
	<b>About the author</b>	<b>201</b>

# 1

## Introduction

### 1.1 Evolution of Microrobotics

The concept of small-scale machines was initially introduced by Richard Feynman in his 1959 lecture, “There’s Plenty of Room at the Bottom” [1]. During this lecture, Feynman proposed the hypothesis that tiny machines could be swallowed to detect and treat diseases within the heart in the future. He also envisioned the potential for these machines to be permanently deployed in the body to assist inadequately functioning organs. This revolutionary idea opened the possibility of small-scale machines acting as miniature surgeons inside the human body, presenting new opportunities for medical therapies. Such a concept was vividly reflected in the science fiction movies *Fantastic Voyage* in 1966 [2] and *Innerspace* in 1987 [3]. In these films, a submarine and its crew were shrunk to microscopic size and then injected into the human body to perform noninvasive surgery, as depicted in Figure 1.1(A). While these miniaturized objects are easy to design and create in artwork, they face significant technological and design challenges in practical applications. The complexity of such small-scale machines necessitates precision engineering, advanced materials, and innovative fabrication techniques.

Over the past few decades, traditional surgical robots have evolved rapidly, demonstrating their feasibility and effectiveness in surgical procedures. For example, the da Vinci surgical system (Intuitive Surgical Inc.) is renowned for improving the precision and dexterity required during operation [4]. The emergence of surgical robots can reduce recovery time,

# 1. Introduction

---

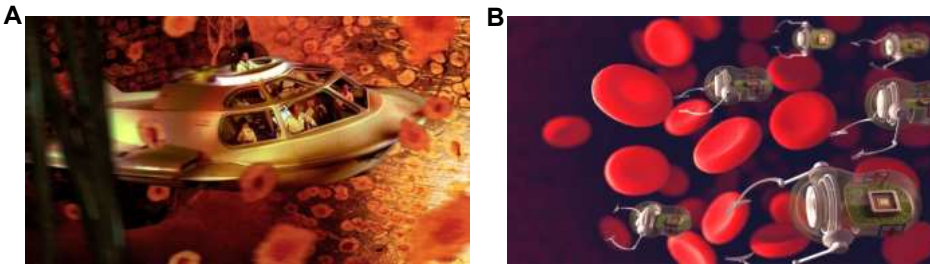


Figure 1.1: Microscale machines in artistic representations. (A) A miniaturized submarine navigates through a blood vessel. This image is copyrighted by *20<sup>th</sup> Century FOX*. (B) The conceptual illustration depicts microrobots interacting with red blood cells, designed for targeted therapeutic applications (Image is sourced from <https://builtin.com/robotics/microrobotics>).

medical complications, infection risks, and postoperative pain in patients. Despite these advantages, traditional surgical robots meet challenges in accessing hard-to-reach and tiny spaces within the human body, such as the circulatory, urinary, and respiratory systems. Surgical procedures in these areas pose increased difficulties and risks, making human errors unavoidable, even for experienced surgeons. Microrobots hold promise for navigating these challenging areas because of their small size [5], [6]. They are envisioned to minimize surgical risks by performing tasks with unprecedented precision (Figure 1.1(B)). However, creating such microrobots faces design and fabrication challenges that arise from the process of miniaturization. It is imperative to address these challenges before they can be deployed in clinical trials. The development of microfabrication techniques lays the foundation for the advent of microrobots.

## 1.1.1 From Micro-Electro-Mechanical Systems (MEMS) Technology to Microrobots

Conventional fabrication techniques, which involve processing bulk materials through cutting, punching, forming, shearing, stamping, and welding, are commonly employed to manufacture large surgical robots. However, these methods lack the precision required for microscale fabrication. This limitation has stimulated the development of micro-electromechanical systems (MEMS) technology, a pivotal advancement in microfabrication.

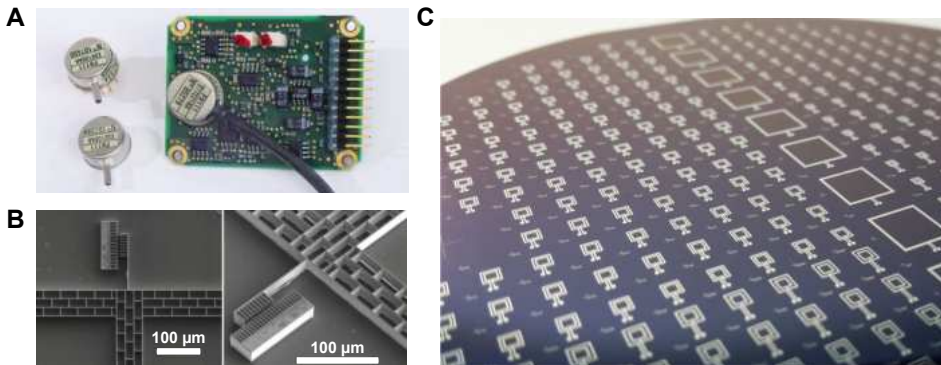


Figure 1.2: Micro-Electro-Mechanical Systems (MEMS) technology. (A) An example of a MEMS sensor for measuring an aircraft's velocity and orientation (Image is adapted from <https://onboard.thalesgroup.com/mems-the-micro-systems-feeding-big-ideas>). (B) Scanning electron microscope micrographs of a MEMS actuator. Reproduced with permission from [7]. Copyright 2012, Springer Science Business Media B.V. (C) A silicon wafer containing MEMS chips (Image is sourced from <https://www.lionix-international.com/mems/custom-mems/mems-production>).

MEMS technology has transformed microfabrication by enabling the creation of microscopic devices that integrate mechanical and electronic components. These devices often include onboard sensors (Figure 1.2(A)), actuators (Figure 1.2(B)), and microelectronics (Figure 1.2(C)). Typically, MEMS devices are fabricated on silicon wafers through photolithography, which employs light to transfer intricate microscale patterns onto a substrate. This technique is foundational to MEMS technology and has evolved to utilize various light sources, including ultraviolet, deep ultraviolet, extreme ultraviolet, and X-ray. Each source offers different wavelengths that enhance resolution in microscale fabrication. MEMS technology facilitates not only the integration of semiconductors but also the development of sophisticated microrobots.

While MEMS technology has significantly advanced the manufacturing of small-scale machines, the size limitation of microrobots restricts their power options compared to macro-scale robots, which typically rely on batteries. To overcome this challenge, microrobots have evolved to harness external fields for power. For instance, magnetic fields have been effectively employed for wireless control of microrobots in fluidic environments

# 1. Introduction

---

[8], [9]. The magnetic microrobots are fabricated with standard MEMS manufacturing processes, including electroplating, photolithography, and etching. The orientation and locomotion of these microrobots are controlled by the induced magnetic torque and force, respectively. However, pulling using magnetic forces is not an effective way to achieve locomotion. The magnetic force decreases rapidly as the robot is scaled down to the microscopic size. Researchers are actively exploring the intricacies of microscale locomotion mechanisms and developing effective strategies to endow microrobots with the motility to navigate and interact with their surroundings. This research is crucial for the development of microrobots.

## 1.1.2 Locomotion at Low-Reynold-Fluid Regimes

The scenarios in science fiction movies are often unrealistic, they primarily arise from the filmmakers' imagination. For example, in *Fantastic Voyage*, a miniaturized crew is depicted as capable of walking inside a submarine; however, such a crew would struggle to overcome the strong adhesive forces between its feet and the floor in reality [10]. Its locomotion would be ineffective due to the constraints imposed by scaling laws [11]. These scale laws indicate that, at the microscale, physical effects that are negligible at the macroscopic level become significant, and *vice versa*. We must abandon our intuitions, as inertial forces no longer dominate viscous forces at the microscale. This shift in physical effects conflicts with our conventional perceptions of movement and design in macro-scale robots.

Microrobots are being developed with a rigorous understanding of locomotion at the microscopic level. We adopt the Navier-Stokes equations to describe the dynamics of fluid and account for the scale-dependent effects that dominate at the microscale. The Navier-Stokes equations are formulated as follows [12]:

$$\begin{aligned} \rho \left( \frac{\partial \mathbf{u}}{\partial t} + (\mathbf{u} \cdot \nabla) \mathbf{u} \right) &= -\nabla p + \eta \nabla^2 \mathbf{u} + \rho \mathbf{b}, \\ \nabla \cdot \mathbf{u} &= 0, \end{aligned} \tag{1.1}$$

where  $\rho$  is the density,  $\mathbf{u}$  is the velocity vector field,  $p$  is the scalar pressure field,  $\eta$  is the viscosity of the fluid,  $\mathbf{b}$  represents external body forces per unit mass that act on the microrobot. The two terms at the left-hand side of Equation 1.1 denote the inertial forces. The Reynolds number denotes

the relative importance of the inertial forces to viscous forces. It is defined as follows [13]:

$$Re \triangleq \frac{\text{Inertia force}}{\text{Viscous force}} = \frac{\rho VL}{\eta}, \quad (1.2)$$

where  $L$  is the characteristic length of the microrobot. In the microscopic realm, the characteristic length of a microrobot is considerably small, leading to a low-Reynold-fluid regime where viscous forces dominate over inertial forces. As a result, the inertial terms can be neglected in the Navier-Stokes equations, simplifying the equations to

$$\begin{aligned} \eta \nabla^2 \mathbf{u} - \nabla p &= -\rho \mathbf{b}, \\ \nabla \cdot \mathbf{u} &= 0. \end{aligned} \quad (1.3)$$

Unlike the nonlinear Navier-Stokes equation (1.1), the simplified Stokes equations (1.3) are linear and time-reversible. One important consequence of the linearity and time-reversibility is the Scallop theorem [13], which highlights a fundamental limitation of microswimmers' locomotion: a swimmer that performs a reciprocal motion cannot achieve net displacement. The reciprocal motion means that the swimmers' shape appears identical when viewed under time reversal. For example, the freestyle swimming of humans by flapping arms would fail to propel in the microscopic world [14]. While the Scallop theorem imposes a fundamental constraint on the locomotion of microswimmers within Stokes flow, researchers are actively investigating various strategies to overcome this limitation.

To achieve effective motion at low-Reynold-fluid regimes, the body configuration of microrobots must break the time-reversibility constraint [15]. This principle is evident in various microorganisms and cells, which exhibit how such configurations generate movement [16], [17]. For instance, bacteria employ a relatively stiff helix driven by a rotating molecular motor to propel themselves through the fluid (Figure 1.3(A)) [18]. They can switch between “running” to move forward and “tumbling” to change direction by reversing the motor's rotation. Similarly, eukaryotic cells, such as spermatozoa and green algae, possess flexible flagella or cilia composed of nine microtubule doublets around the periphery and two in the center (Figure 1.3(B) and 1.3(C)). The conversion of ATP hydrolysis into microtubule sliding enables the flagella or cilia to beat, propelling the cells forward [19], [20]. Such natural mechanisms, which inherently overcome the time-reversibility constraint, offer valuable insights for the design of

# 1. Introduction

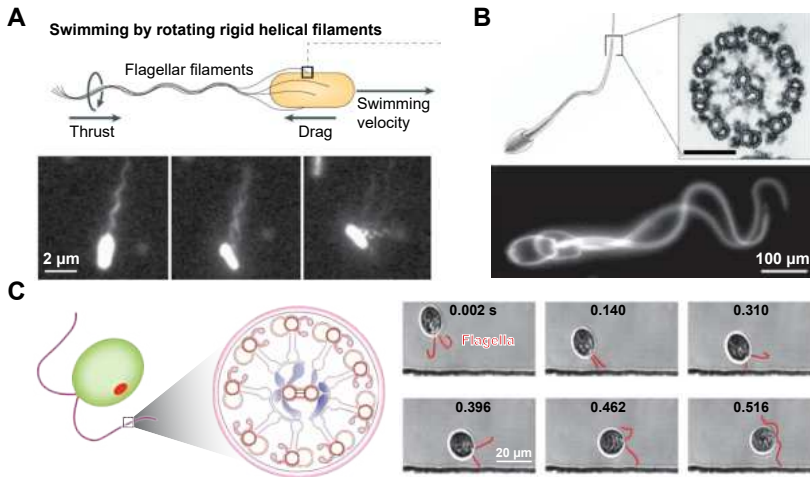


Figure 1.3: Motile microorganisms or cells. (A) *Escherichia coli* swims by rotating rigid helical flagella. Epifluorescence images show the “run-to-tumble” transition. Reproduced with permission from [18]. Copyright 2021, Springer Nature Limited. (B) A sketch of a spermatozoon swimming through the active deformation of its flexible flagellum. The inset shows a cross-section of the flagellar structure, which consists of nine microtubule doublets around the periphery and two in the center. Micrographs illustrate the flagellar beating of a ram spermatozoon at two different time points. Reproduced with permission from [16]. Copyright 2020, Cambridge University Press. (C) *Chlamydomonas* and the structure of its axoneme. The axoneme consists of a 9+2 arrangement of microtubule doublets on which dynein motors initiate doublets sliding and produce the flagella beat. The time-sequence micrographs show the motion of *Chlamydomonas*. Reproduced with permission from [19]. Copyright 2015, Annual Reviews, Inc.

microrobots to achieve effective locomotion in low-Reynolds-number fluids.

## 1.1.3 Bioinspired Microrobots

The innate ability of microorganisms and cells to navigate low-Reynolds-number fluids inspires the development of various microrobots. Magnetically-driven helical microrobots, which imitate the helical flagellar swimming of *Escherichia coli*, were first introduced in 2009 [21]. The fabrication of these helical structures utilizes the self-scrolling of planar metallic patterns formed through photolithography (Figure 1.4(A)). Other fabrica-

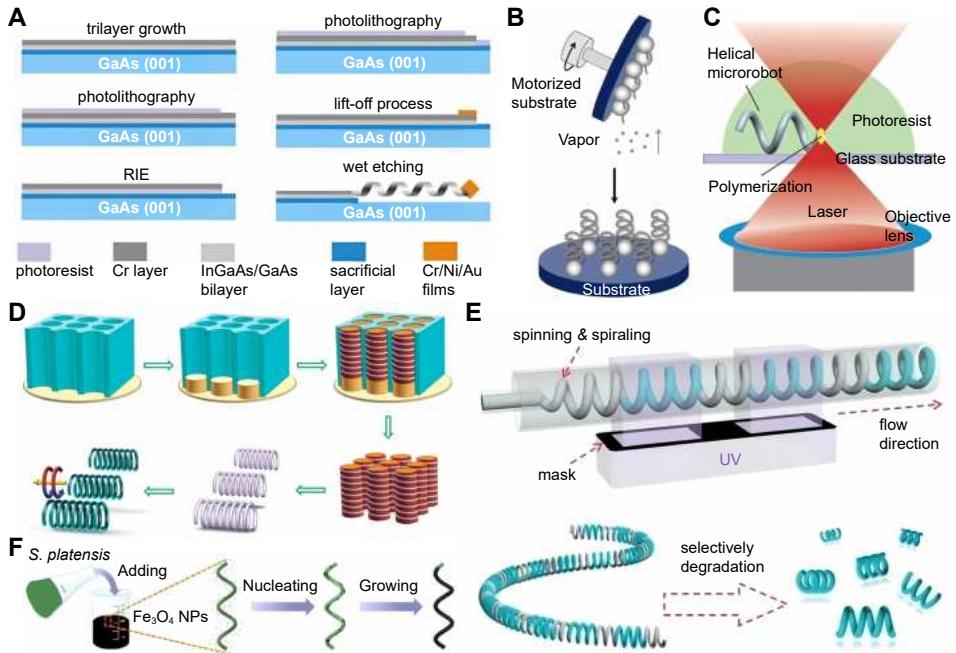


Figure 1.4: Fabrication methods of rigid helical microrobots, including: (A) Self-scrolling (Reproduced with permission from [21]. Copyright 2009, AIP Publishing.). (B) Glancing angle deposition (Reproduced with permission from [22]. Copyright 2017, WILEY-VCH Verlag GmbH & Co. KGaA, Weinheim.). (C) Direct laser writing (Reproduced with permission from [23]. Copyright 2014, Royal Society of Chemistry.). (D) Template-assisted electrodeposition (Reproduced with permission from [24]. Copyright 2014, Royal Society of Chemistry.). (E) Microfluidic lithography (Reproduced with permission from [25]. Copyright 2017, Wiley-VCH Verlag GmbH & Co. KGaA, Weinheim.). (F) Biotemplating synthesis (Reproduced with permission from [26]. Copyright 2017, The Authors, some rights reserved.).

tion methods for helical microrobots include glancing angle deposition (Figure 1.4(B)) [27], [28], direct laser writing (Figure 1.4(C)) [29], [30], template-assisted electrodeposition (Figure 1.4(D)) [24], [31], microfluidic lithography (Figure 1.4(E)) [25], and biotemplating synthesis (Figure 1.4(F)) [26], [32], [33]. When subjected to a rotating magnetic field, these helical microrobots can achieve propulsion through helical flagellar swimming. The superior swimming performance has enabled a wide range of applications in biomedical fields, such as cargo transportation [29], [34], [35],

# 1. Introduction

---

targeted drug/gene delivery [36], [37], biofilm eradication [38], and water remediation [39].

In addition to the inspiration drawn from prokaryotic cells, eukaryotic cells have motivated the advancement of synthetic microrobots made of flexible and deformable materials. These soft bioinspired microrobots acquire locomotion by mimicking the natural flexibility and compliance of flagella and cilia [40], [41]. For instance, Dreyfus *et al.* have engineered a flexible artificial flagellum by linking a chain of colloidal magnetic particles via DNA [42]. When exposed to an in-plane oscillating field, this synthetic flagellum induces beating patterns that resemble the flagellar beating of eukaryotic cells, thus enabling its propulsion. Various fabrication methods have been utilized to create soft bioinspired microrobots, including photolithography [43], [44], electrospinning [45], [46], magnetic assembly [47], [48], and electrodeposition [49], [50]. These microrobots have demonstrated 3D control capabilities using X-ray-guided magnetic fields, highlighting their potential for biomedical applications [51]. The design principles, energy sources, and biomedical applications of soft bioinspired microrobots are summarized in **Chapter 2**.

## 1.2 Research Objectives

Soft bioinspired microrobots are being developed by gaining insights from the behaviors of biological organisms. The current challenges in this field can be categorized into three aspects: understanding the movement and behaviors of biological organisms, applying the knowledge gained from these organisms to facilitate the development of soft bioinspired microrobots, and designing soft bioinspired microrobots with versatility. The following research questions (**RQs**) are identified within these areas.

Sperm cells are the primary inspiration for developing soft bioinspired microrobots because of their effective locomotion and high adaptability to external environments. These cells navigate through male and female reproductive tracts, where they undergo complex interactions with solid boundaries, fluid flows, and other cells. Such external interactions exert forces on the sperm cells. Despite these disturbance forces, the one sperm cell can successfully reach the fertilization site and execute the fusion with an ovum. Its remarkable adaptability in complex environments provides valuable insights into the development of soft bioinspired microrobots.

## RQ.1

How do biological organisms overcome the interactions with external environments during their movement?

In **RQ.1**, we investigate how a time-periodic force influences the flagellar propulsion of sperm cells. This force arises from the cell-to-cell interaction between two sperm cells. To investigate this phenomenon, we develop an elasto-hydrodynamic model that simulates the cell-to-cell interaction. Our theoretical results indicate that interactions between two sperm cells' heads lead to highly symmetrical wave patterns and a reduced bending amplitude of the propagating waves compared to free sperm cells. Notably, the active cell exhibits wave patterns with a higher bending amplitude than the passive cell, which acts as the external disturbance in the study. This increasing bending amplitude allows the active cell to overcome the disturbance force generated by the passive cell. The locomotion mechanism of sperm cells is replicated in soft bioinspired microrobots, enabling them to move forward by generating traveling waves. Our results suggest that these microrobots can effectively overcome disturbance forces by increasing the bending amplitude of their traveling waves, which in turn enhances their swimming efficiency.

Building on the hydrodynamics of sperm cells in navigating disturbance forces, it becomes evident that enhancing the swimming efficiency of soft bioinspired microrobots is crucial for improving their adaptability to external environments. The maximum velocity of magnetically actuated soft microrobots depends on their step-out frequency. These microrobots can synchronize their rotation with external magnetic fields when the applied field rotates with a low frequency. However, there is a step-out frequency beyond which the applied magnetic torque can no longer counterbalance the viscous drag torque acting on the microrobot. When the rotation frequency exceeds this threshold, the microrobots lose synchronization with the external field, causing a rapid decrease in velocity. By increasing the step-out frequency, magnetically actuated soft microrobots can enhance their locomotion efficiencies. Consequently, understanding the factors that influence the step-out frequency of soft bioinspired microrobots is essential for optimizing their swimming efficiency and improving adaptability.

## 1. Introduction

---

### RQ.2

What factors impact the step-out frequency of soft bioinspired microrobots?

In **RQ.2**, we investigate the influence of various factors, such as magnetic properties, geometry, wave patterns of soft bioinspired microrobots, and viscosities of mediums, on the step-out frequency. To this end, we propose an analytic model from magneto-elastohydrodynamics to study the step-out frequency of sperm-like microrobots. These sperm-like microrobots are fabricated using electrospinning and perform magnetic actuation in deionized water and methyl cellulose solutions. Our proposed model can accurately predict the step-out frequencies via the wave patterns observed at any frequency below the actual step-out frequency. This quantitative study of the step-out frequency provides valuable insights into enhancing the efficient locomotion and adaptability of soft bioinspired microrobots.

Due to their efficient locomotion and high adaptability, soft bioinspired microrobots are emerging as viable candidates for microrobotic systems intended for biomedical applications. A complete soft microrobotic system encompasses four key aspects: fabrication, control, imaging, and biomedical applications. However, the costly and complicated fabrication method hinders the widespread use of these soft microrobotic systems in biomedical applications. To maximize their potential, ongoing research focuses on developing simple and affordable fabrication methods without sacrificing high yield.

### RQ.3

How to develop a soft microrobotic system in a facile, cost-effective, and high-throughput manner?

In **RQ.3**, we propose a cost-effective and high-throughput method for fabricating magnetic alginate microrobots, including teardrop and tadpole designs. We achieve fine control over the microrobots' shapes and dimensions by adjusting centrifugally driven flow. We explore the formation mechanism of these shapes and predict the microrobots' shapes using a simulated model. Our comprehensive analysis extends to giving an analytical equation for determining the dimensions of the microrobots. These simula-

tion results guide selecting appropriate fabrication parameters to produce the microrobots with the desired shape and dimension. We demonstrate the rolling motion of the teardrop-like microrobots and the stick-slip motion of the tadpole-like microrobots in response to a rotating field and an oscillating field, respectively. These dual-motion capabilities can adapt to different environments, such as obstacle crossing and navigation in confined spaces. Lastly, we deploy an ultrasound imaging system to observe their motion and degradation, showing their potential for targeted drug delivery in future clinical trials.

### 1.3 Outline of the Thesis

This doctoral thesis is organized into six chapters to address the research questions. **Chapters 2-5** consist of research studies published in international peer-reviewed journals.

**Chapter 2** focuses on design principles, energy sources, and biomedical applications of soft bioinspired microrobots. We highlight the two main design principles: mimicking living organisms or utilizing motile microorganisms and cells. Incorporating externally-responsive material enables these microrobots to change shapes and imitate the motion of living organisms under external stimuli, such as magnetic, acoustic, and optical fields. Additionally, we elucidate how biohybrid microrobots can be guided through the innate taxis of microorganisms. Shifting to applications, we classify biomedical uses of soft bio-microrobots into three aspects: targeted delivery, biopsy, and biofilm removal. These applications offer exciting possibilities for the future of minimally invasive or non-invasive medicine. Furthermore, we identify several challenges that must be addressed in developing soft bioinspired microrobots, including safety, adaptability, long-term motility, swarm control, and customized design. Last, we provide insights into potential strategies for overcoming these challenges, ensuring the advancement of soft bioinspired microrobots.

**Chapter 3** addresses **RQ.1** by introducing an elastohydrodynamic model that elucidates the variations in the flagellar propulsion of sperm cells after experiencing a time-periodic disturbance force. This model predicts the reduction of the mean flagellar curvature and the bending amplitude of sperm cells. To validate this model, we observe the flagellar propulsion in free sperm cells and collinear bundles formed by two cells

## 1. Introduction

---

along opposite directions. Our experimental findings reveal that sperm cells must adapt their flagellar propulsion to navigate under the influence of a time-periodic external force. These results not only confirm the model's accuracy but also provide valuable insights for soft bioinspired microrobots in scenarios where they must operate under external interactions.

In **Chapter 4** and **Chapter 5**, our focus shifts from biological organisms to soft bioinspired microrobots. **Chapter 4** addresses **RQ.2** by formulating an analytic model that combines magnetism and elastohydrodynamics. The model establishes a quantitative relationship between the step-out frequency of soft bioinspired microrobots and their magnetic properties, geometry, wave patterns, and the viscosity of the surrounding medium. As a measure of microrobots' swimming efficiency, the step-out frequency impacts the maximum velocity of the microrobot. By achieving high velocities, microrobots can overcome external disturbances and reach specific locations promptly when executing targeted delivery applications. While improving swimming performance is crucial, cost-effective and high-throughput fabrication methods for soft bioinspired microrobots are equally essential. We answer **RQ.3** in **Chapter 5**, where we propose a centrifugal extrusion method for fabricating soft bioinspired microrobots. Our findings reveal that the extrusion velocity directly influences the shapes of these microrobots, resulting in designs including teardrop-like and tadpole-like microrobots. Furthermore, we demonstrate that the extrusion velocity of flow can be precisely controlled using a centrifugal pump by adjusting the revolution speeds and nozzle sizes. These soft microrobots demonstrate dual-motion patterns that are controlled by programmed magnetic fields. Specifically, the teardrop-like microrobots exhibit rolling motion in response to a rotating field, while the tadpole-like microrobots display stick-slip motion under an oscillating field. These characteristics enable them to navigate obstacles and move through confined spaces. The successful observation of their motion and degradation through ultrasound imaging represents a significant step toward integrating our soft microrobot systems into clinical medicine.

Finally, we showcase the key findings of the doctoral research, with a specific emphasis on biological organisms and synthetic microrobots. **Chapter 6** begins with a comprehensive summary of the contributions made throughout the research and concludes by providing valuable insights into the prospects of soft bioinspired microrobots.

## 1.4 Research Framework Funding

All the research studies that constitute this doctoral thesis have been supported by funds from the European Research Council (ERC) under the European Union's Horizon 2020 Research and Innovation programme under grant 866494 project-MAESTRO, and financial support from the China Scholarship Council (CSC No. 202006120058). All the studies presented in this thesis have been performed with the experimental setups at the **Surgical Robotics Laboratory (SRL)**, in the Department of Biomaterials and Biomedical Technology (formerly known as the Department of Biomedical Engineering) of the University of Groningen and University Medical Center Groningen, Groningen, the Netherlands.

## 1.5 Scientific Output

The studies presented in this doctoral thesis have been a part of the following articles that have been published in the following journals:

### 1.5.1 Peer-Reviewed Journal Articles

1. **Z. Wang**, A. Klingner, V. Magdanz, M. W. Hoppenreijs, S. Misra, and I. S. M. Khalil “*Flagellar propulsion of sperm cells against a time-periodic interaction force*”, *Advanced Biology*, 7(1): 2200210, January 2023.
2. **Z. Wang**, A. Klingner, V. Magdanz, S. Misra, and I. S. M. Khalil “*Soft Bio-Microrobots: Toward Biomedical Applications*”, *Advanced Intelligent Systems*, 6(2): 2300093, February 2024.
3. **Z. Wang**, W. Li, C. Li, A. Klingner, Y. Pei, S. Misra, and I. S. M. Khalil, *Magnetic Alginate Microrobots with Dual-Motion Patterns through Centrifugally Driven Flow Control*, *Materials & Design*, 246: 113337, September 2024.
4. **Z. Wang**, W. Li, A. Klingner, Y. Pei, S. Misra, and I. S. M. Khalil, *Magnetic Control of Soft Microrobots Near Step-Out Frequency: Characterization and Analysis*, *Computational and Structural Biotechnology Journal*, 25: 165-176, December 2024.

# 1. Introduction

---

## 1.5.2 Abstract

1. **Z. Wang**, A. Klingner, V. Magdanz, M. W. Hoppenreijns, S. Misra, and I. S. M. Khalil “*Flagellar propulsion of sperm cells against a time-periodic interaction force*”, Proceedings of the W. J. Kolff Annual Research Days, Groningen, Netherlands, October 2022.

# 2

## Soft Bio-Microrobots: Toward Biomedical Applications

*Note: Following chapter is adapted from the article “Soft Bio-Microrobots: Toward Biomedical Applications” by **Z. Wang**, A. Klingner, V. Magdanz, S. Misra, and I. S. M. Khalil, published in “Advanced Intelligent Systems”, volume 6, issue no. 2, pages 1–21, February 2024.*

### Abstract

Soft bio-microrobots have the potential to execute complex tasks in unexpected and harsh environments of the human body due to their dexterity and flexibility. The architectural designs of soft bio-microrobots either replicate the motion of natural creatures or capitalize on their motility. Based on this design principle, biologically inspired microrobots that imitate the movements and functions of biological systems, such as starfish, bacteria, and sperm cells, as well as biohybrid microrobots that combine motile micro-organisms or cells with functional components have been developed. Herein, an overview of the design principles, energy sources, and biomedical applications of existing soft bio-microrobots is presented. It is shown that the incorporation of externally responsive material to achieve locomotion or manipulation, imparting versatility and multifunctionality enables biologically inspired microrobots to change their shapes and imitate the motion of living organisms under external stimuli, and it is interpreted how biohybrid microrobots are guided through the tactic behavior of microorganisms or cells. Finally, perspectives on key challenges that soft

bio-microrobots must overcome to achieve *in vivo* biomedical applications are given.

### 2.1 Introduction

Soft robots, created with customized compliant elements integrated into mechanical structures, have made a significant impact in practical applications [52]. They have attracted extensive interest in both research and industrial fields, including deep-sea exploration [53], underwater investigation [54], and surgery [55]. Unlike rigid-linked robots, soft robots are made of flexible or extensible materials and can deform in reaction to stimuli. These flexible or extensible materials would undergo continuous deformation when exposed to external fields, such as magnetic [56], [57], light [58], [59], electric [60], [61], and acoustic fields [62], [63]. This feature can be harnessed to achieve locomotion or manipulation, imparting versatility and multifunctionality to soft robots. Moreover, the compliance of soft robots allows them to conform to complex or irregular shapes. Consequently, soft robots can interact with their surroundings, providing a unique advantage for a wide range of applications that necessitate a high degree of dexterity and flexibility. The property of compliance and flexibility will likely enhance the capabilities of robots irrespective of scale. The miniaturization of soft robots can open up a new avenue for microscale manipulation.

The size limitations of large soft robots pose challenges in surgical applications, as they are unsuitable for use in confined spaces. Developing soft microrobots that can be deployed in compact spaces or hard-to-reach positions is crucial. Microrobots, unlike macroscale robots powered by batteries, must adopt offboard power. This is because the power of onboard batteries drastically attenuates with the volume. When the size of robots is reduced to micro/nanometers, the inertial force is dominated by the viscous force, which is the so-called low Reynolds (Re) number regime [13]. Our intuition built in the macro world is not applicable to microrobots. The reciprocal motion of microrobots will lead to no net displacement. To move in low-Re, the body configuration of microrobots must break the time-reversibility. In nature, many microorganisms provide us with the cue to achieve movement in low-Re. The whip-like motion of the flagellum allows microorganisms to move forward [64]. For instance, the green algae, *Chlamydomonas reinhardtii*, is a two-flagellated microorganism that can

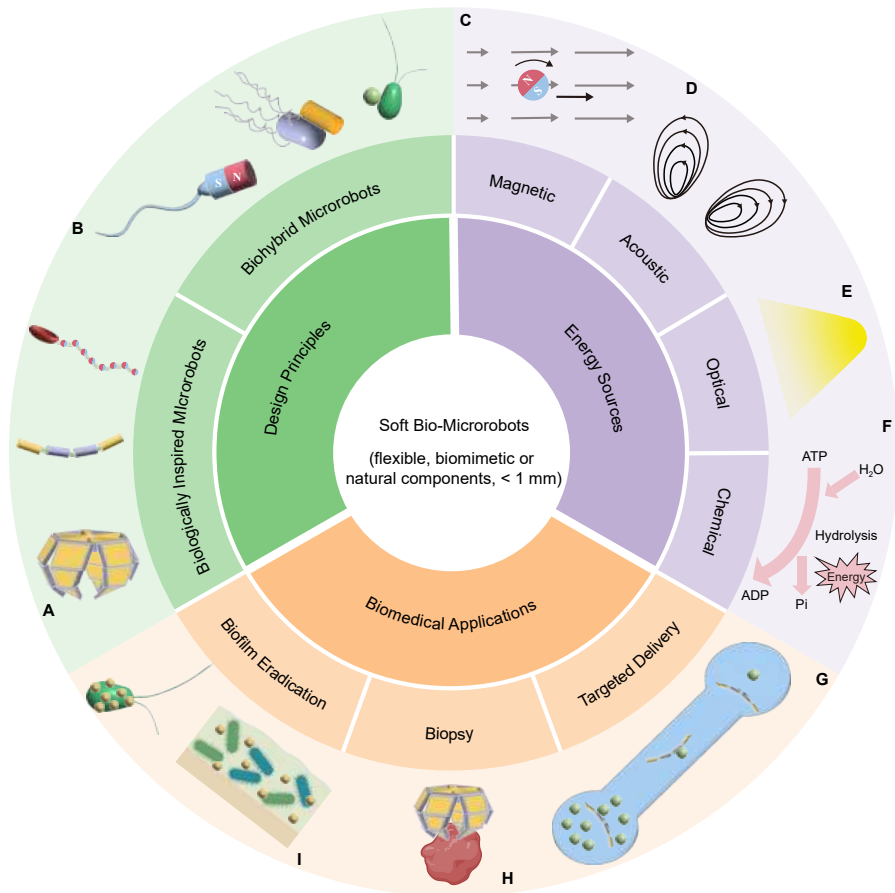


Figure 2.1: Schematic illustration of soft bio-microrobots, including their design principles, energy sources, and biomedical applications. Biologically inspired design results in (A) microrobots with joints, flexible segments, and continuous bodies. Biohybrid microrobots are created through (B) sperm-, bacteria- and algae-driven mechanisms. The energy sources, including (C) magnetic, (D) acoustic, (E) optical, and (F) chemical power, are used to actuate soft bio-microrobots. The biomedical applications encompass (G) targeted delivery, (H) biopsy, and (I) biofilm eradication.

display ciliary and flagellar beat patterns [65]. As a typical puller, it relies on two synchronized flagella in the front to push the fluid backward and pull the cell body forward. On the contrary, spermatozoa have their flag-

## 2. *Soft Bio-Microrobots: Toward Biomedical Applications*

---

ellum in the back and the passive head in the front, forming propagating waves backward, pushing the cell body to move [20]. The design of soft bio-microrobots has been greatly influenced by this flagellum-like motion.

Emulating the motion of microorganisms can enable soft bio-microrobots to break the time-reversibility and propel in low-Re. To this end, the fabrication of soft bio-microrobots necessitates the use of soft and flexible materials that can be difficult to work with conventional fabrication methods. Recently, 3D printing [66], [67], soft lithography [68], [69], electrodeposition [50], [70], biotemplated synthesis [26], [32], [71], and lamination methods [72] have been utilized to fabricate biomimetic soft microrobots. Soft microrobots composed of multiple segments can be produced through the electrodeposition of soft and rigid materials, and they can exhibit flagellum-like motion in response to external stimuli. The cyclic rotation of the externally responsive segment causes the nonresponsive segment to rotate at different amplitudes, leading to nonreciprocal motion. Owing to their soft flagella, microorganisms, and cells, such as sperm [73], bacteria [74], and algae [75], can supply the required mobility for soft bio-microrobots. The integration of motile microorganisms or cells with functional components creates soft microrobots with the ability to move and serve desired biomedical purposes. The inspiration from nature has been effectively incorporated into the design of soft bio-microrobots, promoting the development of soft bio-microrobots [76].

In this review, some relevant examples will be given to summarize the development of soft bio-microrobots, including their design principles, energy sources, and biomedical applications (see Figure 2.1). We first discuss the design principles in Section 2.2. Since biomimetics is the primary design methodology for soft bio-microrobots, they can be divided into two types: biologically inspired and biohybrid microrobots. Biologically inspired microrobots encompass microrobots with joints, microrobots with soft segments, and microrobots with soft and continuous bodies inspired by spermatozoa (Figure 2.1(A)), while biohybrid microrobots include sperm-based microrobots, bacteria-driven microrobots, and algal microrobots (Figure 2.1(B)). The fabrication method, materials, and actuation methodology are discussed for each example of soft bio-microrobots. The energy sources of soft bio-microrobots include magnetic, acoustic, optical, and chemical power (Figure 2.1(C)-(F)), which is discussed in Section 2.3. Catalytic micromotors, which achieve propulsion by means of chemical en-

ergy produced in catalytic reactions, are out of the scope of soft and flexible bio-microrobots. The term “chemical energy (power)” refers to the energy converted in the metabolic process of microorganisms or cells throughout this text. The energy is ultimately transformed into kinetic energy of soft bio-microrobots. Soft bio-microrobots are able to acquire propulsion by flagellum-mimicking or flagellar beating. In the presence of external fields, the flexible component of soft bio-microrobots can respond to them and mimic the flagellar beating, thereby generating movement. Microorganisms and cells with deformable flagella can be combined with functional materials through physical binding or chemical bonding, providing motility for soft bio-microrobots. External stimuli such as oxygen, pressure, chemicals, magnetic fields, light, and temperature changes are essential cues for microorganisms or cells to find food, avoid harmful environments, and interact with surrounding environments. These inherent tactic behaviors of microorganisms and cells ease the directional control of biohybrid microrobots. Section 2.4 introduces and generalizes biomedical applications of soft bio-microrobots in three aspects, including targeted delivery (Figure 2.1(G)), biopsy (Figure 2.1(H)), and biofilm removal (Figure 2.1(I)). In the last section, we give our insights and reveal the confronting challenges in the realm of soft bio-microrobots.

## **2.2 Design Principles of Soft Bio-Microrobots**

Soft bio-microrobots are often created with designs inspired by living organisms or by utilizing microorganisms and cells capable of swimming to produce thrust. Nature has provided several sources of inspiration for the development of soft bio-microrobots. The main fabrication methodology of soft bio-microrobots is based on biomimetics, which guides us in replicating living organisms and constructing similar designs. Biologically inspired microrobots can exhibit movements similar to those of living organisms under external stimuli. Conversely, biohybrid microrobots have biological microorganisms or cells integrated as the power source, structural unit, or loading entity. With simple modifications to biomedical materials, they are capable of performing biomedical tasks [77]. In summary, biologically inspired microrobots imitate microorganisms to obtain motility, whereas biohybrid microrobots rely on the inherent motility of microorganisms or cells.

### 2.2.1 Biologically Inspired Microrobots

Biologically inspired microrobots refer to soft microrobots replicating the motion and function of living organisms. During microrobots fabrication, soft materials are utilized to facilitate the deformation of their bodies, mimicking the movement or manipulation of living organisms. For example, microgrippers with flexible joints imitate human hands and complete the task of grasping. Figure 2.2(A) displays that a microgripper grips like a human fist when the residual stress is released by the trigger of chemicals or temperature. Moreover, the flexibility of soft segments permits deformation in response to external stimuli, thereby enabling microrobots to replicate the swimming strategy of microorganisms that are propelled by flagella (see Figure 2.2(B)). Biologically inspired structures, such as flexible joints, soft segments, and soft continuous bodies, empower microrobots to achieve similar functionality to living organisms.

### 2.2.2 Microrobots with Joints

Flexible joints are able to improve the agility of robots when executing complex manipulations. In the presence of joints, human hands can bend at interphalangeal joints and grasp objects. Through the coordination of joints in each finger, the human hand can grip and unfold to perform pick-and-place. Grippers, which can pick and place objects, are a typical example inspired by the human hand. Conventional grippers are usually tethered to electric cables or pneumatic tubes, which regulate the actuation and operation. However, these tethers restrict the miniaturization and maneuverability of the grippers. The emergence of untethered microgrippers can address these problems and offer a way for manipulating individual cells, and microbes, and carrying out targeted cell examination and evaluation [78], [79].

Randhawa and coworkers have fabricated mobile microgrippers based on Micro-Electro-Mechanical Systems techniques [80]. The microgripper comprises trilayer joints capable of gripping after releasing residual stress of the chromium/copper metallic bilayer, as shown in Figure 2.2(C). Once the microgripper is detached from the substrate, the residual stress is released, but the supportive layer maintains the microgripper open. Gripping can be triggered after dissolving the supportive layer. The incorporation of magnetic materials, such as nickel and iron, enables the microgrippers

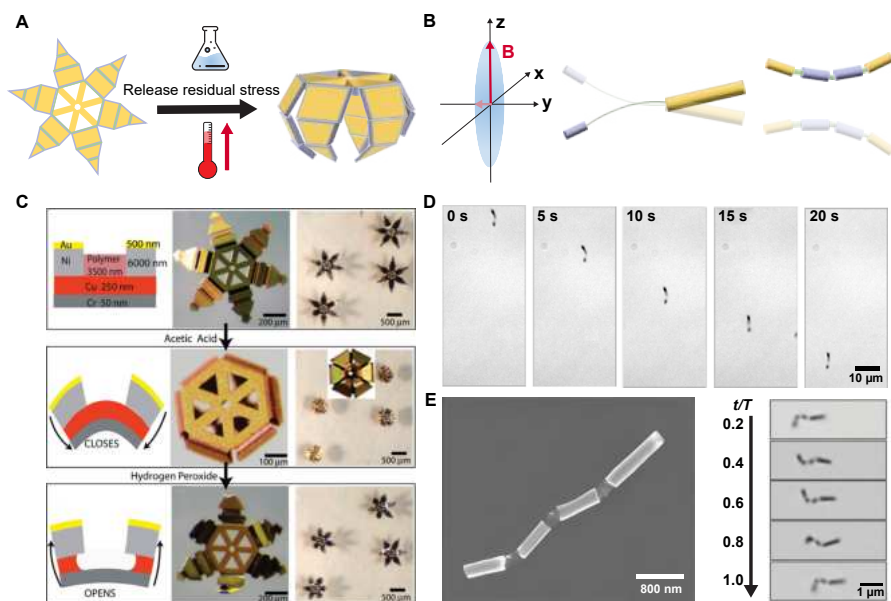


Figure 2.2: Microrobots with joint or soft segments. (A) Schematics of the chemically and thermally triggered closing of a microgripper. (B) Rotating motions of segmented microrobots under a rotating magnetic field. (C) Schematic diagrams and optical microscopy images of the microgripper with a trilayer joint, including the release, opening, and closing of the microgripper. Reproduced with permission from [80]. Copyright 2008, American Chemical Society. (D) Time-lapse images of the three-segment microrobots' motion in a urine sample under the rotating magnetic field. The three-segment microrobot is fabricated through the sequential electrodeposition of gold, silver, and nickel. Reproduced with permission from [50]. Copyright 2010, American Chemical Society. (E) SEM image of the fish-like microrobots and image sequences showing the motion of the microrobot during one cycle by applying an oscillating magnetic field. Reproduced with permission from [81]. Copyright 2016 WILEY-VCH Verlag GmbH & Co. KGaA, Weinheim.

to move with a magnet. By replacing the supportive polymer with a thermochemically responsive one, Leong *et al.* have realized the closing of the microgrippers through the remote trigger of chemicals and temperature under biological conditions [82]. The aforementioned microgrippers are incompatible with living organisms because of the use of chemicals and metals. To utilize microgrippers in a biocompatible manner, Gracias *et al.* [83] have developed a methodology for activating the closing of microgrip-

pers via enzymes. The sequential degradation of two biopolymers under the respective enzymes realizes the closing and opening of microgrippers. Through this operation, an object can be remotely picked and placed at the desired location. However, the metallic microgrippers can only grasp once due to the lack of ability to re-close and re-open.

Irreversible grasping is insufficient to fulfill the demand of complex manipulation *in vivo*, and the production of disposable microgrippers is deemed to be a profligate method. Furthermore, biocompatibility and biodegradability are important considerations for robotic surgery. Researchers have dedicated their efforts to developing biocompatible microgrippers with the capability of repeatable grasping. With thermal-responsive hydrogels as the material of the main body, Fusco *et al.* have fabricated untethered and self-folding microrobot platforms via photolithography [84]. The microrobot platform consists of a group of magnetic alginate microbeads and a near-infrared (NIR) light-responsive hydrogel bilayer structure. The hydrogel bilayer acts as a closed microgripper to grasp magnetic alginate microbeads after releasing the residual stress. The thermally triggered characteristic of hydrogel allows the microgripper to open and release the microbeads over 40°C. Compared to the metallic microgrippers, the hydrogel microgrippers can not pick up objects due to their claws with low stiffness [85]. By embedding a stiff segmented polymer (polypropylene fumarate) in the soft hydrogel, Breger *et al.* [86] have proposed a polymeric microgripper with the gripping ability and biodegradability. When triggered by heat, the microgrippers can fold completely and present strong stiffness to excise cells. They have the ability of repeatable grasping in response to temperature change. Despite the fact that microgrippers have achieved the grasping ability of human hands, their mobility is limited to magnetic force attraction, thereby constraining their remote pick-and-place capability. To enhance the motility of soft bio-microrobots, researchers are developing microrobots with soft bodies that imitate the flagellar motion of microorganisms or cells.

### 2.2.2.1 Microrobots with Soft Segments

By mimicking the flagellar motion, microrobots with soft segments can alleviate the issue of the motility deficiency experienced by microgrippers when executing biomedical tasks. To enable the deformation during the

movement, soft metallic or polymeric segments are incorporated into microrobots [87]. The presence of soft segments allows segmented microrobots to bend when subjected to external stimuli. The heterogeneous response of each segment causes time-dependent deformation and consequently enables the microrobots to mimic flagellar beating. The design of segmented microrobots provides an attractive route for replicating the movement of natural microorganisms or cells that are propelled by flagella.

Wang and co-workers have used a template electrodeposition method to fabricate bio-microrobots with soft segments. The three-segment microrobots consist of gold, silver, and nickel segments that are sequentially deposited into the alumina membrane micropores using the electrodeposition [50]. The length of each segment can be tuned with the deposition time. In the three-segment microstructure, the gold 'head' and nickel 'tail' are linked by a flexible segment made of a partially dissolved silver part. Figure 2.2(D) shows the motion of the three-segment microrobot under a rotating magnetic field. Through the flexible silver segment, the rotating nickel segment drives the gold head to rotate with a different amplitude, thereby breaking the time-reversibility and inducing movement. They have also demonstrated that the forward and backward motion could be achieved by tuning the length of the nickel and gold segments. In contrast to catalytic microrobots that can only work in low ionic-strength conditions, the segmented microrobots break the ionic-strength limitation and display excellent motility. By combining magnetic actuation with catalytic propulsion, Gao *et al.* [88] have developed soft bio-microrobots with hybrid actuation mechanisms. In addition to the previously described three segments, they have added a platinum segment at the golden head. The platinum reacts with hydrogen peroxide to generate oxygen bubbles, which propels the soft microrobots forward [89]. Under the rotating field without the hydrogen peroxide, the soft microrobot reverses its swimming direction and moves towards the nickel side. This hybrid actuation manner can enable microrobots to face the situation of fuel depletion and salt limitation. Soft polymeric materials can also be utilized for the fabrication of soft segments in segmented microrobots. Jang *et al.* [90] have utilized polypyrrole (PPy) to construct the elastic tail of a magnetic three-link microrobot. The elastic tail of the microrobots is connected to two magnetic nickel links via flexible polymer hinges. The hinge's length can be adjusted to change the magnetic dipolar interaction between several nickel links as well as the

flexibility of the soft microrobots. The elasticity of PPy allows the three-link microrobot to bend during each stroke, thereby imitating the flagellar beating. Each stroke is generated when the two nickel links respond to the oscillating field. The segmented microrobots with the flagellum-like flexible tail can also be actuated by an acoustic field [91]. During the actuation excitation, the flexible tail generates propagating waves to propel the head forward as the flagellum of spermatozoa does.

Besides flagellum-inspired microrobots, segmented microrobots can imitate the motion of other creatures. One of the fascinating natural sources is fish species. Most fishes swim with lateral body undulations from head to tail [92]. Li *et al.* [81] have reported a magnetic fish-like microrobot composed of four segments (see the image in Figure 2.2(E)). To emulate the deformable body of a fish, two gold segments are electrodeposited as the head and the caudal fin, two nickel segments make up the main body, and three flexible porous silver segments connect the gold and nickel segments. Under the oscillating field, the fish-like microrobots bend the magnetic body, causing the entire body to swing, as shown in Figure 2.2(E). The other segmented microrobots include limbed microrobots by linking magnetic Janus microparticles with soft hydrogel structures [93]. The magnetic Janus microparticles are stabilized with the desired orientation of the easy axis of magnetization through the rigid structures. When exposed to an oscillating field, the magnetic Janus microparticles bend the soft hydrogel after the alignment with the field. The limbed microrobots present lizard-like motion. Inspired by the efficient freestyle strokes for humans, Li *et al.* have proposed a symmetric multisegmented microrobot with two nickel arms, capable of “freestyle” swimming at low-Re [94]. In response to the field, two arms exhibit nonplanar freestyle stroke but with synchronized oscillatory deformations, leading to more efficient swimming ability than existing helical or planar flexible microrobots. However, these microrobots are still comprised of rigid components that limit their ability to achieve complex deformation, as opposed to those assembled from soft and continuous bodies.

### 2.2.2.2 Microrobots with Soft and Continuous Bodies

Microrobots with soft and continuous bodies enable them to adapt to intricate environments within the human body. As male gametes, sperm cells

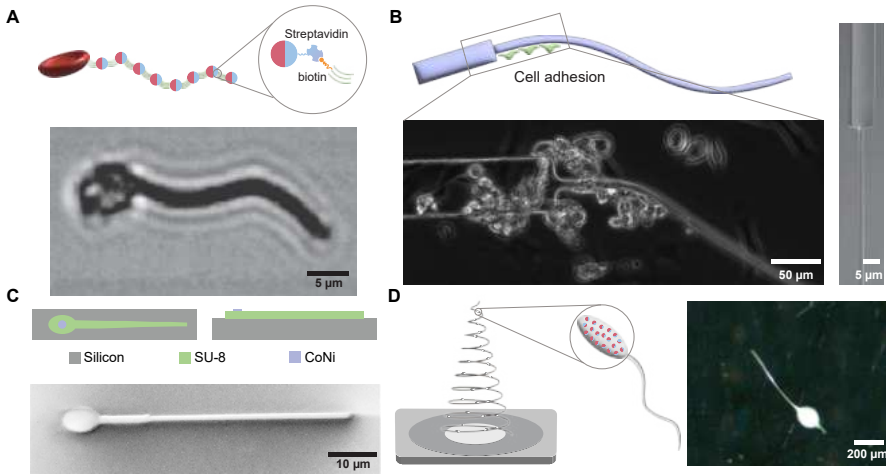


Figure 2.3: Microrobots with soft and continuous bodies. (A) A chain of magnetic particles linked by DNA is attached to a red blood cell to form a sperm-like micro-robot. Reproduced with permission from [42]. Copyright 2005, Nature Publishing Group. (B) The PDMS filament with a rigid head and a compliant tail is actuated by a small, single cluster of contractile cells generating a force through their contraction. Reproduced with permission from [44]. Copyright 2014, Nature Publishing Group. (C) Schematic illustration of the fabrication of MagnetoSperm, and its SEM image. Reproduced with permission from [43]. Copyright 2014, AIP Publishing. (D) Schematic illustration of the fabrication of a sperm-like microrobot through electrospinning, and the optical microscopy image of the electrospun sperm-like microrobot. Reproduced with permission from [46]. Copyright 2016, AIP Publishing.

with continuous flagellar deformation are capable of moving to the ovum and achieving fertilization. In the female reproductive tract, they need to travel through the cervix, uterus, utero-tubal junctions, and oviduct before arriving at the ovum [20]. Soft flagella allow sperm cells to pass through the utero-tubal junction, a narrow lumen filled with viscous mucus [95]. The sperm flagellum is a hair-like appendage deformed by the shear and bending forces generated by dynein motors. The deformation of the flagellum results in propagating waves from the head to the tail. The surrounding fluid, in turn, pushes the cell forward, thereby facilitating the movement of sperm cells through narrow passages in the body.

To imitate the flagellum of sperm cells, multiple streptavidin magnetic particles have been linked by biotin double-stranded DNAs to form a long

## 2. *Soft Bio-Microrobots: Toward Biomedical Applications*

---

and flexible chain [42], as displayed in Figure 2.3(A). The DNA linkers and magnetic particles provide the flexibility and magnetic dipole of the filament, respectively. Moreover, the filament is attached to a red blood cell to constitute a sperm-like microrobot. Under the oscillating field, the filament generates the propagating waves after the alignment of magnetic particles with the external field. This is the first instance of microscopic microrobots emulating the sperm's motion. Apart from the magnetic actuation method, Williams *et al.* [44] have employed cardiomyocytes to actuate the polydimethylsiloxane (PDMS) filament. In Figure 2.3(B), the filament with a short, rigid head and a long but slender tail, is fabricated by filling a sperm-shaped channel in a silicon wafer with liquid PDMS, which is followed by the selective culture of cardiomyocytes on the tail. The contraction of cardiomyocytes deforms the soft tail to produce the propagating waves, thereby inducing propulsive thrust to propel the microrobots. Besides, Figure 2.3(C) exhibits MagnetoSperms with a magnetic head and a flexible tail through photolithography and physical vapor deposition [43]. This sperm-like microrobot can be actuated under an oscillating weak field. The magnetization of the magnetic head aligns along the external field and undulates the flexible tail to generate movement. The sperm-inspired microrobots fabricated via photolithography can also be actuated by acoustic field [96], [97]. The artificial flagellum is driven to oscillate and generate the propagating waves when it responds to acoustic streaming. Khalil *et al.* [46] and Liu *et al.* [45] have fabricated magnetic sperm-shaped microrobots via electrospinning, as shown in Figure 2.3(D). During the fabrication process, the polymer solution, including the flexible polymeric material (polystyrene or polycaprolactone), solvent, and magnetic particles, is ejected from a needle with a blunt tip. On account of the electrostatic repulsion among the surface charges, the jet formed at the needle tip deforms into a Taylor cone [98]. As the jet is stretched into a slender filament, it solidifies quickly under a high voltage and finally deposits on the grounded collector. Bead formation during electrospinning can be attributed to a lot of factors and should be avoided in most applications. For sperm-inspired microrobots, researchers favor the formation of beads that serve as sperm heads. Overall, biologically inspired microrobots have demonstrated exceptional swimming performance. Biohybrid microrobots take it a step further by incorporating living organisms to achieve enhanced motility and functionality.

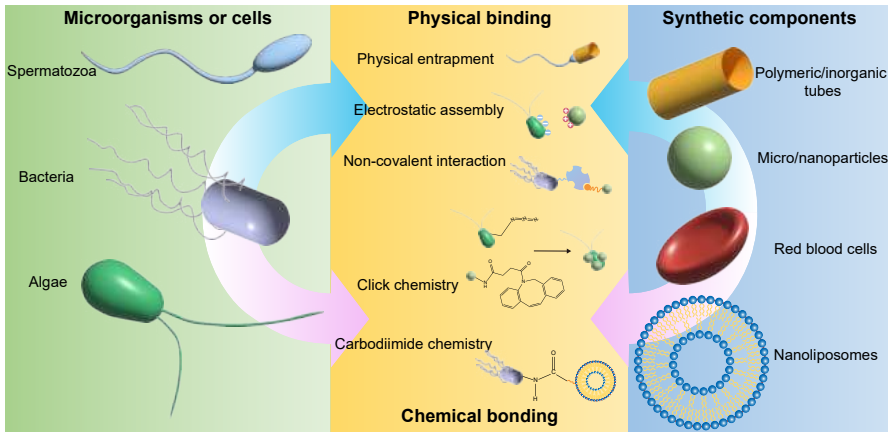


Figure 2.4: Biohybrid microrobots are comprised of motile microorganisms or cells and functional components. Microorganisms or cells such as bacteria, algae, and spermatozoa can be combined with functional components including polymeric or inorganic tubes, micro/nanoparticles, red blood cells, and nanoliposomes through physical binding or chemical bonding. These functional components can endow microrobots with the ability to complete biomedical tasks, steer, and visualize.

## 2.3 Biohybrid Microrobots

Biohybrid microrobots consist of motile microorganisms or cells and functional components. Spermatozoa, bacteria, and algae are widely used to power biohybrid microrobots due to their exceptional motility. Their counterparts, such as polymeric/inorganic tubes, micro/nanoparticles, red blood cells (RBCs), and nanoliposomes (NLs) can endow biohybrid microrobots with additional capability, including magnetic steerability, drug loading and release, and interaction with targeted cells. The functional components can be integrated with motile microorganisms or cells through physical binding or chemical bonding, as shown in Figure 2.4. For example, the magnetic microtube can trap and transport microorganisms along the magnetic field. However, this physical binding approach may be unstable. The integration of chemical bonding in biohybrid microrobots offers a stable connection between microorganisms or cells and functional components, and allows the release of microorganisms or cells under external stimuli. According to the category of microorganisms or cells, biohybrid microrobots encompass sperm-based microrobots, bacteria-driven micro-

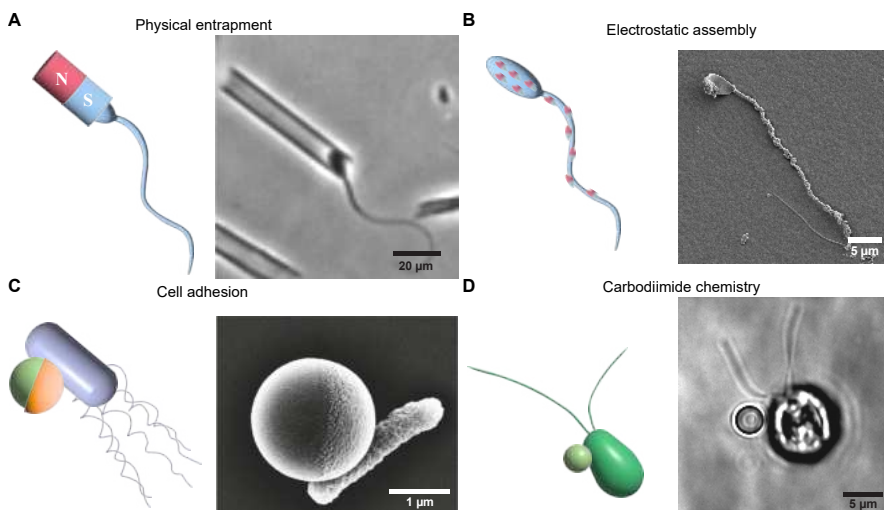


Figure 2.5: The biohybrid microrobots using spermatozoa, bacteria, or algae. (A) Optical image of a spermbot, which consists of a sperm cell and a magnetic microcap. (B) IRONSperm: the cryo-scanning electron micrograph shows a bovine sperm cell covered with iron oxide particles through the electrostatic assembly. (C) SEM image of the bacterium *E. coli* attached to the Janus particle. Reproduced with permission from [99]. Copyright 2015 WILEY-VCH Verlag GmbH & Co. KGaA, Weinheim. (D) Optical microscopy image of a bead attached to the alga *C. reinhardtii*. Reproduced with permission from [100]. Copyright 2005, The National Academy of Sciences of the USA.

robots, and algal microrobots.

### 2.3.1 Sperm-Based Microrobots

Through the coordinated cooperation of dynein motors, including their attachment and detachment from the flagellar microtubule, the sliding of the microtubule is transformed into the bending motion of the flagellum [101], which ultimately leads to sperm cells' swimming. Alive sperm cells can be attached to artificial components to realize directional control, biomedical tasks, and visualization. Spermbots [73], which consist of a sperm cell and an artificial magnetic microtube (see Figure 2.5(A)), is the first example of sperm-actuated microrobots. The magnetic cap is created through the rolled-up technology [102] and randomly captures alive sperm cells. The

incorporation of an iron layer in the cap enables live sperm cells to realize directional control under a magnetic field. A point-to-point closed-loop control has been implemented to precisely control the spermbot using four electromagnetic coils and visual feedback through a microscopic camera system [103]. A thermally responsive polymer has been utilized to enable a remote release mechanism for the sperm cell [104]. After the temperature is elevated by a few degrees, the tubular cap unfolds and releases the captured sperm cell. The remote-controlled capture and release without damage to sperm cells are significant for assisted fertilization. To realize spatially and temporally controlled release, a magnetically driven microcarrier and a synthesized protein-based hyaluronic acid (HA) microflake have been employed to transport and capture sperm cells, respectively [105]. A helical microcarrier is fabricated by two-photon polymerization lithography and coated with a thin iron film. It transports the sperm-loaded microflakes consisting of hyaluronic acid. Sperm cells can bind to HA microflakes through their innate HA receptors [106]. Upon reaching the targeted location under magnetic guidance, the HA microflake undergoes enzymatic hydrolysis, leading to the release of sperm cells from the microcarrier. The ultimate goal of sperm-driven microrobots is to aid in fertilization as sperm cells are the reproductive cells in males [30]. As a method to trigger single sperm maturation and protection from oxidative stress with the help of artificial microstructures, Ridzweski et al. have used gelatin spermbots for the pH-triggered release of heparin [107]. The gelatin-based spermbots also allowed the successful degradation of microrobots. To address the problems of low sperm count, also called oligospermia, Rajabasadi *et al.* [108] have developed a 4D-printed multifunctional microcarrier to transport and deliver multiple sperm cells. The captured sperm cells undergo capacitation *in situ* after contacting the loaded heparin in the microcarrier. The hyaluronidase-loaded polymersomes functionalized on the microcarrier's surface can facilitate the degradation of cumulus cells, addressing the issue of infertility due to the lack of hyaluronidase. Even though the incorporation of a magnetic microcarrier enables the directional control of sperm cells, the sperm cells reduce their speed when they are captured by the artificial microcap or microcarrier. Motile sea urchin sperm have also been used in combination with magnetic nanoparticles to create chemotactic sperm microrobots for active drug delivery [109]. As much as spermbots are beneficial due to their onboard power source, their lifetime is limited to

a few hours which makes their fabrication and implementation for *in vivo* applications challenging.

Another typical sperm-based microrobot is a type of sperm-templated microrobot. Figure 2.5(B) shows the biotemplated IRONSperm, which is comprised of nonmotile sperm cells and rice grain-shaped magnetic nanoparticles via the electrostatic self-assembling [110]. Sperm cells are not alive after binding to magnetic nanoparticles, as opposed to spermbots. Therefore, IRONSperm does not undulate its flagellum through the coordination of dynein motors. The power of IRONSperm is provided by an external field, guaranteeing its long-term motility. In the presence of the field, the passive flagellum will bend under the alignment of magnetic nanoparticles with the external field and generate propagating waves to propel the cell body. Khalil *et al.* [111] have demonstrated that IRONSperms with the passive flagellum can exhibit waveforms to match that of motile cells by adjusting the external field. With the template of the biological entity, chemotherapeutic agents can be absorbed [110]. The biocompatibility of IRONSperms sets it apart from sperm-inspired microrobots made entirely of synthetic materials and shows its huge prospects for biomedical applications. IRONSperm clusters can be formed under the influence of magnetic attraction and electrostatic self-assembly [112]. Compared to one single IRONSperm, the cluster can highly increase the drug loading capability and be localized using ultrasound imaging for *in vivo* applications. Although IRONSperm has shown promise for targeted drug delivery, it still needs further development for efficient and controlled drug loading and release at the target sites.

### 2.3.2 Bacteria-Driven Microrobots

Bacteria-driven microrobots stand out from various types of biohybrid microrobots, considering their efficient propulsion speed, interaction ability, and sensing capability in physiological and pathophysiological conditions [113]. Some bacteria have demonstrated that they can adhere well to a polymeric or metal layer due to their charged and hydrophobic cell membrane. By combining bacteria with polymeric particles, polymer tubes, RBCs, NLs, or nanoparticles, bacteria-driven microrobots can be bestowed with additional functionalities, such as magnetic maneuverability, drug encapsulation and release, and fluorescence. The common bacteria

used in the development of bacteria-driven include *Serratia marcescens* (*S. marcescens*), *Escherichia coli* (*E. coli*), and *Magnetococcus marinus*. *S. marcescens* is a species of gram-negative bacterium with appendages of helical flagella. The rotation of these flagella is powered by a rotary motor embedded in the bacterial cell wall [114]. The peculiar helical structure can break the time-reversibility in the low-Re regime. However, the motion of *S. marcescens* is subjected to stochastic direction changes, which impedes their precise control. To address this problem, *S. marcescens* have been attached to magnetic beads through streptavidin-biotin binding [115]. The bacteria provide the power of motility, while the magnetic beads offer the magnetic dipole to realize the steering control of the bacteria under the magnetic field. They have demonstrated the controlled steering of the microrobots driven by *S. marcescens*. The dimension of these microrobots is smaller than sperm-like microrobots, thereby allowing them to navigate in tiny passages. Moreover, Zhuang *et al.* have demonstrated the microrobots driven by *S. marcescens* exhibit both unidirectional and bidirectional pH-tactic behaviors in the configured pH gradients [116]. *S. marcescens* can stop and resume their motion after being triggered by chemical signals [74], [117] and ultraviolet light [118]. The pH-tactic, chemotactic, phototactic, and magnetic control can be combined for the motion control of microrobots driven by *S. marcescens* in the future.

Not all bacteria can adapt to the human body temperature, certain bacteria's motility is sensitive to temperature. Nonpathogenic *E. coli*, which are commonly found in the lower gastrointestinal tract, can maintain or even increase their swimming speed at 37°C. *E. coli* is one type of peritrichously flagellated bacterium that propels itself through the rotation of helical flagella. During the “run” motion, all flagella rotate counterclockwise and form a bundle. In this case, *E. coli* move in a straight path. At the “tumbling” motion, one or more flagellar motors reverse their rotation. As a result, the flagella unbundle, enabling the bacterium to change its orientation [119]. *E. coli* are promising entities for the fabrication and actuation of soft bio-microrobots due to their motility and adaptability. The ability of *E. coli* to adhere to a variety of metals, such as platinum, iron, titanium, and gold, has been demonstrated. Stanton and co-workers have reported a biohybrid Janus robot by attaching *E. coli* to polystyrene particles or silicon dioxide covered with a metal layer [99], as shown in Figure 2.5(C). These bacteria-driver microrobots show the ability to de-

2

liver the particles along the magnetic field when the iron is coated on the particles. They have also fabricated electropolymerized microtubes to trap *E. coli* [120]. The polydopamine-modified microtube is positively charged and acts as a surface attractant for the negatively charged *E. coli*. Besides, the layer of nickel nanoparticles for magnetic guidance and urease to act as a bacterium “killer” are included in the microtube. The urease decomposes urea and creates a local distribution of ammonia to inhibit the bacterium swimming. Compared with the spherical chassis, the microtubular chassis can reduce the rotating motion and the torque when attaching to the bacteria. RBCs are excellent companions for bacteria due to their abundance, biocompatibility, biodegradability, non-immunogenicity, inert intracellular environment, and handling convenience. Alapan *et al.* [121] have reported a biohybrid microrobot composed of motile *E. coli* and RBCs loaded with an anticancer drug and iron oxide nanoparticles for actively guided drug delivery. The onboard power is provided by the bacteria, while the magnetic guidance is realized through the loaded magnetic nanoparticles. On-demand hyperthermia activated by the NIR light is realized to terminate the bacteria after drug delivery. A genetically engineered *E. coli* based biohybrid microrobot has been decorated with magnetic nanoparticles for externally guided magnetic control, and pH- and light-responsive nanoliposomes for on-demand cargo delivery in tumor spheroids [122].

Magnetotactic bacteria are motile prokaryotes that are able to biomineralize nanometric magnetic particles, known as magnetosomes [123]. These magnetosomes are organized as well-ordered chains, allowing bacteria to behave like a compass needle and navigate along the earth’s magnetic field. Moreover, magnetotactic bacteria are nonpathogenic and easy to chemically functionalize. All of these properties make magnetotactic bacteria viable candidates for *in vivo* biomedical applications. *Magnetococcus marinus* strain MC-1 is one type of spherical magnetotactic bacteria (MTB) with two flagella bundles, synchronously pushing the cell forward. Martel and co-workers have realized the control of MC-1 through a customized electronic system [124]. They have also found that the swimming of MC-1 can stop with sufficient field strength. A closed-loop navigation control on the MC-1 has been achieved based on the visual feedback from a clinical magnetic resonance imaging system. After that, a swarm of MC-1 bacteria is formed in 2D [125] and 3D [126] configurations through a time-varying magnetic field. In addition, bacteria aggregation is suited to undertake

tasks in intricate microvascular networks of the human body. The bacterial-driven microrobots swarm can achieve high targeting efficacy and deliver an adequate dose of therapeutics to tumor cells. The other magnetotactic bacterium, *Magnetospirillum magnetotacticum* (MS-1), has a helical shape and is propelled by a polar flagellum at each end of the cell. Khalil *et al.* has realized a point-to-point control on the movement of MS-1 after understanding the characteristic of its magnetic moment [127]. A null-space control system is presented to achieve point-to-point control of MS-1 by capitalizing on the redundancy of magnetic-based manipulation systems. When designing bacteria-driven microrobots, the careful evaluation and selection of motile bacteria are crucial. In particular, the selection process should take into account the intended biomedical applications, size, swimming speed, and ability to interact with polymeric materials. Schürle *et al.* have demonstrated the magnetic torque-driven enhanced crossing of biological barriers to enter deep tumor tissue by the implementation of liposome-functionalized *Magnetospirillum magneticum*-driven microrobots [128].

### 2.3.3 Algal Microrobots

As eukaryotic swimmers with facile culture processes, microalgae present high speed, phototactic guidance capability, and autofluorescence. For example, *Chlamydomonas reinhardtii* (*C. reinhardtii*) is a unicellular green alga with a spherical-shaped head and two flagella. The full beat cycle of *C. reinhardtii* is composed of a power stroke and a recovery stroke. During the power stroke, each flagellum extends and bends at the proximal end, sweeping back like the breaststroke. The flagellum then folds during the recovery stroke to reduce viscous drag. This strategy is used to break the time-reversibility. *C. reinhardtii* can perform photosynthesis for oxygen production, which can relieve the hypoxic conditions at the wound site. Due to these characteristics, *C. reinhardtii* can be an ideal choice to achieve targeted cargo delivery. Weibel *et al.* have utilized *C. reinhardtii* as a “microoxen” to move microbeads [100]. The microoxen can be steered using the phototaxis of *C. reinhardtii*. Polymeric microbeads are loaded to the microoxen via a photocleavable linker and released photochemically in Figure 2.5(D). *C. reinhardtii* can also be combined with magnetic materials to mimic magnetotactic bacteria. Santomauro *et al.* have found *C. rein-*

*hardtii* can be magnetized after incorporating terbium [129]. The modified algae can show comparable magnetic moments as MTBs and be magnetically steered. *Eudorina elegans* (*E. elegans*) is a multicellular green alga species with a size ranging from 10 to 200  $\mu\text{m}$ . *E. elegans* exists in the form of colonies, which consist of 16, 32, or 64 individual cells with a similar size as *C. reinhardtii*. They display positive phototaxis and swim towards a light source. This property makes it possible to control the movement of *E. elegans* and exploit them in micro/nanodevices, biological chips, and biomedical applications. Xie *et al.* [130] have built an algae guiding system to steer *E. elegans*. The motion along predefined trajectories such as zigzags and triangles could be realized under optical control with a specific wavelength. The inherent autofluorescence ability of the microalgae enables them to be visualized and tracked in real time. These algal microrobots with biocompatibility and controllability hold great promise for cancer treatments. Akolpoglu *et al.* [131] have created a high-throughput fabrication of *C. reinhardtii*-based microrobots by electrostatic assembly with magnetic nanoparticles. On-demand cancer drug delivery has been demonstrated with these biohybrid microrobots.

### 2.4 Energy Sources for Soft Bio-Microrobots

Because of their tiny size, soft bio-microrobots can not use onboard batteries to power themselves as macro robots do. Existing soft bio-microrobots move by converting the power of the external field to their kinetic power or using the self-propulsion of microorganisms or cells. The common external fields include magnetic, optical, and acoustic fields. The incorporation of the external field could be a stimulus to deform the body of soft bio-microrobots for movement or manipulation. In addition, by consuming molecules that contain chemical energy, microorganisms or cells achieve inherent mobility, which is utilized in the self-propulsion approach. Upon the modification with externally responsive materials, live microorganisms and cells can be transformed into maneuverable microrobots when subjected to external fields. In the next sections, we give a comprehensive explanation in terms of energy sources used by soft bio-microrobots.

### 2.4.1 Magnetic Actuation

Magnetic actuation is a practical choice for controlling microrobots in minimally invasive medicine because of its high penetration capability and safety with biological samples [132], [133]. The two types of magnetic actuation are force actuation and torque actuation. In this section, we shall present the fundamental laws that govern the magnetic force and torque exerted on the soft-magnetic bodies of microrobots. Magnetic microrobots experience a magnetic force,  $\mathbf{F}$ , and a magnetic torque,  $\boldsymbol{\tau}$ , provided that a magnetic field is applied. The magnetic force,  $\mathbf{F}$ , exerted on the microrobot can be expressed as,  $\mathbf{F} = V(\mathbf{M} \cdot \nabla)\mathbf{B}$ , where  $V$  and  $\mathbf{M}$  are the volume and the magnetization of the magnetic material of the microrobot, respectively, and  $\mathbf{B}$  is the magnetic flux density of the external magnetic field. The magnetization depends on the external field, as the relationship  $\mathbf{M} = \chi_a \mathbf{H}$  holds, where  $\chi_a$  and  $\mathbf{H}$  are the susceptibility tensor of the material and the magnetic field strength, respectively. In a magnetic gradient field, the magnetic microrobot experiences both magnetic torque driving the magnetization to align with the external field and the magnetic force pointing to the direction of increasing strength, as shown in Figure 2.6(A). The magnetic force has been utilized for pulling the microrobots [8], [134], resulting in linear movement of microrobots. Its direction can be tuned with that of the gradient.

In a uniform magnetic field, magnetic torque is the only form of energy transmission to power magnetic microrobots. The magnetic torque,  $\boldsymbol{\tau}$ , can be given by,  $\boldsymbol{\tau} = V\mathbf{M} \times \mathbf{B}$ . The magnetic microrobot is magnetized and generates magnetization when subjected to the magnetic field. In the presence of a magnetic torque, the magnetization of the microrobot will align with the direction of the external field. To ensure the continuous movement of microrobots, the magnetic field should vary in time or space. Figure 2.6(B) exhibits the common magnetic fields used for torque actuation, including rotating field [21], [29], conical rotating field [110], and oscillating field [43], [135]. The rotating field is characterized by a field vector that rotates in a plane, frequently at a constant angular velocity. On the other hand, the conical rotating field refers to an out-of-plane field that follows a cone, which is typically produced by a rotating field vector and a static field vector perpendicular to it. Lastly, the oscillating field is defined by a field vector moving up and down in the plane and is commonly used

## 2. Soft Bio-Microrobots: Toward Biomedical Applications

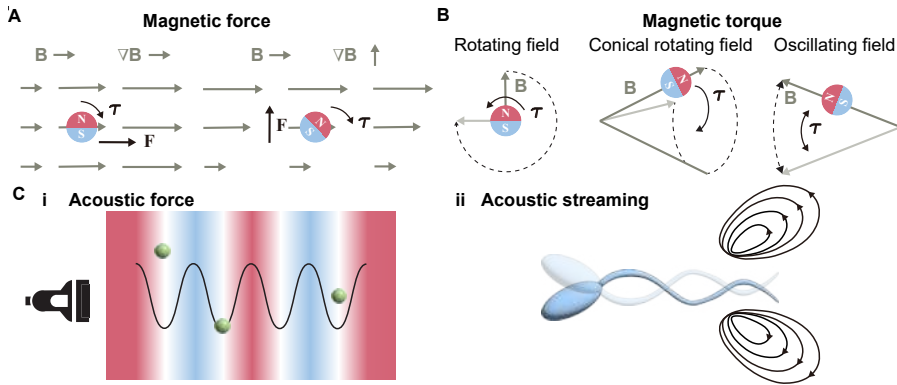


Figure 2.6: Actuation mechanisms of soft bio-microrobots. (A) Magnetic force actuation. The magnetic force is generated by the field gradient along the direction of the field and the field gradient perpendicular to the direction of the field. (B) Magnetic torque actuation. The magnetic torque is generated by the rotating field vector in a plane, the rotating field along the mantle of a cone, and an oscillating field in a plane. (C) Schematics of acoustically actuated mechanisms. (i) Acoustic radiation force acts on spherical microrobots, which aggregate at the acoustic pressure nodes and antinodes. (ii) Schematic of acoustic streaming at the tip of a sperm-like microrobot. The acoustic streaming generated by the deformation of the flagellum propels the microrobot forward.

to produce flagellar motion in soft bio-microrobots [136]. Although the magnetic field has been proven to be an effective energy source in wireless actuation, other energy sources can be used individually or in combination to enhance the capability of the microrobots.

### 2.4.2 Acoustic Actuation

Since ultrasound technology has been widely used in medical diagnosis and therapeutics, researchers have focused on the development of microrobots powered by an acoustic field. The acoustic field can be exploited in the forms of acoustic radiation force and acoustic streaming [137]. When a standing wave is applied to a resonator, it reflects back and forth and creates a hydrodynamic drag force, known as the acoustic radiation force,  $\mathbf{F}_{\text{rad}}$ , in a fluid for driving microrobots to the acoustic pressure nodes and antinodes, as shown in Figure 2.6(C)-i. The direction of force can be changed with the corresponding wave function [138]. The magnitude of

the acoustic radiation force is given by,  $F_{\text{rad}} = 2\alpha I/c$ , where  $\alpha$  is the absorption coefficient of the medium,  $I$  is the temporally averaged intensity at the spatial location, and  $c$  is the sound speed [139]. The radiation forces include the primary and secondary radiation forces. The primary radiation forces are generated due to the interaction between the acoustic field and the microrobots in the medium. The reflected wave from the microrobot can induce the secondary radiation forces on an adjacent microrobot [63]. The primary radiation force propels microrobots to the nodal position, while the secondary radiation forces make microrobots mutually attract or repel, and generate a stable microrobot swarm [140]. However, the standing wave can not be established in the human body in a predictable manner, as complex and heterogeneous environments can affect the formation of standing waves. For example, the presence of internal organs, bones, and tissues with different mechanical properties can scatter and absorb the acoustic wave. Therefore, the acoustic force is a challenging actuation method for *in vivo* biomedical applications of microrobots.

Acoustic streaming is a steady fluid flow formed by viscous attenuation of an acoustic wave [141]. Due to the excitation of the acoustic streaming, the flagellum-like segmented microrobots produce propagating waves (see Figure 2.6(C)-ii), thereby propelling themselves forward. Soft bio-microrobots can be fabricated *in situ* and actuated by acoustic streaming. In the presence of the streaming effect, the flagellum of the soft microrobot oscillates and generates propulsive thrust [97]. Acoustic streaming can also be enhanced with solid boundaries such as a sharp extrusion [96], [142] or the “horse-shoe” structure [143]. The vibration of these structures induces counter-flowing vortices in the near field that result in a steady flow in the far field, thus generating controllable acoustic waves. Although the acoustic actuation method has been extensively used in soft microrobots, it still faces the challenge of directional control of soft bio-microrobots. The precision of motion control influences the *in vivo* application prospects of soft bio-microrobots.

### 2.4.3 Optical Actuation

The optical actuation can be exploited in synthetic microrobots and phototaxis microorganisms. In terms of synthetic microrobots, light-responsive materials are implemented to constitute the main body of the microrobots.

The optically actuated microrobots rely on the deformation of body parts to achieve movement [144]. The most used light-responsive material is liquid-crystalline elastomers (LCEs) that can deform when exposed to light. LCEs possess the entropy elasticity of an elastomer and the self-organization of the liquid crystalline phase. Their entropy elasticity enables them to stretch and bend, while the self-organizing characteristic provides the ability to respond to external stimuli and adjust their structure. There are two main mechanisms for the shape deformation of light-responsive materials. The first one is the shape change of part of the molecule after exposure to light, and the second one utilizes intermediate heating induced by light absorption to change a shape. The photothermal effect can result in an order-disorder phase transition in LCEs [145], as shown in Figure 2.7(A)-i. Palagi *et al.* [58] have shown that soft microrobot can mimic the metachronal waves of ciliated protozoa. The biomimetic motion is achieved by incorporating photoactive LCEs and controlling their shape through spatially and temporally modulated monochromatic light. The LCEs deform upon illumination based on the principle of the photoisomerization of the covalently bound azobenzene dye and a light-induced thermal effect.

Some microalgae possess positive (swim towards the light source) or negative (swim away from the light source) phototaxis when triggered by an external light source. For example, *C. reinhardtii* exhibits the positive phototaxis to increase photosynthesis, yet it also swims away from light to avoid damage to molecular complexes used in photosynthesis [146]. The photoreceptors on cell membranes can detect the direction of illumination, and enable cells to find an appropriate condition to complete photosynthesis (see Figure 2.7(A)-ii). The nutrition produced during photosynthesis provides the energy for locomotion. The second requirement for phototaxis is motility, which is provided by the flagella of microorganisms or cells. We will elaborate on the locomotion mechanisms of microorganisms and cells in the next section.

### 2.4.4 Self-Propulsion

Microorganisms and cells are able to move owing to their sophisticated appendages, known as flagella. The soft flagella generate bending waves through self-organization and powering of their internal molecular motors.

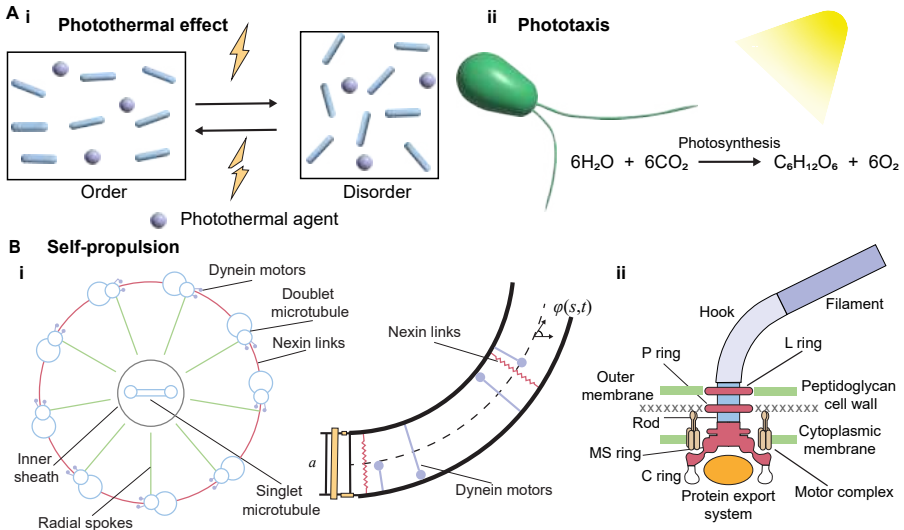


Figure 2.7: Actuation mechanisms of soft bio-microrobots. (A) The mechanism of optical actuation. (i) Liquid-crystalline elastomers deform after Photothermal-induced order-disorder phase transition triggered by lights. (ii) Phototaxis of microalgae is triggered by their photosynthesis. (B) Chemically powered self-propulsion of microorganisms or cells. (i) Schematics of the cross-section of the eukaryotic flagellar axoneme. The flagellum is bent by the shear force, which is produced by the attachment and detachment of dynein motors. (ii) Schematic side view of the  $\text{H}^+$  or  $\text{Na}^+$  bacterial flagellar motor. The motor, spanning the outer membrane, peptidoglycan cell wall, and cytoplasmic membrane, has a series of hinges with a rod inside. Attached to the rod is a curved ‘hook’ protein linked to the flagellum. The flagellum is made of thousands of repeating units of the protein flagellin.

After interacting with the surrounding fluid, the deformable flagella will induce propulsive thrust. Therefore, motile microorganisms and cells can serve as viable candidates for microrobots used for biomedical applications. The generic flagellated microorganisms and cells include spermatozoa [147], flagellated bacteria [148], [149], and algae [65]. To understand the locomotion mechanism of eukaryotic flagella (sperm cells and algae), the flagellar structure should first be clarified. Figure 2.7(B)-i shows the illustration of the flagellar axoneme, which is known as the “9+2” structure [20]. Nine pairs of microtubule doublets and a central pair of singlet microtubules comprise the flagellar axoneme. The adjacent microtubule doublets are

## 2. Soft Bio-Microrobots: Toward Biomedical Applications

---

connected by nexin links, while radial links bind the central pair of single microtubules to the surrounding microtubule doublets. Dynein motors are distributed along the nine pairs of microtubule doublets. They undergo cycles of attachment and detachment to generate shear force with the force density,  $f$ , by hydrolyzing the adenosine triphosphate, thus causing the sliding between the microtubule doublets and bending of the flagellum. The flagellum oscillates in a time-periodic manner such that the elastic force and the bending force are balanced by the viscous force. The tangent angle,  $\varphi(s, t)$ , is used to characterize the flagellar deformation of a flagellum, as shown in Figure 2.7(B)-i. The flagellum elasto-hydrodynamics is given by the balance of the elastic force per meter square,  $-E\varphi_{ssss}$ , the internal bending force per meter square,  $af_{ss}$ , and the viscous force per meter square,  $\xi_{\perp}\varphi_t$ , where  $E$  is the bending stiffness of the flagellum, the subscript  $s$  and  $t$  denote spatial derivative and temporal derivative, respectively, and  $a$  and  $\xi_{\perp}$  are the constant of the two polar filaments and the normal drag coefficient of the flagellum, respectively [150]. This nonlinear differential equation can assist in analyzing the deformation of the flagellum during the movement. The solved position of the flagellum can be implemented into other theories, such as resistive force theory [147], and regularized Stokeslets theory [151], to characterize its propulsion ability. The excellent motility and deformability allow spermatozoa and algae to swim in the compact space of the human body. Prokaryotic (bacterial) flagella are fundamentally different from eukaryotic flagella in that the thrust of the tail is generated at the base of the tail. It consists of a rotary enzymatic motor which is embedded in the bacterial membrane and is fueled by  $H^+$  or  $Na^+$  transport driven by an electrochemical gradient [152], as shown in Figure 2.7(B)-ii. The bacterial flagella follow this rotation passively, which is in contrast to the bending wave motion of spermatozoa with active molecular motors all along the tail.

### 2.5 Biomedical Applications of Soft Bio-Microrobots

The above sections discuss the design principles and energy sources of soft bio-microrobots, forming the basis for their use in biomedical applications. The flexible structure of soft bio-microrobots allows them to navigate through narrow blood vessels or bend around tight corners within the human body. Furthermore, the soft composition of their bodies can reduce

the risk of scratching healthy tissue or cells when performing biomedical tasks *in vivo*. These advantages make soft bio-microrobots highly effective and versatile tools for biomedical applications. In this section, we will introduce the related biomedical applications of soft bio-microrobots, including targeted delivery and surgery.

### 2.5.1 Targeted Delivery

Because cancer treatment still relies on the circulatory system of the human body to deliver anti-cancer drugs, the efficacy of reaching the cancer lesions is extremely low through this passive manner [153]. Meanwhile, a drug that is not targeted specifically to tumor cells can cause side effects on healthy cells and organs. An active delivery system using the proposed microrobots can increase the accumulation of drugs in the cancer lesions, as well as reduce the risk of side effects. Therefore, microrobots capable of precise control and cargo loading are suitable medical tools for actively targeted cargo delivery. The delivered cargo can be drugs, micro/nanoparticles, and living cells. Untethered microgrippers can be steered using a magnet, and they use the stiff phalanges to pick up beads after the gripper closure is triggered by chemicals and temperature [82]. Figure 2.8(A) shows the thermally triggered capture of a dyed bead from several clear beads. The beads inside the grippers can be released intact by mechanical disruption. Unlike microgrippers, segmented microrobots can load cargo through physical and chemical binding. Gao *et al.* have reported on the targeted delivery of drug-loaded magnetic polymeric particles by utilizing segmented microrobots [154]. The drug-loaded magnetic microparticles can be magnetically attracted by the nickel segment when the segmented microrobots pass close by them under the magnetic field. After reaching the HeLa cells, the flexible silver segment of the microrobots is bound to the cell and enables the slow release of drugs from the microparticles, as shown in Figure 2.8(B).

Compared with synthetic soft microrobots, sperm cells are more advantageous to operate in physiological environments due to their nontoxic qualities. Xu *et al.* have proposed an efficient drug delivery system using spermbots [155], as sketched in Figure 2.8(C). The spermbot carries an anticancer drug, doxorubicin hydrochloride (DOX-HCL), through physical encapsulation. This drug delivery system has high drug-carrying stability during the delivery process due to the compact membrane of sperm

## 2. Soft Bio-Microrobots: Toward Biomedical Applications

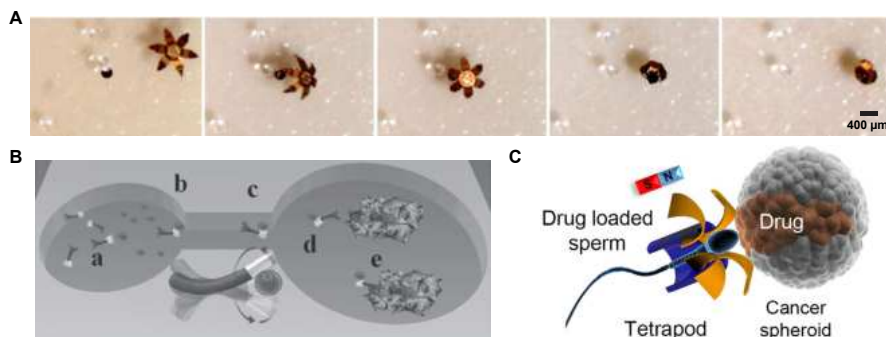


Figure 2.8: Targeted delivery applications of soft bio-microrobots. (A) Optical microscopy image sequence showing the thermally triggered capture of a dyed bead from several clear beads. Reproduced with permission from [82]. Copyright 2009, The National Academy of Sciences of the USA. (B) Schematic depicting the process as a segmented microrobot (a) captures the drug-loaded magnetic polymeric particles in the loading reservoir, (b) transports it through the channel, (c) approaches the targeted cell, (d) sticks on the targeted cells, and (e) releases the drug. Reproduced with permission from [154]. Copyright 2012, WILEY-VCH Verlag GmbH & Co. KGaA, Weinheim. (C) Schematic of a drug-loaded sperm (spermbot) targeted delivering to a cancer spheroid. Reproduced with permission from [155]. Copyright 2017, American Chemical Society.

cells. The magnetic cap is designed to have a tetrapod microstructure and releases the captured sperm cells when it hits a substantial barrier. This capability is exploited to liberate the drug-carrying sperm cells in the scenario when the spermbots strike the cancer spheroid. To increase successful cargo load, Xu *et al.* [156] have fabricated a spermbot system that transports up to three human sperm cells using a streamlined microcap. The spermbot system can carry a hydrophilic drug, DOX-HCL, via uptake by sperm cells, and a hydrophobic drug, camptothecin, on the microcap for the treatment of cervical cancer and ovarian cancer. This method of co-drug administration opens new doors for future targeted drug delivery. The biotemplated IRONSperms have loaded DOX-HCL for therapeutic tasks [110]. DOX-HCL molecules can be absorbed and distributed in the whole body of IRONSperms through physical encapsulation. The tight sperm membrane ensures the stability of drug encapsulation and avoids drug leakage during the movement.

Proliferative tumor cells can rapidly consume oxygen, thereby resulting in a hypoxic region with less oxygen compared to normal cells. MTBs have been used to transport drug-loaded NLs into hypoxic regions of tumors via their magneto-aerotaxis [157]. This feature can help MTB-driven microrobots to improve the targeting ratio of drugs to the tumor cells. Meanwhile, the existence of magnetosomes enables MTBs to swim along the external field and precisely navigate to the tumor cells. As the non-pathogenic bacteria in the human body, *E. coli* has been demonstrated to carry microparticles [158], [159], NLs [122], and RBCs [121], [160] for targeted active delivery. Through streptavidin-biotin binding, the bacterial membrane can be connected with the RBC membrane, magnetic nanoparticles, or NLs. Apart from the above linking manner, the bacterial membrane can also be attached to the surface of synthetic microparticles through electrostatic interaction [158], [161], hydrophobic interaction [162], [163], and carbodiimide chemistry [164], [165]. The magnetic guidance ability can be achieved by embedding magnetic nanoparticles into microparticles and RBCs or directly linking magnetic nanoparticles with the membrane of bacteria. The anti-cancer drug model, DOX, can be encapsulated into RBCs to minimize the leakage during the delivery process, and released when exposed to pH or NIR light. Akolpoglu *et al.* have proposed *E. coli*-driven microrobots capable of colonizing tumor spheroids for on-demand release of the drug molecules [122] (see Figure 2.9(A)). NLs carrying DOX and photothermal agents, indocyanine green (ICG), which enables the release of DOX by NIR stimulus, are attached to *E. coli* through streptavidin-biotin binding. The excellent swimming ability of *E. coli* allows microrobots to navigate through biological matrices, which is promising for drug delivery in viscoelastic and solid environments.

Microalgae have been demonstrated to possess natural biodegradability and desirable cytotoxicity in physiological environments [26]. The fabrication procedure of algal microrobots is facile, cost-effective, and fast. The negatively charged algae membrane can assemble with the positively functionalized magnetic polystyrene particles [166], as shown in Figure 2.9(B). The magnetic polystyrene particles are deposited with a positively charged polyelectrolyte layer, which can enhance the adhesion of bacteria to the microparticles through strong electrostatic interactions [158]. Moreover, the existence of magnetic polystyrene particles ascertains the maneuverability of algal microrobots under a magnetic field. The fluorescent isothiocyanate

## 2. Soft Bio-Microrobots: Toward Biomedical Applications

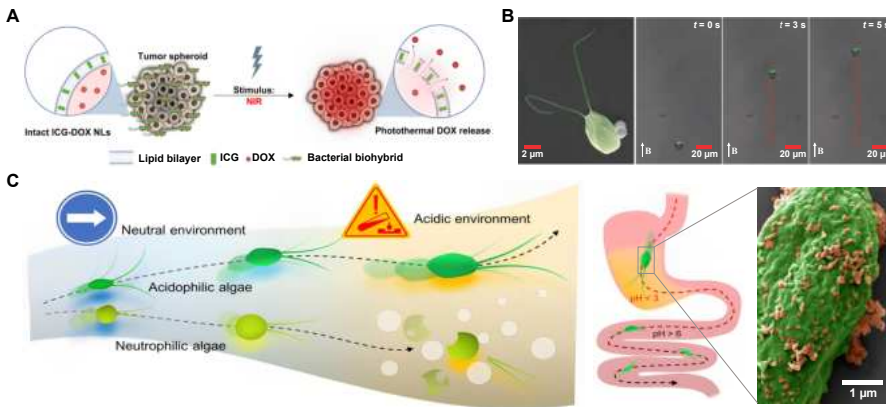


Figure 2.9: Targeted delivery applications of soft bio-microrobots. (A) Bacteria-driven microrobots carrying stimuli-responsive ICG-DOX NLs are localized on tumor spheroids and release their payload upon NIR stimulus. Reproduced with permission from [122]. Copyright 2022, AAAS. (B) SEM image of an algal micro-robot (pseudocolored green, *C. reinhardtii*). 2D propulsion trajectories of the algae microrobots under a uniform field. Reproduced with permission from [166]. Copyright 2018, WILEY-VCH Verlag GmbH & Co. KGaA, Weinheim. (C) Schematic of acidophilic algae microrobots for *in vivo* delivery applications in GI tract. Acidophilic algae robots are capable of prolonged motion in both neutral and acidic environments, whereas neutrophilic algae are corroded and degraded in highly acidic environments. Reproduced with permission from [167]. Copyright 2022, AAAS.

labeled dextran is loaded into magnetic polystyrene particles and delivered to HeLa cells as a proof-of-concept active cargo delivery demonstration. The proposed targeted drug delivery is realized by injecting drug-loaded microrobots near lesions. Oral delivery to the gastrointestinal (GI) tract has been utilized in the last decades because of its high patient compliance, noninvasiveness, and low cost. The microrobotic-based capsule towards oral delivery in the GI tract is restricted by the short propulsion lifetime. Natural algae with the advantage of fast and long-lasting swimming performance can effectively address this limitation. Zhang *et al.* [168] have reported an efficient algal microrobotic system, where fluorescent dye or cell membrane-coated nanoparticle functionalized algal microrobots are embedded inside a pH-responsive capsule. The capsule layer can protect algal microrobots from harsh gastric environments in the stomach. Upon the release from the capsule, the algal microrobots swim in the intesti-

nal fluid for more than 12 hours and release the carried DOX to treat GI diseases. Zhang *et al.* [167] have also harnessed acidophilic microalgae, *Chlamydomonas pitschmannii* (*C. pitschmannii*), to construct biohybrid microrobotic system towards GI delivery applications, as shown in Figure 2.9(C). *C. pitschmannii* shows a remarkable swimming ability even in acidic environments ( $\text{pH} < 4$ ) and maintains its swimming speed for long periods. Thus, this ability enables *C. pitschmannii* to pass through the GI tract with the low pH condition. The algal microrobots are fabricated by combining the acidophilic microalgae with RBC membrane-coated nanoparticles that load a green fluorescent dye. The long-time retention of fluorescent signals in both the stomach and the small intestine validates the microrobots based on *C. pitschmannii* can help to improve chemotherapeutic performance in the GI tract. Due to the maneuverability of soft bio-microrobots, they can be directed by external stimuli to transport cargo to specific positions. The cargo is released and takes effect after reaching the targeted location, thereby improving targeted efficiency compared with systemic administration. In addition, their small size enables them to access hard-to-reach locations in the human body, which holds the potential for microsurgery with minimal trauma.

### 2.5.2 Surgery

Large surgical tools can be teleoperated by a clinician, yet are not able to arrive at hard-to-reach positions in the human body. Due to the microscale size, the microrobotic systems make it possible to remotely interfere in the circulatory system, the urinary system, and the central nervous system with tiny passages [5]. In ocular medicine, the molecule passively diffuses in the eye. However, the diffusion is hampered by the tight macromolecular matrix in the vitreous. Wu *et al.* [169] have reported magnetically helical microrobots with a perfluorocarbon surface coating that minimizes the interaction of the microrobots with the macromolecular network in the vitreous. The microrobots swarm penetrates the tight macromolecular matrix of the porcine vitreous and reaches the retina within 30 min under the magnetic field. Standard optical coherence tomography is used to visualize the microrobots swarm and send feedback on the position to the user. The alternative potential strategy for surgery is to combine large surgical tools, such as endoscopy, and untethered microrobots. The endoscopy en-

ables rapid deployment and long-distance delivery across organs and tissue, while microrobots can access the deep regions within tortuous ducts, such as tympanostomy tube [38] and bile duct [170], [171], that are difficult to reach with the endoscope. Therefore, microrobotic systems open a new avenue for surgery.

### 2.5.2.1 Biopsy

A biopsy is a medical procedure that takes a small sample of body tissue for further histological, cytological, or genetic examination. Biopsies are required in a wide range of organs including the liver, breast, lung, and skin. Untethered microgrippers can achieve the retrieval of an object from a far location owing to their grasping capability. The thermochemically triggered microgrippers have been demonstrated to capture clusters of live fibroblast cells without damaging the cell viability [82]. The *in vitro* biopsy has been performed on a tissue sample from a bovine bladder as well. The enzymatically triggered microgrippers can carry the cells without destroying RNA structure [83]. Afterward, Gultepe *et al.* have demonstrated *ex vivo* tissue excision of a porcine liver and *in vivo* tissue retrieval from a porcine biliary tree using thermally responsive untethered microgrippers [172]. The high-quality RNA and DNA from the retrieved tissue can be utilized to undertake diagnostics. Single-cell manipulation is crucial for biosensing, surgery, robotics, and cell analysis. Jin *et al.* [173] have exploited a thermally responsive wax layer to fabricate untethered microgrippers to actively capture or excise single cells in a biocompatible manner. Wax is chemically and biologically inert and biocompatible and widely used in food products, as well as displays a range of phase-transition temperatures of relevance to biology and the human body. Therefore, this microgripper does no harm to the human body when performing the biopsy. Figure 2.10(A) includes the optical microscopy images that show the process of a microgripper capturing and excising cells from a cell cluster, and the immunofluorescence images that display single-cell and two-cell captured by the microgripper.

### 2.5.2.2 Biofilm Eradiction

Biofilms are a cluster of aggregates of bacterial cells encased in a matrix of extracellular polymeric. The extracellular polymeric substances (EPS)

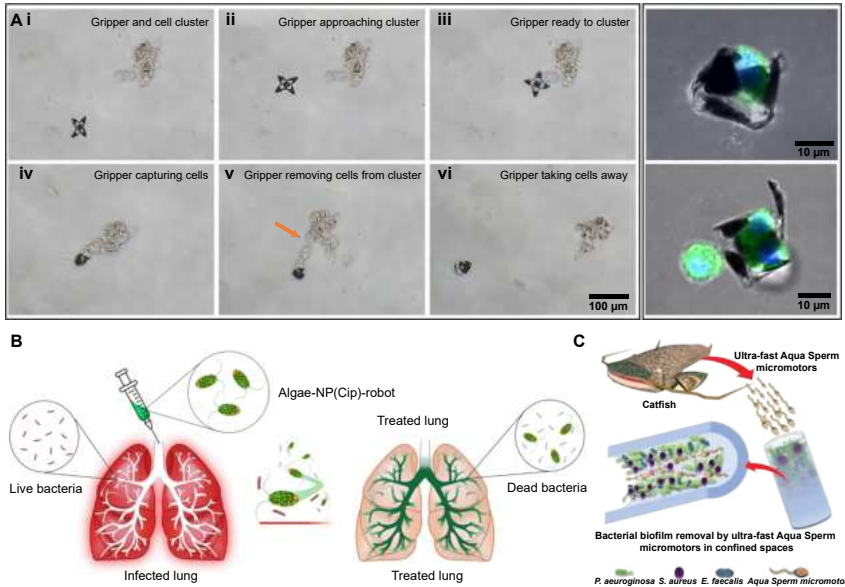


Figure 2.10: Surgical applications including biopsy and biofilm eradication of soft bio-microrobots. (A) Optical microscopy images (i)-(vi) show the process of a micro-gripper capturing and excising cells from a cell cluster. Immunofluorescence images exhibit suspended fibroblast cells captured by the grippers, including single-cell and two-cell captures. Reproduced with permission from [173]. Copyright 2020, American Chemical Society. (B) Schematic depicting the utilization of algal microrobots for the treatment of a bacterial lung infection. Reproduced with permission from [168]. Copyright 2022, Springer Nature. (C) Schematic representation of sperm microrobots destroying three species of bacterial biofilm colonized on medical and laboratory tubing. Reproduced with permission from [174]. Copyright 2021, Wiley-VCH GmbH.

protect bacterial cells from hostile environments, antibiotics, or the immune systems of host organisms [175]. Biofilms are ubiquitous in industrial settings, such as sewage treatment, bioleaching, and the food industry. One of the most commonly used methods for treating clinical bacterial infections is the administration of antibiotics. However, this approach is ineffective because the antibiotics randomly circulate in biological fluids and may be blocked by EPS. Microrobots provide a feasible method for targeted drug delivery to eradicate biofilms due to the capability of pen-

etrating the matrix owing to their size and propulsive thrust [176]. Stanton *et al.* [177] have exploited the nonpathogenic magnetotactic bacteria to integrate with antibiotics-loaded microtubes to establish a controllable microrobotic system capable of targeting an infectious biofilm. The microrobots can respond to the external magnetic field and reach the biofilm. Unlike bacteria-driven microrobotic systems facing potential pathogenicity or immunogenicity, algal microrobotic systems allow on-demand biofilm eradication in a safer way. Shchelik *et al.* [178] have leveraged the surface engineering of microalgae to fabricate an antibiotics-loaded biohybrid microrobotic system. The antibiotics are conjugated to the microalgae surface via click chemistry. The direct control of algal microrobots is demonstrated using the phototactic properties of the cells. To avoid the immune clearance of soft bio-microrobots by alveolar macrophages, Zhang *et al.* [179] have created algal microrobots by attaching antibiotic-loaded neutrophil membrane-coated polymeric nanoparticles to natural microalgae. The neutrophil membrane can shield microalgae from the immune system and enable specific binding with target pathogens. Figure 2.10(B) depicts the utilization of algal microrobots for the treatment of a bacterial lung infection. Besides, Mayorga-Martinez *et al.* [174] have found catfish sperm can penetrate and disturb three species of bacterial biofilms colonized on medical and laboratory tubing through mechanical removal, as shown in Figure 2.10(C). Using their ultra-fast speed, the biofilms can be destroyed in a short time. Sperm cells have also been proven to possess the ability to overcome time-periodic interaction force [180], which makes them promising for penetrating the EPS of biofilms. Sperm-driven microrobots are a promising option for overcoming biological barriers. However, the maneuverability and propulsive thrust of these sperm-driven microrobots when facing these barriers have yet to be demonstrated.

### 2.6 Challenges

Living microorganisms and cells display remarkable swimming abilities due to their soft flagella, serving as a classic illustration of movement in the low-Re regime. Motile microorganisms and cells can provide motility and possess cell membranes with good adhesion to accessories, such as polymeric materials, RBCs, or NLs, which allow for drug loading and prevent release during delivery to the target position. The functional materials

---

enable biohybrid soft microrobots to execute biomedical tasks. On the other hand, flexible materials have been widely used to fabricate synthetic soft microrobots to mimic the motion of the flagellum or replicate the gripping abilities of human hands. Biologically inspired and biohybrid microrobots are two categories of soft bio-microrobots. The summary of soft bio-microrobots has shown their potential to advance minimally invasive medicine, such as targeted delivery and surgery. Nevertheless, there is still a long way from the translation to clinical applications. Great challenges hindering the development of soft bio-microrobots still exist.

Safety is the most important issue for soft bio-microrobots used for *in vivo* applications. As foreign materials, soft bio-microrobots should be removed from the body after completing their biomedical tasks. However, the post-application retrieval or resorbability of soft bio-microrobots has not been considered and presented in most research. Hence, the fully biodegradable soft bio-microrobots can be a major advancement towards clinical trials. After soft bio-microrobots complete the designated mission in the body, their degradation into nontoxic byproducts will greatly minimize the risk of potential inflammation and other complications, as well as reduce the postoperative recovery time. The incorporation of magnetic materials for directional control of soft bio-microrobots is common in the fabrication process. These magnetic materials typically include magnetic metal layers or magnetic nanoparticles. Although an iron and platinum bilayer can be noncytotoxic and biocompatible after an annealing step [181], it can not be absorbed or metabolized in the human body. It has been shown that magnetic metal layers such as nickel and cobalt are detrimental to tissues and cells. In addition, the strong stiffness of the metal layer used in soft bio-microrobots could result in scratching or harm to healthy tissue or cells during movement. In addition, the resorbability of magnetic nanoparticles depends on their size. The magnetic nanoparticles smaller than 10 nm can be resorbed through renal clearance within a few days, whereas those larger than 100 nm are slowly removed by the spleen and the liver [153]. Therefore, synthetic material should be evolved to possess biocompatibility and biodegradability in the future. Besides, the selection of microorganisms and cells for biohybrid soft microrobots must consider their safety in the human body. Researchers have harnessed nonpathogenic microorganism species to create biohybrid microrobots, but an approach to avoid detection by the immune system is often lacking. Commensal

## 2. *Soft Bio-Microrobots: Toward Biomedical Applications*

---

bacteria found in the human body can be used to construct biohybrid microrobots, as the commensal bacterial physiology is related to the host behavior and they can evade the clearance of the immune system in the host. In the future, commensal bacteria species or microorganisms with cell-mimicking properties could be a viable choice to fabricate biohybrid microrobots for precision nanomedicine. Overall, the complexity of cellular and organismal immune response to the bio-microrobots remains to be studied beyond the cytotoxicity of the involved materials.

The design and manufacture of soft bio-microrobots are specific to each biomedical application, so there is not a single generic soft bio-microrobot for all applications. Considering varying conditions in the human body, soft bio-microrobots must adapt to the complex conditions in the specific organs or cells. Therefore, a strategic method should be given to guide the design of soft bio-microrobots based on the specific application scenario. For example, the soft bio-microrobots aiming for GI delivery should be able to withstand the acid environments in the stomach. Also, when soft bio-microrobots are utilized in the field of ocular medicine, they need to penetrate through the tight macromolecular matrix in the vitreous. To this end, soft bio-microrobots with the ability to penetrate should be designed, which is also crucial for reaching tumor issues and bacterial cells in biofilms. Meanwhile, the fabrication method should satisfy the requirements of simplicity, cost-effectiveness, and high productivity. In the future, a facile and reliable fabrication method should be developed to mass-produce soft bio-microrobots. The architecture of soft bio-robotics will develop towards microrobot intelligence. Soft bio-robotics will have control systems to control other components, such as power components, interactive components, and functional components. The construction of these components will enable the invention of intelligent microrobots to perform more complex tasks than biomedical applications, for example, data storage and data processing. However, more advanced components that are gifted with perception and intelligence need the development of micro/nanofabrication techniques [182].

As the human body is the target environment for most soft bio-microrobots, they must have the ability to adapt to complicated conditions and maintain long-term motility in the human body. The motion and navigation of soft bio-microrobots in physiological environments can be impacted by the presence of proteins, lipids, nucleic acids, high ionic strength, and

varying pH levels. Furthermore, the movement of soft bio-microrobots in non-Newtonian and inhomogeneous physiological fluids remains uncertain due to their complex properties. The challenge of overcoming biological barriers such as biofouling, blood flow, the blood-brain barrier, and cell membranes is also yet to be fully addressed. In precision nanomedicine, the therapeutic drugs need to enter the cell to exert on the nuclei or cytosol of cells. The cell membrane, comprised of a phospholipid bilayer, proteins, and polysaccharides, can act as a barrier by preventing the entry of drug-loaded soft bio-microrobots into cells. The surface of soft bio-microrobots is absorbed by plasma protein and identified by mononuclear phagocytic cells of the reticuloendothelial system in the blood vessel [183], leading to their removal from the bloodstream. Maintaining long-term and exceptional motility in the body remains a substantial challenge for soft bio-microrobots.

Microorganisms and cells have been a major inspiration for the development of soft bio-microrobots. Nevertheless, the current soft bio-microrobots lack the ability to sense and respond to surrounding environments, as seen in many microorganisms and cells. Those abilities are known as chemotaxis, magnetotaxis, phototaxis, rheotaxis, and thermotaxis. For instance, MTBs and microalgae can respond to the external magnetic field and light illumination, respectively. Sperm cells can navigate toward the ovum primarily through rheotaxis, thermotaxis, and chemotaxis. Although the swimming ability of current biohybrid soft microrobots is comparable with that of the microorganisms and cells, the inherent abilities of microorganisms and cells are not well explored and harnessed in biomedical applications. Replicating the structure of microorganisms and cells is only the first step, these tactic behaviors should be implemented into soft bio-microrobots to realize real biomimetics engineering.

Soft bio-microrobot swarms can improve the targeting efficacy and carry a larger amount of drugs to treat diseases. Moreover, the aggregation of soft bio-microrobots will be easier to track *in vivo* compared to one single microrobot. In microrobotic systems, the tracking precision affects the implementation of the control algorithm and the precision control of microrobots in the human body. Currently, tracking a microrobot inside the human body is still a grand challenge because of the limited resolution, penetration depth, or adverse effects of current imaging techniques [184]. Therefore, developing soft bio-microrobot swarms can not only improve

## 2. *Soft Bio-Microrobots: Toward Biomedical Applications*

---

drug targeting efficiency but also lower the difficulty of tracking. However, the collective behavior of soft bio-microrobots is complicated because it involves complex interaction with the fluidic environments, external field, surrounding microrobots, and adjacent soft bio-microrobots. In the future, the underlying mechanism needs to be understood to develop soft bio-microrobot swarms with advanced functions and explore their adaptability in complex environments.

### 2.7 Conclusions

This review summarizes the state-of-the-art of soft bio-microrobots for targeted cargo delivery and surgery. Limited by the size of microrobots, batteries are not a suitable power source as the deliverable energy scales with volume. By converting the power of external fields or utilizing the self-propulsion of microorganisms or cells, soft bio-microrobots are capable of swimming in the low-Re regime. The functional components of soft bio-microrobots enable them to be guided, respond to the surrounding environments, and execute *in vivo* biomedical tasks. The development of soft bio-microrobots is shifting from mimicking the swimming ability of creatures to endowing them with the same characteristics as creatures. The future of soft bio-microrobots must move towards simplicity, safety, adaptability, and intelligence. Although there is still a considerable journey ahead for clinical application, soft bio-microrobots with the above properties will advance minimally invasive medicine and revolutionize human life in the future.

# 3

## Flagellar Propulsion of Sperm Cells Against a Time-Periodic Interaction Force

3

*Note: Following chapter is adapted from the article “Flagellar Propulsion of Sperm Cells Against a Time-Periodic Interaction Force” by Z. Wang, A. Klingner, V. Magdanz, M. W. Hoppenreijs, S. Misra, and I. S. M. Khalil (2023), published in “Advanced Biology”, volume 7, issue no. 1, pages 1–16.*

### Abstract

Sperm cells undergo complex interactions with external environments, such as a solid boundary, fluid flow, as well as other cells before arriving at the fertilization site. The interaction with the oviductal epithelium, as a site of sperm storage, is one type of cell-to-cell interaction that serves as a selection mechanism and releases mature sperm cells upon ovulation. Abnormal sperm cells with poor swimming performance, the major cause of male infertility, are filtered out by these selection mechanisms. In this study, collinear bundles, consisting of two sperm cells, generate propulsive thrusts along opposite directions and allow us to observe the influence of cell-to-cell interaction on flagellar wave patterns. The developed elasto-hydrodynamic model demonstrates that steric and adhesive forces lead to highly symmetrical wave patterns and reduce the bending amplitude of the propagating wave. It is measured the free cells exhibit a mean flagellar cur-

vature of  $6.4 \pm 3.5$  rad/mm and a bending amplitude of  $13.8 \pm 2.8$  rad/mm. After forming the collinear bundle, the mean flagellar curvature and bending amplitude are decreased to  $1.8 \pm 1.1$  rad/mm and  $9.6 \pm 1.4$  rad/mm, respectively. This study presents consistent theoretical and experimental results important for understanding the adaptive behavior of sperm cells to the external time-periodic force encountered during sperm-egg interaction.

## 3.1 Introduction

In nature, microorganisms are capable of being propelled by the helical or wave-like motion of one or more flagella, as it is found in many bacteria [157], algae [65], and sperm cells [20]. They exhibit distinct wave patterns that respond to external stimuli, including chemicals [185]–[188], hydrodynamic drag [189], temperature, [190] or mechanical forces [191]–[193]. For instance, the flagella of *Salmonella typhimurium* are normal left-hand helices at the solution with a neutral pH. In weakly acidic and alkaline conditions, the flagella are changed to coiled helices with a reduced pitch. The lower or higher pH environments transform the coiled helices into curly right-hand helices. Bacteria with the flagella of normal helices can perform smooth swimming, yet the coiled and curly helices are used in the tumbling motion to seek a new direction in response to chemotaxis [194], [195]. The drastically polymorphic transformation of microorganisms can either optimize their motility or improve their survivability. For example, the parasite *Trypanosoma brucei* utilizes a long slender flagellum to propel itself in bodily fluids and penetrate the blood vessel to invade extravascular tissue. After entering the bloodstream with heterogeneous biochemical composition, the long slender flagellum of the parasite is transformed into a shorter stumpy one to ensure its survival [196].

As an important role in fertilization, sperm cells swim in male and female reproductive tracts under the influence of physical or chemical stimuli. They are able to respond to stimuli (such as chemoattractant molecules, fluid flow, temperature, and surface) and use these signals to navigate to the ovum and achieve fertilization. For example, chemical gradients in the sex hormone progesterone direct sperm cells toward the ovum [197]. Chemotaxis provides a short-distance guidance mechanism for spermatozoa. The changes in calcium ion concentration induced by the presence of the chemoattractant can modulate the wave patterns of sperm cells, thus

resulting in different swimming paths and redirecting sperm cells to the source of the attractant (i.e., the ovum). Additionally, rheotaxis has been found to serve as a long-distance guidance mechanism, as motile sperm cells are able to swim against the fluid flow present in the female reproductive tract [198]. When the temperature increases, the wave amplitude near the proximal end decreases. Consequently, sperm cells would swim with an enhanced velocity and linearity due to the decrease in the side-to-side displacement of the proximal end [199]. A temperature gradient has been found in several mammalian female reproductive tracts and sperm cells swim to the warmer region at the oviduct [200], assuming that thermotaxis is an additional mechanism for guidance. Swimming along surfaces is known as a physical guidance mechanism of sperm cells [201]. It has been observed that sperm cells rotate to become nearly tangential to the surface.

To explicitly elucidate the locomotion behavior of microorganisms with a single flagellum or multiple flagella, elastohydrodynamic models are developed to study the hydrodynamic interaction between the elastic flagella and surrounding fluid. By combining the hydrodynamic computation and the high-speed tracking experiments, Friedrich *et al.* have concluded that cell-body rocking plays a major role in the flagellar synchronization of green algae *Chlamydomonas reinhardtii* instead of the direct hydrodynamic interaction [202]. Hilfinger *et al.* [203] have developed a nonlinear wave equation to describe wave patterns of sperm cells. They have presented the numerical results of the nonlinear wave equation at different boundary conditions and found the reconstructed wave patterns through the equation are approximated by those observed experimentally. Later, Walker *et al.* [204] have extended the elastohydrodynamic model of sperm cells to the three-dimensional space, such that the model can explain the complex three-dimensional motion of sperm cells. In the female reproductive tract, sperm cells inevitably interact with other cells before achieving fertilization. However, the effect of cell-to-cell interaction on wave patterns of sperm cells has not been investigated, and the relevant elastohydrodynamic model has not been developed.

Infertility is a universal health issue affecting 48 million couples and 186 million individuals [205]. Half of the infertile couples have low sperm count, abnormal sperm cells with poor motility, or blockages along the reproductive tract. In this work, we investigate the wave pattern of sperm cells

under a time-periodic interaction force. This time-periodic interaction is observed in a bundle of bovine sperm cells assembled in the opposite direction (Figure 3.1). An elasto-hydrodynamic model is developed to interpret the interactions between the elastic forces of sperm flagella, the interaction forces of two cells, and the hydrodynamic drag forces of the surrounding fluids. We use Fourier analysis of the measured wave pattern in two types of fluids with low and high viscosities, measure the wave variables of the free cells that are not affected by time-periodic interaction forces, and compare that to the case where the cells form the collinear bundles. Our model can explain the variation of the pattern of sperm cells after forming a collinear bundle. Moreover, we provide new tools to assess the motility of sperm cells by analyzing the flagellar motion, and advance the understanding of cell-to-cell interaction in reproductive health.

## 3.2 Actively Propagated Waves along Two Collinear Flagella

### 3.2.1 Cell-to-Cell Interactions

Sperm cells produce propagating waves toward the distal end of the flagellum to push the cell forward. During cell-to-cell interaction, two cells can form a collinear bundle with two flagella in opposite orientations by means of the head-to-head attachment. Steric and adhesive interactions are two essential effects in this attachment manner [206]. One cell is attracted to the other by adhesive molecules located at the adhesive region, as shown in Figure 3.1(A). Adhesive regions have been observed on the acrosome, the tip region of bovine sperm heads [207]. The position vectors  ${}^i\mathbf{r}_a(t)$  and  ${}^j\mathbf{r}_a(t)$  are the closest pair of vertices within the adhesive region of two cells. The adhesive force  ${}^i\mathbf{F}_{\text{adh}}(t)$  is applied to the sperm head of the  $i$ th cell, which points from  ${}^i\mathbf{r}_a(t)$  to  ${}^j\mathbf{r}_a(t)$ , while the adhesive torque  ${}^i\mathbf{M}_{\text{adh}}(t)$  is generated on the center  ${}^i\mathbf{r}(t)$  of  $i$ th sperm head. The adhesive force and torque are given by the following expressions:

$$\begin{aligned} {}^i\mathbf{F}_{\text{adh}}(t) &= \kappa_a({}^j\mathbf{r}_a(t) - {}^i\mathbf{r}_a(t)), \\ {}^i\mathbf{M}_{\text{adh}}(t) &= ({}^i\mathbf{r}_s(t) - {}^i\mathbf{r}(t)) \times {}^i\mathbf{F}_{\text{adh}}(t) \quad (i = 1, 2), \end{aligned} \quad (3.1)$$

where  $\kappa_a$  is the adhesive elastic constant of the sperm head. The adhesive force is produced only if  $|{}^i\mathbf{r}_a(t) - {}^j\mathbf{r}_a(t)| < l_a$ , and  $l_a$  is the characteristic

### 3.2 Actively Propagated Waves along Two Collinear Flagella

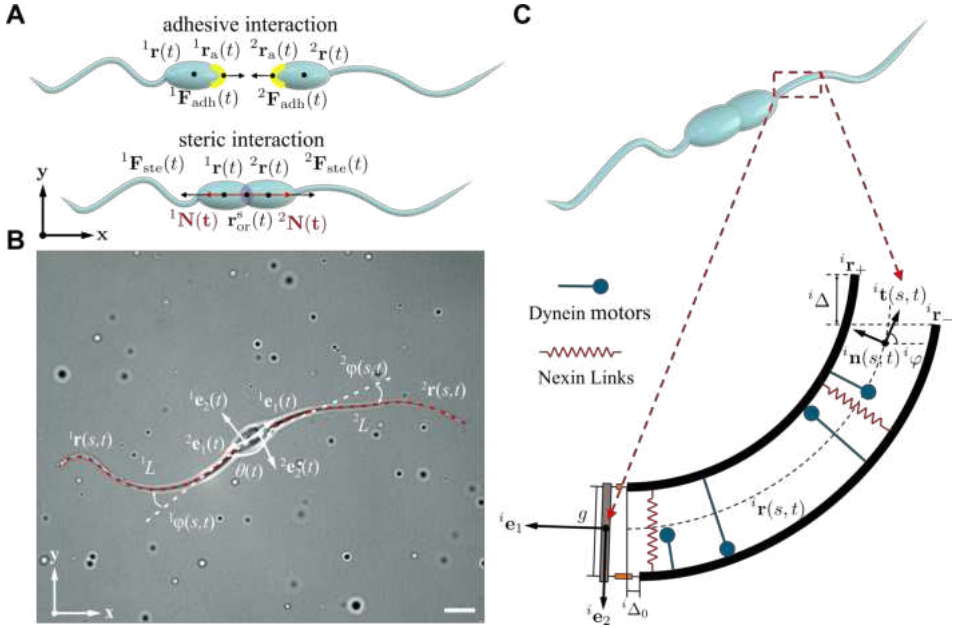


Figure 3.1: The modeling of a collinear bundle with two flagella in opposite directions. (A) Adhesive and steric interaction of two cells. Due to the existence of the adhesive regions (the yellow-labeled part), the adhesive forces  ${}^1\mathbf{F}_{adh}(t)$  and  ${}^2\mathbf{F}_{adh}(t)$  are generated on the position  ${}^1\mathbf{r}_a(t)$  and  ${}^2\mathbf{r}_a(t)$ , respectively. The steric forces  ${}^1\mathbf{F}_{ste}(t)$  and  ${}^2\mathbf{F}_{ste}(t)$  are applied to the centroid  $\mathbf{r}_{or}^s(t)$  of the overlapped region (the purple part) with the direction vectors  ${}^1\mathbf{N}(t)$  and  ${}^2\mathbf{N}(t)$ , respectively. The position vectors  ${}^1\mathbf{r}(t)$  and  ${}^2\mathbf{r}(t)$  denote the centers of the sperm heads of two cells, respectively, in the laboratory frame of reference  $(\mathbf{x}, \mathbf{y})$ . (B) Two bovine sperm cells adhere to each other into a collinear bundle in which the transverse waves propagate in opposite directions. The wave propagation of two cells is characterized by the tangent angles  ${}^1\varphi(s, t)$  and  ${}^2\varphi(s, t)$ , respectively, along the arclength  $s$  at time instant  $t$ . Two tangent angles  ${}^1\varphi(s, t)$  and  ${}^2\varphi(s, t)$  are described at the position  ${}^1\mathbf{r}(s, t)$  and  ${}^2\mathbf{r}(s, t)$  with respect to the body frames of reference  $({}^1\mathbf{e}_1, {}^1\mathbf{e}_2)$  and  $({}^2\mathbf{e}_1, {}^2\mathbf{e}_2)$ , respectively. The angle  $\theta(t)$  denotes the relative orientation of two sperm heads. The scale bar is  $10 \mu\text{m}$ . (C) Schematic representation of two-dimensional projection of flagellar axoneme. Two polar filaments  ${}^i\mathbf{r}_+$  and  ${}^i\mathbf{r}_-$  with a distance of  $g$  are connected by nexin links. The length mismatch of two filaments at the proximal end is  ${}^i\Delta_0$ , and the sliding displacement at the distal end is  ${}^i\Delta(s, t)$ . The unit vectors  ${}^i\mathbf{t}(s, t)$  and  ${}^i\mathbf{n}(s, t)$  are the tangent and normal vector at the position of the segment on the flagellum, respectively.

### 3. Flagellar Propulsion of Sperm Cells Against a Time-Periodic Interaction Force

---

distance where the adhesive connection of two cells breaks down. The adhesive interaction contributes to the approaching of two cells. Regarding the steric interaction of two cells, the steric force  ${}^i\mathbf{F}_{\text{ste}}(t)$  is imposed on the vector position  $\mathbf{r}_{\text{or}}^c(t)$ , the centroid of the overlapped region. The unit vector  ${}^i\mathbf{N}$  normal to the overlapped region of the two sperm heads denotes the direction of the steric force  ${}^i\mathbf{F}_{\text{ste}}(t)$  (see Figure 3.1(A)). The steric force  ${}^i\mathbf{F}_{\text{ste}}(t)$  imposed on the  $i$ th cell results from the steric interaction with the  $j$ th cell, while the steric torque  ${}^i\mathbf{M}_{\text{ste}}(\mathbf{t})$  acts on the center  ${}^i\mathbf{r}(t)$  of sperm head. The force and torque arising from the steric interaction can be as follows [206]:

$$\begin{aligned} {}^i\mathbf{F}_{\text{ste}}(t) &= 0.5\kappa_c({}^iv(t) + {}^jv(t))\Delta t {}^i\mathbf{N}(t), \\ {}^i\mathbf{M}_{\text{ste}}(\mathbf{t}) &= (\mathbf{r}_{\text{or}}^s(t) - {}^i\mathbf{r}(t)) \times {}^i\mathbf{F}_{\text{ste}}(t), \end{aligned} \quad (3.2)$$

where  $\kappa_c$  is the steric elastic constant of the sperm head,  $\Delta t$  is the time step, and  ${}^iv(t)$  and  ${}^jv(t)$  are the average path velocity of  $i$ th and  $j$ th cell with respect to the laboratory frame of reference  $(\mathbf{x}, \mathbf{y})$  in Figure 3.1(B), respectively. Affected by the steric interaction, two cells behave repulsively and separate apart. The forces and torques generated during the interaction act on the sperm cell and affect the wave pattern as external stimuli. To characterize wave patterns of sperm cells during cell-to-cell interaction, the elasto-hydrodynamics, which deal with the interaction between actively elastic flagellum, the hydrodynamic drag, and the other cell, is studied below.

#### 3.2.2 The Elasto-Hydrodynamic Flagellum

Although it is unknown whether sperm bundles can fertilize the ovum, the bundle formation is likely to enhance the swimming speed of the cells [208], [209]. Multiple sperm cells can form a collinear bundle without the need for any external stimuli. The unique configuration of collinear bundles allows us to understand the swimming behavior when the head is not free. In our experiments, the collinear bundle consists of two bovine sperm cells in opposite directions. The body frames of reference  $({}^1\mathbf{e}_1, {}^1\mathbf{e}_2)$  and  $({}^2\mathbf{e}_1, {}^2\mathbf{e}_2)$  of the two cells are located at the centers  ${}^1\mathbf{r}(t)$  and  ${}^2\mathbf{r}(t)$ , respectively, of their heads such that the orthonormal vectors  ${}^1\mathbf{e}_1$  and  ${}^2\mathbf{e}_1$  are oriented along the major axis of the sperm head of the first and second cell, respectively. Two ellipsoidal sperm heads with major diameter  $2a$  and minor diameter

$2b$  are connected to the flagella of length  ${}^1L$  and  ${}^2L$  at  $-a^1\mathbf{e}_1$  and  $-a^2\mathbf{e}_1$ , respectively, as shown in Figure 3.1(B). The relative orientation of two cells is characterized by  $\theta(t)$ , which is the angle between the orthonormal vectors  ${}^1\mathbf{e}_1$  and  ${}^2\mathbf{e}_1$ . The flagellar axoneme can be regarded as two filaments including distributed contractile elements to induce transverse propagating waves and generate flagellar propulsion. Figure 3.1(C) shows the planar projection of the flagellar axoneme. Two polar filaments  ${}^i\mathbf{r}_+$  and  ${}^i\mathbf{r}_-$  of the flagellar axoneme are connected by elastic nexin links with the constant distance of  $g$  [210]. Once the sliding displacement  ${}^i\Delta(s, t)$  exists between two polar filaments, the bending force is generated and causes the flagellum bending. The bending force density,  ${}^if_{\text{ben}}(s, t) = k {}^i\Delta(s, t)$ , is proportional to the sliding displacement with elastic sliding resistance  $k$ . Moreover, the sliding displacement can be determined through the tangent angle  ${}^i\varphi$ . The expression of sliding displacement is given by [211]

$${}^i\Delta(s, t) = \int_0^s (|\partial_{s'} {}^i\mathbf{r}_-| - |\partial_{s'} {}^i\mathbf{r}_+|) ds' = {}^i\Delta_0(t) + g({}^i\varphi(s, t) - {}^i\varphi_0(t)), \quad (3.3)$$

where  ${}^i\Delta_0$  and  ${}^i\varphi_0$  are the length mismatch of two polar filaments and the tangent angle of the centerline at the proximal end, respectively. The internal force, which is composed of the elastic force and the bending force, along the flagellum can be expressed as follows:

$${}^i\mathbf{F}_{\text{int}} = (-{}^iE {}^i\varphi_{ss} + {}^if_{\text{ben}}(s, t)g) {}^i\mathbf{n}(s, t), \quad (3.4)$$

where  ${}^iE$  is the bending stiffness of the  $i$ th flagellum, the subscript  $s$  denotes arclength derivative, and  ${}^i\mathbf{n}(s, t)$  is the unit normal vector along the arclength  $s$  of the  $i$ th flagellum at the time instant  $t$ .

Sperm flagellum oscillates in a time-periodic manner such that the elastic force and the bending force are balanced by the viscous drag force determined by the resistive-force theory [147] (see Experimental section). Note that the elastic force tends to straighten the flagellum, the bending force is the cause of the propagating waves, and the viscous drag force propels sperm cells forward. The average path velocity,  $v$ , of the collinear bundle is relatively small because the two cells are swimming along opposite directions. The force dipole field strength generated by the  $i$ th cell scales as  $|{}^ip| \sim \eta v {}^iL^2$  [212], where  $\eta$  is the viscosity of the fluid, and is lower

### 3. Flagellar Propulsion of Sperm Cells Against a Time-Periodic Interaction Force

---

than that of a free sperm cell owing to the low average path velocity of the collinear bundle (Figure 3.1(B)). In addition, since the collinear bundle consists of two sperm cells along opposite directions, their flagella are far from each other, and the hydrodynamic interaction between the two flagella is negligible compared to the direct head-to-head interaction. Therefore, the resistive force theory is applicable to calculate the resistive drag for a given flagellum geometry. The flagellum elasto-hydrodynamics is governed by the balance of elastic force, bending force, and viscous drag force on every segment, and we have

$$-{}^i E {}^i \varphi_{ssss} + g^2 k {}^i \varphi_{ss} = {}^i \xi_{\perp} {}^i \varphi_t, \quad (3.5)$$

where  ${}^i \xi_{\perp}$  is the normal drag coefficient of the  $i$ th flagellum. The governing equation can be numerically solved after specifying four boundary conditions. The wave patterns can be reconstructed based on the solved tangent angle  ${}^i \varphi(s, t)$ . The distal end of the flagellum is free from force and torque owing to the lack of motor elements. Thus, we have the following boundary equations,

$$-{}^i E {}^i \varphi_{ss}({}^i L, t) + g {}^i f_{\text{ben}}({}^i L, t) = 0, \quad (3.6)$$

$$-{}^i E {}^i \varphi_s({}^i L, t) = 0. \quad (3.7)$$

The proximal end of the flagellum experiences the drag force of the sperm head, steric force, and adhesive force when interacting with the other cell. Additionally, we assume that the proximal end of the sperm cell is fixed over the course of movement. Therefore, the boundary equations on the proximal end are given by

$$-{}^i E {}^i \varphi_{ss}(0, t) + g {}^i f_{\text{bend}}(0, t) = -({}^i \mathbf{F}(t) + {}^i \mathbf{F}_{\text{ste}}(t) + {}^i \mathbf{F}_{\text{adh}}(t)) \cdot {}^i \mathbf{n}(0, t), \quad (3.8)$$

$$-{}^i E {}^i \varphi_{sss}(0, t) + g^2 k {}^i \varphi_s(0, t) = 0, \quad (3.9)$$

where  ${}^i \mathbf{F}$  is the drag force acting on the flagellum of the  $i$ th cell by the sperm head. For a sperm cell, the drag force  ${}^i \mathbf{F}$  can be expressed as follows:

$${}^i \mathbf{F}(t) = ({}^i F_{\text{amp}} \cos(\omega t + {}^i \theta_{\text{pha}}) + {}^i F_{\text{off}}) {}^i \mathbf{n}(0, t), \quad (3.10)$$

where  ${}^i F_{\text{amp}}$  and  ${}^i F_{\text{off}}$  are the force amplitude and force offset of the drag force  ${}^i \mathbf{F}(t)$ , respectively, and  $\omega$  is the angular frequency of the flagellar beat.

The angle  ${}^i\theta_{\text{pha}}$  is the initial phase of sinusoidal variation of the drag force. In the case of free cells, we have two equations  ${}^i\mathbf{F}_{\text{ste}}(t) = \mathbf{0}$  and  ${}^i\mathbf{F}_{\text{adh}}(t) = \mathbf{0}$ . With these boundary equations, the wave pattern of the sperm bundle can be reconstructed in the laboratory frame of reference  $(\mathbf{x}, \mathbf{y})$  by solving the governing equation. The kinematics of a sperm bundle are introduced in the next section.

### 3.2.3 Kinematics of Sperm Bundles

The position vectors of two flagellar centerlines with respect to the body frames of reference are determined by [213]

$${}^i\mathbf{r}(s, t) = {}^i\mathbf{r}(t) - a {}^i\mathbf{e}_1(t) - \int_0^s \cos {}^i\varphi(\ell, t) {}^i\mathbf{e}_1(t) + \sin {}^i\varphi(\ell, t) {}^i\mathbf{e}_2(t) d\ell. \quad (3.11)$$

Equation 3.11 gives the flagellar kinematics of a sperm bundle. The total force and moment of the bundle should be studied to further investigate its swimming characteristics. Each cell in a sperm bundle experiences the propulsive thrust  ${}^i\mathbf{F}_{\text{pro}}(t)$  along the sperm flagellum, the viscous drag force  ${}^i\mathbf{F}_{\text{hea}}(t)$  on the sperm head, and the interaction force  ${}^i\mathbf{F}_{\text{ste}}(t)$  and  ${}^i\mathbf{F}_{\text{adh}}(t)$  exerted by the other cell. Thus, the force balance equation of each cell can be described as follows:

$${}^i\mathbf{F}_{\text{tot}}(t) = {}^i\mathbf{F}_{\text{pro}}(t) + {}^i\mathbf{F}_{\text{hea}}(t) + {}^i\mathbf{F}_{\text{ste}}(t) + {}^i\mathbf{F}_{\text{adh}}(t) = \mathbf{0}. \quad (3.12)$$

The total propulsive thrust  ${}^i\mathbf{F}_{\text{pro}}(t)$  can be calculated through the integral of the propulsive force density  ${}^i\mathbf{f}(s, t)$  along the flagellum length. The propulsive force density  ${}^i\mathbf{f}(s, t)$  is derived from the resistive-force theory. In addition, the viscous drag force  ${}^i\mathbf{F}_{\text{hea}}(t)$  on the sperm head of the  $i$ th cell is given by

$${}^i\mathbf{F}_{\text{hea}}(t) = 6\pi a\eta C_1 {}^i\mathbf{v}_1(t) + 6\pi a\eta C_2 {}^i\mathbf{v}_2(t), \quad (3.13)$$

where  ${}^i\mathbf{v}_1(t)$  and  ${}^i\mathbf{v}_2(t)$  are the translational velocity and the transverse velocity of  $i$ th cell along  ${}^i\mathbf{e}_1$  and  ${}^i\mathbf{e}_2$ , respectively. The coefficients  $C_1$  and  $C_2$  are the geometric parameters of the ellipsoid heads of the sperm cells. To further determine the angular speeds of two sperm cells, the moment

### 3. Flagellar Propulsion of Sperm Cells Against a Time-Periodic Interaction Force

---

balance equation for each cell is constructed. The moment balance equation on the  $i$ th cell can be expressed as follows:

$${}^i\mathbf{M}_{\text{tot}}(t) = {}^i\mathbf{M}_{\text{hea}}(t) + {}^i\mathbf{M}_{\text{ste}}(\mathbf{t}) + {}^i\mathbf{M}_{\text{adh}}(\mathbf{t}) + \int_0^{iL} {}^i\mathbf{r}(s, t) \times {}^i\mathbf{f}(s, t) ds = 0, \quad (3.14)$$

where  ${}^i\mathbf{M}_{\text{hea}}(t)$  is the viscous drag torque on the sperm head of the  $i$ th cell. According to the low Reynold number (Re) hydrodynamics, the viscous drag torque  ${}^i\mathbf{M}_{\text{hea}}(t)$  is proportional to the angular speed  ${}^i\boldsymbol{\omega}_{\text{hea}}(t)$  of the sperm cell as  ${}^i\mathbf{M}_{\text{hea}}(t) = 8\pi\eta ab^2 C_3 {}^i\boldsymbol{\omega}_{\text{hea}}(t)$ , where the coefficient  $C_3$  represents the geometric parameter of the sperm head. Through Equations 3.12-3.14, the translational, the transverse, and the angular speed of the two cells can be calculated. Then the body frames of reference of two cells at every time instant can be known after determining the positions and orientations of two sperm heads. The modeling of the interaction of two cells is completely established.

## 3.2.4 Numerical Results

### 3.2.4.1 The Formation of Collinear Bundles

In the presence of steric and adhesive interaction, two cells can form a sperm bundle through the head-to-head attachment. Figure 3.2(A) shows the relative orientation of the two cells with initial orientation  $\theta_0$  ranging from  $30^\circ$  to  $150^\circ$  over the formation of the sperm bundle. Regardless of the initial orientation  $\theta_0$ , the configuration of the sperm bundle depends on the resultant interaction torque,  ${}^i\mathbf{M}_{\text{ite}} = {}^i\mathbf{M}_{\text{adh}} - {}^i\mathbf{M}_{\text{ste}}$ . We give a detailed explanation of the formation of a collinear bundle and an aligned bundle when  $\theta_0$  is  $90^\circ$ . Initially, the first cell is oriented horizontally, while the second cell swims vertically. When the adhesive torque  ${}^i\mathbf{M}_{\text{adh}}$  is overwhelmed by the torque  ${}^i\mathbf{M}_{\text{ste}}$  resulting from the steric force, the collinear bundle is formed. The head-to-head interaction of the two cells is illustrated in Figure 3.2(B). The first cell (the red) rotates clockwise under the effect of the negative torque  ${}^1\mathbf{M}_{\text{ite}}$ . Since the steric and adhesive torques acting on the second cell (the blue) are opposite to those on the first cell, the second cell rotates counter-clockwise after experiencing the positive torque  ${}^2\mathbf{M}_{\text{ite}}$ .

### 3.2 Actively Propagated Waves along Two Collinear Flagella

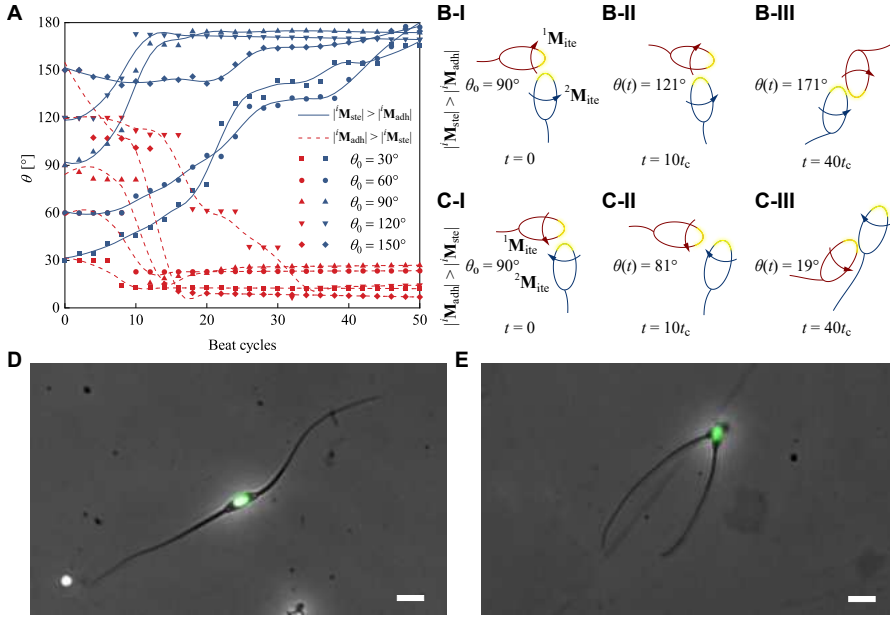


Figure 3.2: Two types of sperm bundles. (A) The numerical results of the relative orientation  $\theta(t)$  of two sperm heads with initial orientation  $\theta_0$ . (B) The relative orientation of two sperm heads in time sequences when the steric torque  $|\mathbf{M}_{ste}|$  is greater than the adhesive torque  $|\mathbf{M}_{adh}|$ . The resultant interaction torques  ${}^1\mathbf{M}_{ite}$  and  ${}^2\mathbf{M}_{ite}$ ,  ${}^i\mathbf{M}_{ite} = {}^i\mathbf{M}_{adh} - {}^i\mathbf{M}_{ste}$ , with opposite directions are applied to the sperm heads of the first and second cell, respectively. We assume that counterclockwise rotation is the positive rotation direction. Therefore, the first cell rotates clockwise under the effect of the negative resultant torque, and the second cell rotates counterclockwise. The relative orientation  $\theta(t)$  increases in three beat cycles, and the time of one beat cycle is  $t_c$ . (C) The relative orientation of two sperm heads in time sequences when  $|\mathbf{M}_{adh}| > |\mathbf{M}_{ste}|$ . In this case, the first cell rotates counterclockwise, and the second cell rotates clockwise. The relative orientation  $\theta(t)$  decreases in three beat cycles. The fluorescent images of (D) the collinear bundle and (E) the aligned bundle. The scale bar is  $10 \mu\text{m}$ .

The relative orientation between two cells increases progressively in time sequences and finally oscillates around  $180^\circ$ . Conversely, two cells will form the aligned bundle if  $|\mathbf{M}_{adh}| > |\mathbf{M}_{ste}|$ . Because the torque arising from the adhesive force is predominant, the first cell rotates counter-clockwise, and the second cell displays the contrary rotation, as depicted in Figure 3.2(C).

### 3. Flagellar Propulsion of Sperm Cells Against a Time-Periodic Interaction Force

---

The relative orientation of two cells decreases from  $90^\circ$  to around  $19^\circ$ , and finally oscillates around  $25^\circ$ . Two representative configurations of sperm bundle can be seen in Figure 3.2(D) and 3.2(E). We demonstrate that the configuration of the sperm bundle is decided by the resultant torque due to the steric and adhesive interaction, irrespective of the initial orientations of the two cells.

#### 3.2.4.2 The Influence of a Time-Periodic force

In nature, two cells can form a bundle through the head-to-head, tail-to-tail, and head-to-tail attachment. However, the vast majority of motile sperm cells form bundles by attachments between the heads. Moreover, under the head-to-head attachment, one cell experiences the time-periodic force generated by the other cell with the time-periodic flagellar deformation. Therefore, the collinear bundle provides a unique opportunity to investigate the response of sperm cells to an external time-periodic force exerted on the sperm head. We show the numerical results when two cells form a collinear bundle. The flagellar deformation at every beat cycle is obtained upon solving the governing equation, while the kinematics of two cells are determined through Equations 3.12-3.14. Using the developed model, we simulate the interaction of two cells for continuous beat cycles, and study the variation of the wave patterns of sperm cells after forming the collinear bundle. In the simulation, two cells are initially placed with the opposite orientations. The entire movement can be divided into two phases. The first phase shows the free swimming of the two cells, and the wave patterns of the two cells are presented in Figure 3.3(A). The second phase is when the two cells form the collinear bundle, that is to say, the adhesive forces and steric forces are applied additionally to the sperm cells. Figure 3.3(A) also shows the wave patterns of the two cells after forming the collinear bundle. When the interaction occurs, the adhesive force is first produced and acts to pull two cells closer. Subsequently, the steric force arises owing to the overlap of two sperm heads. Since the steric force is stronger than the adhesive force, the two cells separate until the adhesive force is dominant again. Two cells go through the above interaction periodically.

In terms of the governing equation, the force,  ${}^i\mathbf{F}_{\text{prx}}(t) = {}^i\mathbf{F}(t) + {}^i\mathbf{F}_{\text{adh}}(t) + {}^i\mathbf{F}_{\text{ste}}(t)$ , on the proximal end modulates the flagellar deformation of the

### 3.2 Actively Propagated Waves along Two Collinear Flagella

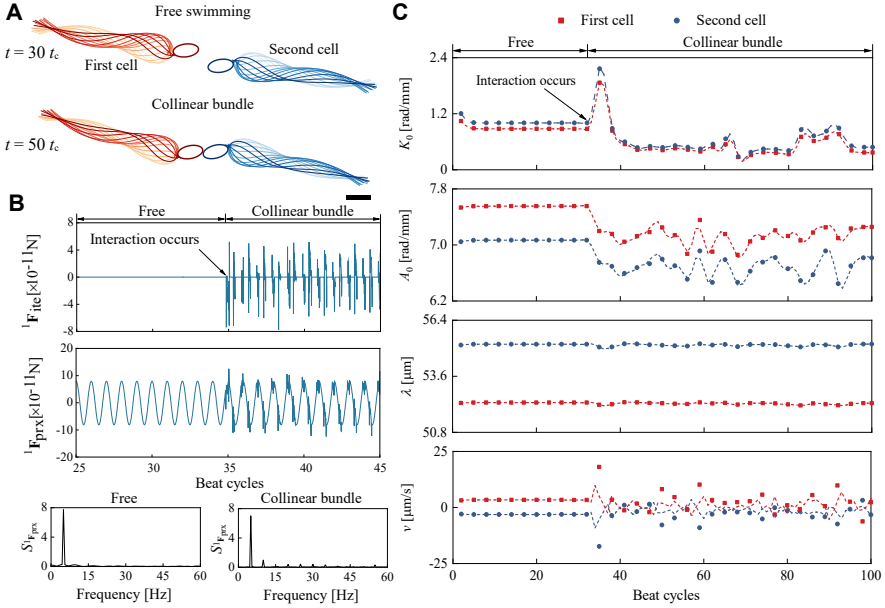


Figure 3.3: The numerical results by modeling the interaction of two sperm cells. (A) The simulated wave patterns of two cells when freely swimming and after forming the collinear bundle (darker curves for later times). The scale bar is  $10 \mu m$ . (B) The interaction force  ${}^1\mathbf{F}_{ite}$  on the sperm head of the first cell and the force  ${}^1\mathbf{F}_{prx}$  on the proximal end of the first cell. Power spectrum of  ${}^1\mathbf{F}_{prx}$  during the free swimming and after forming the collinear bundle. (C) The mean flagellar curvature  $K_0$ , the bending amplitude  $A_0$ , and the wavelength  $\lambda$  of the simulated wave pattern are extracted over one hundred beat cycles. The average path velocities  $v$  of two cells decrease during the interaction.

sperm cell. Figure 3.3(B) shows the variation of force  ${}^1\mathbf{F}_{prx}$  exerted on the first cell. When two cells freely swim, the force  ${}^1\mathbf{F}_{prx}$  is only comprised of the drag force  ${}^1\mathbf{F}$ , which shows the sinusoidal variation with time. After that, the two cells start to interact, and adhesive force and steric force are added to the drag force. Therefore, the wave pattern of sperm cells changes after forming the collinear bundle. The force  ${}^1\mathbf{F}_{prx}$  oscillates with the angular frequency  ${}^1\omega$  of the flagellar beat, which is reflected by the power spectrum in Figure 3.3(B). Also, we display the variation of the interaction force,  ${}^i\mathbf{F}_{ite}(t) = {}^i\mathbf{F}_{adh}(t) + {}^i\mathbf{F}_{ste}(t)$ , on the first cell with respect to time in Figure 3.3(B). The curve implies that the first cell experiences the

### 3. Flagellar Propulsion of Sperm Cells Against a Time-Periodic Interaction Force

---

time-periodic interaction force after forming the collinear bundle. Therefore, the collinear bundle can be a qualified objective to study the effect of a time-periodic force on the wave pattern.

Next, the Fourier analysis (see Experimental Section) is used to analyze the wave pattern obtained from the numerical results. Figure 3.3(C) displays the variation of wave variables of two sperm cells over one hundred beat cycles. The wave patterns are time-periodic when two cells freely swim, whereas the wave variables become unsteady after forming the collinear bundle. It can be attributed to the varying interaction force on the two sperm heads. When freely swimming, the mean flagellar curvature  ${}^1K_0$ , the bending amplitude  ${}^1A_0$ , and the wavelength  ${}^1\lambda$  are 0.88 rad/mm, 7.55 rad/mm, and 52.29  $\mu\text{m}$ , respectively, and  ${}^2K_0$ ,  ${}^2A_0$ , and  ${}^2\lambda$  are 1.00 rad/mm, 7.07 rad/mm, and 55.20  $\mu\text{m}$ , respectively. The discrepancy in the wave variables of the two cells is caused by the different bending stiffness,  ${}^1E = 1.8 \times 10^{-21} \text{ N} \cdot \text{m}^2$  and  ${}^2E = 2.5 \times 10^{-21} \text{ N} \cdot \text{m}^2$ . Subsequently, the steric and adhesive forces are imposed on the sperm cells. The wave variables  ${}^1K_0$  and  ${}^1A_0$  are decreased to  $0.48 \pm 0.15$  rad/mm and  $7.12 \pm 0.12$  rad/mm, respectively, and  ${}^1\lambda$  is kept at  $52.23 \pm 0.04 \mu\text{m}$ . The interaction causes an impact on the wave patterns of the second cell as well. During the interaction, the wave variables  ${}^2K_0$ ,  ${}^2A_0$ , and  ${}^2\lambda$  are  $0.55 \pm 0.17$  rad/mm,  $6.67 \pm 0.14$  rad/mm, and  $55.15 \pm 0.05 \mu\text{m}$ , respectively. Therefore, the mean flagellar curvature  $K_0$  and the bending amplitude  $A_0$  of two cells are reduced, but there is no obvious difference in the wavelength  $\lambda$  after forming the collinear bundle.

The average value  $\langle \mathbf{F}_{\text{prx}} \rangle$  and the root mean square  $\text{RMS}(\mathbf{F}_{\text{prx}})$  of the force on the proximal end can explain the variation of  $K_0$  and  $A_0$  after forming the collinear bundle, respectively. The average force  $\langle \mathbf{F}_{\text{prx}} \rangle$  denotes the time-symmetry of the force. A time-symmetrical force on the proximal end leads to the symmetrical wave patterns, since the propagating wave is directly modulated by the force on the proximal end. Therefore, the closer  $\langle \mathbf{F}_{\text{prx}} \rangle$  is to 0, the smaller  $K_0$  is. The average force  $\langle {}^1\mathbf{F}_{\text{prx}} \rangle$  applied to the proximal end of the first cell is  $1.0 \times 10^{-12} \text{ N}$  during the free swimming. It decreases to  $5.2 \times 10^{-13} \text{ N}$  after forming the collinear bundle. For the second cell, the average force  $\langle {}^2\mathbf{F}_{\text{prx}} \rangle$  is decreased from  $1.0 \times 10^{-12} \text{ N}$  to  $5.4 \times 10^{-13} \text{ N}$ . It agrees well with the decrease of the mean flagellar curvatures  ${}^1K_0$  and  ${}^2K_0$ . The decrease in the average force can be attributed to the addition of the interaction force after forming the collinear bundle. On the other hand,

the root mean square of force  $\text{RMS}(\mathbf{F}_{\text{prx}})$  denotes the force amplitude, which affects the bending amplitude of the propagating wave. The values of  $\text{RMS}(\mathbf{F}_{\text{prx}})$  for both two cells decrease from approximately  $5.7 \times 10^{-11}$  N to  $5.5 \times 10^{-11}$  N after forming the collinear bundle. The interaction force  ${}^i\mathbf{F}_{\text{ite}}(t)$  against the drag force  ${}^i\mathbf{F}(t)$  causes the attenuation of force amplitude, thereby resulting in the decrease of the bending amplitude  $A_0$ . Figure 3.3(C) also describes the swimming characteristic of two cells over one hundred beat cycles. Affected by steric and adhesive force, the average path velocities of sperm cells strongly weaken after forming the collinear bundle.

Besides, our developed model can predict the effect of other parameters on the wave patterns of sperm cells after forming the collinear bundle. The phase shift,  $\Delta\theta_{\text{pha}} = {}^2\theta_{\text{pha}} - {}^1\theta_{\text{pha}}$ , between the propagating waves of two cells and the elastic sliding resistance  $k$  are changed in our model. In the context below, the variation extent of the wave variables is expressed through the percentage. The phase shift  $\Delta\theta_{\text{pha}}$  ranges from  $0^\circ$  to  $180^\circ$  by keeping  ${}^1\theta_{\text{pha}} = 0^\circ$  and setting  ${}^2\theta_{\text{pha}} \in [0^\circ 180^\circ]$ . The flagellar deformation is determined by the force acting on the proximal end of the flagellum. We use Equation 3.10 to express the force on the proximal end of free sperm cells. By varying the initial phase  ${}^i\theta_{\text{pha}}$  in Equation 3.10, the initial phase of the propagating wave is changed with that of the force. The propagating wave at the latest time (see the darkest curves of the second cell in Figure 3.4(A)) moves from left to right, when the initial phase  ${}^2\theta_{\text{pha}}$  increases from  $0^\circ$  to  $180^\circ$ . Therefore, the change of the initial phase is indicated by the shift of the propagating wave. Figure 3.4(A) shows the wave patterns of two cells with different phase shifts  $\Delta\theta_{\text{pha}}$  during the free swimming and after forming the collinear bundle. The variations of  $K_0$  ( $\Delta K_0$ ) with  $\Delta\theta_{\text{pha}}$  are displayed in Figure 3.4(B)-I. The negative percentage indicates that  $K_0$  of the cell decreases after forming the collinear bundle irrespective of  $\Delta\theta_{\text{pha}}$ . To validate the relationship between the average force  $\langle \mathbf{F}_{\text{prx}} \rangle$  and  $K_0$ , the variations of the average force  $\Delta \langle \mathbf{F}_{\text{prx}} \rangle$  are shown in Figure 3.4(B)-II. The flagellar deformation at every time instant is determined by the instantaneous force  $\mathbf{F}_{\text{prx}}$  imposed on the proximal end. If the force is symmetrical with respect to time, the time-symmetrical wave pattern is formed. Therefore, when the average force  $\langle \mathbf{F}_{\text{prx}} \rangle$  decreases, the wave pattern of the cell will be more symmetrical. The bending amplitude  $A_0$  increases during the interaction if the phase shift  $\Delta\theta_{\text{pha}}$  exceeds  $90^\circ$ , as

### 3. Flagellar Propulsion of Sperm Cells Against a Time-Periodic Interaction Force

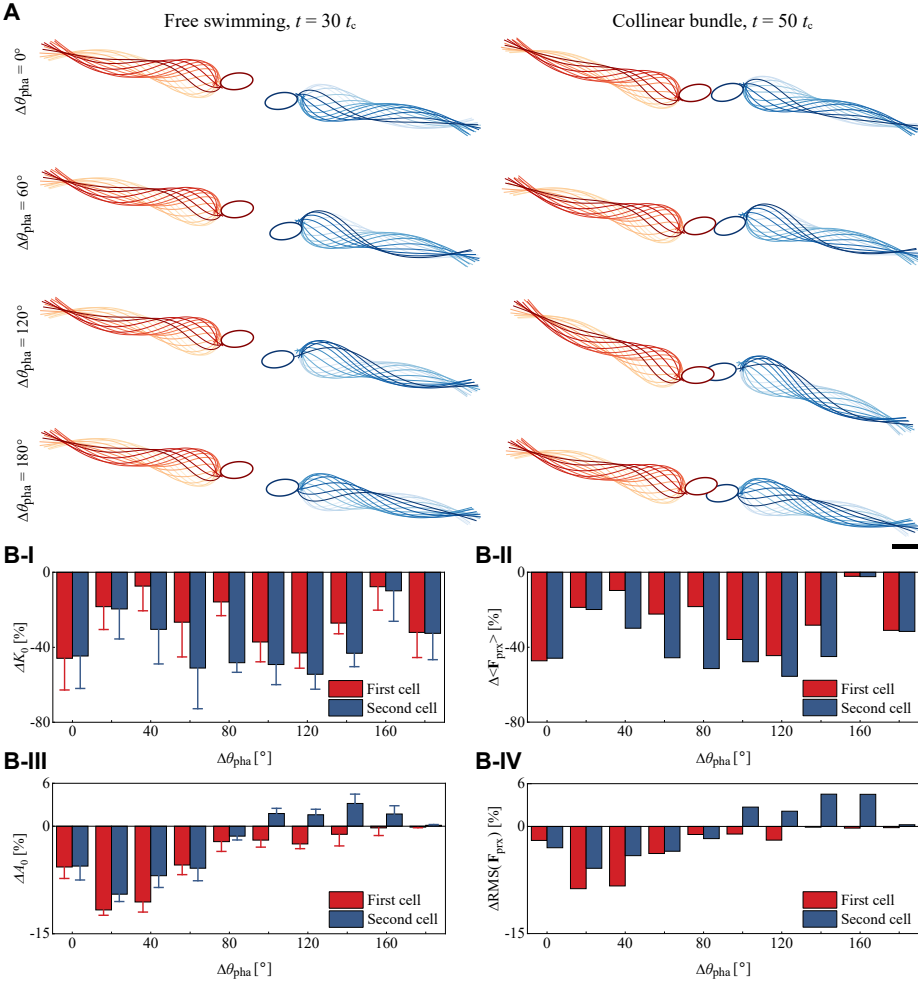


Figure 3.4: The numerical results in case of propagating waves of two cells with different phase shifts  $\Delta\theta_{\text{pha}}$ . (A) The wave patterns of two cells in case of the different phase shifts  $\Delta\theta_{\text{pha}}$ . The scale bar is  $10 \mu\text{m}$ . (B) The numerical results of the wave variables and force under  $\Delta\theta_{\text{pha}}$  ranging from  $0^\circ$  to  $180^\circ$ . (B-I) The variation percentage of the mean flagellar curvature,  $\Delta K_0$ , for two cells. (B-II) The variation percentage of the average forces,  $\Delta \langle \mathbf{F}_{\text{prx}} \rangle$ , acting on the proximal end of two cells. (B-III) The variation percentage of the bending amplitude,  $\Delta A_0$ , for two cells. (B-IV) The variation percentage of the root mean square of the forces,  $\Delta \text{RMS}(\mathbf{F}_{\text{prx}})$ , acting on the proximal end of two cells.

### 3.2 Actively Propagated Waves along Two Collinear Flagella

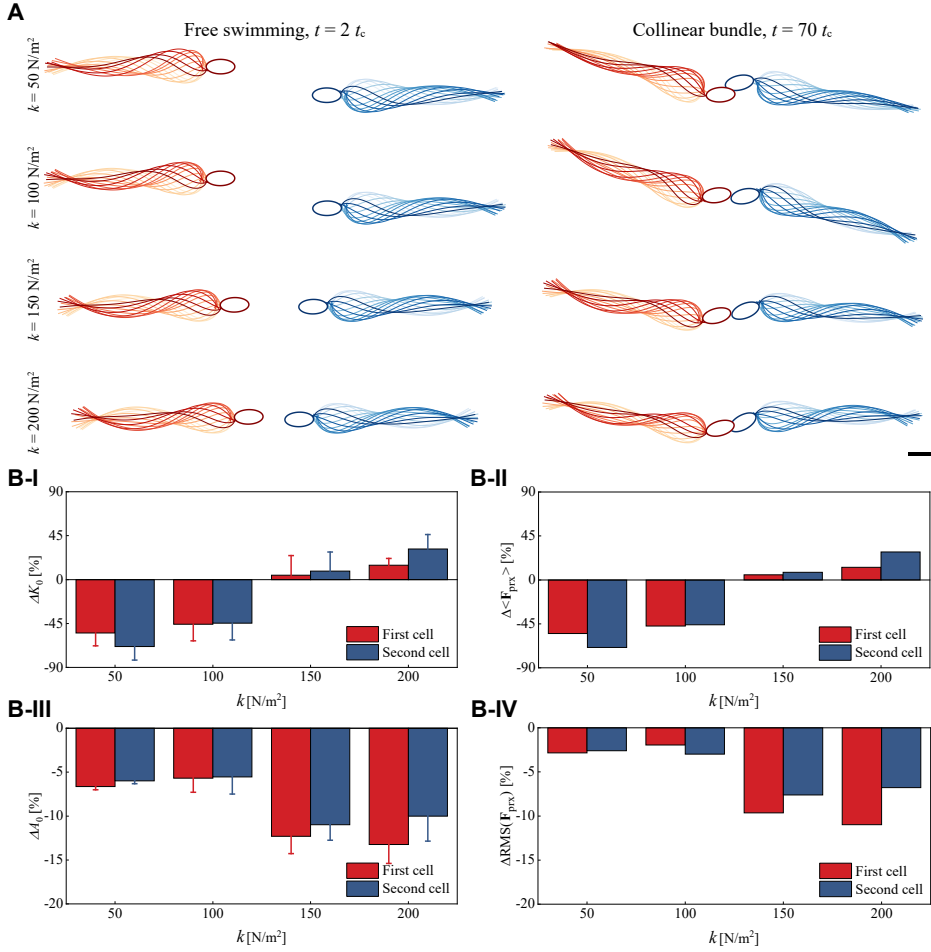


Figure 3.5: The numerical results in the case of two sperm cells with varying elastic sliding resistance  $k$ . (A) The wave patterns of two cells in case of different  $k$ . The scale bar is  $10 \mu\text{m}$ . (B) The numerical results under  $k$  from  $50 \text{ N/m}^2$  to  $200 \text{ N/m}^2$ . (B-I) The variation percentage of the mean flagellar curvature,  $\Delta K_0$ , for two cells. (B-II) The variation percentage of the average forces,  $\Delta \langle \mathbf{F}_{\text{prx}} \rangle$ , acting on the proximal end of two cells. (B-III) The variation percentage of the bending amplitude,  $\Delta A_0$ , for two cells. (B-IV) The variation percentage of the root mean square of the forces,  $\Delta \text{RMS}(\mathbf{F}_{\text{prx}})$ , acting on the proximal end of two cells.

shown in Figure 3.4(B)-III. This reflects that the interaction force boosts

### 3. Flagellar Propulsion of Sperm Cells Against a Time-Periodic Interaction Force

---

the bending of the propagating wave in this case. Basically, the sperm cell changes the phase of wave patterns by adjusting the initial phase  ${}^i\theta_{\text{pha}}$  of the drag force  ${}^i\mathbf{F}$ . When the initial phase  ${}^i\theta_{\text{pha}}$  exceeds  $90^\circ$ , the direction of the interaction force becomes the same as that of the drag force  ${}^i\mathbf{F}$ . Thus, the bending of the flagellum of the cell is facilitated after interacting with the other cell. Figure 3.4(B)-IV shows the variations of the root mean square of the force  $\Delta\text{RMS}(\mathbf{F}_{\text{prx}})$  versus different phase shifts  $\Delta\theta_{\text{pha}}$ . When  $\Delta\theta_{\text{pha}}$  is greater than  $90^\circ$ ,  $\Delta\text{RMS}(\mathbf{F}_{\text{prx}})$  is positive, which is in agreement with the increase of  ${}^2A_0$  after forming the collinear bundle.

3 The flagellar axoneme of sperm cells varies across species. In mammalian sperm cells, the axoneme is surrounded by outer dense fibers, mitochondria, and plasma membrane at the midpiece. The principal piece is surrounded by outer dense fibers, fibrous sheath, and plasma membrane, and the distal end is only enveloped by plasma membrane [20]. In terms of non-mammalian sperm cells, such as sea urchins, tunicates, and teleosts the axonemes are simply enclosed by a plasma membrane [214]. The outer surroundings are likely to resist the sliding of two polar filaments, resulting in the varying elastic sliding resistance  $k$  among different species. Regarding the different elastic sliding resistance  $k$ , the wave patterns of two cells are shown in Figure 3.5(A) during the free swimming and after forming the collinear bundle. Upon increasing the elastic sliding resistance, it is harder to bend the flagellum with the stiffer nexin links. Therefore, the bending amplitude of the wave pattern decreases with the elastic sliding resistance, and the mean flagellar curvature also decreases compared to the cells with the normal flagellum. The variations  $\Delta K_0$  and  $\Delta A_0$  with respect to the elastic sliding resistance are displayed in Figure 3.5(B)-I and 3.5(B)-III. It is noted that the mean flagellar curvature  $K_0$  increases during the interaction when  $k$  is larger than  $100 \text{ N/m}^2$ . In the case of the flagellum with the stiffer nexin links, the angular speed of the sperm head is decreased due to the reduced bending amplitude of the propagating wave. The two sperm heads will not exchange their positions as they do with the normal flagellum. Therefore, the interaction force preferable to one direction increases the time-asymmetry of the force  $\mathbf{F}_{\text{prx}}$ . Regardless of the elastic sliding resistance, the bending amplitude decreases after the formation of the collinear bundle because the interaction force suppresses the bending of the propagating wave. Figure 3.5(B)-II and 3.5(B)-IV show the variation of the average force  $\Delta\langle\mathbf{F}_{\text{prx}}\rangle$  and the variation of the force amplitude

$\Delta\text{RMS}(\mathbf{F}_{\text{prx}})$  with respect to the different elastic sliding resistance  $k$ , which corresponds with the sign of  $\Delta K_0$  and  $\Delta A_0$ , respectively. Our model can help us have a comprehensive understanding of the influence of different flagellar properties on the wave patterns and explain the variation of wave patterns of sperm cells in the collinear bundle.

### 3.3 Experimental results

In the female reproductive tract, sperm cells need to go through the vagina, cervix, uterus, utero-tubal junctions, and oviduct [95]. Due to the heterogeneity of biochemical composition, the viscosity of the fluid varies when sperm cells arrive at different locations of the reproductive tract. As the viscosity of the fluid increases, the hydrodynamic drag will change, thus affecting the wave patterns of sperm cells. Nevertheless, sperm cells are able to adapt to fluidic environments with a range of viscosities in the reproductive tract. We experimentally observe the wave patterns of free sperm cells and collinear bundles in SP-TALP solution with the viscosity of  $1.2 \text{ mPa} \cdot \text{s}$  and dextran solution with the viscosity of  $25 \text{ mPa} \cdot \text{s}$  (see Experimental Section). After determining the positions of the flagellum centerline, the Fourier analysis is implemented to extract wave variables of sperm cells. The wave variables of sperm cells under zero force and a time-periodic interaction force are shown in the **Table 3.1**. In SP-TALP solution, the wave variables  $K_0$ ,  $A_0$ , and  $\lambda$  of the free cells are  $6.4 \pm 3.5 \text{ rad/mm}$ ,  $13.8 \pm 2.8 \text{ rad/mm}$ , and  $73 \pm 7 \text{ } \mu\text{m}$ , respectively. In the dextran solution, the wave patterns of free cells can be reconstructed by that with  $K_0$  of  $3.3 \pm 3.0 \text{ rad/mm}$ ,  $A_0$  of  $9.4 \pm 3.8 \text{ rad/mm}$ , and  $\lambda$  of  $57 \pm 8 \text{ rad/mm}$ . As the viscosity of the medium increases, the wave variables  $K_0$ ,  $A_0$ , and  $\lambda$  show a downward trend in accordance with the conclusion from others [215], [216].

#### 3.3.1 Sperm Cells under Time-Periodic Interaction

In the SP-TALP medium, the collinear bundle (see Figure 3.6(A)) exhibits the time-periodic wave patterns. The wave variables of two cells at the continuous beat cycles are extracted in Figure 3.7(A). Note that no considerable difference in the wave patterns of the two cells is observed over the movement. The collinear bundle shows a steady swimming velocity of

### 3. Flagellar Propulsion of Sperm Cells Against a Time-Periodic Interaction Force

Table 3.1: Wave variables and swimming performance of the flagellar propulsion with the beat frequency of  $f$  under zero and the time-periodic interaction force. In the experiments, the wave variables and swimming performance of free sperm cells are averaged over three consecutive beat cycles ( $n = 11$ ), while the average wave variables and swimming performance of sperm cells under interaction force are calculated from twenty beat cycles in each collinear bundle ( $n = 3$ ). In the model, the wave variables and swimming performance of free sperm cells and sperm cells under interaction force are averaged at the first and the second phases, respectively. To compare the mean values obtained with sperm cells and collinear bundles, we used the two-sided Student's  $t$ -tests. The statistical  $t$ -test indicates the significant difference in the flagellar propulsion between free sperm cells and collinear bundles.

Viscosity	Configuration	Cell index	$K_0$ [rad/mm]	$A_0$ [rad/mm]	$\lambda$ [ $\mu\text{m}$ ]	$f$ [Hz]	$v$ [ $\mu\text{m/s}$ ]
$\eta = 1.2 \text{ mPa}\cdot\text{s}$	Free cell (Experiment)	-	$6.39 \pm 3.47$	$13.80 \pm 2.81$	$72.99 \pm 6.48$	$14.49 \pm 4.18$	$115.99 \pm 28.22$
	Collinear bundle (Experiment)	1	$1.75 \pm 1.15$	$9.57 \pm 1.38$	$53.39 \pm 4.83$	$4.57 \pm 0.55$	$25.62 \pm 3.51$
		2	$1.20 \pm 0.80$	$4.97 \pm 0.45$	$79.15 \pm 3.80$	$4.56 \pm 0.34$	
	Collinear bundle (Theory)	1	$0.48 \pm 0.15$	$7.12 \pm 0.12$	$52.23 \pm 0.04$	4.57	$3.34 \pm 2.57$
		2	$1.00 \pm 0.55$	$6.67 \pm 0.14$	$55.14 \pm 0.05$	4.56	
	$\eta = 25 \text{ mPa}\cdot\text{s}$	Free cell (Experiment)	-	$3.33 \pm 3.07$	$9.37 \pm 3.85$	$56.86 \pm 8.28$	$13.09 \pm 4.35$
Collinear bundle (Experiment)		1	$1.85 \pm 0.78$	$5.32 \pm 1.17$	$54.19 \pm 5.06$	$2.63 \pm 0.42$	$18.69 \pm 8.80$
		2	$1.29 \pm 0.88$	$3.76 \pm 0.98$	$86.74 \pm 21.78$	$2.61 \pm 0.37$	
Collinear bundle (Theory)		1	$0.64 \pm 0.01$	$6.18 \pm 0.01$	$49.13 \pm 0.01$	2.63	$0.53 \pm 0.13$
		2	$0.67 \pm 0.01$	$5.43 \pm 0.01$	$51.00 \pm 0.02$	2.61	

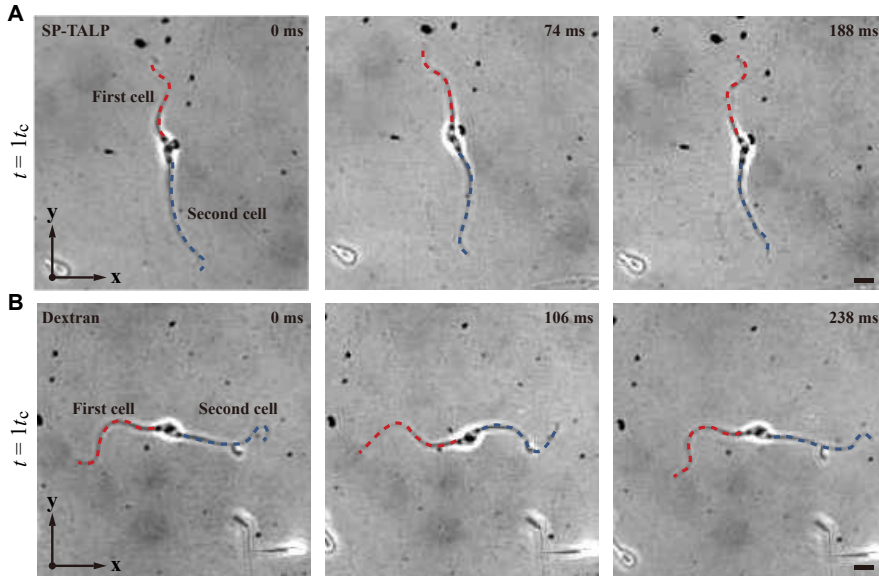


Figure 3.6: The respective propagating waves of the collinear bundle in (A) SP-TALP solution with the viscosity of  $1.2 \text{ mPa} \cdot \text{s}$  and (B) dextran solution with the viscosity of  $25 \text{ mPa} \cdot \text{s}$  in time sequences. The scale bar is  $10 \text{ }\mu\text{m}$ . See the supplementary materials Video 3-S1.

around  $25.7 \text{ }\mu\text{m/s}$ , as depicted in Figure 3.7(B). The first cell (the upper cell in Figure 3.6(A)) presents the wave-pattern with the mean flagellar curvature,  $K_0 = 1.8 \pm 1.1 \text{ rad/mm}$ , the bending amplitude,  $A_0 = 9.6 \pm 1.4 \text{ rad/mm}$ , and the wavelength,  $\lambda = 53 \pm 5 \text{ }\mu\text{m}$ . For the second cell (the bottom one in Figure 3.6(A)), the mean flagellar curvature, the bending amplitude, and the wavelength of the second cell are  $1.2 \pm 0.8 \text{ rad/mm}$ ,  $5.0 \pm 0.4 \text{ rad/mm}$ , and  $79 \pm 4 \text{ }\mu\text{m}$ , respectively. In the presence of the interaction force, the symmetry of the wave pattern of the collinear bundle is higher in comparison with the free sperm cell. Furthermore, the bending amplitude of the propagating wave decreases after forming the collinear bundle. It implies that the interaction force restricts the bending of the propagating wave to a great extent. The velocity of a sperm cell is directly related to its beat frequency, wavelength, and bending amplitude, where the relationship  $v \sim A_0^2 f \lambda$  holds [217]. According to the extracted wave variables, the first cell possesses a faster swimming velocity than the second cell ow-

### 3. Flagellar Propulsion of Sperm Cells Against a Time-Periodic Interaction Force

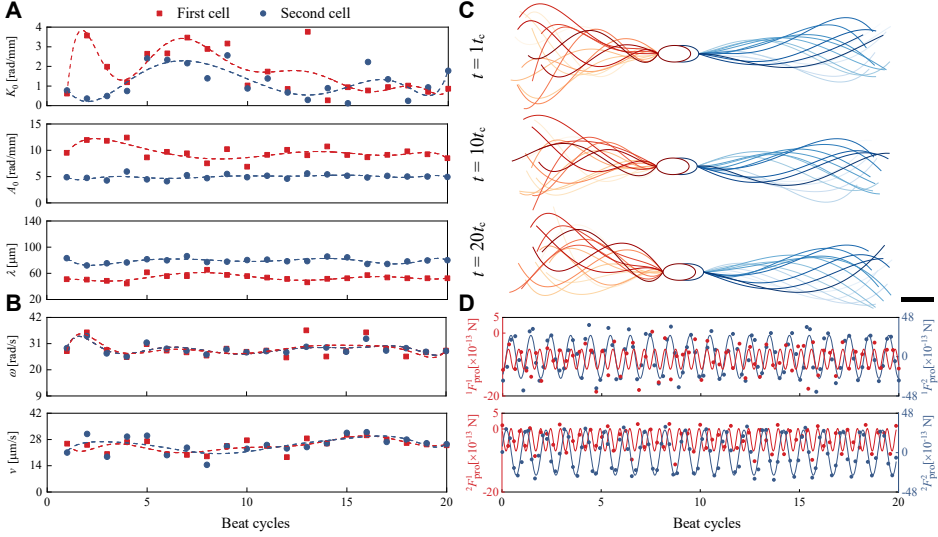


Figure 3.7: The measured results of the collinear bundle in SP-TALP solution ( $n = 3$ ). (A) Wave variables of the collinear bundle are measured over twenty cycles. (B) Swimming characteristic of the collinear bundle. (C) The actual wave patterns of the collinear bundle at three cycles. The scale bar is  $10 \mu\text{m}$ . (D) The propulsive forces generated by the flagella of the collinear bundle are calculated over twenty cycles. The components  ${}^i F_{\text{pro}}^1$  and  ${}^i F_{\text{pro}}^2$  are along the orthonormal vectors  ${}^i \mathbf{e}_1$  and  ${}^i \mathbf{e}_2$  of the  $i$ th cell, respectively.

ing to its larger bending amplitude and smaller wavelength. Figure 3.7(C) illustrates the actual wave patterns of the collinear bundle at three beat cycles. The collinear bundle in low-viscosity fluid presents nearly unchanged wave patterns within its entire swimming, which is in accordance with the small variation of the wave variables over twenty cycles. In addition, the propulsive thrust components  ${}^i F_{\text{pro}}^1$  and  ${}^i F_{\text{pro}}^2$ , which compose the propulsive force,  ${}^i \mathbf{F}_{\text{pro}} = {}^i F_{\text{pro}}^1 {}^i \mathbf{e}_1 + {}^i F_{\text{pro}}^2 {}^i \mathbf{e}_2$ , are calculated over twenty beat cycles based on the resistive-force theory (see Figure 3.7(D)). The minor variation in the wave variables corresponds with the approximately time-periodic variation of the propulsive thrust. Among the force competition between  $\langle {}^1 F_{\text{pro}}^1 \rangle = (8.3 \pm 1.4) \times 10^{-13} \text{ N}$  and  $\langle {}^2 F_{\text{pro}}^1 \rangle = (3.5 \pm 0.6) \times 10^{-13} \text{ N}$ , the first cell with the greater average propulsive force pushes the second cell and determines the moving direction of the collinear bundle.

The other collinear bundle (see Figure 3.6(B)) is formed in the dextran

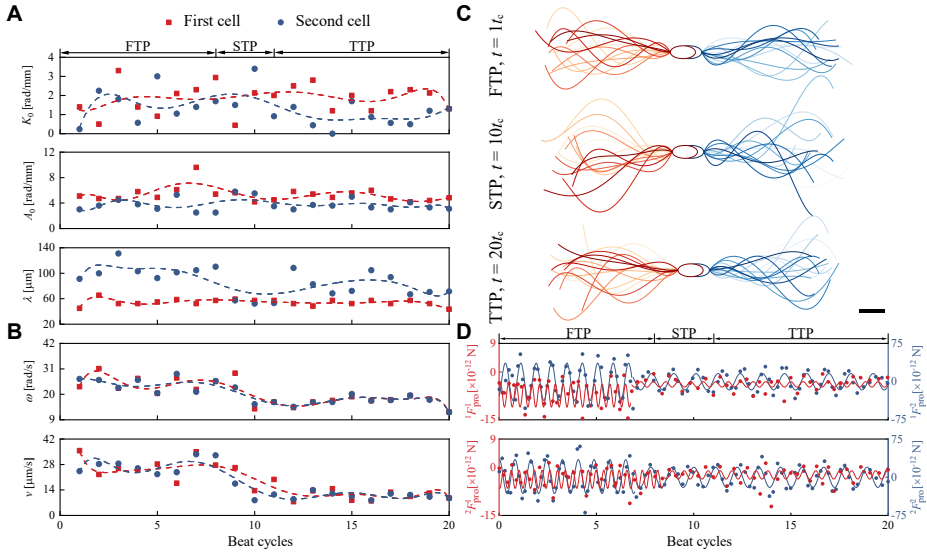


Figure 3.8: The collinear bundle in dextran solution ( $n = 3$ ). (A) Wave variables and (B) Swimming characteristic of two cells are measured at the first time period (FTP, the first to the eighth beat cycle), the second time period (STP, the ninth to the eleventh beat cycle), and the third time period (TTP, the twelfth to the twentieth beat cycle). (C) The actual wave patterns of the collinear bundle in one beat cycle of three time periods. The scale bar is  $10 \mu\text{m}$ . (D) The propulsive forces components  ${}^i F_{\text{pro}}^1$  and  ${}^i F_{\text{pro}}^2$  generated by the flagella of the collinear bundle are calculated over twenty beat cycles.

solution. The two cells' variation curves of the wave variables versus beat cycles are plotted in Figure 3.8(A). In the course of the movement, the first cell (the left cell in Figure 3.6(B)) displays the wave pattern with a slight variation. In terms of the second cell (the right cell in Figure 3.6(B)), the wave variables but the wavelength show a negligible discrepancy over the swimming course. At the first time period (FTP, the first to the eighth beat cycle), the wavelengths of the first and the second cell are  $54 \pm 6 \mu\text{m}$  and  $104 \pm 12 \mu\text{m}$ , respectively. The collinear bundle swims with the velocity of  $27.5 \pm 4.1 \mu\text{m/s}$ , as shown in Figure 3.8(B). At the second time period (STP, the ninth to the eleventh beat cycle), the wave pattern of the second cell goes through a transition from the large wavelength  ${}^2\lambda = 104 \pm 12 \mu\text{m}$  to the small wavelength  ${}^2\lambda = 54 \pm 3 \mu\text{m}$ . Although the two cells show similar wave patterns during this time period, the collinear bundle can

### 3. Flagellar Propulsion of Sperm Cells Against a Time-Periodic Interaction Force

---

3

move with the velocity of  $12.4 \pm 4.7 \mu\text{m/s}$ . At the third time period (TTP, the twelfth to the twentieth beat cycle), the wavelength of the second cell increases to  $82 \pm 16 \mu\text{m}$ . The swimming velocity of the collinear bundle decreases to  $10.8 \pm 2.0 \mu\text{m/s}$ . The changes in wave variables at different beat cycles arise from the heterogeneity of the wave patterns, as depicted in Figure 3.8(C). Figure 3.8(D) shows the propulsive thrust components of sperm cells in the collinear bundle based on the extracted wave variables. The thrust displays the sinusoidal variation, but the frequency is changed as the angular frequency of sperm cells after the eighth beat cycle. During the FTP, the average propulsive forces  ${}^i F_{\text{pro}}^1$  of the first cell and the second cell are calculated to be  $7.4 \times 10^{-12} \text{ N}$  and  $3.6 \times 10^{-12} \text{ N}$ , respectively. During the STP, the propulsive thrust components  $\langle {}^1 F_{\text{pro}}^1 \rangle$  and  $\langle {}^2 F_{\text{pro}}^1 \rangle$  decrease to  $2.8 \times 10^{-12} \text{ N}$  and  $2.3 \times 10^{-12} \text{ N}$ , respectively. During the TTP, the propulsive thrust component  $\langle {}^1 F_{\text{pro}}^1 \rangle$  of the first cell is  $3.9 \times 10^{-12} \text{ N}$ , while  $\langle {}^2 F_{\text{pro}}^1 \rangle$  of the second cell is  $3.1 \times 10^{-12} \text{ N}$ . From the standpoint of force, the decrease of resultant propulsive thrust on the collinear bundle explained the reduced velocity at the TTP in comparison with that at the FTP. However, the velocity of the collinear bundle at the TTP is smaller than that at the STP, while the resultant propulsive thrust is greater at the TTP. It can be attributed to the fact the velocity of the collinear bundle is mainly determined by the angular frequency of the flagellar beat.

#### 3.3.2 Flow Field and Bending Moment

The regularized Stokeslets theory (see Experimental Section) can predict the fluid response for a given point force along the flagellum. Therefore, we utilize the regularized Stokeslets theory to predict the fluid response for the point forces on the sperm flagellum. The time-averaged flow fields  $\mathbf{u}(\mathbf{x})$  around the free sperm cells and the collinear bundles are calculated as shown in Figure 3.9(A)-(D). For the free sperm cell, the time-averaged flow field increases toward the distal end. This is because the rate of wave propagation increases as the bending stiffness decreases over the length [218]. Moreover, the increase in the flow field along the flagellum indicates that the bending wave is initiated at the proximal end. With the increase of the fluid viscosity, the time-averaged flow field decreases owing to the decrease of the bending amplitude of the propagating waves. Compared to the free sperm cells, the collinear bundle generates a smaller averaged flow field

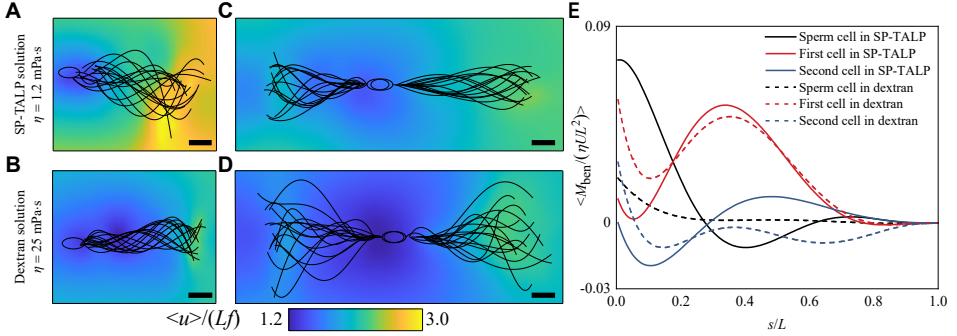


Figure 3.9: The time-averaged flow field of the free sperm cell in (A) SP-TALP solution ( $n = 11$ ) and (B) dextran solution ( $n = 11$ ) and the collinear bundle in (C) SP-TALP solution ( $n = 3$ ) and (D) dextran solution ( $n = 3$ ). The scale bar is  $10 \mu\text{m}$ . (E) Nondimensional time-averaged bending moments  $\langle M_{ben}/(\eta UL^2) \rangle$  are calculated over one beat cycle for the free sperm cell and the collinear bundle in SP-TALP and dextran solution.

due to its smaller bending amplitude. For every single cell in the collinear bundle, the identical fluid behavior as a free sperm cell that the flow field increases from the proximal end to the distal end is noted in Figure 3.9(C) and 3.9(D). Due to the zero-torque and zero-force condition at the distal end, the time-averaged flow field reaches the maximum at this location. It implies that the wave propagation is initiated and coordinated from the proximal end of the collinear bundle.

Additionally, the bending moment  $M_{ben}$  used for adjusting the wave pattern can be derived from the positions of the flagellar centerline (see Experimental Section). Figure 3.9(E) shows the respective nondimensional time-averaged bending moments  $\langle M_{ben}/(\eta UL^2) \rangle$  [219], where  $U$  is the magnitude of the flagellum velocity,  $\mathbf{U} = \mathbf{U}_\perp + \mathbf{U}_\parallel$  (see Experimental Section). In the case of the free sperm cell in the SP-TALP solution, the time-averaged bending moment decreases to zero at one-third of the flagellum. The maximum displacement of the flagellum can be observed at the corresponding position in Figure 3.9(A). For the free sperm cell in the dextran solution, the time-averaged bending moment is always positive, accounting for the increase of the bending amplitude of the propagating wave toward the distal end. Figure 3.9(E) also describes the distributed nondimensional time-averaged bending moment along two flagella of the collinear bundle.

### 3. *Flagellar Propulsion of Sperm Cells Against a Time-Periodic Interaction Force*

---

The first cell (the left cell in Figure 3.9(C) and 3.9(D)) possesses a greater nondimensional time-averaged bending moment than the second cell (the right cell in Figure 3.9(C) and 3.9(D)). In the low-viscous fluid, the first cell motivates the positive bending moment along the entire flagellum. It is consistent with the first cell showing the increasing bending amplitude toward the distal end, as shown in Figure 3.9(C). The wave pattern of the second cell over one beat cycle exhibits the maximum bending amplitude at the  $s/L = 0.3$  and the  $s/L = 1$ , which corresponds with the maximum displacement at the respective locations. In the high-viscous fluid, two cells generate the bending moment with the unchanged direction to produce the propagating wave with increasing displacement over the flagellum. Compared to free sperm cells, sperm cells in the collinear bundle can overcome the interaction force by generating a greater time-averaged bending moment.

#### 3.4 Discussion

Prior to fusing with the ovum, sperm cells are likely to experience various physical and chemical interactions in the female reproductive tracts. Spermatozoa interact with the oviductal epithelial cells, which can be understood as one selection mechanism. Only uncapacitated sperm cells can bind to the oviduct and be stored there. Upon ovulation and capacitation, sperm cells become hyperactivated and thereby detach from the oviductal epithelial cells. This process controls the timing of the arrival of matured sperm cells at the ovum [220]. On the other hand, sperm cells need to interact with the zona pellucida for successful fusion. Acrosomal enzymes are released during the acrosome reaction that allows the penetration of the zona pellucida in combination with hyperactivity, which allows mechanical penetration and removal of the cumulus cells [221]. These interactions will inevitably affect flagellar propulsion of sperm cells, and filter out the abnormal sperm cells with poor motility. High-quality sperm cells are able to migrate further in the female reproductive tract, and only one sperm cell can finally fertilize the ovum. Regardless of the interaction with fluid flow, the surface, or the cells, the effect acts on sperm cells in the form of a force. Herein, cell-to-cell interaction serves as a case to study the effect of an interaction force on the flagellar propulsion of sperm cells. Through our developed model, we first study the configuration of the sperm bundle

when two cells interact. Two configurations, a collinear bundle, and an aligned bundle, can be formed after the interaction. Irrespective of the initial orientations of two cells, the configuration of the sperm bundle depends on the resultant interaction torque on sperm cells (Figure 3.2(A)). The collinear bundle can be formed when the interaction is dominant by steric interaction. In this case, one cell rotates clockwise, while the other cell rotates counterclockwise since its resultant torque is opposite (Figure 3.2(B)). On the contrary, if the adhesive interaction is stronger than the steric interaction, one cell rotates counterclockwise and the other cell rotates clockwise, thereby forming an aligned bundle.

To understand the effect of a time-periodic force on the flagellar propulsion of sperm cells, we measured the wave patterns of the collinear bundles. By means of the Fourier analysis of the measured wave patterns, we find that wave patterns with smaller mean flagellar curvature and bending amplitude are exhibited by the sperm cells in the collinear bundles than free sperm cells. Likewise, our numerical results show a similar decrease in the mean flagellar curvature, bending amplitude, and swimming velocity for the collinear bundle, which qualitatively agrees with the experimental results (Table 3.1). After forming the collinear bundle, the interaction force, consisting of steric and adhesive force, is applied to the proximal end of the sperm flagellum and against the drag force exerted by the sperm head. The wave pattern displays the shape with the high time symmetry under the effect of the interaction force. Since the interaction force is opposite to the drag force, the bending amplitude of the propagating wave is suppressed, thereby leading to wave patterns with a smaller bending amplitude compared to free sperm cells. During the fusion with an ovum, the sperm head will be subjected to a time-periodic reaction force. Thus, it is likely that sperm cells exhibit the same wave patterns in the female reproductive tract. Our theoretical model and experiments provide tools to investigate the behavior of the cell during interactions with its surroundings. These sperm cells with excellent motility can travel through the physical barrier in the reproductive tract and arrive at the fertilization site. Our work can inspire future research in the field and can be used for analyzing sperm motility by means of wave patterns analysis, reducing the complexity of the current semen analysis in the field of reproductive health.

Moreover, our theoretical study shows that the mean flagellar curvature and the bending amplitude are not invariably reduced in terms of the wave

### 3. Flagellar Propulsion of Sperm Cells Against a Time-Periodic Interaction Force

---

3

pattern of sperm cells in the collinear bundles. When the initial phase of the propagating wave of cells exceeds  $90^\circ$ , the mean flagellar curvature of wave patterns of sperm cells decreases (Figure 3.4(B)-I), yet the bending amplitude increases after forming the collinear bundle (Figure 3.4(B)-III). In this case, the drag force reverses to be in the same direction as the interaction force. The force at the proximal end, comprised of the drag force and the interaction force, increases after forming the collinear bundle (Figure 3.4(B)-IV), thereby facilitating the bending of the propagating wave. In addition, the mean flagellar curvature increases (Figure 3.5(B)-I), and the bending amplitude decreases (Figure 3.5(B)-III) for the collinear bundle when the elastic sliding resistance exceeds  $50 \text{ N/m}^2$ . As the elastic sliding resistance of the flagellum increases, the nexin links can be considered as the stiffer spring. The sperm flagellum with the higher elastic sliding resistance will be harder to bend. Therefore, sperm cells display wave patterns with a smaller mean flagellar curvature and bending amplitude, and the angular speed of the sperm head is reduced. Two sperm heads will not experience the switch of position during the overlap, which results in the interaction force pointing to one side. In this manner, the time-asymmetrical interaction force is generated and applied to the proximal end of the sperm flagellum, enhancing the asymmetry of the wave patterns. Our developed model can predict the variation of the wave patterns of sperm cells with different flagellar properties after forming the collinear bundle, although we can not control these variables of sperm cells in the biological world.

In addition, our experimental results indicate that sperm cells can overcome the time-periodic interaction force by generating a greater internal bending moment. The importance of the distributed contractile elements in the flagellum is underlined when sperm cells face the external force. During the journey to the ovum, sperm cells are likely to contact the boundary, fluid flow, and other cells. Our results reveal the underlying mechanism of the adaptive behavior, when encountering a time-periodic force. In terms of the design of soft micro-nanorobots [222]–[224], the component that can generate adjustable bending moments should be included to overcome the external force, so that soft microrobots with high adaptability can be better applied to *in vivo* biomedical applications when facing an external force.

Our hydrodynamic model captures the true behavior of two sperm cells when they form a collinear bundle *in vitro*. The numerical results reveal a decrease in the mean flagellar curvature and the bending ampli-

tude of the cells, agreeing with the experimental results in low- and high-viscosity fluids. However, there is a deviation in the average path velocity of the collinear bundle between the experimental and numerical results (Table 3.1). The difference between experimental and numerical results is attributed to the deviation between the internal bending moment of the motile sperm cells which affects their motility. Moreover, the environments are more complicated in the female reproductive tract. In addition to the viscoelastic property of the biological fluid [95], secretory cells and ciliated cells extensively distributed in the reproduction tract [225] also affect the wave patterns of sperm cells on the path to the ovum. Although our model addresses a specific type of interaction, that is the collinear bundle, the presented theoretical and experimental framework can be used to obtain a different generalization for other types of interactions. For other configurations of sperm bundles or the interaction with secretory cells and ciliated cells, only the interaction force needs to be determined in the hydrodynamic model. As part of future studies, our model will be upgraded to systematically analyze wave patterns of sperm cells when encountering various interactions *in vivo*.

### 3.5 Conclusions

Our hydrodynamic model and experiments allow us to understand the variation of the wave patterns of sperm cells when swimming against a time-periodic interaction force. Our hydrodynamic model indicates that the wave pattern of sperm cells in the collinear bundle becomes symmetric, and the bending amplitude of the propagating wave decreases. Moreover, it manifests that the variation of wave pattern is also influenced by other parameters such as the initial phase and the elastic sliding resistance. When the initial phase of the propagating wave exceeds  $90^\circ$ , the bending amplitude increases after forming the collinear bundle. For the flagellum with high elastic sliding resistance, the mean flagellar curvature increases in terms of the wave patterns of the collinear bundle. As the viscosity increases, the mean flagellar curvature, the bending amplitude, and the velocity of the collinear bundle are reduced according to the numerical results. Similarly, we experimentally find that the mean flagellar curvature and bending amplitude of wave patterns of sperm cells decrease after forming a collinear bundle. Furthermore, wave variables of the collinear

### 3. Flagellar Propulsion of Sperm Cells Against a Time-Periodic Interaction Force

---

bundle decrease with the viscosity of the fluid, and the swimming performance of the collinear bundle diminishes due to the reduced frequency of the flagellar beat. Our study provides crucial insights into the hydrodynamic interactions of sperm cells not only with time-periodic interaction forces, but also with other dynamic interaction forces encountered *in vivo*. Further understanding of such cell-to-cell interaction will elucidate crucial processes preceding fertilization. Although we investigate a specific mode of cell-to-cell interaction, sperm cells physically interact with other bodies in the surrounding fluid. They bind to the cilia of the oviduct and interact with the cumulus cells and zona pellucida. Even though these interactions are complex in nature, physically, they can also be seen as dynamic and impose forces on the sperm cells. Our study contributes to understanding the spermatozoa's response to such external physical forces and the resulting change in their flagellar motion. This knowledge can also advance the understanding of a sperm cell's ability to overcome these forces. Furthermore, our work provides a novel way to study sperm motility when encountering external dynamic forces, and inspires technological improvements in assisted reproduction.

3

## 3.6 Experimental Section

### 3.6.1 Sperm Cell Video Microscopy

Cryopreserved bovine sperm cells are thawed in a 37°C water bath for 2 min before resuspending the thawed semen in 1 mL SP-TALP (modified sperm tyrode's albumin lactate phosphate medium, Caisson Labs). The sample is centrifuged at 300 g for 5 min, the supernatant is removed and resuspended in 1 mL fresh SP-TALP which results in a sperm concentration of about  $3 \times 10^6$  sperms/mL. Sperm cells are then diluted 1:1 in either 10  $\mu$ L SP-TALP (resulting in 1.2 mPa · s viscosity) or 10  $\mu$ L 20% dextran solution (dextran from *Leuconostoc* spp., Mr 70000. 31390-25G from Sigma-Aldrich resulting in 10% dextran with about 25 mPa · s viscosity at 40°C [226]). The samples are mixed and filled into a 10  $\mu$ L Leja slide. Video microscopy is performed in a Zeiss microscope with a phase contrast 40X objective and highspeed camera to obtain videos with 500 images per second.

### 3.6.2 Fourier Analysis of Wave-Pattern

Sperm flagella are characterized by the tangent angles,  ${}^i\varphi(s, t)$ , enclosed between the local tangent of the flagellum of  $i$ th cell and the orthonormal vector  ${}^i\mathbf{e}_1$ . The tangent angle can be approximately described using its zeroth and the first Fourier mode as follows [111], [215]:

$$\begin{aligned} {}^i\varphi(s, t) &\approx {}^i\varphi_0(s) + {}^i\varphi_1(s)e^{i\omega t} + {}^i\varphi_1^*(s)e^{-i\omega t} \\ &\approx K_0s + 2A_0s \cos(\omega t - 2\pi s/\lambda). \end{aligned} \quad (3.15)$$

Three key parameters that determine the wave patterns of sperm cells can be extracted from the Fourier decomposition. The zeroth Fourier mode,  ${}^i\varphi_0(s) = K_0s$ , characterizes the time-averaged mean shape of the flagellum. The mean flagellar curvature  $K_0$  denotes the symmetry of wave patterns over one beat cycle. Second, the bending amplitude  $A_0$  along the tail is extracted from the absolute value of the first mode,  $|{}^i\varphi_1(s)| = A_0s$ , reflecting the bending of the flagellum. Third,  $\lambda$  is the wavelength and obtained by fitting  $2\pi s/\lambda$  to the phase angle of the complex first Fourier mode  $-\arg {}^i\varphi_1^*(s)$ .

### 3.6.3 Calculation of the Drag-Based Thrust

The resistive-force theory is also known as the local drag theory. Suppose that the flagellum is subject to an external drag which is uniformly distributed over the flagellum. The external drag can be decomposed into two components tangent and normal to the surface of the flagellum. The tangent vectors are expressed by  ${}^i\mathbf{t}(s, t) = (\partial {}^i\mathbf{r}(s, t)/\partial s)/|\partial {}^i\mathbf{r}(s, t)/\partial s|$ , and the normal vectors  ${}^i\mathbf{n}(s, t)$  along the  $i$ th flagellum are determined through the expression  ${}^i\mathbf{n}(s, t) = (\partial {}^i\mathbf{t}(s, t)/\partial s)/|\partial {}^i\mathbf{t}(s, t)/\partial s|$ . The velocities along the local tangent and normal velocity of  $i$ th flagellum are calculated by

$${}^i\mathbf{U}_{\parallel}(s, t) = ({}^i\dot{\mathbf{r}}(s, t) \cdot {}^i\mathbf{t}(s, t)) {}^i\mathbf{t}(s, t), \quad {}^i\mathbf{U}_{\perp}(s, t) = {}^i\dot{\mathbf{r}}(s, t) - {}^i\mathbf{U}_{\parallel}(s, t). \quad (3.16)$$

Then the propulsive thrust generated by one segment of the  $i$ th flagellum is as follows:

$${}^i\mathbf{f}(s, t) = {}^i\xi_{\perp} {}^i\mathbf{U}_{\perp}(s, t) + {}^i\xi_{\parallel} {}^i\mathbf{U}_{\parallel}(s, t). \quad (3.17)$$

The tangent and normal drag coefficients of  $i$ th flagellum are given by [227]

$${}^i\xi_{\perp} = \frac{4\pi\eta}{\ln(\frac{2L}{d}) + 0.193}, \quad {}^i\xi_{\parallel} = \frac{2\pi\eta}{\ln(\frac{2L}{d}) - 0.807}, \quad (3.18)$$

where  $d$  is the diameter of the flagellum.

### 3.6.4 Calculation of the Fluid Response

Regularized Stokeslets theory is implemented to predict the produced flow field. Assuming the surface of collinear bundle are covered with  $N$  Stokeslets boundary points, the flow field  $\mathbf{u}(\mathbf{x})$  caused by traction forces  $\mathbf{F}_k$  at the position  $\mathbf{r}_k$  is given by [151]

$$\begin{aligned} \mathbf{u}(\mathbf{x}) &= \sum_{k=1}^N \frac{-\mathbf{F}_k}{2\pi\eta} \left[ \ln(\sqrt{r_k^2 + \varepsilon^2} + \varepsilon) - \frac{\varepsilon(\sqrt{r_k^2 + \varepsilon^2} + 2\varepsilon)}{(\sqrt{r_k^2 + \varepsilon^2} + \varepsilon)^2} \right] \\ &+ \frac{1}{4\pi\eta} [\mathbf{F}_k \cdot (\mathbf{x} - \mathbf{r}_k)] (\mathbf{x} - \mathbf{r}_k) \left[ \frac{\sqrt{r_k^2 + \varepsilon^2} + 2\varepsilon}{(\sqrt{r_k^2 + \varepsilon^2} + \varepsilon)^2 \sqrt{r_k^2 + \varepsilon^2}} \right] \quad (3.19) \\ &= \mathbf{G}(\mathbf{x})\mathbf{F}_k, \end{aligned}$$

where  $r_k = |\mathbf{x} - \mathbf{r}_k|$  is the distance between the observation point  $\mathbf{x}$  and source points  $\mathbf{r}_k$ ,  $\varepsilon$  represents the surface area where the force is distributed,  $\varepsilon = 0.25ds \simeq 0.25\Delta s$ , and  $\Delta s = 2r$ .  $\mathbf{G}(\mathbf{x})$  is the regularized Green's function.

### 3.6.5 Bending Moment of the Flagellum

The coordinates of the flagellar centerline are acquired from the videos of sperm cells. For each frame in the videos, twenty equal points with the coordinates of  $(x, y)$  along the flagellum are marked and tracked via a custom-written MATLAB routine (The MathWorks, Inc., Natick, MA, USA). The bending moment  $M_{\text{ben}}$  along the flagellum can be determined through the following expression [228]:

$$\frac{\partial^2 M_{\text{ben}}(x, t)}{\partial x^2} = \xi_{\perp} \frac{\partial y(x, t)}{\partial t} + E \frac{\partial^4 y(x, t)}{\partial x^4}. \quad (3.20)$$

The bending moment can be utilized to study the internal activity of the sperm flagellum.

### 3.6.6 Statistical Analysis

The time-averaged velocity  $\langle u \rangle$ , and the distributed bending moment,  $M_{\text{ben}}$ , of all groups are processed in the normalization method. Unless otherwise

indicated, all the presented data are displayed as mean $\pm$ s.d. The sample sizes ( $n$ ) are provided in the figure legends. To assess the differences in the flagellar propulsion between free sperm cells and collinear bundles, the two-sided Student's  $t$ -test is conducted. The difference is regarded to be statistically significant if  $p < 0.05$ . A custom-made MATLAB routine is used to perform statistical analysis.

## 3.7 Supplementary Video

### **Video 3-S1. Flagellar propulsion of collinear bundles.**

This video shows the flagellar propulsion of collinear bundles in low-viscosity SP-TALP and high-viscosity dextran solutions. During the propulsion, one sperm cell propels another within the bundle by producing distinct wave patterns.



# 4

## Magnetic Control of Soft Microrobots Near Step-Out Frequency: Characterization and Analysis

4

*Note: Following chapter is adapted from the article “Magnetic Control of Soft Microrobots Near Step-Out Frequency: Characterization and Analysis” by Z. Wang, W. Li, A. Klingner, Y. Pei, S. Misra, and I. S. M. Khalil, published in “Computational and Structural Biotechnology Journal”, volume 25, pages 165-176, December 2024.*

### Abstract

Magnetically actuated soft microrobots hold promise for biomedical applications that necessitate precise control and adaptability in complex environments. These microrobots can be accurately steered below their step-out frequencies where they exhibit synchronized motion with external magnetic fields. However, the step-out frequencies of soft microrobots have not been investigated yet, as opposed to their rigid counterparts. In this work, we develop an analytic model from the magneto-elastohydrodynamics to establish the relationship between the step-out frequency of soft sperm-like microrobots and their magnetic properties, geometry, wave patterns, and the viscosity of the surrounding medium. We fabricate soft sperm-like microrobots using electrospinning and assess their swimming abilities in mediums with varying viscosities under an oscillating magnetic field. We observe slight variations in wave patterns of the sperm-like microrobots

## 4. Magnetic Control of Soft Microrobots Near Step-Out Frequency: Characterization and Analysis

---

as the actuation frequency changes. Our theoretical model, which analyzes these wave patterns observed without exceeding the step-out threshold, quantitatively agrees with the experimentally measured step-out frequencies. By accurately predicting the step-out frequency, the proposed model lays a foundation for achieving precise control over individual soft microrobots and enabling selective control within a swarm when executing biomedical tasks.

### 4.1 Introduction

Microrobots actuated by external fields are gaining attention owing to their ability to navigate hard-to-reach positions within the human body. This capability can potentially enhance the precision and dexterity of current surgical procedures [5]. Among a variety of actuation manners, such as light [229], magnetic [21], electric [230], acoustic [231], and thermal [232], magnetic actuation has been extensively studied due to its nontoxic and real-time properties. In recent decades, proof-of-concept studies on magnetic microrobots have been carried out to demonstrate their potential for various biomedical applications, such as multimodal locomotion in nonideal environments [233], enhanced targeted drug delivery [234], and macrophage polarization [235]. Apart from energy sources, the body configurations of microrobots must break time-reversibility to enable movement at low-Reynolds-number flows. Spermatozoa, which achieve propulsion by undulating their soft and flexible flagellum, have inspired the design of mobile microrobots. Magnetically actuated sperm-like microrobots have emerged as promising candidates for executing biomedical tasks within confined and intricate spaces of the body's natural pathways [236].

Magnetically actuated sperm-like microrobots encompass sperm-inspired, sperm-driven, and sperm-templated microrobots. Various microfabrication methods have been proposed to develop these microrobots. Sperm-inspired microrobots are designed using biomimetic principles to imitate the flagellar beating of spermatozoa. For instance, Dreyfus *et al.* [42] have attached magnetic particles to DNA through the biotin-streptavidin interaction, forming a flexible magnetic filament. When subjected to an oscillating magnetic field, this filament exhibits whip-like deformations and generates propulsive thrust. Building on these principles, the bulk fabrication of sperm-inspired microrobots has been achieved using photolithography

and electrospinning [43], [46]. Sperm-driven microrobots can move forward by utilizing the innate motility of spermatozoa. Magdanz *et al.* [73] have fabricated the spermbot, which consists of a sperm cell entrapped in a magnetic microtube. The incorporation of magnetic microtubes allows for the control of sperm cells' swimming directions under a magnetic field. Furthermore, by fabricating the microtube with a thermo-responsive polymer, the entrapped sperm cells can be released by elevating the temperature [104]. Such a gentle release method keeps the sperm cells intact, which is crucial for assisted fertilization [30], [237]. Sperm-template microrobots refer to the biohybrid microrobots constructed using sperm cells as templates. IRONSperm comprises a sperm cell and rice grain-shaped magnetic nanoparticles via electrostatic self-assembly [110]. In contrast to the spermbot, sperm cells are immotile after binding to magnetic nanoparticles. The IRONSperm does not rely on the ATP consumed by spermatozoa to undulate its flagellum. Instead, its power is provided by external magnetic fields, thus ensuring its long-term locomotion. Such persistent locomotion is the prerequisite for magnetic microrobots intended for minimally invasive medicine, while precise wireless control is equally essential [238]. Wireless control of magnetic microrobots is typically achieved below their step-out frequencies, where they exhibit synchronized motion with the field. This synchronization is crucial for biomedical applications as it enables precise navigation and predictable behavior of the microrobot, minimizing the risk of uncontrolled movement that could cause damage to tissues or cells.

The step-out frequencies of magnetic microrobots are influenced by various factors, such as their magnetization, geometries, field strength, and viscosity of the surrounding medium. Discrepancies in the step-out frequencies lead to distinct responses of magnetic microrobots to the same applied magnetic field [239]. This characteristic can be leveraged as a general method for selective control in multi-microrobot systems. Mahoney *et al.* [240] have theoretically studied the swimming performance of rotating magnetic microrobots constructed with either a permanent magnet or a soft ferromagnet. By operating both microrobots above their step-out frequencies, the researchers have controlled the velocity ratio of the two geometrically identical but magnetically distinct rolling microrobots, thus steering them to move along different paths. In addition to magnetization, the surface wettability of microrobots impacts their step-out frequency, as it affects the viscous drag force exerted by the surrounding

## 4. Magnetic Control of Soft Microrobots Near Step-Out Frequency: Characterization and Analysis

---

medium. Wang *et al.* have fabricated a swarm of artificial bacterial flagella (ABFs) that are geometrically and magnetically identical but differ in the step-out frequencies due to variations in surface wettability. Selective control of this ABFs swarm can be accomplished by operating at a frequency below the step-out frequency of the selected group yet above that of the other [241]. Compared with the rigid microrobots above, soft microrobots, capable of substantial and compliant deformation, are more adaptive to changing physical and chemical conditions within the body [242]. However, their flexible characteristic introduces complex interactions with external environments, including the applied magnetic field and the surrounding medium. These combined interactions have not been fully explored, limiting our understanding of the swimming behavior and control mechanisms of soft microrobots.

4

In this work, we propose a theoretical model to study the step-out frequency of magnetically actuated soft microrobots. The step-out frequency is reached when the equilibrium between interactions with the magnetic field and the fluid medium is established. To validate our model, we fabricate soft sperm-like microrobots using electrospinning and sonication cutting (Figure 4.1) and investigate their step-out frequencies under an oscillating magnetic field. The effect of the medium's viscosity on the step-out frequencies of these microrobots is assessed by performing swimming tests in deionized (DI) water and methyl cellulose (MC) solutions. We characterize their geometries and magnetization using a scanning electron microscope (SEM) and a vibrating sample magnetometer (VSM), respectively, to elucidate the effects of magnetism and fluid dynamics. Energy-dispersive X-ray spectroscopy (EDS) elemental mapping results indicate that magnetic nanoparticles are primarily distributed in the head of the sperm-like microrobot. Based on this experimental observation, we exclusively consider the magnetic torque on the head and develop a magneto-elastohydrodynamic model. This model elaborates the relationship between the step-out frequencies of the sperm-like microrobots and their magnetization, geometries, wave patterns, and the viscosity of the medium. Our methodology combines an established model for calculating the magnetic torque on the microrobot with an elastohydrodynamic model extensively used in studies of natural sperm cells. This integration allows us to investigate the interplay between magnetism, structural flexibility, and fluid dynamics, thereby advancing our understanding of the

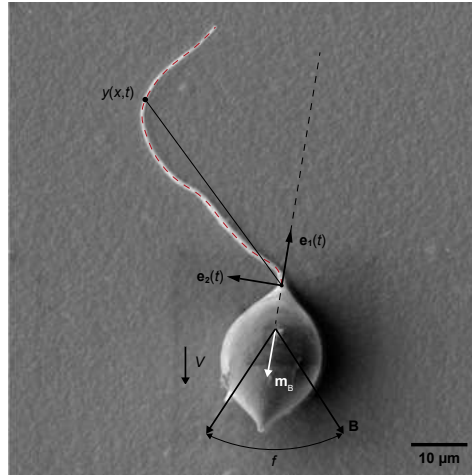


Figure 4.1: When subjected to an oscillating magnetic field denoted as  $\mathbf{B}$  with an actuation frequency of  $f$ , the head of the microrobot becomes magnetized toward  $\mathbf{m}_B$  and aligns with the field. The oscillation of the head drives the tail's deformation,  $y(x, t)$ , in the material frame of reference  $(\mathbf{e}_1(t), \mathbf{e}_2(t))$ . This reference frame is established at the proximal end of the tail such that the orthonormal vector  $\mathbf{e}_1(t)$  is along the major axis of the head. Traveling waves propagate along the tail, leading to a propulsive thrust that propels the head to swim at a velocity of  $V$ .

swimming performance of sperm-like microrobots.

## 4.2 Results and Discussion

### 4.2.1 Fabrication and Magnetic Actuation of Soft Sperm-Like Microrobots

Sperm cells exhibit planar traveling waves to achieve propulsion using their flexible and slender tail [20]. To create sperm-like microrobots, it is essential to replicate the flexibility and slenderness of sperm tails. Several strategies have been explored to achieve this, such as the use of flagella from microorganisms [243] and the fabrication of soft nanowires [49], [244] or fibers [46]. Specifically, fibers can be fabricated through various methods, including phase separation [245], microfluidic techniques [246], drawing [247], and self-assembly [248]. However, these methods are time-consuming and have

## 4. Magnetic Control of Soft Microrobots Near Step-Out Frequency: Characterization and Analysis

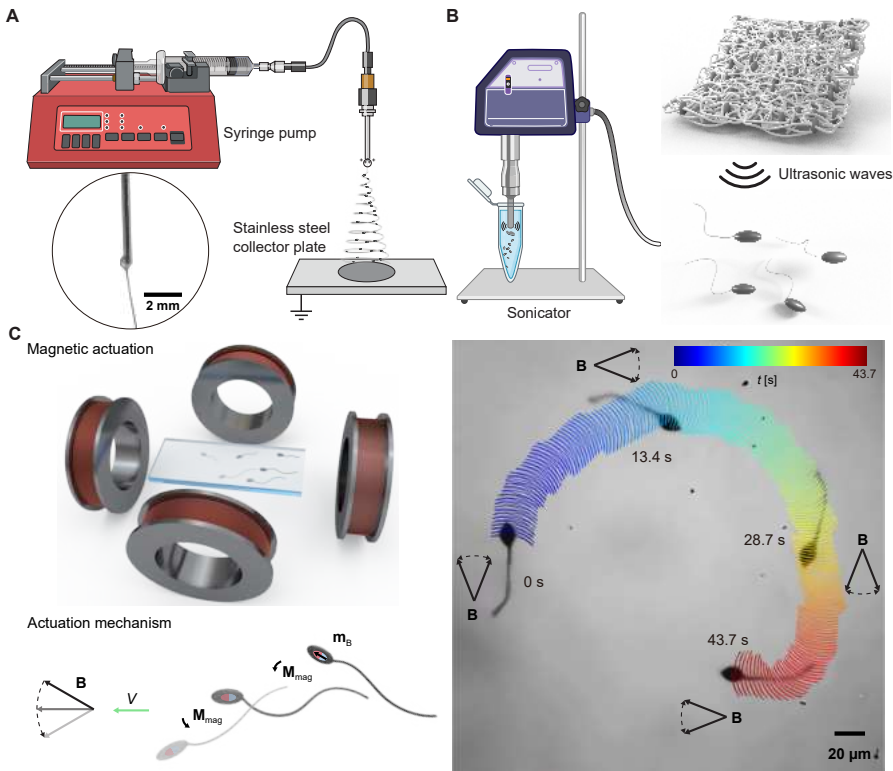


Figure 4.2: The fabrication process and magnetic actuation of sperm-like microrobots. (A) Schematics illustrate the fabrication of beaded fibers using electrospinning. The ejection of fibers from the Taylor cone is depicted in the circular inset. (B) Schematics showcase the ultrasonic breaking of beaded fibers into individual sperm-like microrobots. (C) Upon exposure to an oscillating magnetic field,  $\mathbf{B}$ , the head of the sperm-like microrobot is magnetized to  $\mathbf{m}_B$  and experiences a magnetic torque,  $\mathbf{M}_{\text{mag}}$ . The continuous oscillation of the head, driven by this torque, enables the tail to generate traveling waves to achieve movement. The microscopy image captures the movement and directional change of a sperm-like microrobot in response to the oscillating field, while the colorful curve represents its time-dependent trajectory (blue for earlier times, red for later times).

constraints on fiber length and material selection. Electrospinning offers several advantages over other methods, such as cost-effectiveness, mass production, and suitability for a wide range of polymers [249].

The soft sperm-like microrobots were fabricated using a customized

electrospinning machine and a sonicator, as described in Materials and Methods. Figure 4.2(A) depicts the electrospinning process used to produce beaded fibers, while Figure 4.2(B) illustrates how these fibers are broken up to yield sperm-like microrobots. After sonication cutting, the resulting structures include individual beads, individual fibers, strings of beads, and the desired sperm-like microrobot. Figure 4.S1 presents the rates of output for all structures, with sperm-like microrobots achieving a yield of 44.7%. These microrobots possess magnetization due to the  $\text{Fe}_3\text{O}_4$  nanoparticles, allowing them to respond to external magnetic fields. The elastic polystyrene fibers ensure tail deformation and facilitate the generation of planar traveling waves. Figure 4.2(C) clarifies the mechanism of magnetic actuation for the sperm-like microrobots. These microrobots achieve planar flagella propulsion when subjected to an in-plane oscillating magnetic field, in contrast to the helical flagellar propulsion observed under an out-of-plane precession magnetic field [49]. The locomotion capability of this torque-driven microrobot is influenced by its magnetic property. The as-prepared sperm-like microrobots undergo subsequent characterization to assess their geometry, chemical composition, and magnetization.

### 4.2.2 Geometric, Chemical, and Magnetization Characterization

The detailed beaded fibers were observed through SEM characterization. The SEM image presented in Figure 4.3(A) shows the presence of beads that can function as the head of sperm-like microrobots. The emergence of these beads is attributed to the polymer solution's low viscosity and the limited density of surface charges on the droplet [98]. With the inclusion of magnetic nanoparticles, these beaded fibers can generate a magnetic moment when exposed to an external magnetic field. This field further induces a magnetic torque that drives the soft tail to undergo undulations, leading to the planar flagellar propulsion [15]. Figure 4.3(B) illustrates the induced magnetic moment of the beaded fibers under an external field ranging from -1000 mT to 1000 mT. The magnetization response of the beaded fibers varies with the applied field strength and serves as the basis for calculating the maximum magnetic torques acting on the microrobots.

Upon sonication cutting, the beaded fibers were fragmented to produce sperm-like microrobots. The microrobot's geometrical and chemical prop-

## 4. Magnetic Control of Soft Microrobots Near Step-Out Frequency: Characterization and Analysis

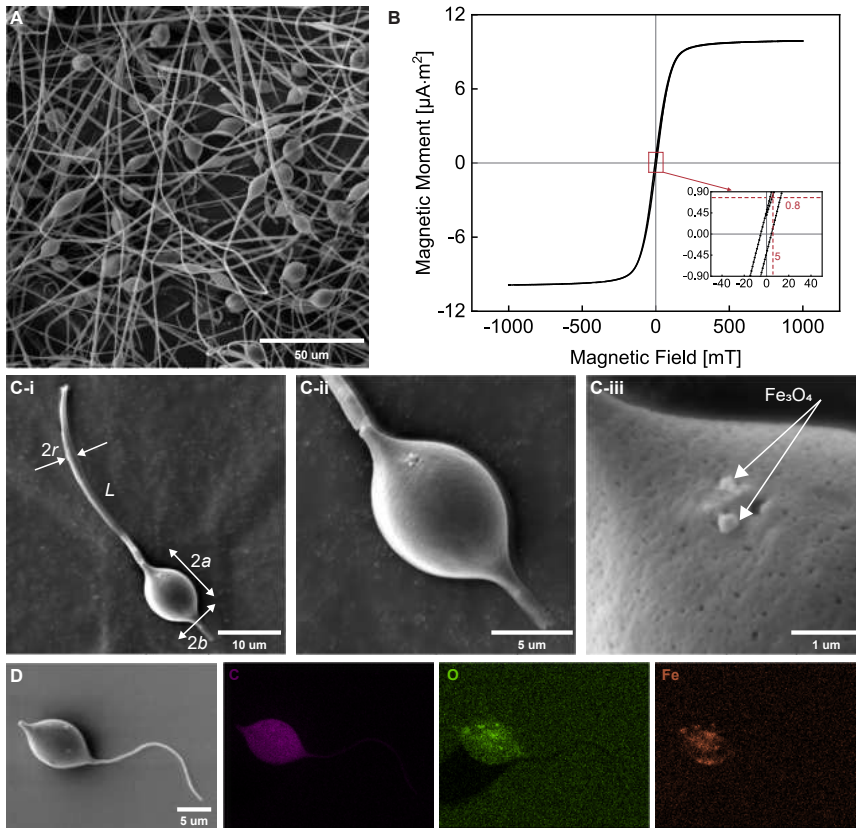


Figure 4.3: The geometric, chemical, and magnetization characterization of beaded fibers and sperm-like microrobots. (A) SEM image of the beaded fibers. (B) Magnetic hysteresis loop of the beaded fibers. The inset shows the generated magnetic moment of the fibers under the magnetic field ranging from  $-50$  mT to  $50$  mT. For instance, a field strength of  $5$  mT is applied, inducing a magnetic moment of  $0.8 \mu\text{A} \cdot \text{m}^2$  on the fibers, as indicated by the red dashed lines. (C) SEM images are taken of the sperm-like microrobot, including (i) the full microrobot and (ii) (iii) a zoom-in view of its head. The geometrical parameters of the sperm-like microrobot, including the radius of the tail,  $r$ , the tail length,  $L$ , the major radius,  $a$ , and the minor radius,  $b$ , of the ellipsoidal head, are displayed in (i). (D) Energy-dispersive X-ray spectroscopy (EDS) elemental mapping images of C, O, and Fe in the sperm-like microrobot are shown.

erties were characterized using SEM and EDS elemental mapping, respec-

tively. Figure 4.3(C)-i presents the SEM image of a sperm-like microrobot, which consists of a slender tail and an ellipsoidal head. Further examination of the zoomed-in SEM images in Figure 4.3(C)-ii and 4.3(C)-iii reveals that some magnetic nanoparticles are located on the surface of the microrobot's head. EDS elemental mapping was performed to assess the distribution of  $\text{Fe}_3\text{O}_4$  within the entire structure of the microrobot. The results show that C, O, and Fe are mainly distributed in the head owing to the larger volume relative to the tail (Figure 4.3(D)). The mapping image of Fe also indicates that  $\text{Fe}_3\text{O}_4$  nanoparticles reside inside the head, rather than merely on its surface. Considering the distribution of  $\text{Fe}_3\text{O}_4$  nanoparticles within the sperm-like microrobot, the magnetic torque exerted on the tail is relatively minor compared to that exerted on its head.

### 4.2.3 Nondimensional Analysis

The EDS elemental mapping indicates a trivial amount of magnetic nanoparticles on the tail. Consequently, the magnetic torque exerted on the head is considered the sole energy source for actuating the microrobot. In response to an oscillating magnetic field, denoted as  $\mathbf{H}$ , the magnetic head of the sperm-like microrobot becomes magnetized, exhibiting a magnetization per unit volume of  $\mathbf{m}_H$ . This results in a magnetic torque,  $\mathbf{M}_{\text{mag}}$ , which is given by

$$\mathbf{M}_{\text{mag}} = \mu_0 v \mathbf{m}_H \times \mathbf{H}, \quad (4.1)$$

where  $\mu_0$  is the permeability of free space,  $v$  is the volume of the sperm-like microrobot's head.

As the microrobot moves through a medium, it encounters viscous drag torques,  $\mathbf{M}_{\text{head}}$  and  $\mathbf{M}_{\text{tail}}$ , on its head and tail, respectively. These viscous drag torques are defined by the analytical function that accounts for the geometry of the microrobot. The sperm-like microrobot features an ellipsoidal head attached to a soft tail, as observed in Figure 4.3(C)-i. The geometrical parameters include the radius of the tail,  $r$ , the tail length,  $L$ , the major radius,  $a$ , and the minor radius,  $b$ , of the ellipsoidal head. The bending stiffness,  $E$ , of the tail is calculated by multiplying the electrospun fiber's Young's modulus by the area moment of inertia of the fiber's cross-section. Chwang and Wu [250] derived the viscous drag torque on a prolate ellipsoid, which is utilized to express  $\mathbf{M}_{\text{head}}$  as follows:

$$|\mathbf{M}_{\text{head}}| = 8ab^2\pi C_1\eta\omega. \quad (4.2)$$

#### 4. Magnetic Control of Soft Microrobots Near Step-Out Frequency: Characterization and Analysis

---

The torque coefficient,  $C_1$ , is associated with the ellipsoid's eccentricity, denoted as  $\epsilon = \sqrt{1 - (b/a)^2}$ , and  $\eta$  is the viscosity of the surrounding medium. The interaction between medium and tail is described by resistive force theory [147]. The local viscous drag force on the tail depends on its local velocity relative to the medium. Based on the assumption of small amplitude, the small segment on the tail moves with the local velocity normal to the major axis of the head [251], [252]. The viscous drag torque on the tail can be determined via the following equation:

$$|\mathbf{M}_{\text{tail}}| = \int_0^L \xi_{\perp} x dy/dt dx, \quad (4.3)$$

where  $\xi_{\perp}$  is the normal drag coefficient of the tail. A sine wave of constant amplitude,  $y(x, t) = y_0 e^{i2\pi(ft - x/\lambda)}$ , represents the wave patterns in response to the oscillating magnetic field with the frequency of  $f$ . The wave variables  $y_0$  and  $\lambda$  are the averaged bending amplitude and wavelength of the wave patterns, respectively.

The bending wave along the tail, which enables the propulsion of the sperm-like microrobot, is achieved through the magneto-elastohydrodynamic coupling between the deformable tail, the external field, and the surrounding medium. Without loss of generality, we conduct a nondimensional analysis of this magneto-elastohydrodynamics. The nondimensional viscous drag torques,  $\mathcal{M}_{\text{head}}$  and  $\mathcal{M}_{\text{tail}}$ , on the head and the tail are given by,

$$\mathcal{M}_{\text{head}} = \mathcal{R}_{\text{head}} \text{Sp}^4, \quad \mathcal{M}_{\text{tail}} = \mathcal{R}_{\text{tail}} \text{Sp}^4, \quad (4.4)$$

where  $\mathcal{R}_{\text{head}}$  and  $\mathcal{R}_{\text{tail}}$  are nondimensional drag coefficients determined by the geometry of the head and the wave patterns, respectively. The nondimensional drag coefficient of the head is given by the analytic function  $\mathcal{R}_{\text{head}} = 8ab^2\pi C_1\eta/L^3\xi_{\perp}$ , while that of the tail depends on the wave variables  $y_0$  and  $\lambda$ , expressed as  $\mathcal{R}_{\text{tail}} = y_0\lambda/2\pi L^2$ . In addition, the nondimensional magnetic torque,  $\mathcal{M}_{\text{mag}}$ , is expressed by:

$$\mathcal{M}_{\text{mag}} = \mathcal{M} \left| \hat{\mathbf{m}}_{\text{H}} \times \hat{\mathbf{H}} \right|, \quad (4.5)$$

where  $\mathcal{M} = \mu_0 v |\mathbf{m}_{\text{H}}| |\mathbf{H}| L/E$  is the magnetic number, which denotes the ratio between the magnetic and elastic torques, and the 'hat' symbol represents the normalized form of the variable. The sperm number Sp, defined

as the equation  $\text{Sp} = L(\xi_{\perp}\omega/E)^{1/4}$ , characterizes the relative importance of elastic force to viscous drag force, representing the floppiness of the tail [?]. It can be determined by constructing a nondimensional torque balance equation between Equations 4.4 and 4.5:

$$\text{Sp} = \sqrt[4]{\frac{\mathcal{M}\hat{\mathbf{m}}_{\text{H}} \times \hat{\mathbf{H}}}{\mathcal{R}_{\text{head}} + \mathcal{R}_{\text{tail}}}}, \quad (4.6)$$

When the angular frequency, represented by  $\omega$ , of the oscillating magnetic field matches the step-out angular frequency, denoted as  $\omega_{\text{so}}$ , the cumulative viscous drag torque equals the maximum magnetic torque. The step-out frequency,  $f_{\text{so}} = \omega_{\text{so}}/2\pi$ , can be obtained by studying the maximum magnetic torque and the viscous drag torque. The maximum nondimensional magnetic torque,  $\text{Max}(\mathcal{M}_{\text{mag}})$ , on the soft-magnetic ellipsoidal body, is as follows [253]:

$$\text{Max}(\mathcal{M}_{\text{mag}}) = \frac{\mu_0 v |n_{\text{rad}} - n_{\text{axi}}| |\mathbf{m}_{\text{H}}|^2 L}{2E} \quad (4.7)$$

where the demagnetization factors,  $n_{\text{rad}}$  and  $n_{\text{axi}}$ , are along all radial directions and the major axis of the ellipsoidal body, respectively. Substituting Equation 4.7 to Equations 4.6, the sperm number  $\text{Sp}_{\text{so}}$  at the step-out frequency is obtained as:

$$\text{Sp}_{\text{so}} = \sqrt[4]{\frac{\mu_0 v |n_{\text{rad}} - n_{\text{axi}}| |\mathbf{m}_{\text{H}}|^2 L}{2E(\mathcal{R}_{\text{head}} + \mathcal{R}_{\text{tail}})}}. \quad (4.8)$$

Equation 4.8 reveals that the sperm number at the step-out frequency depends on the magnetization, the geometry of the sperm-like microrobots, the viscosity of the medium, and the wave patterns of the tail.

#### 4.2.4 Derivation of the Equation for Step-Out Frequency and Velocity at Step-Out Frequency

Combining Equation 4.8 with the definition of the sperm number, we can derive the step-out angular frequency,  $\omega_{\text{so}}$ , as follows:

$$\omega_{\text{so}} = \frac{\mu_0 v |n_{\text{rad}} - n_{\text{axi}}| |\mathbf{m}_{\text{H}}|^2}{2(8ab^2\pi C_1\eta + y_0\lambda L\xi_{\perp}/2\pi)}, \quad (4.9)$$

## 4. Magnetic Control of Soft Microrobots Near Step-Out Frequency: Characterization and Analysis

---

where wave variables  $y_0$  and  $\lambda$  are extracted according to experimentally observed wave patterns. The sperm-like microrobots experience zero magnetic force in the gradient-free field. Their propulsive thrust comes from the transmission of transverse waves along the tail [254], which needs to counteract the viscous drag force on the head. Consequently, we can establish the following force-balance equation to determine the swimming velocities, denoted as  $V$ , of sperm-like microrobots,

$$\int_0^L \frac{(\xi_{\perp} - \xi_{\parallel})(dy/dt) \frac{dy}{dx} - V \left( \xi_{\parallel} + \xi_{\perp} \left( \frac{dy}{dx} \right)^2 \right)}{1 + \left( \frac{dy}{dx} \right)^2} dx = 6\pi\eta a C_2 V, \quad (4.10)$$

where  $\xi_{\parallel}$  is the tangent drag coefficient of the tail, and  $C_2$  is the nondimensional drag coefficient that depends on the dimensions of the sperm-like microrobot's ellipsoidal head. Likewise, the swimming velocity is influenced by the wave patterns of the microrobot. Variables used in the calculations of the step-out frequency and swimming velocity are indicated in Table 4.S1.

### 4.2.5 Wave Pattern Analysis at the Step-Out Frequency

To validate our theoretical model, we performed swimming tests of the sperm-like microrobots in DI water, 0.1% w/v, 0.2% w/v MC solutions to investigate their step-out frequencies. The viscosities of these mediums were measured via a rheometer. Figure 4.4(A) and 4.4(B) shows the measured shear stress at different shear rates for the two MC concentrations (see Material and Methods). The results indicate that both MC solutions exhibit constant viscosities despite changes in shear rate. In these two MC solutions, the sperm-like microrobots exhibit distinct swimming velocities. Their propulsion and corresponding trajectories on the head are shown in Figure 4.4(C) and 4.4(D). We exclusively consider the head's displacement along the oscillating axis of the field for evaluating the swimming performance of the sperm microrobot. In the 0.1% MC solution, the sperm-like microrobot moves around 96  $\mu\text{m}$  in a period of 47.8 s, compared to 98.6 s in the 0.2% MC solution. The decrease in the velocity can be attributed to the increasing viscous drag force within the more viscous medium. Moreover, the viscosity is likely to impact the wave patterns.

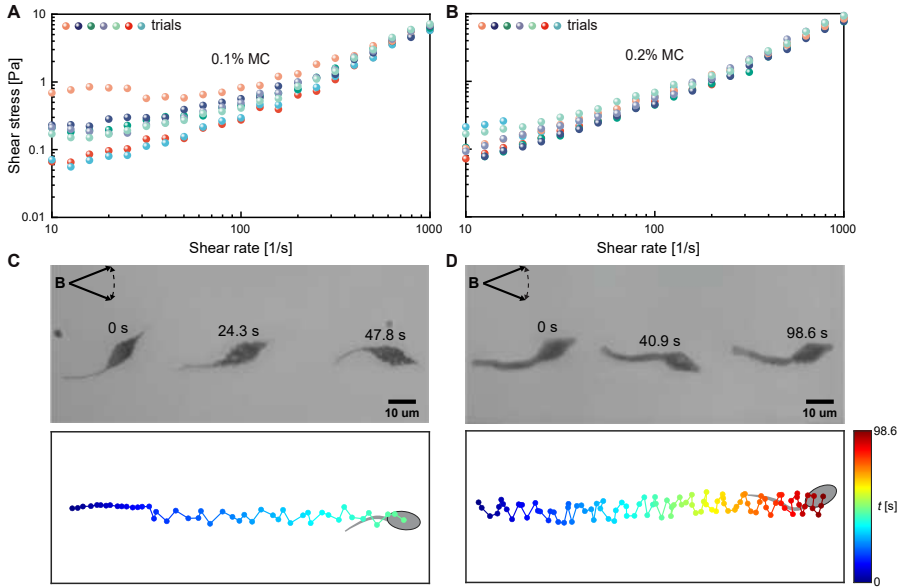


Figure 4.4: The rheological behavior of methyl cellulose (MC) solutions at varying w/v% concentrations and the propulsion of sperm-like microrobots within these mediums. Viscosity measurement of (A) 0.1% and (B) 0.2% MC solutions for seven trials. Each trial is differentiated by the symbols with different colors. The average viscosities for 0.1% and 0.2% MC solutions across seven trials are  $4.4 \text{ mPa} \cdot \text{s}$  and  $5.7 \text{ mPa} \cdot \text{s}$ , respectively. Sequential frames capture the microrobots' propulsion over the same distance in (C) 0.1% and (D) 0.2% MC solutions and their corresponding time-dependent trajectories on the head are depicted (blue for earlier times, red for later times).

The analysis of these wave patterns is undertaken using nonlinear curve fitting, a technique employed to study wave patterns of living spermatozoa [215], [255]. The coordinates of the tail's deformation of sperm-like microrobots were obtained from the captured videos (see Materials and Methods). Figure 4.5(A) shows the propulsion of the sperm-like microrobots in DI water, 0.1% MC, and 0.2% MC solutions, with the red dashed line profiling the centerline of the tail. The tail deformation over one complete beat cycle is illustrated in Figure 4.5(B). In all cases, the bending wave initiates from the proximal end and propagates toward the distal end. As the viscosity increases, the transverse displacement of the bending wave decreases, which can be attributed to the increased viscous drag

## 4. Magnetic Control of Soft Microrobots Near Step-Out Frequency: Characterization and Analysis

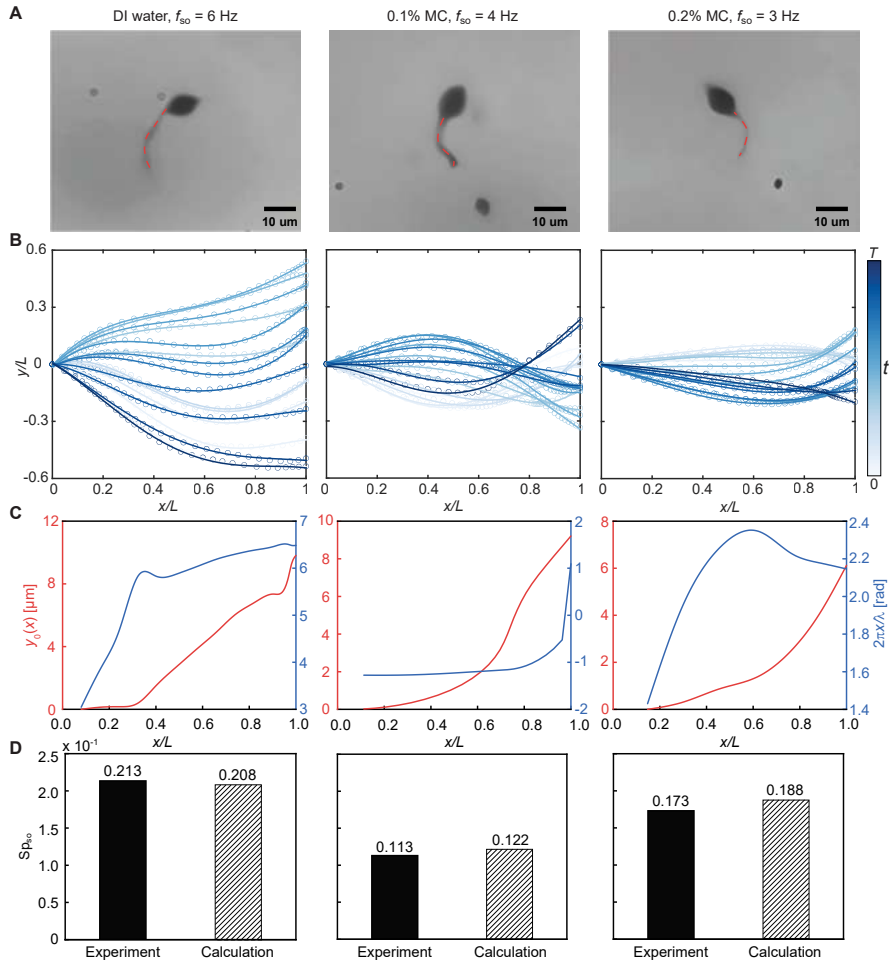


Figure 4.5: Observation and analysis of sperm-like microrobots' wave patterns at their step-out frequencies in various media. (A) Tail's deformation of sperm-like microrobots in deionized (DI) water, 0.1%, and 0.2% MC solutions at their step-out frequencies. The red dashed line describes the centerline of the bending tail. (B) The transverse displacement  $y(x, t)$  is determined from the tail deformation throughout one entire beat cycle, with the circles as marked points along the tails connected by polynomial curves (darker curves for later times).  $T$  is the time for one beat cycle. (C) Time-averaged bending amplitude,  $y_0(x)$ , and the phase angle,  $2\pi x/\lambda$ , are extracted from the observed wave patterns in DI water, 0.1%, and 0.2% MC solutions. (D) Experimental and calculated sperm number at the step-out frequency. The calculated sperm number at the step-out frequency is determined by substituting the extracted wave variables into Equation 4.8.

force. The wave variables  $y_0$  and  $\lambda$  are obtained by analyzing the extracted curves using the nonlinear curve fitting method, as shown in Figure 4.5(C). The time-averaged bending amplitude,  $y_0(x)$ , exhibits an increasing trend that corresponds to the increasing amplitude along the tail (refer to Figure 4.5B). Similarly, the phase angle,  $2\pi x/\lambda$ , shows a rise along the tail, which reveals that the planar waves propagate from head to tail and, in turn, lead to the propulsion from tail to head. Based on the extracted wave variables, we can calculate the sperm number at the step-out frequency using Equation 4.8. Figure 4.5(D) shows the quantitative agreement between the experimental and the calculated sperm number at the step-out frequency, confirming the validity of our proposed model.

#### 4.2.6 Analysis of Wave Patterns Observed without Exceeding Step-Out Frequency

Wave patterns of living spermatozoa undergo noticeable variations in response to changes in the beat frequency. These variations might result from an alteration in the viscosity of the surrounding medium [256], [257], the external force [180], or chemoattractant molecules [258], [259]. Unlike spermatozoa, which deform their flagella through the coordinated cooperation of dynein motors, sperm-like microrobots passively undulate their tails via magnetic torque. Further investigation is needed to understand the effect of actuation frequency on the wave patterns exhibited by sperm-like microrobots.

The wave patterns of the sperm-like microrobot in DI water, ranging from 1 Hz to 6 Hz, are illustrated in Figure 4.6(A). The frequency of 6 Hz corresponds to the step-out frequency in the trial. The wave variables for each frequency, extracted in Figure 4.6(B), align with the observed slight change in the wave patterns as the frequency increases. These slightly changed wave patterns suggest that the undulations of the sperm microrobot remain synchronized with the external field across this range of actuation frequencies. The calculated sperm number closely matches the experimentally measured value at the step-out frequency (Figure 4.6(C)). We also examined the wave patterns of the sperm-like microrobots below the step-out frequency in 0.1% and 0.2% MC solutions, as shown in Figures 4.7(A) and 4.8(A). The wave variables for these mediums are extracted and plotted against actuation frequencies (Figures 4.7(B) and 4.8(B)). Minor variations

## 4. Magnetic Control of Soft Microrobots Near Step-Out Frequency: Characterization and Analysis

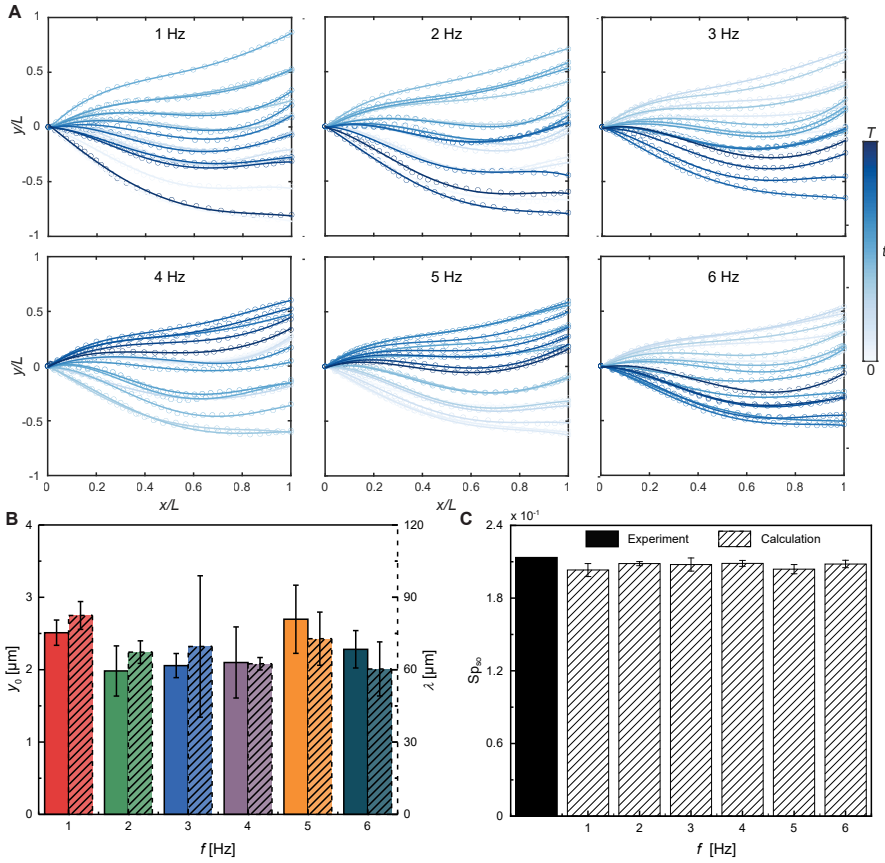


Figure 4.6: Analysis of the sperm-like microrobot's wave patterns in DI water. (A) The wave patterns of the sperm-like microrobots are displayed at actuation frequencies ranging from 1 Hz to 6 Hz (6 Hz is the step-out frequency in this trial. Darker curves for later times). (B) Average bending amplitude  $y_0$  and wavelength  $\lambda$  versus different actuation frequencies. (C) The solid black bar is the experimental sperm number,  $Sp_{so}$ , at the step-out frequency. The bars filled with diagonal lines represent the calculated  $Sp_{so}$ , obtained by substituting the wave variables extracted from 1 Hz to 6 Hz into Equation 4.8.

in the wave variables across frequencies introduce slight deviations between the calculated and experimental sperm numbers at the step-out frequency (Figures 4.7(C) and 4.8(C)). The precise prediction of the sperm number at the step-out frequency is attributed to the near-constant nondimensional

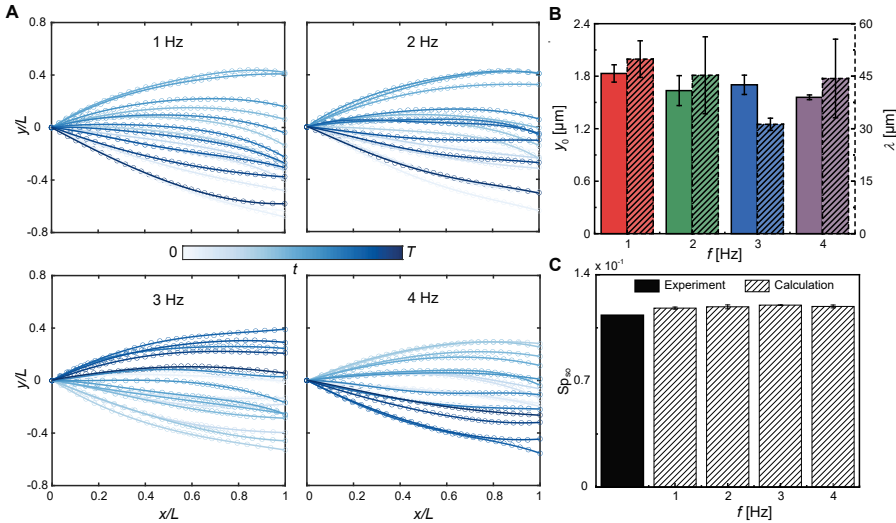


Figure 4.7: Analysis of the sperm-like microrobot's wave patterns in 0.1% MC solution. (A) The wave patterns of the sperm-like microrobots are displayed at actuation frequencies ranging from 1 Hz to 4 Hz (4 Hz is the step-out frequency in this trial. Darker curves for later times). (B) Average bending amplitude  $y_0$  and wavelength  $\lambda$  versus different actuation frequencies. (C) The solid black bar is the experimental sperm number,  $Sp_{so}$ , at the step-out frequency. The bars filled with diagonal lines represent the calculated  $Sp_{so}$ , obtained by substituting the wave variables extracted from 1 Hz to 4 Hz into Equation 4.8.

drag coefficients across actuation frequencies. Our findings emphasize that step-out frequencies of the magnetically actuated soft sperm-like microbots can be theoretically calculated after analyzing their wave patterns at any frequency below the step-out threshold. This approach simplifies the current way of determining the step-out frequencies of sperm-like microbots by measuring their frequency responses across a wide range of frequencies.

Our theoretical model can accurately predict the step-out frequency of the sperm-like microrobot by analyzing the wave patterns observed at any frequency without exceeding the step-out threshold. This feature enhances the utility of our model, which is supported by theoretical and empirical evidence. Equation 4.9 indicates that the step-out frequency depends on the wave variables  $y_0$  and  $\lambda$ . During oscillating actuation, the head oscil-

## 4. Magnetic Control of Soft Microrobots Near Step-Out Frequency: Characterization and Analysis

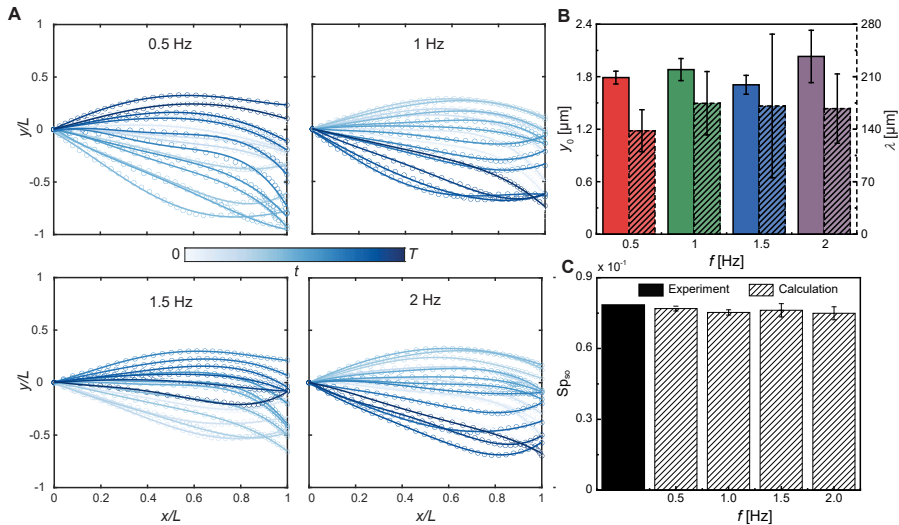


Figure 4.8: Analysis of the sperm-like microrobot's wave patterns in 0.2% MC solution. (A) The wave patterns of the sperm-like microrobots are displayed at actuation frequencies ranging from 0.5 Hz to 2 Hz (2 Hz is the step-out frequency in this trial. Darker curves for later times). (B) Average bending amplitude  $y_0$  and wavelength  $\lambda$  versus different actuation frequencies. (C) The solid black bar is the experimental sperm number,  $Sp_{so}$ , at the step-out frequency. The bars filled with diagonal lines represent the calculated  $Sp_{so}$ , obtained by substituting the wave variables extracted from 0.5 Hz to 2 Hz into Equation 4.8.

lates with the field, leading to the planar undulation of the flexible tail. The amplitude of the head's oscillation is determined solely by the amplitude of the external field, provided that the head of the microrobot can synchronously follow the external field. As long as the actuation frequency is below the step-out frequency, the head maintains a constant oscillating amplitude, resulting in only slight variations in wave patterns across different frequencies. Our experimental results, presented in Figures 6B, 7B, and 8B, demonstrate these minor variations in wave variables at frequencies below the step-out threshold. This observed behavior may also be relevant to the soft microrobots consisting of a magnetic rigid component at one end connected to a non-magnetic soft thin segment. When such a microrobot oscillates synchronously with the external field at a constant amplitude, its wave patterns exhibit slight variations across different fre-

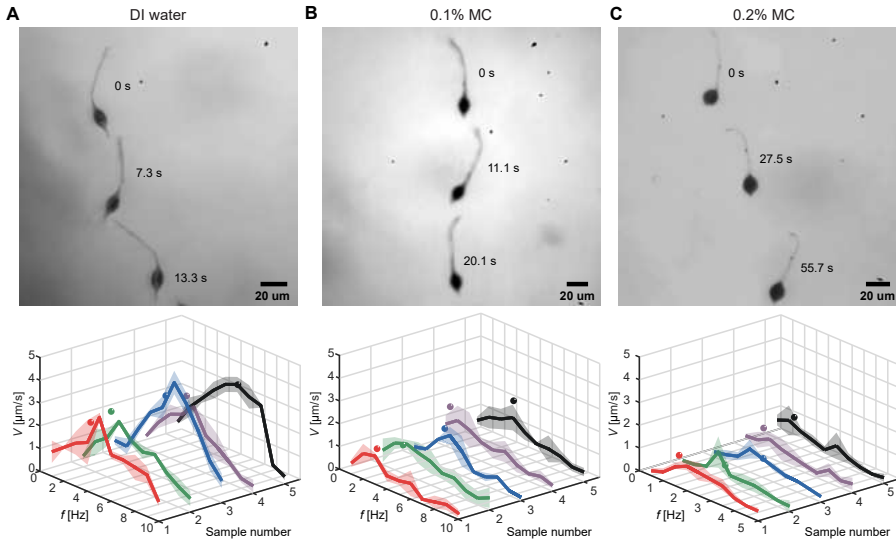


Figure 4.9: Comparison between experimental and calculated results on the swimming performance of sperm-like microrobots in (A) DI water, (B) 0.1% MC, and (C) 0.2% MC solutions. The upper images illustrate the sequence of the microrobot's movement in DI water, 0.1% MC, and 0.2% MC solutions. The lower plots show frequency response and theoretical calculation of sperm-like microrobots in these mediums. The solid lines denote the averaged velocity of five sperm-like microrobots across a range of actuation frequencies, with the error band representing the standard deviation. The sphere symbols represent the theoretical calculation on the step-out frequency and the maximum velocity derived using Equations 4.9 and 4.10.

quencies before the step-out threshold. Our findings are not limited to our specific sperm-like microrobots but are likely applicable to this broader class of soft microrobots, enhancing the relevance and utility of our theoretical model.

### 4.2.7 Model Validation and Guidance

After conducting the requisite characterizations, we obtained the variables required for Equations 4.9 and 4.10. These equations are utilized to determine the step-out frequency and the maximum velocity achieved by the sperm-like microrobot at this frequency. The sperm-like microrobots can propel themselves by generating traveling waves under an oscillating mag-

#### 4. Magnetic Control of Soft Microrobots Near Step-Out Frequency: Characterization and Analysis

---

netic field (see upper images in Figure 4.9 and Movie 4-S1). The swimming velocity of each sperm-like microrobot is measured within a frequency range of 1-10 Hz in DI water, 0.1% MC solution, and a range of 0.5-5 Hz in 0.2% MC solution, as depicted in the lower plots of Figure 4.9. Note that the maximum velocity of the sperm-like microrobot with a tail length of 15  $\mu\text{m}$  can reach 4.4  $\mu\text{m/s}$ , approximately 0.3 body lengths per second. The velocities of sperm-like microrobots initially increase with the frequency until the step-out frequency, where they exhibit the maximum velocities. The step-out frequencies of sperm-like microrobots in DI water are in the range of 4-6 Hz (Figure 4.9(A)). The observed discrepancy is attributed to the varying amount of the magnetic nanoparticles in each sperm-like microrobot. In 0.1% MC solution, the step-out frequencies decrease to the range of 3-5 Hz (Figure 4.9(B)), while the step-out frequencies reduce further to the range of 2-3 Hz in 0.2% MC solution (Figure 4.9(C)). The decrease in the step-out frequency with the increased viscosity of the medium corresponds with Equation 4.9. Moreover, the velocities of sperm-like microrobots decrease when they encounter larger viscous drag forces in mediums with higher viscosities. The wave variables, geometrical parameters, the viscosities of the mediums, and the magnetization obtained at the above sections are substituted into Equations 4.9 and 4.10, yielding the predicted values for the step-out frequency,  $f_{so}$ , and the swimming velocity,  $V$ , of each sperm-like microrobot. The theoretical results are in good agreement with the experimental results, substantiating the robustness and reliability of the proposed model.

Actuated under the predicted step-out frequency, magnetically actuated soft microrobots with low step-out frequencies can still exhibit precise motion and execute complicated tasks. The proposed model can help prevent situations where an excessively high actuation frequency undermines the precision of a microrobot's motion. Additionally, the step-out frequency directly impacts the maximum swimming velocity of soft microrobots, as this velocity is proportional to the step-out frequency. The calculation of the maximum velocity allows us to analyze the microrobots' swimming capability, which is crucial for tailoring the microrobots to specific tasks. For instance, fast movement enables the microrobots to promptly reach specific locations when executing targeted delivery applications. Conversely, slow and precise movements are required for handling delicate or intricate operations in micromanipulation tasks. Furthermore,

accurately predicting the maximum velocity is critical for effective navigation and trajectory planning of magnetic microrobots, especially in open-loop control systems, where position feedback is unavailable. To achieve a high step-out frequency, inducing a large magnetic moment on the microrobot is a viable approach. This magnetic moment can be enhanced through methods such as increasing the field strength, raising the volume fraction of magnetic material, and incorporating hard magnetic material during fabrication. Although augmenting the head's geometry can heighten the volume fraction of magnetic material, it also inadvertently elevates the viscous drag on the microrobot, resulting in a decrease in the step-out frequency. Therefore, careful consideration of the microrobot's geometry is essential to strike an optimal balance between magnetic moment enhancement and minimized viscous drag effects. To conclude, accurately predicting step-out frequencies and the maximum velocities is pivotal for ensuring the precision and efficiency of soft microrobots in biomedical applications.

### 4.3 Conclusion

In this paper, we have proposed an analytic model for determining the step-out frequency of magnetically actuated soft microrobots. This model enhances our understanding of the relationship between the step-out frequency and various factors, including the microrobot's geometry, magnetization, wave patterns, and the viscosity of the surrounding medium. The experimental results not only validate the accuracy of our proposed analytic model for the step-out frequency but also reveal the independence of wave patterns from actuation frequency, in contrast to natural sperm cells. This distinct behavior allows our analytic model to accurately predict the step-out frequency of the sperm-like microrobot by evaluating the observed wave patterns at any frequency below the step-out threshold. The accurate prediction of the step-out frequency using our model has important implications for the control and navigation of individual microrobots as well as swarms of microrobots. The synchronized motion of individuals is crucial for executing complex tasks and maneuvers as it enables precise navigation and predictable behavior of the microrobot. Furthermore, the model can facilitate selective control within a swarm by allowing different microrobots to be actuated at frequencies below their respective step-out frequencies. This selective control enables the targeted and coordinated movement of

#### 4. *Magnetic Control of Soft Microrobots Near Step-Out Frequency: Characterization and Analysis*

---

individual microrobots within the swarm.

While our current model offers valuable insights into the control of sperm-like microrobots, several limitations remain to be addressed in future research. These limitations include three-dimensional navigation of the sperm-like microrobots, model optimization to study the step-out frequency during this navigation, real-time tracking of the wave patterns, and the optimized magnetization profile for enhanced swimming efficiency. Considering that sperm-like microrobots with helical flagellar waves exhibit higher swimming efficiency than those with planar flagellar waves and resemble the motion of natural sperm cells, it is crucial to develop a theoretical model for determining the step-out frequency of these microrobots under a precession magnetic field. This involves the tracking of wave patterns in three dimensions. Moreover, the real-time analysis of wave patterns should be combined with the actuation strategies to determine the appropriate actuation frequency, which depends on the application scenarios, such as synchronized and efficient control of individuals and selective control in a swarm. Additionally, alternative designs, such as sperm-like microrobots with a magnetic soft tail, might exhibit higher step-out frequencies and swimming efficiencies. To explore these possibilities, the current model should be upgraded to incorporate the magnetic torque on the tail. The upgraded model would enable the formulation of an optimization problem to study the ideal magnetization profile along the tail of the microrobot, aiming for achieving optimal step-out frequency or swimming velocity. The inclusion of magnetization along the tail will cause the axis of rotation to vary from the head's centroid, impacting the viscous drag torque on the head. Generalizing the model to account for rotation about any arbitrary axis is meaningful yet challenging. The analytical form for the viscous drag torque when considering arbitrary rotation axes is complex and unknown. Numerical calculations might offer a way to determine this viscous drag torque when the ellipsoid rotates about any axis. These calculations would allow for understanding the effects of different rotation axes on the viscous drag torque and further determining the step-out frequency of the sperm-like microrobot with a magnetic tail.

## 4.4 Materials and Methods

### 4.4.1 Preparation of Polymer Solution for Electrospinning

The polymer solution was prepared by mixing dimethylformamide (DMF) (227056-1L, anhydrous, 99.8%, Sigma-Aldrich, The Netherlands) with a combination of  $\text{Fe}_3\text{O}_4$  nanoparticles (637106-25G, nanopowder, 50-100 nm particle size (SEM), 97% trace metals basis, Sigma-Aldrich, The Netherlands) and polystyrene (430102-1KG, Mw 192,000, Sigma-Aldrich, The Netherlands) at a weight/volume (w/v) ratio of 25%. The mass ratio between  $\text{Fe}_3\text{O}_4$  and polystyrene was 1:2. The detailed procedures are described below. First, 2.5 g polystyrene beads were dissolved in DMF with magnetic stirring for 3 h. Subsequently, 1.25 g  $\text{Fe}_3\text{O}_4$  nanoparticles were dispersed in the solution using an ultrasonic bath for 5 min. Finally, the polymer solution was left on a roller mixer overnight to ensure a uniform blend.

### 4.4.2 Fabrication of Soft Sperm-Like Microrobots

The prepared polymer solution was loaded into a syringe and subsequently mounted on a syringe pump. Operating at the pre-programmed flow rate of 1.2 mL/h, the solution was pumped out, forming a positively charged droplet under a high voltage of 15 kV. The electrostatic repulsion among the surface charges caused the droplet to deform into a Taylor cone at the nozzle tip. As the charged jet was stretched into a slender filament from the cone, it rapidly solidified under the high voltage and finally deposited onto the grounded collector [98]. A sonicator (VCX 130, Sonics & Materials, Inc., USA) generates ultrasonic waves that disrupt the beaded fibers at the junction between the fiber and the beads by operating for 10 s. This process results in sperm-like microrobots comprised of an ellipsoidal bead and a uniform fiber.

### 4.4.3 SEM Characterization

The morphology and geometry of the sperm-like microrobots were investigated by scanning electron microscope (Lyra 3 XM, Tescan, Czech Republic) operating at 5 kV. Furthermore, the chemical composition of the

## *4. Magnetic Control of Soft Microrobots Near Step-Out Frequency: Characterization and Analysis*

---

microrobot and the distribution of Fe signals were characterized by energy-dispersive X-ray spectroscopy (EDS) elemental mapping. A 20 nm thick layer of gold was deposited on the microrobots to increase the conductivity for SEM characterizations and EDS mapping.

### **4.4.4 Magnetization Measurements**

The magnetic hysteresis loop of beaded fibers was obtained using the embedded vibrating sample magnetometer in a physical property measurement system (9T 2-400K, Quantum Design, Belgium) at room temperature. The applied field ranged from -1000 mT to 1000 mT.

### **4.4.5 Preparation of Methyl Cellulose (MC) Solutions**

Methyl Cellulose (MC) (M0512-100G, Sigma Aldrich, The Netherlands) solutions with the w/v concentrations of 0.1% and 0.2% were prepared using the following method. First, 1.5 g of MC was thoroughly dissolved in 150 mL of deionized (DI) water with magnetic stirring for 12 h. The resulting MC solution was filtered twice via suction filtration using a filter with a pore size of 12  $\mu\text{m}$ . This produced a stock MC solution with the w/v concentration of 1%, which was stored in the refrigerator at 4°C. The 0.1% and 0.2% w/v MC solution were obtained by diluting the 1% w/v MC stock solution with DI water.

### **4.4.6 Viscosity Measurements**

The viscosity measurements of the MC solutions were conducted at room temperature using a rheometer (MCR 92, Anton Paar, Austria) with a cone-plate geometry. A shear rate ranging from 10 to 1000 1/s was applied to the MC solution, and the rheometer recorded the resulting shear stress. The viscosities of the mediums can be calculated through the ratio of shear stress to shear rate.

### **4.4.7 Magnetic Actuation and Microscopic Observation Setup**

An electromagnetic coil system was built to generate an oscillating magnetic field in a 2D plane. The current applied to two pairs of coils was pro-

duced and amplified using the XenusPlus EtherCAT (XE2-230-20, Copley Controls, Canton, USA). This current output system was controlled by a C++—based program. During swimming tests, the oscillating magnetic field with an oscillation angle of  $70^\circ$  and a field strength of 5 mT was generated. The actuation frequency was alternated by controlling the frequency of the output current from XenusPlus EtherCAT. The propulsion of the sperm-like microrobots was recorded using a microscopic observation setup, which consists of a charge-coupled device camera (AVA1000-100GM, Basler AG, Ahrensburg, Germany) and an optical microscope with a 10x objective lens (HI PLAN 10x/0.25 PH, Leica, Germany).

#### 4.4.8 Position Acquisition of Wave Patterns

Our approach combines image processing techniques and custom-written MATLAB scripts to accurately capture and analyze the wave patterns of our sperm-like microrobots. The detailed procedures are described below. First, the pre-processing is conducted on the captured videos of sperm-like microrobots' propulsion using Fiji software. This includes selecting the region of interest, creating reversed images, subtracting the background, and saving the processed frames as a tiff stack for the subsequent processing. In the processed image stack, the head of the microrobot appears as a bright spot owing to the high concentration of magnetic nanoparticles. A threshold is applied to filter the head. For tail tracking, we employ a Gaussian filter to smooth each frame in the stack, followed by tracking the wave patterns using gradient vector flow and active contour models in a customized MATLAB script [260], [261]. Active contours, which are deformable curves, are used to locate the boundaries of the microrobot's tail. The external force, known as gradient vector flow (GVF), is computed as a diffusion of the gradient vectors of a gray-level edge map derived from the image and incorporated into the active contour model. The vector field converges toward the pixels of the tail with the maximum intensity. The active contours are deformed according to the GVF to acquire the positions of the wave patterns, enhancing the tracking precision.

## 4.5 Supplementary Figure

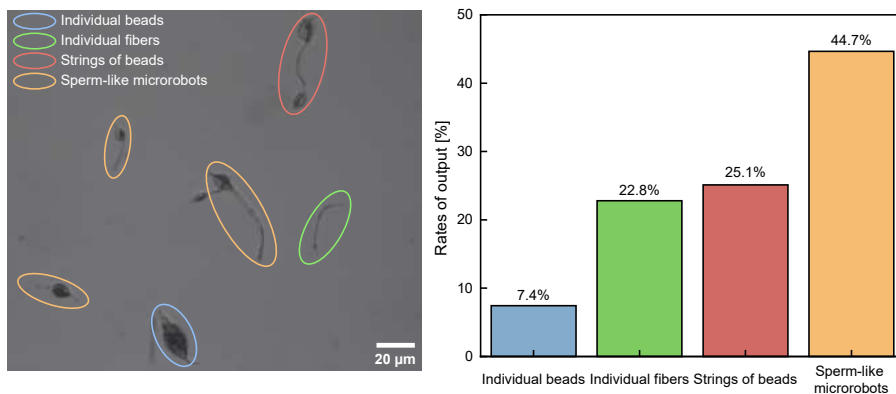


Figure 4.S1: Various structures after sonication cutting include individual beads, individual fibers, strings of beads, and sperm-like microrobots. The rates of output for each structure are statistically analyzed, with a sample size of  $n = 200$ .

## 4.6 Supplementary Table

Table 4.S1: Values, calculations, or measurement methods of the variables used in the calculations.

tail length $L$ , tail radius $r$ , the major radius $a$ and minor radius $b$ of the head	These variables are measured from scanning electron microscopy (SEM) and optical micrographs.
volume of the head $v$	$v = \frac{4}{3}\pi ab^2$
the permeability of free space $\mu_0$ , the magnetization of the head $\mathbf{m}_H$ , the bending stiffness of the tail $E$	$\mu_0 = 4\pi \times 10^{-7} \text{ T} \cdot \text{m/A}$ $ \mathbf{m}_H  = 2.96 \times 10^3 \text{ A/m}$ $E = 3.71 \times 10^{-16} \text{ N} \cdot \text{m}^2$
demagnetization factors $n_{\text{rad}}$ and $n_{\text{axi}}$ along all radial directions and major axis of the ellipsoidal head, the ratio $R$ of major radius to the minor radius	$n_{\text{axi}} = \frac{1}{R^2 - 1} \left( \frac{R}{2\sqrt{R^2 - 1}} \ln \left( \frac{R + \sqrt{R^2 - 1}}{R - \sqrt{R^2 - 1}} \right) - 1 \right)$ $n_{\text{axi}} + 2n_{\text{rad}} = 1 \quad R = a/b$
torque coefficient $C_1$ and drag coefficient $C_2$ , the ellipsoidal head's eccentricity	$C_1 = \frac{4}{3}\epsilon^3 \left( \frac{2 - \epsilon^2}{1 - \epsilon^2} \right) \left[ -2\epsilon + (1 + \epsilon^2) \ln \frac{1 + \epsilon}{1 - \epsilon} \right]^{-1}$ $C_2 = \frac{8}{3}\epsilon^3 \left[ -2\epsilon + (1 + \epsilon^2) \ln \frac{1 + \epsilon}{1 - \epsilon} \right]^{-1}$ $\epsilon = \sqrt{1 - (b/a)^2}$
viscosity of the medium $\eta$	This variable is measured using a rheometer, The viscosities of deionized (DI) water, 0.1% methylcellulose (MC), and 0.2% MC solution are 1 mPa·s, 4.4 mPa·s, and 5.7 mPa·s, respectively.
normal drag coefficient $\xi_{\perp}$ and tangent drag coefficient $\xi_{\parallel}$ of the tail	$\xi_{\perp} = \frac{4\pi\eta}{\ln(L/r) + 0.193} \quad \xi_{\parallel} = \frac{2\pi\eta}{\ln(L/r) - 0.807}$
wave variables $y_0$ and $\lambda$	Wave variables are determined via the nonlinear curve fitting method, as introduced in <i>section 3.5</i> . They are dependent on the wave patterns of sperm-like microrobots.

## 4.7 Supplementary Movie

**Movie 4-S1. Movement of magnetically actuated soft sperm-like microrobots in deionized (DI) water, 0.1%, and 0.2% methyl cellulose (MC) solutions.**

This video shows the movement of sperm-like microrobots through planar flagellar propulsion under an in-plane oscillating magnetic field with a strength of 5 mT.

# 5

## Magnetic Alginate Microrobots with Dual-Motion Patterns through Centrifugally Driven Flow Control

*Note:* Following chapter is adapted from the article “Magnetic Alginate Microrobots with Dual-Motion Patterns through Centrifugally Driven Flow Control” by **Z. Wang**, W. Li, C. Li, A. Klingner, Y. Pei, S. Misra, and I. S. M. Khalil, published in “Materials & Design”, volume 246, pages 1-11, October 2024.

### Abstract

Mobile microrobots have gained increasing attention in biomedical applications because they can be precisely actuated to targeted positions in a tiny space. However, their use in biomedical applications is hindered by the costly and complicated fabrication method. Herein, a facile fabrication method is proposed to produce magnetic alginate microrobots with adjustable dimensions, including teardrop and tadpole shapes, via tunable centrifugally-driven flows. The formation of these microrobots is interpreted by finite element analysis, revealing that the transition between the dripping and jetting regimes of the flow alters the microrobot’s shape. The dimensions of the microrobots are quantitatively analyzed based on the flow’s extrusion velocity, controlled by nozzle diameters and revolution speeds. Incorporating magnetic nanoparticles into the alginate-based hydrogel enables the microrobots to exhibit distinct motion patterns under a

## 5. *Magnetic Alginate Microrobots with Dual-Motion Patterns through Centrifugally Driven Flow Control*

---

magnetic field. The teardrop-like microrobot can reach a maximum rolling velocity of approximately  $2.7$  body length  $\text{s}^{-1}$  at  $2$  Hz, while the maximum stick-slip velocity of the tadpole-like microrobot reaches about  $0.42$  body length  $\text{s}^{-1}$  at  $5$  Hz, comparable to the existing bioinspired magnetic microrobots. The dual motion patterns allow these microrobots to overcome obstacles and navigate in vertically constrained environments. Last, an ultrasound imaging system is deployed to monitor the locomotion and degradation of the microrobots, showing their potential for targeted drug delivery applications.

### 5.1 Introduction

Untethered microrobots are emerging viable tools for minimally invasive medicine due to their miniaturization, maneuverability, and versatility [5], [262]–[264]. Building on these attributes, the precision operability of untethered microrobots, such as helical microrobots and microrobotic swarms, has been a focus of research and improvement over the past few decades. To better navigate complex environments with unpredictable disturbances and obstacles, advanced control strategies have been introduced to refine these microrobots' control precision and performance [265]–[268]. These advancements in control strategies equip these small-scale robots with the potential to operate in confined spaces and assist surgeons in performing surgeries at hard-to-reach positions. Moreover, their precise operability and capability to transport cargo can address problems in systemic drug delivery, such as poor accumulation at target sites [269], quick emergence of antibiotic resistance [270], and side effects to healthy cells or organs [271]. However, integrating these robots into clinical practice is challenging because technical hurdles and design complexities exist in their fabrication [272], [273]. For instance, robots at the macro level are equipped with a suite of sensors, actuators, power sources, and programmable control units, which are difficult to replicate on a microrobot because of size constraints. Biomimicry offers a promising design methodology for the fabrication of microrobots. By mimicking the design principles observed in living microorganisms or cells, microrobots can be bestowed with the intricate functionalities of their large counterparts, thus enabling them to interact with complex environments [76], [274]. These bioinspired microrobots, with their bionic characteristics, are designed to interact with the

---

surrounding environments and even camouflage without alarming other creatures [275]. Furthermore, the biomimetic principles applied in the design of helical microrobots have been modified to include a sharp cutting tip, which allows them to mechanically eliminate blood clots effectively [276].

Natural organisms, such as fish, tadpoles, and sperm, achieve locomotion by undulating their tails. Bioinspired microrobots have been designed to replicate this locomotion mechanism through various fabrication methods, including photolithography [44], [277], electrodeposition [81], and direct laser writing [278]. Tadpole-like microrobots, consisting of a head of magnetic microbead and a tail of magnetic nanoparticles chain, have been constructed through a magnetically assisted in situ polymerization method. This process involves magnetizing a microbead, which subsequently attracts magnetic nanoparticles via magnetic forces to form a chain. The as-prepared tadpole-like structure is encapsulated within a hydrogel following ultraviolet polymerization [279]. Tan *et al.* have reported a one-step formation method for sperm-like magnetic microrobots by developing a vortex turbulence-assisted microfluidics platform [280]. Monodispersed magnetic alginate/oil droplets are first formed within the microfluidics platform. Subsequently, a slender tail is extracted from the droplets due to the vortex flow generated by a rotational magnetic stirrer. In addition, sperm-like microrobots have been fabricated by cutting electrospun beaded fibers into segments where the bead and fiber serve as the head and the tail, respectively [46]. These bioinspired microrobots can move forward through the undulatory propulsion of their tails, akin to the swimming of fish, tadpoles, and sperm. Despite considerable efforts to advance fabrication methods for magnetic microrobots, challenges persist within the mentioned methods. The existing fabrication methods, involving tedious procedures and expensive equipment, are not suitable for mass production.

Microfluidics is a promising microfabrication technique that has wide-ranging applications in biology [281], chemistry [282], medical diagnostics [283], and engineering [284]. In the design of microfluidic devices, pumps are crucial for moving fluid through narrow channels. Centrifugal pumps provide many advantages, including the ability to handle highly viscous liquids, operate without introducing bubbles, and ease of accessibility. In this study, we demonstrate the bulk fabrication of magnetic alginate microrobots, including teardrop and tadpole shapes, through centrifugal pump-

## 5. Magnetic Alginate Microrobots with Dual-Motion Patterns through Centrifugally Driven Flow Control

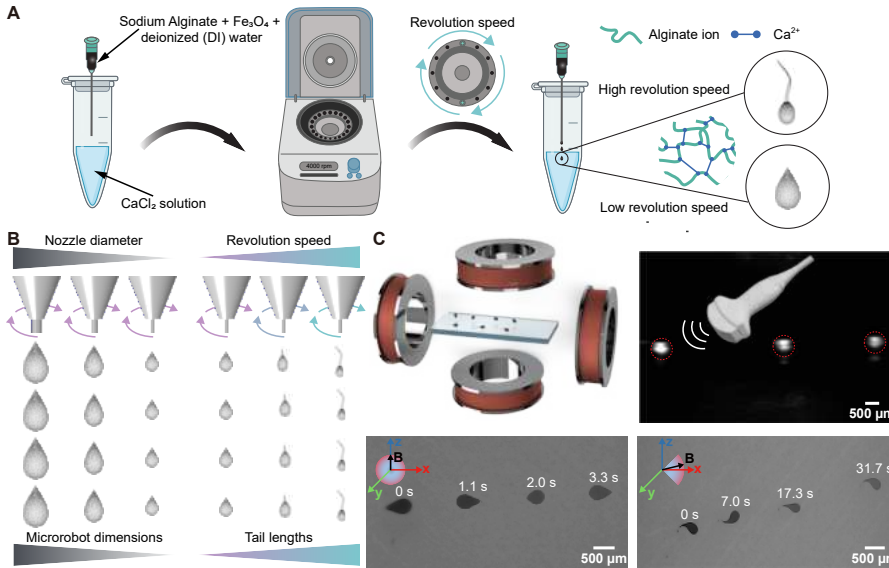


Figure 5.1: Fabrication, actuation, and imaging of magnetic alginate microrobots. (A) Magnetic alginate microrobots, including teardrop and tadpole shapes, are fabricated through centrifugally driven flow and cross-linking method using  $\text{Ca}^{2+}$  ions. (B) The shapes and dimensions of the microrobots are adjusted by varying the revolution speed of a centrifuge and the diameter of a nozzle. (C) Magnetic actuation is conducted in an electromagnetic coil system. The micrographs show the rolling motion of a teardrop-like microrobot under a rotating field and the stick-slip motion of a tadpole-like microrobot under an oscillating field. The ultrasound (US) image shows three teardrop-like microrobots at the wall of a water tank.

ing. These microrobots are produced by finely controlling centrifugally driven flows and subsequent cross-linking of the magnetic alginate solution (Figure 5.1(A)). The shapes and dimensions of the microrobots are tailored by adjusting the flow velocity, impacted by nozzle diameters and the centrifuge's revolution speeds (Figure 5.1(B)). Increasing flow velocity induces a transition from the dripping phase, where droplets form, to the jetting phase, which produces elongated jets. These droplets and jets serve as the head and tail of the microrobots, respectively. Characterizations are conducted to assess their morphologies, dimensions, chemical composition, and locomotion capabilities. The adoption of magnetic actuation ensures operational safety by eliminating the need for harmful chemical fuels. Lastly,

the imaging by the ultrasound imaging system and the degradation experiments are conducted, showcasing our microrobots' potential for precise drug delivery in clinical settings (Figure 5.1(C)).

## 5.2 Results and Discussion

### 5.2.1 Fabrication of Magnetic Alginate Microrobots

Sodium alginate is selected as the material of the microrobots due to its biocompatible and biodegradable properties [285]. A facile method is proposed to fabricate the microrobots, as shown in Figure 5.1(A). The alginate solution mixed with  $\text{Fe}_3\text{O}_4$  nanoparticles is pumped from the nozzle by centrifugal forces and subsequently comes into contact with the  $\text{CaCl}_2$  solution within a centrifuge tube. This contact initiates the gelation process, where the liquid alginate solution transforms into a solid gel. During this process,  $\text{Ca}^{2+}$  ions form links between alginate chains to create a three-dimensional network. The existence of magnetic nanoparticles enables the actuation of microrobots in a magnetic field. Note that the centrifugally driven flow, and consequently the shape and the dimension of the microrobot, can be controlled by adjusting the revolution speeds of the centrifuge. The variability of the revolution speeds allows for the fabrication of teardrop-like and tadpole-like microrobots.

### 5.2.2 Characterization and Formation Simulations of Magnetic Alginate Microrobots

Several factors, including viscoelasticity, density, surface tension, and flow velocity of the magnetic alginate solution, play an important role in droplet formation when the solution is centrifugally expelled from the nozzle. A rheological study is conducted on the solution to investigate its viscosity (see Materials and Methods). Shear stress on the solution was measured with a rheometer across a range of shear rates, as exhibited in the red curve of Figure 5.S1(A). Dynamic viscosities of the solution, calculated from the slope of the red curve, are depicted in the blue curve. The magnetic alginate solution is characterized by decreasing viscosities with increasing shear rates, indicating its shear-thinning behavior. Figure 5.S1(B)-I shows the storage modulus ( $G'$ ) and loss modulus ( $G''$ ) of the solution. The viscous

## 5. Magnetic Alginate Microrobots with Dual-Motion Patterns through Centrifugally Driven Flow Control

behavior of the solution dominates its elastic behavior, as indicated by the fact that  $G''$  exceeds  $G'$ . Figure 5.S1(B)-II displays the viscoelastic behavior of the magnetic alginate hydrogel. The storage modulus ( $G'$ ) and the loss modulus ( $G''$ ) significantly increase after the sol-gel transition. Upon reaching a critical shear stress, microcrack formation occurs in the gel, increasing  $G''$  after the plateau. This is because the broken bridge fragments in the gel move and generate internal viscous friction. With the continuously increasing shear stress, the microcracks grow and merge into a macro crack. The entire gel begins to flow and the viscosity of the gel will exceed its elasticity. In addition, the density of the solution is determined by weighing the solution with a known volume, while the surface tension of the magnetic alginate solution is measured using the pendant drop method (see Materials and Methods and Figure 5.S2). The molecules in the solution exhibit strong cohesive forces, facilitating the formation of a spherical flow. However, the centrifugal force distorts the spherical shape to a prolate ellipsoid. The finite element analysis method, which considers the interplay between liquid and air phases and the impact of centrifugal force, is essential to comprehend the formation mechanism of the magnetic alginate microrobots.

Level set methods have been employed in various applications such as incompressible two-phase flows [286], viscoelastic fluid flows [287], and fluid-structure interactions [288]. In this study, we utilize the two-phase level set method to track the moving liquid interface [289], [290]. The two-phase level-set equation is given by,

$$\frac{\partial \varphi}{\partial x} + \mathbf{u} \cdot \nabla \varphi = \gamma \nabla \cdot \left( \varepsilon \nabla \varphi - \varphi(1 - \varphi) \frac{\nabla \varphi}{|\nabla \varphi|} \right). \quad (5.1)$$

Here  $\mathbf{u}$  is the flow velocity, and the level set function,  $\varphi$ , which ranges from 0 to 1, indicates the phase: values below 0.5 denote the air phase, and those above 0.5 indicate the liquid phase. The parameter  $\gamma$  denotes the reinitialization parameter, while  $\varepsilon$  controls the thickness of the interface. Additionally, the dynamics of the magnetic alginate solution during centrifugal pumping is governed by the following equations,

$$\begin{aligned} \rho \frac{\partial \mathbf{u}}{\partial t} + \rho(\mathbf{u} \cdot \nabla) \mathbf{u} &= \nabla \cdot [-p \mathbf{I} + \mu (\nabla \mathbf{u} + (\nabla \mathbf{u})^T)] + \mathbf{F}_{\text{st}} + \mathbf{F}_{\text{c}} \\ \nabla \cdot \mathbf{u} &= 0, \end{aligned} \quad (5.2)$$

where  $\rho$  is the solution's density,  $t$  is time,  $p$  is pressure,  $\mathbf{I}$  is the identity matrix,  $\mu$  is the viscosity of the solution,  $\mathbf{F}_{\text{st}}$  is the surface tension force,  $\mathbf{F}_{\text{c}}$  is the centrifugal force exerted on the solution. These forces are given by the following equations,

$$\mathbf{F}_{\text{st}} = \pi d_{\text{n}} \sigma \hat{\mathbf{n}}, \quad \mathbf{F}_{\text{c}} = -m \omega^2 r \hat{\mathbf{n}}, \quad (5.3)$$

where  $d_{\text{n}}$  is the diameter of the nozzle,  $\sigma$  is the surface tension of the solution,  $\hat{\mathbf{n}}$  is the unit vector along the axial direction of the nozzle,  $m$  is the mass of the extruded liquid,  $\omega$  is the revolution speed of the centrifuge,  $r$  is the distance of the solution from the central axis of rotation, and  $\omega^2 r$  represents the relative centrifugal force.

After substituting Equation 5.3 into Equations 5.1 and 5.2 and solving the governing equations, the extrusion of the magnetic alginate solution from the nozzle was simulated. The simulation depicts the emergence of teardrop-like and tadpole-like flows under varying revolution speeds, as illustrated in Figure 5.2(A). The dripping and jetting regimes of the flow contribute to its final morphology. During the dripping regime, a pendant droplet forms at the nozzle tip when the centrifugal force is applied. This droplet grows in size due to the continuous supply of the solution. The surface tension force acts to minimize the droplet's surface area, whereas the centrifugal force attempts to detach the droplet from the nozzle tip. The break-off of the droplet occurs when the centrifugal force balances the surface tension force. In the jetting regime, the droplet extends to a long tail owing to the increasing centrifugal force. Viscous resistance resists the elongation and break-off of the tail, thus stabilizing the extruded flow's shape. In contrast, the Plateau-Rayleigh instability would lead to thinning of the flow at the tail segment. The break-off of the flow occurs when the viscous resistance can no longer maintain the integrity of the tail [291]. Lastly, the tail partially retracts back into the droplet, which is influenced by both the flow velocity and the elasticity of the solution. Figure 5.2(A)-I and II illustrates the simulated flow obtained at low and high revolution speeds, respectively. The surface tension and the centrifugal force result in the initial formation of a droplet flow, as displayed in Figure 5.2(A)-I. Subsequently, a short tail emerges because the low revolution speed brings about limited fluid volume ejected from the nozzle. This tail retracts owing to elastic and inertial forces within the fluid. Ultimately, a teardrop flow is produced and becomes a gel after contact with  $\text{CaCl}_2$  solutions. At the high

## 5. Magnetic Alginate Microrobots with Dual-Motion Patterns through Centrifugally Driven Flow Control

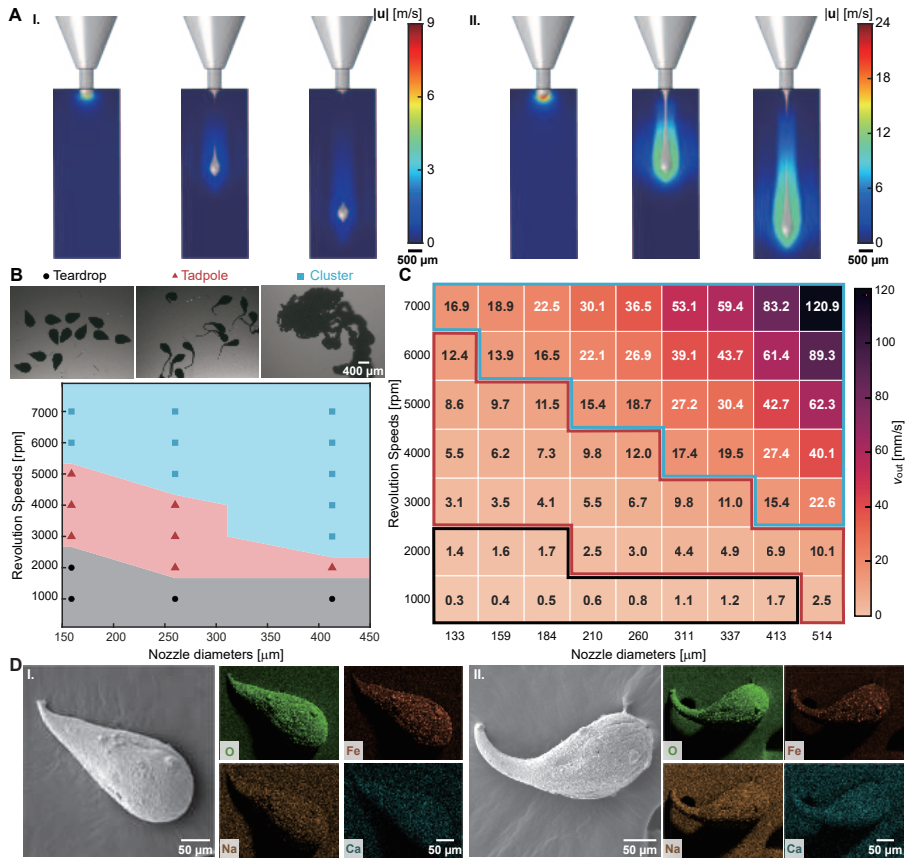


Figure 5.2: Characterization, phase diagram, and simulation results (see Materials and Methods). (A) Simulation results show the formation of (I) a teardrop-like flow and (II) a tadpole-like flow over time. The colormap represents the flow velocity  $\mathbf{u}$ . (B) Micrographs and phase diagram of the magnetic alginate microrobots with different morphologies under varying experimental conditions. (C) The heatmap depicts the extrusion velocity  $V_{out}$  at the nozzle tip under different experimental conditions (see Materials and Methods). The values within the rectangular box represent the predicted extrusion velocity  $v_{out}$  under the corresponding experiment conditions. (D) Scanning electron microscope (SEM) imaging and energy-dispersive X-ray spectroscopy (EDS) elemental mapping images of O, Fe, Na, and Ca in (I) the teardrop-like and (II) the tadpole-like microrobots.

revolution speed, the droplet is initially formed, and then the tadpole-like

flow with the longer tail is extruded until the Plateau-Rayleigh instability occurs. The tail retraction is negligible compared to its overall length, as depicted in Figure 5.2(A)-II. Our simulations indicate that as the revolution speed increases, the flow transitions from the dripping to the jetting regime, resulting in a shift from teardrop-like to tadpole-like flows.

Guided by the simulation results, we fabricated the magnetic alginate microrobots by varying nozzle diameters and revolution speeds. Figure 5.2(B) presents the micrographs and phase diagram of microrobots under various experimental conditions. As the revolution speeds increase, the microrobots transform through three stages: teardrop-like microrobots, tadpole-like microrobots, and clusters. Shape transitions of the microrobots come at varying revolution speeds depending on the nozzle diameters. During the fabrication, the needles with diameters of 159  $\mu\text{m}$  (30 gauge), 260  $\mu\text{m}$  (26 gauge), and 413  $\mu\text{m}$  (22 gauge) are used and referred to as S-, M-, and L-sized nozzles below. The teardrop-like and tadpole-like microrobots were fabricated using the L-sized nozzle at revolution speeds of 1000 and 2000 revolutions per minute (rpm), respectively, as indicated by the black circle and red triangle symbols in the phase diagram. The blue square symbols denote the formation of clusters. Using the M-sized nozzle, the shift from the tadpole-like microrobots to undesired clusters occurs at 5000 rpm. To avoid the formation of clusters, the revolution speed should be kept below 6000 rpm when utilizing the S-sized nozzle. Notably, the change in nozzle diameters and revolution speeds results in the variation of the flow's extrusion velocity  $V_{\text{out}}$  at the nozzle tip. Figure 5.S3 details the  $V_{\text{out}}$  using the S-, M-, and L- sized nozzles at 1000 rpm. The extrusion velocity has the highest value at the center of the cross-section and decreases to zero at the nozzle walls due to the no-slip boundary condition. The maximum velocity is used to represent the extrusion velocity. The heatmap in Figure 5.2(C) correlates the simulated extrusion velocity with experimental conditions. After analyzing these results with the phase diagram, we determined that the shift from the teardrop-like microrobots to the tadpole-like microrobots occurs at extrusion velocities between 1.7 mm/s and 3.0 mm/s. Moreover, the heatmap indicates that the undesired clusters are produced when the extrusion velocity exceeds 13.9 mm/s. The extruded velocities of the different nozzles at varying revolution speeds have been theoretically studied. These simulations can thus guide the fabrication process, allowing for the prediction of microrobot shapes under varying

## 5. *Magnetic Alginate Microrobots with Dual-Motion Patterns through Centrifugally Driven Flow Control*

---

experimental conditions (see the regions surrounded by the colored lines in Figure 5.2(C)).

The extrusion velocity not only shapes the microrobots but also impacts the yield of the microrobots. Table 5.S1 displays the yield of magnetic alginate microrobots under different experimental conditions, ranging from 5 to 12,000 per minute. This variance demonstrates a positive correlation with the extrude flow velocity simulated in Figure 5.2(C), indicating that higher extrusion velocities facilitate greater yield. To clarify the influence of the extrusion velocity on the microrobots' morphology, Figure 5.2(D) presents scanning electron microscope (SEM) images that detail the teardrop-like and tadpole-like microrobots. Notably, the tadpole-like microrobot shown in the SEM image was produced at a lower revolution speed compared to that in the micrograph. Moreover, the dehydration process during SEM sample preparation can lead to shrinkage of the magnetic alginate microrobots. Thus, the tail lengths of the tadpole-like microrobots in the SEM and optical brightfield micrographs are distinct. A zoom-in SEM image on the tail of a tadpole-like microrobot and the corresponding EDS elemental mapping images of Na and Ca are presented in Figure 5.S4. The Na EDX signals are less distinct from the grid background, which we attribute to the relatively small amount of Na element in the robots, as most  $\text{Na}^+$  are replaced by  $\text{Ca}^{2+}$  during the gelation process. The presence of  $\text{Fe}_3\text{O}_4$  clusters on the surface of the magnetic microrobot is indicated by the enlarged SEM image in Figure 5.S5(A). In conjunction with these observations, energy-dispersive X-ray spectroscopy (EDS) mapping analysis reveals the coexistence of O, Fe, Na, and Ca elements. The elemental analysis in Figure 5.S5(B) demonstrates an atomic percentage of 73.55% C, 22.75% O, 1.06% Fe, and 2.64% Ca. The weight ratio of  $\text{Fe}_3\text{O}_4$  within the microrobot is calculated to be around 5.79%.

### 5.2.3 Size Scalability of Magnetic Alginate Microrobots

To understand the effect of the nozzle diameters and the revolution speeds on microrobot dimensions, we analyzed teardrop-like and tadpole-like microrobots produced under various conditions. The dimension of these microrobots decreases as the inner diameter of the nozzle narrows, as shown in the SEM micrographs of Figure 5.3(A) and the optical brightfield micrographs of Figure 5.S6(A). Moreover, increasing the revolution speeds

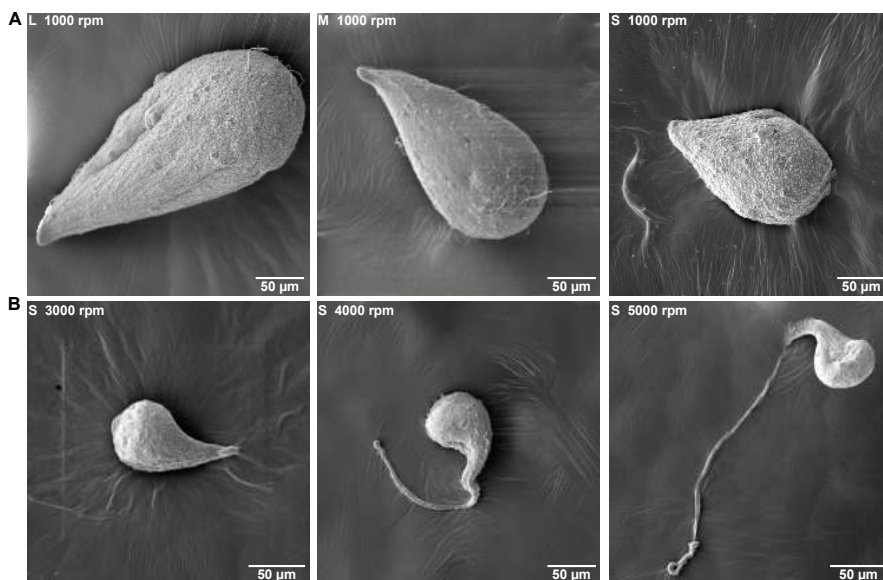


Figure 5.3: SEM images of (A) teardrop-like microrobots fabricated using the L-, M-, and S-sized nozzles at 1000 rpm, and (B) tadpole-like microrobots fabricated using the S-sized nozzle at increasing revolution speeds (including 3000 rpm, 4000 rpm, and 5000 rpm). The L-, M-, and S-sized nozzles refer to the 22-, 26-, and 30-gauge needles, respectively, with the diameters of 413  $\mu\text{m}$ , 260  $\mu\text{m}$ , 159  $\mu\text{m}$ .

results in the tail elongation of tadpole-like microrobots (see Figure 5.3(B) and Figure 5.S6(B)). Hence, it is essential to understand the relationship between the dimensions of these microrobots and experimental conditions.

Two terms regarding the dimension of the magnetic alginate microrobots, Feret diameter, and MinFeret diameter, are first introduced. The Feret diameter of the microrobot refers to the longest distance between any two points along the perimeter of the tadpole-like microrobot's head or the teardrop-like microrobot, also known as the maximum caliper diameter. The MinFeret diameter represents the minimum caliper diameter. These dimensions of the microrobots obtained via the corresponding experimental conditions are displayed in the first two columns of Figure 5.4(A). At a revolution speed of 1000 rpm, the Feret diameters averagely decrease from 649  $\mu\text{m}$  to 420  $\mu\text{m}$ , and the average MinFeret diameters decline from 374  $\mu\text{m}$  to 321  $\mu\text{m}$  across the L-, M-, and S-sized nozzles. With a fixed noz-

## 5. Magnetic Alginate Microrobots with Dual-Motion Patterns through Centrifugally Driven Flow Control

---

zle diameter, both the Feret and the MinFeret diameters decrease as the revolution speed increases.

As previously mentioned, the droplet breaks off when the centrifugal force equals the surface tension force. Assuming a sphere flow detaches from the nozzle tip, the diameter  $d_{\text{sphere}}$  of the spherical flow can be determined by the following equation [292],

$$d_{\text{sphere}} = \sqrt[3]{\frac{6d_n\sigma}{\rho\omega^2r}}. \quad (5.4)$$

The predicted diameters of the spherical flow across various revolution speeds using the L-, M-, and S-sized nozzles are plotted as black lines in Figure 5.4(B). A noticeable deviation is observed in comparison to the experimental data highlighted by blue and red error bars. To accurately reflect the dimensions of the microrobots, the calibrated coefficients  $a_{\text{max}}$  and  $a_{\text{min}}$  are introduced to account for the shrinkage of the droplet in the directions of the Feret and the MinFeret diameters, respectively. This shrinkage can be attributed to the volume loss during the gelation of the alginate solution. The revised equation for estimating the Feret and the MinFeret diameters of the microrobot is as follows,

$$d_x = (1 - a_x) \sqrt[3]{\frac{6d_n\sigma}{\rho\omega^2r}}, \quad (x = \text{min, max}). \quad (5.5)$$

The fitted blue and red lines in Figure 5.4(B), representing the predicted Feret and MinFeret diameters, respectively, closely align with the experimental data. The shrinkage coefficients  $a_{\text{max}}$  are determined to be -0.0808, 0.0173, and 0.0373 for the microrobots fabricated with the L-, M-, and S-sized nozzles. The value approximately 0 of  $a_{\text{max}}$  denotes nearly zero shrinkage in the direction of the Feret diameter. Conversely, the shrinkage coefficients  $a_{\text{min}}$ , derived from the red lines' fitting, have values of 0.3282, 0.2387, and 0.2203, which imply an approximate 26% shrinkage along the MinFeret diameter. The values derived from the formula combining these coefficients,  $1 - (1 - a_{\text{max}})(1 - a_{\text{min}})^2$ , are calculated to be 51.22%, 43.04%, and 41.47%, reflecting the volume shrinkage of the microrobot's volume after the gelation. Further analysis, depicted in Figure 5.S7, reveals additional relationships between nozzle diameter and microrobot dimensions. The shrinkage coefficients along the Feret diameter,  $a_{\text{max}}$ , are -0.0553 and

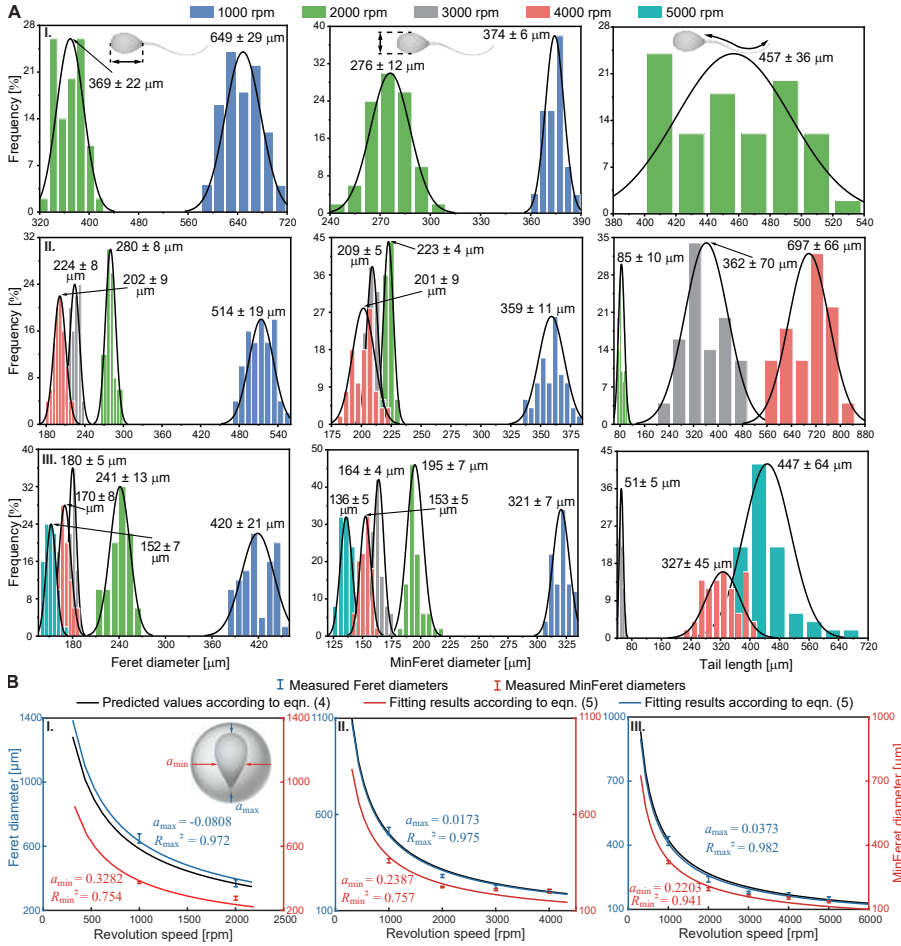


Figure 5.4: Size distribution of teardrop-like and tadpole-like microrobots. (A) Frequency histograms show Feret diameters, MinFeret diameters, and tail lengths of the microrobots fabricated using the (I) L-, (II) M-, and (III) S-sized nozzles ( $n = 50$  for each figure). Histograms are fitted with Gaussian distribution (solid lines), and the data is given by mean  $\pm$  standard deviation. (B) The relationship between the revolution speeds and the Feret diameters, the MinFeret diameters of the microrobots obtained via (I) the L-, (II) M-, and (II) S-sized nozzles. The black curves represent the fitting results through Equation 5.4. The blue and red curves are the best-fit lines through Equation 5.5 according to the measured values marked by error bars. The fitting extent is expressed through the value of  $R_x^2$  ( $x = \min, \max$ ), while  $a_x$  represents the shrinkage ratio of the extruded alginate solution after the gelation, as shown in the inset.

## 5. *Magnetic Alginate Microrobots with Dual-Motion Patterns through Centrifugally Driven Flow Control*

---

0.0575 for the microrobots fabricated under 1000 and 2000 rpm, respectively. Conversely, the shrinkage coefficients along the MinFerret diameter,  $a_{\min}$ , have values of 0.3193 and 0.2682. These shrinkage ratios along the Feret and MinFerret diameters are in good agreement with the values calculated from the curves in Figure 5.4(B). The calculated volume shrinkage of the microrobots after gelation is 51.10% and 49.53%, respectively, when fabricated at 1000 and 2000 rpm. This characteristic is impacted by the concentration of magnetic alginate solution and  $\text{CaCl}_2$  solution. With the assumption of consistent volume shrinkage after the gelation, our findings enable the prediction of magnetic alginate microrobots' Feret and MinFerret diameters under various experimental conditions.

The tail lengths of the tadpole-like microrobots are measured and presented in the frequency histograms, which are fitted with the Gaussian distribution (represented by solid lines in the third column of Figure 5.4(A)). It is observed that the tail lengths increase with the revolution speeds when the nozzle diameter remains constant. In particular, the average tail length of the tadpole-like microrobot is 457  $\mu\text{m}$  using the L-sized nozzle at 2000 rpm. With the M-sized nozzles, this length ranges from 85  $\mu\text{m}$  to 697  $\mu\text{m}$  as revolution speeds rise. For the L-sized nozzles, the increase is from 51  $\mu\text{m}$  to 447  $\mu\text{m}$ . The pinch-off of the flow from the nozzle occurs when the centrifugal force overcomes the viscous resistance and the surface tension force. This results from the appearance of a thin neck in the flow, which ultimately collapses due to Plateau-Rayleigh instability. A quantitative relationship between the tail length and the experimental conditions is challenging to formulate since the forces involved in this process are difficult to predict with analytical models. Thus, only the positive correlation of the tail length with revolution speeds is reported.

### 5.2.4 Locomotion and Dual Motion Capability of Magnetic Alginate Microrobots

The demonstrated scalability of our fabrication method allows for tailoring microrobots' dimensions, which are critical for their locomotion capabilities under magnetic fields. The locomotion experiments of the magnetic alginate microrobots are conducted in a glass petri dish filled with deionized water. When actuated by a uniform magnetic field with a strength of 25 mT, these microrobots settle near the wall of the petri dish (see Mate-

rials and Methods and Movie 5-S1). For the teardrop-like microrobots, a rotating field around the  $\mathbf{y}$  axis is applied, as illustrated in Figure 5.5(A)-I. These microrobots are typical surface walkers, achieving net translation through rolling near a surface [293], [294]. The rolling motion is captured in the micrographs of Figure 5.5(A)-I. The microrobot aligns its long axis to the field direction and rotates in the same direction as the field. For the tadpole-like microrobots, we first conduct their swimming motions in an oscillating field along the  $\mathbf{y}$  axis within the  $XOY$  plane, as illustrated in Figure 5.S8. The microrobot can swim via the undulation of the tail, exhibiting a maximum velocity of about  $110.4 \mu\text{m/s}$  at  $5\text{Hz}$ . The propulsion of our tadpole-like microrobot during the swimming motion is driven by the deformation of its tail, which is composed of alginate hydrogels cross-linked with calcium ions. These hydrogels exhibit Young's moduli in the range of  $100\text{-}600 \text{ kPa}$  [295], making them suitable for creating deformable microstructures. The tail of the microrobot features a tapered geometry that progressively reduces bending stiffness towards the rear. This design concentrates the deformation at the rear, where the tail is more flexible. Moreover, the tail's high length-to-diameter ratio allows it to bend more easily under the forces generated by the oscillating head. These small deformations contribute to the tadpole-like microrobot's swimming motion.

In comparison to the existing magnetic microrobots inspired by sperm, fish, and tadpoles, our microrobots are inefficient microswimmers (see Table 5.S2). However, these microrobots show relatively high locomotion efficiency in the stick-slip motion when in contact with a substrate. Given that most current magnetic microrobots are fabricated using high-density materials, such as high molecular weight polymers, magnetic micro/nanoparticles, and metals, they tend to sink to the substrate bottom. Therefore, wall effects are inevitable for magnetic microrobots during locomotion. Rather than viewing this as a limitation, we leverage these wall effects to enhance our microrobots' locomotion capabilities. Our tadpole-like microrobot exploits these interactions to achieve higher motility in stick-slip motion compared to its swimming motion. The stick-slip motion is induced under an oscillating field around the  $\mathbf{y}$  at an angle  $\theta$  of  $60^\circ$  axis within the  $YOZ$  plane, as clarified in Figure 5.5(A)-II. The magnetic torque lifts the microrobot's head during the first half of the cycle; subsequently, the head descends with the field and strikes the wall boundary in the second half of the cycle. This motion occurs when the contact point be-

## 5. Magnetic Alginate Microrobots with Dual-Motion Patterns through Centrifugally Driven Flow Control

---

tween the microrobot and the wall boundary slips, similar to the stick-slip motion observed by Pawashe *et al.* [296]. The simulated fluid dynamics around the microrobots in rolling and stick-slip motions are depicted in Figure 5.5(B). During the rolling motion, the flow velocity increases at the front and the rear of the teardrop-like microrobot. Conversely, for the tadpole-like microrobot, the maximum flow velocity is observed at its tail end, with considerably lower flow velocity around the head. This suggests that the greater flow velocity at the tail enables the microrobot to move forward during the stick-slip motion.

To clarify the role of the tail in the locomotion, we conduct comparative experiments between the tadpole-like and teardrop-like microrobots during the stick-slip motion. Our findings indicate the velocity along the oscillating axis is negligible for the teardrop-like microrobot, in contrast to the significantly higher velocity observed for the tadpole-like microrobot, as shown in Figure S9A. Furthermore, we compute the fluid distribution around both microrobots (Figure 5.S9(B)). The results demonstrate that the presence of the tail leads to a larger flow velocity at the rear end, underscoring the role of the tail in enhancing locomotion during stick-slip motion. To further investigate the effects of the tail's length, width, and curvature on the rear flow velocity, we conduct simulations to compute the fluid distribution around the microrobots with varying geometric parameters of the tail. Figure 5.S10(A) demonstrates that the rear flow velocity increases with the tail length. The higher flow velocity at the tail's rear results in a faster velocity, which corresponds well with our observation that the tadpole-like microrobot exhibits a faster stick-slip motion with a longer tail (Figure 5.5(C)-II). Conversely, variation in the tail width gives rise to negligible changes in the rear flow velocity, as depicted in Figure 5.S10(B). Figure 5.S10(C) indicates the effects of the maximum curvature at the rear half of the tail. As the tail's curvature increases, the maximum flow velocity shifts to the tail segment with the maximum curvature, accompanied by a decrease in the rear flow velocity. This reduction might contribute to a decrease in the velocity of the tadpole-like microrobot.

Next, the locomotion ability of each group of magnetic alginate microrobots was quantitatively assessed. During one rotation cycle, the teardrop-like microrobot moves forward at a distance proportional to its perimeter. Therefore, the teardrop-like microrobot's velocity increases with the perimeter size at a constant actuation frequency. This correlation aligns

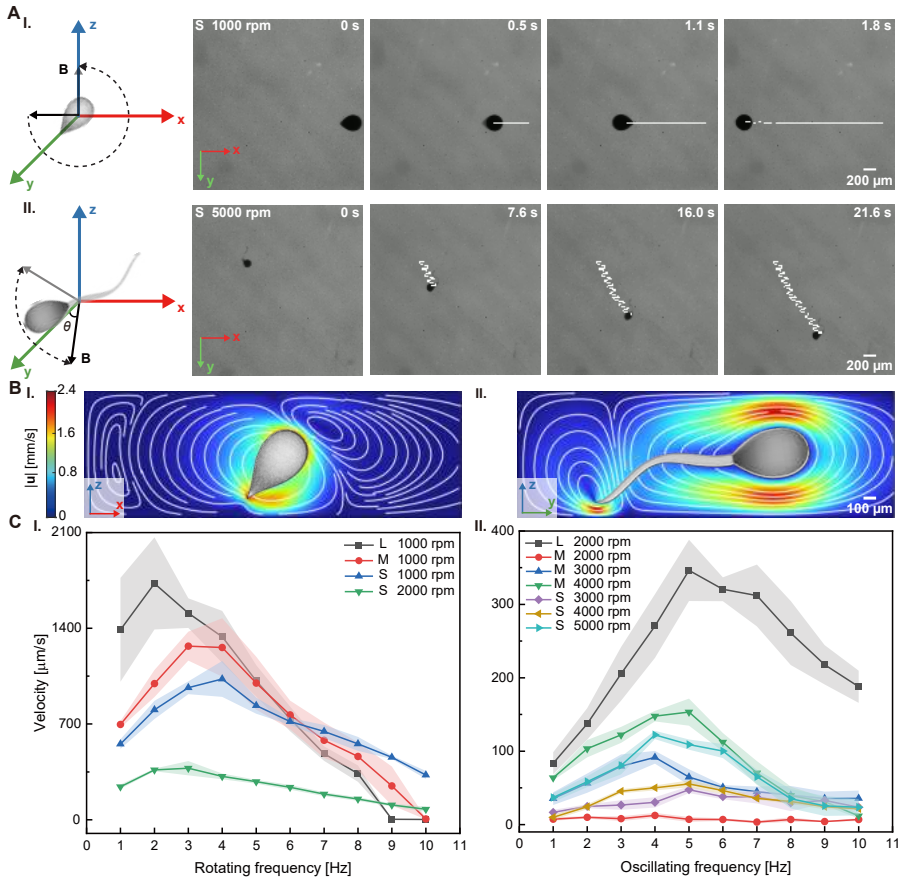


Figure 5.5: Locomotion characterization of teardrop-like and tadpole-like microbots. (A) Time-lapse micrographs of (I) the teardrop-like microrobot's rolling motion under a rotating magnetic field and (II) the tadpole-like microrobot's stick-slip motion under an oscillating magnetic field with an oscillating angle of  $\theta$ . White curves represent their motion trajectories. (B) Simulated fluid distribution around (I) the teardrop-like microrobot under rolling motion and (II) the tadpole-like microrobot under stick-slip motion (see Materials and Methods). (C) Frequency response curves of (I) teardrop-like microrobots' rolling motion and (II) tadpole-like microrobots' stick-slip motion. The legend describes the corresponding experimental conditions.

with the experimental results shown in Figure 5.5(C)-I. The teardrop-like microrobots fabricated with the L-sized nozzle show the maximum veloci-

## 5. Magnetic Alginate Microrobots with Dual-Motion Patterns through Centrifugally Driven Flow Control

---

ties of  $1728 \mu\text{m/s}$  at 2 Hz. The velocity increases with the frequency and decreases dramatically beyond the step-out frequency [240]. Figure 5.5(C)-I illustrates that teardrop-like microrobots of varying dimensions exhibit distinct step-out frequencies, ranging from 2 to 4 Hz. The tadpole-like microrobots demonstrate considerably lower velocities than the teardrop-like microrobots, yet they exhibit higher step-out frequencies than the latter. Their frequency response curves are displayed in Figure 5.5(C)-II. The tadpole-like microrobots obtained at 2000 rpm using the L-sized nozzle exhibit a maximum velocity of  $346 \mu\text{m/s}$  at 5 Hz. The velocity would increase with the tail length, as demonstrated by the frequency response curves of the tadpole-like microrobots fabricated using the S- and M-sized nozzles. An exception was observed for those produced at 2000 rpm using the M-sized nozzle, which shows nearly zero velocities. This can be attributed to their respective short tail length (around  $85 \mu\text{m}$ ) in contrast to the head size with the average Feret diameter of  $280 \mu\text{m}$ .

5

A summary of recent magnetic microrobots inspired by sperm, fish, and tadpoles is presented in Table 5.S2 to evaluate the locomotion capabilities of our tadpole-like microrobots. It outlines their fabrication methods, step-out frequencies, maximum velocities, types of motion, and locomotion efficiencies. During the swimming motion, the tadpole-like microrobot achieves a locomotion efficiency of 0.13 body lengths/s through its tail undulation. When it switches to the stick-slip motion, the microrobot can improve the locomotion efficiency to 0.42 body lengths/s. This motion mode employs both the tail undulation and interactions with a wall. The improvement in locomotion efficiency considers practical environments, as most magnetic microrobots are operated close to walls for locomotion and biomedical applications. The locomotion efficiency of our tadpole-like microrobots with the stick-slip motion is comparable to or exceeds that of many existing tadpole-like and sperm-like microrobots. Additionally, our tadpole-like microrobots exhibit a step-out frequency of 5 Hz, which is modest but close to some recent magnetic microrobots inspired by sperm and tadpoles [110], [279], [280]. For accurate tracking and control, magnetic microrobots are typically actuated below 5 Hz for *in vivo* applications [171], [297], [298]. Consequently, our microrobots maintain functional utility in practical biomedical scenarios with a step-out frequency of 5 Hz.

To showcase the capabilities of two distinct motions, we performed obstacle crossing and navigation in constrained spaces using the two lo-

comotion modes of the magnetic alginate microrobots, as illustrated in Figure 5.S10 and Movie 5-S2. The teardrop-like microrobot utilizes rolling motion to successfully climb over the obstacle, while the tadpole-like microrobot, employing stick-slip motion, is unable to cross (Figure 5.S10(A)). Although the teardrop-like microrobots demonstrate obstacle-crossing abilities and higher speeds, they have limitations in environments with vertical constraints due to their rolling motion along their long axis. Each rolling cycle of the teardrop-like microrobots involves a full rotation, which could be restrictive when navigating them in environments with limited vertical space. In contrast, the stick-slip motion of the tadpole-like microrobots does not undergo an entire rotation. This motion pattern and compact design allow them to pass through the vertically constrained channel, as shown in Figure 5.S10(B). Such adaptability is crucial for potential applications in the cardiovascular system or minimally invasive diagnostics in the gastrointestinal tract, where microrobots must navigate through varied and confined spaces.

### 5.2.5 Ultrasound Imaging of Magnetic Alginate Microrobots' Locomotion and Degradation

The locomotion capability of microrobots is a prerequisite for microrobotic systems, tracking microrobots is also important after deployment. The localization of microrobots can be easily achieved through a microscope *in vitro*. However, optical imaging proves ineffective *in vivo* due to its limited ability to penetrate tissue. To overcome this limitation, advanced imaging modalities, such as magnetic resonance imaging (MRI), ultrasound (US) imaging, computed tomography (CT), positron emission tomography (PET), and single-photon emission computed tomography (SPECT) are incorporated into microrobotic systems [184], [299]. In this study, a US imaging system was utilized to track the position of the magnetic alginate microrobots, capitalizing on the acoustic impedance mismatch between the microrobot and the surrounding fluid. Magnetic actuation systems, including systems with permanent magnets and systems with electromagnets, are commonly employed to actuate microrobots [132], [300]. Considering the specific requirements for a large operational area, permanent magnet systems are favored for *in vivo* applications [301]–[303]. The experimental setup, which includes a rotating permanent magnet system and a US imag-

## 5. Magnetic Alginate Microrobots with Dual-Motion Patterns through Centrifugally Driven Flow Control

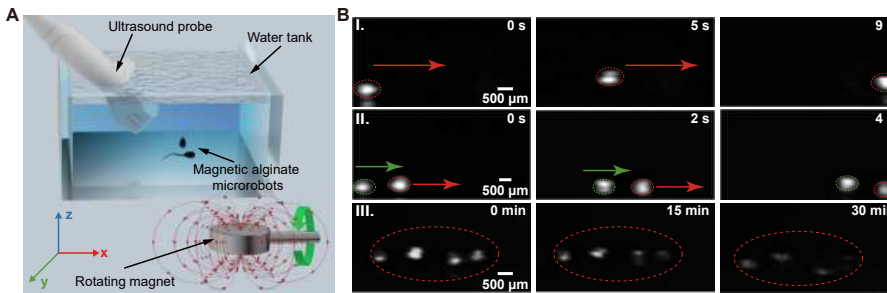


Figure 5.6: Ultrasound imaging of streamlined microrobots. (A) Schematic of the experimental setup for magnetic actuation and ultrasound imaging of streamlined microrobots. (B) Time-lapse ultrasound images show (I) the rolling motion of a single microrobot, (II) the rolling motions of two microrobots, and (III) the degradation of multiple microrobots.

ing system, is illustrated and presented in Figure 5.6(A) and Figure 5.S11.

The locomotion and degradation of the magnetic alginate microrobots were monitored via the US imaging systems (see Movies 5-S3 and 5-S4). In the experiment, these microrobots were placed in a water tank, while the US probe was submerged in the water at an angle of  $45^\circ$  [304]. Notably, the teardrop-like microrobots and the tadpole-like microrobots exhibited rolling motion in the presence of the rotating permanent magnet. The US imaging experiments were conducted on the teardrop-like microrobots fabricated at 1000 rpm using the L-sized nozzle, whose average Feret diameter is  $649 \mu\text{m}$ . The US imaging system was operated at its highest frequency of 14 MHz to enable the highest pixel resolution (see Materials and Methods). Time-lapse sequences of the rolling motions of single and two teardrop-like microrobots are presented in Figures 5.6(B)-I and 5.6(B)-II. Furthermore, the stability and degradation of the magnetic alginate microrobots were validated in the simulated gastric fluid ( $\text{pH} = 1.2$ ) and the phosphate-buffered saline (PBS) solution ( $\text{pH} = 7.4$ ). Figure 5.S12 indicates the microrobots can remain intact within the acid fluid for one day and completely degrade in the PBS in one hour. The degradation of the multiple microrobots was captured by the US imaging system, as shown in Figure 5.6(B)-III. The imaging signal intensity of the microrobots weakens over time, implying their degradation. After 20 min, the weak imaging signal can still be observed. This is because the clusters of magnetic nanoparticles remain

---

adhered to the substrate after the degradation of the alginate hydrogel. The degradation can be attributed to the swelling of the alginate particles in the PBS solution [305], offering the potential to achieve drug release using these alginate microrobots. Moreover, the stability in acidic fluids can ensure the microrobots' integrity when passing through the stomach, making them suitable for use in orally administered pharmaceutical pills [306].

### 5.3 Conclusion

In summary, we present a simple and high-throughput fabrication method for constructing magnetic alginate microrobots, including teardrop-like and tadpole-like microrobots, using a centrifugally driven flow. The dimensions of the teardrop-like microrobots can be adjusted by tuning the nozzle diameters, while the tail lengths of the tadpole-like microrobots vary with the revolution speeds. Our simulation results reveal that the extruded flow velocity varies with the nozzle diameters and revolution speeds, enabling customization of the microrobots' shapes and dimensions. A quantitative analysis of the microrobots' dimensions is thoroughly performed and validated against experimental measurements. Moreover, the teardrop-like and tadpole-like microrobots can exhibit rolling and stick-slip motion by programming the external fields to capitalize on their different morphologies. The dual motion patterns of our microrobots enable them to adapt to different environments, including obstacle crossing and navigation in vertically constrained spaces. Moreover, the tadpole-like microrobots achieve locomotion performance comparable to or better than some of the more complex and costly bioinspired magnetic microrobots. Last, the locomotion and degradation of these microrobots are successfully detected with a clinical US imaging system. The biodegradability of our microrobots opens up possibilities for cargo/drug delivery, as cargo or drugs can be encapsulated within the microrobots during fabrication and released after complete degradation. This feature, combined with their dual-motion patterns and efficient locomotion, positions our microrobots as versatile tools for various biomedical applications.

In addition to alginate sodium, the proposed fabrication method is versatile in material selection. It can employ any monomer that undergoes a sol-gel transition when exposed to liquid crosslinkers. This adaptabil-

## 5. *Magnetic Alginate Microrobots with Dual-Motion Patterns through Centrifugally Driven Flow Control*

---

ity enables the incorporation of specialized functional materials, designed to fulfill the specific functionalities of microrobots. Nevertheless, our current work needs further exploration. While the comparable locomotion efficiency of our microrobots to existing sperm-like and tadpole-like microrobots, our results indicate a low step-out frequency. Given that most previous studies on the wireless actuation of microrobots have been conducted below their step-out frequencies, increasing the step-out frequency of our microrobots is crucial. Strategies to achieve this include increasing the strength of the applied magnetic field, using high-magnetization materials, and modifying the surface wettability of the microrobots. Furthermore, the teardrop and tadpole contours have been known to reduce fluidic drag during translating motion. The motion modes presented in our study do not fully capitalize on this streamlined contour of the microrobots, as the fluid flow does not consistently move smoothly around the streamlined contour during locomotion. This indicates the necessity for additional research to investigate how these streamlined contours can be better utilized to enhance locomotion efficiency or upstream motility. In future research, we can explore these effects by employing the actuation of magnetic force or catalytic reaction to achieve translating motion.

5

### 5.4 Materials and Methods

#### 5.4.1 Preparation and Gelation of Magnetic Alginate Solution

The concentration of 4% w/v sodium alginate solution was prepared using the following procedure. First, 0.6 g Alginic acid sodium salt from brown algae (71238-250G, Sigma-Aldrich, The Netherlands) was dissolved in 15 mL of deionized (DI) water. The mixture was magnetically stirred for 3 hours in an oil bath at a speed of 500 rpm and a temperature of 45°C. Then 0.25 g Fe<sub>3</sub>O<sub>4</sub> (637106-25G, Sigma-Aldrich, The Netherlands) was added to the prepared solution and uniformly dispersed using sonication. The gelation of magnetic alginate solution occurred in 5% w/v CaCl<sub>2</sub> solution, which was prepared by dissolving 2 g of calcium chloride dihydrate (223506-25G, Sigma-Aldrich, The Netherlands) in 40 mL DI water. The contact with CaCl<sub>2</sub> solution was facilitated via centrifugal pumping, where the centrifugal force was provided by a centrifuge (5417 R, Eppendorf, The

Netherlands). In the experiments, the centrifuge's revolution speeds varied from 1000 to 7000 revolutions per minute (rpm). The corresponding relative centrifugal forces (also referred to as G force) for each speed were as follows: 1000 rpm (106 G), 2000 rpm (425 G), 3000 rpm (956 G), 4000 rpm (1699 G), 5000 rpm (2655 G), 6000 rpm (3824 G), and 7000 rpm (2824 G).

### 5.4.2 Viscosity and Oscillatory Shear Rheology Measurement

The dynamic viscosity and oscillatory shear rheology measurement of magnetic alginate solution and hydrogel were performed at room temperature (25 °C) using a rheometer (MCR 92, Anton Paar, The Netherlands) with a parallel-plate geometry (PP25, diameter: 25 mm). Shear rates ranging from 0.01 s<sup>-1</sup> to 1000 s<sup>-1</sup> were applied to the solution, and the rheometer recorded the resulting shear stress. The dynamic viscosities of the solution were calculated through the ratio of shear stress to shear rate. In addition, an oscillatory test was conducted to investigate the viscoelastic behavior of the solution and the hydrogel. Amplitude sweeps were carried out to measure the storage and loss moduli. The shear strain range was set from 0.1% to 1000% for the solution and from 0.01% to 10% for the hydrogel, with an oscillatory frequency of 1 Hz.

### 5.4.3 Pendant Drop Method

The surface tension of the magnetic alginate solution was measured using the pendant drop method. A three-prong clamp secured a syringe filled with the solution to a vertical support rod. A camera (D5600, Nikon Corporation, Japan) with a lens (AF-S 18-140mm, Nikon Corporation, Japan) was utilized to record the deformation of a droplet suspended at the tip of the syringe. The droplet's shape is determined by the balance of the surface tension force and the gravitational force acting on the droplet. The equation that estimates the surface tension  $\sigma$  can be given by,  $\sigma = \frac{\Delta\rho g D_E^2}{H}$ , where  $\Delta\rho$  is the density difference between the magnetic alginate solution and air,  $g$  is the gravitational constant,  $D_E$  is the maximum diameter of the pendant droplet, and  $H$  characterizes the deformation of the droplet due to gravity [307].

#### 5.4.4 SEM Characterization

Prior to SEM characterization, the magnetic alginate microrobots were prepared through fixation, dehydration, and freeze-drying. The fixation was conducted overnight in 2.5% glutaraldehyde solution (diluted in 50% glutaraldehyde solution, 340855-25ML, Sigma-Aldrich, The Netherlands). The microrobots were dehydrated using a series of ethanol gradients (25%, 50%, 75%, 100%) following the fixation. Subsequently, the dehydrated samples were transferred to a freezing dryer with a temperature of  $-108^{\circ}\text{C}$  and a pressure below 5 mPa. The as-prepared samples were mounted in the carbon tape for further SEM observation (Lyra 3 XM, Tescan, Czech Republic). Finally, the microrobots were analyzed using SEM imaging and EDS elemental mapping at an electron beam voltage of 7 KV. To enhance their conductivity, the microrobots were deposited with a 20 nm thick layer of gold.

#### 5.4.5 Experimental Setup

The locomotion test of the magnetic alginate microrobots was carried out in an electromagnetic coil system, which can generate a uniform magnetic field of up to 50 mT at its center. The currents applied to the electromagnetic coils were produced and amplified using the XenusPlus EtherCAT (XE2-230-20, Copley Controls, Canton, USA). This current output system was controlled by a C++—based program. The locomotion of the microrobots was recorded at a rate of 25 frames per second using a microscopic observation setup, which consisted of a charge-coupled device camera (AVA1000-100GM, Basler AG, Ahrensburg, Germany) and an optical microscope with a 2x objective lens. To conduct ultrasound imaging of the microrobots' motion and degradation, the experiment setup was comprised of an ultrasound imaging system (L14-5 scanner, Ultrasonix Medical Corporation, Canada), a water tank including the magnetic microrobots, and a permanent NdFeB magnet. The imaging probe held by a robot arm (Research 3, Franka Emika, Germany) was obliquely submerged into the water tank with an image frequency of 14 MHz and a depth of 1 cm. The permanent magnet was driven by a stepper motor, providing a rotating magnetic field to actuate the microrobots.

### 5.4.6 Finite Element Analysis

Finite element analysis is conducted in COMSOL Multiphysics (version 6.2, COMSOL AB, Sweden) to investigate flow profiles of the microrobots, as well as the formation of teardrop-like and tadpole-like flows. The modules and boundary conditions are indicated below for each simulation result. In Figure 5.2(A), laminar flow, level set, and multiphysics modules were utilized to simulate the formation of teardrop-like and tadpole-like flow. The laminar flow module featured an inlet at the top of the nozzle and an outlet at the bottom of the centrifuge tube. To facilitate the flow extrusion, we introduced a volume force that simulated centrifugal force and varied with revolution speeds. The level set module assigned initial values 1 to the air phase ( $0 < \varphi < 0.5$ ) and initial values 2 to the liquid phase ( $0.5 < \varphi < 1$ ). The initial interface was positioned at the nozzle tip. Within the multiphysics module, the properties (including density and dynamic viscosity) of air and the magnetic alginate solution were specified, and the surface tension coefficient was measured using the pendant drop method. To simulate the extrusion velocities depicted in Figure 5.2(C), the laminar flow module was employed. The inlet was set at the top of the nozzle, and the outlet was positioned at the nozzle tip. As part of the initial boundary conditions, the volume force was introduced to simulate the centrifugal force, which was adjusted according to the revolution speeds. The nozzle model was calibrated to match the actual dimensions of real needles. A laminar flow module was utilized to simulate the flow profiles in Figures 5.5(B), 5.S9(B) and 5.S10. The boundary conditions specified an inlet at the left boundary of the pipe and an outlet at the right boundary, with no inlet flow velocity applied. Moving mesh settings included a deforming domain and prescribed deformation to represent rolling and stick-slip motions. For the rolling motion, the angle  $\alpha$  between the major axis along the Feret diameter and  $\mathbf{x}$  axis varied as  $\alpha = 2\pi ft$ , where  $f$  represented the rotating frequency. The stick-slip motion involved an oscillating pattern, with the angle  $\alpha$  varying as  $\alpha = A * \sin(2\pi ft)$ , where  $f$  was the oscillating frequency and  $A$  was the maximum oscillating angle. To implement these motion patterns, we prescribed the deformation using the equation  $dx = ((\cos \alpha - 1) * X + (-\sin \alpha) * Y, \sin \alpha * X + (\cos \alpha - 1) * Y)^T$ , where  $(X, Y)$  represents the coordinates of the microrobots at the previous time instant.

# 5. Magnetic Alginate Microrobots with Dual-Motion Patterns through Centrifugally Driven Flow Control

## 5.5 Supplementary Figures

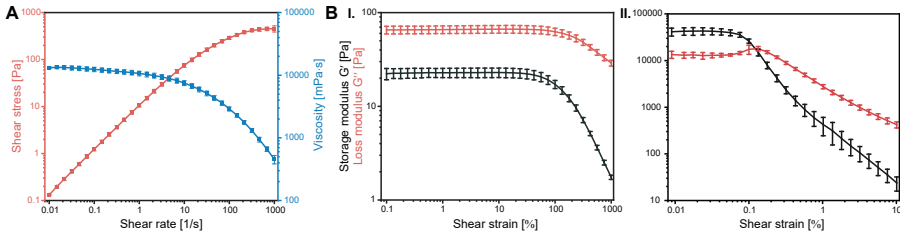


Figure 5.S1: Rheological behavior of the magnetic alginate solution and hydrogel, including (A) the viscosity of the magnetic alginate solution, and (B) the viscoelastic behavior of (I) the magnetic alginate solution and (II) hydrogel.

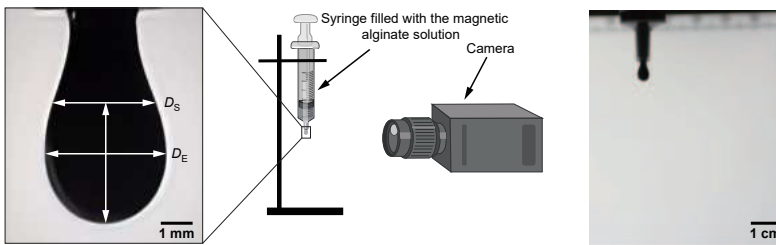


Figure 5.S2: Setup for measuring the surface tension of the magnetic alginate solution. The captured image at the right shows a hung droplet at the tip of a syringe, while the left image zooms in the droplet.  $D_E$  is the maximum diameter of the pendant droplet, and  $D_S$  is the diameter of the droplet at a distance equal to  $D_E$  from the bottom of the droplet.

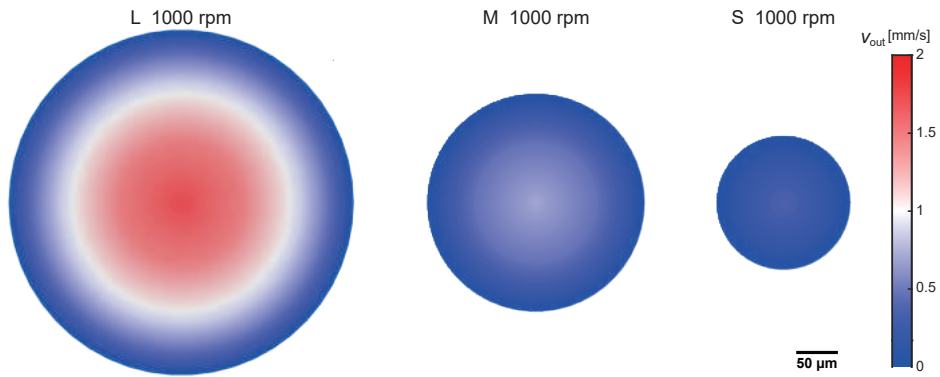


Figure 5.S3: Simulation results of the extrusion velocity  $V_{out}$  from the tip of the L-, M-, and S-sized nozzles at 1000 rpm. The L-, M-, and S-sized nozzles refer to the 22-, 26-, and 30-gauge needles, respectively, with the diameters of 413  $\mu\text{m}$ , 260  $\mu\text{m}$ , and 159  $\mu\text{m}$ .



Figure 5.S4: Zoomed-in scanning electron microscopy (SEM) image on the tail of a tadpole-like microrobot and energy-dispersive X-ray spectroscopy (EDS) elemental mapping images of Na and Ca.

## 5. Magnetic Alginate Microrobots with Dual-Motion Patterns through Centrifugally Driven Flow Control

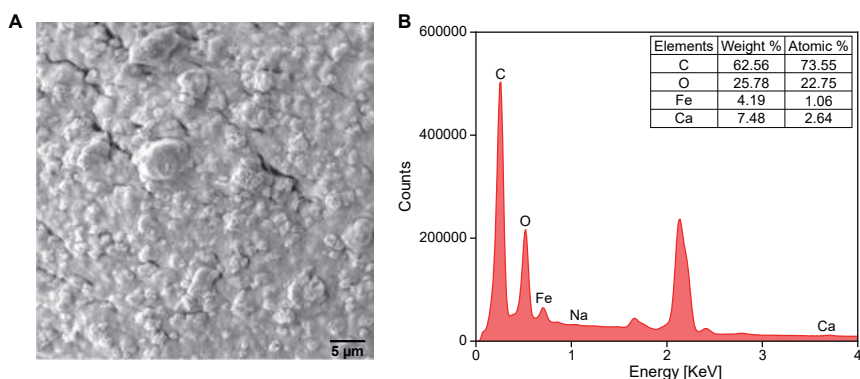


Figure 5.S5: Characterization of the magnetic alginate microrobot. (A) Enlarged SEM image shows the surface morphology of the microrobot. (B) EDS spectra and elemental analysis of the microrobot.

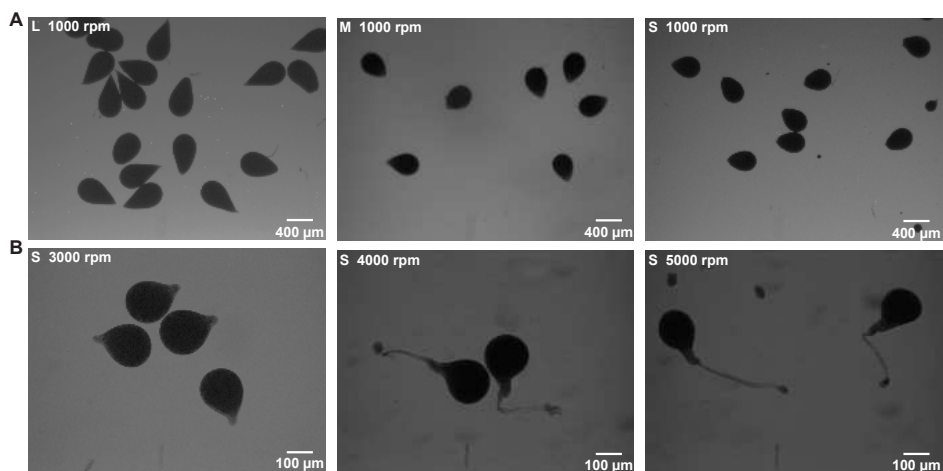


Figure 5.S6: Micrographs of (A) teardrop-like microrobots fabricated using the L-, M-, and S-sized nozzles at 1000 rpm, and (B) tadpole-like microrobots fabricated using the S-sized nozzle at increasing revolution speeds (including 3000 rpm, 4000 rpm, and 5000 rpm). The left corner denotes the experimental conditions for the magnetic alginate microrobots, including the nozzle dimension and the revolution speed.

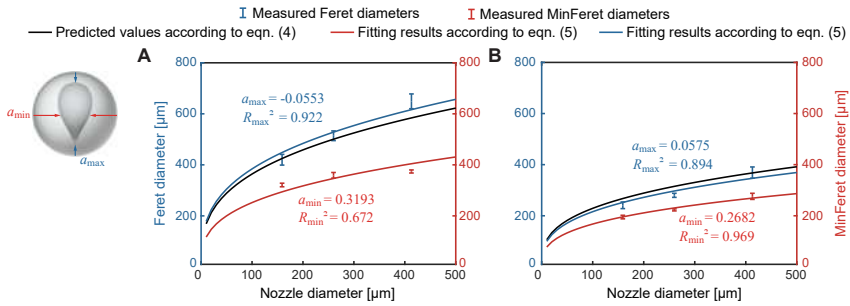


Figure 5.S7: The relationship between the nozzle diameter and the Feret diameters, the MinFeret diameters of the magnetic alginate microrobots. The data are measured from the microrobots fabricated at (A) 1000 rpm and (B) 2000 rpm using the S-, M-, and L-sized nozzles.

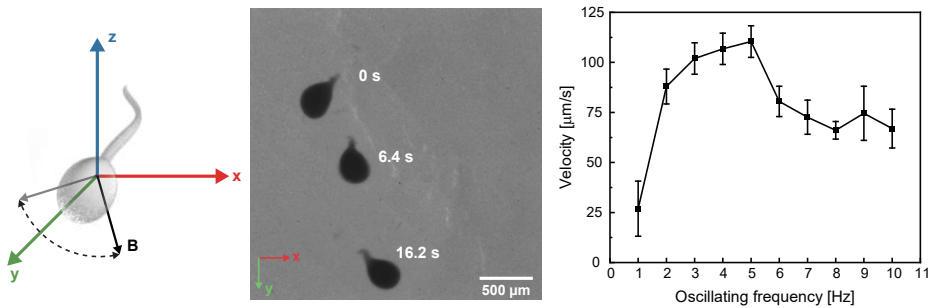


Figure 5.S8: Swimming test of the tadpole-like microrobots under an oscillating field within the  $XOY$  plane. Time-lapse micrograph of the tadpole-like microrobot's swimming motion. Swimming velocity of the microrobot versus frequency is plotted.

## 5. Magnetic Alginate Microrobots with Dual-Motion Patterns through Centrifugally Driven Flow Control

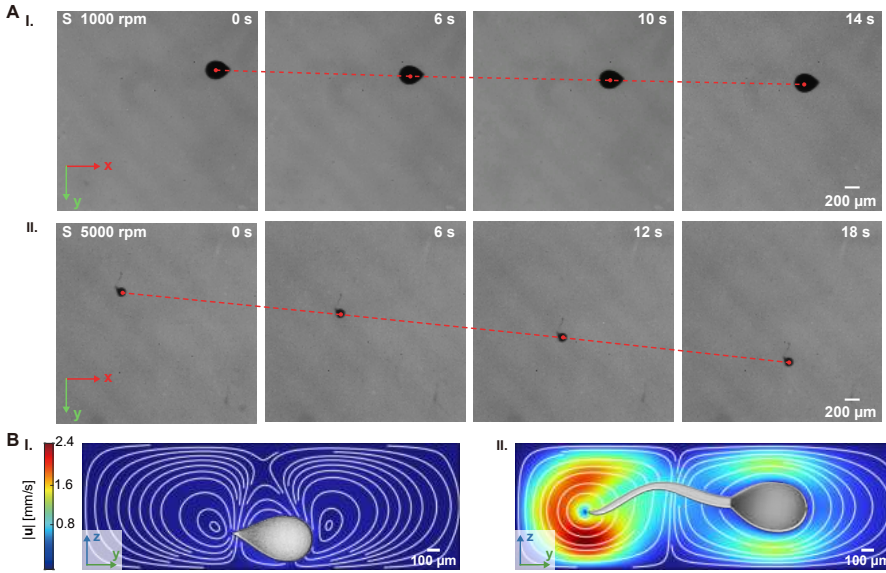


Figure 5.S9: Comparison of stick-slip motion between the teardrop-like and tadpole-like microrobots. (A) Time-lapse micrographs of (I) the teardrop-like and (II) the tadpole-like microrobots' stick-slip motion. (B) Simulated fluid distribution around (I) the teardrop-like and (II) the tadpole-like microrobots during stick-slip motion.

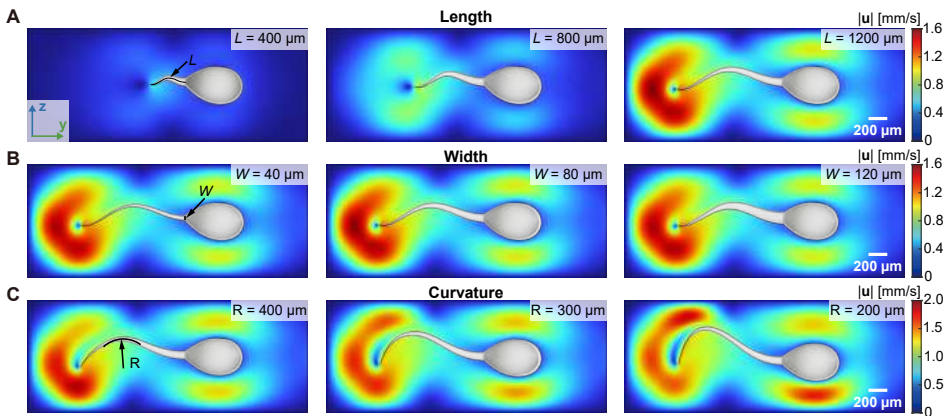


Figure 5.S10: Simulated fluid distribution around the tadpole-like microrobots with varying (A) tail lengths, (B) widths, and (C) curvatures during the stick-slip motion.

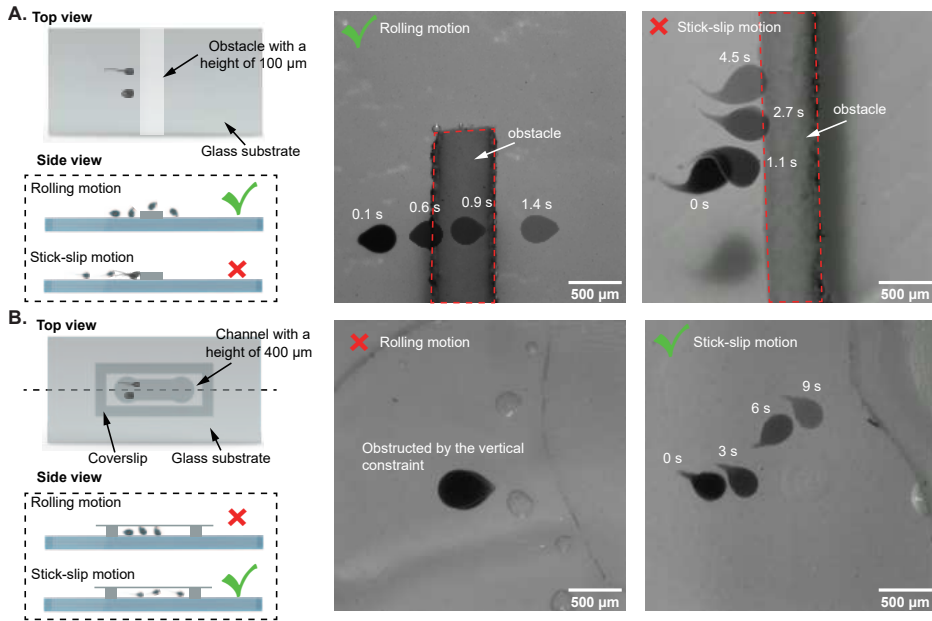


Figure 5.S11: Dual-motion patterns in different environments. (A) Locomotion of microrobots over a 100  $\mu\text{m}$  high obstacle: Time-lapse micrographs show the locomotion of microrobots as they encounter the obstacle. The teardrop-like microrobot utilizes rolling motion to successfully climb over the obstacle, while the tadpole-like microrobot, employing stick-slip motion, is unable to cross. (B) Locomotion of the microrobots in a vertically limited channel. Time-lapse micrographs depict the microrobots moving within a channel that has a height of 400  $\mu\text{m}$ , fabricated by laser cutting a 400  $\mu\text{m}$  thick acrylic plate. The teardrop-like microrobot with the rolling motion is obstructed by the vertical constraint of the channel, while the tadpole-like microrobot with the stick-slip motion can pass through the channel.

## 5. *Magnetic Alginate Microrobots with Dual-Motion Patterns through Centrifugally Driven Flow Control*

---

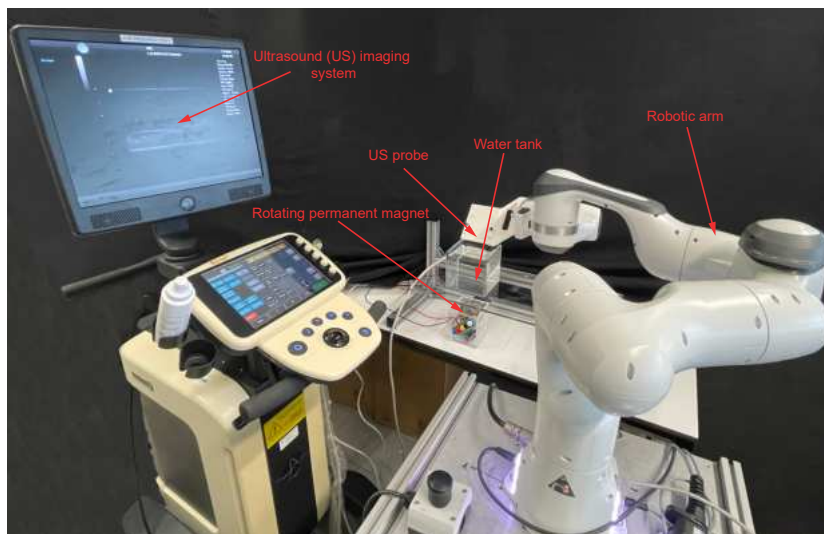


Figure 5.S12: Experimental setup for ultrasound imaging of magnetic alginate microrobots actuated by a rotating permanent magnet.

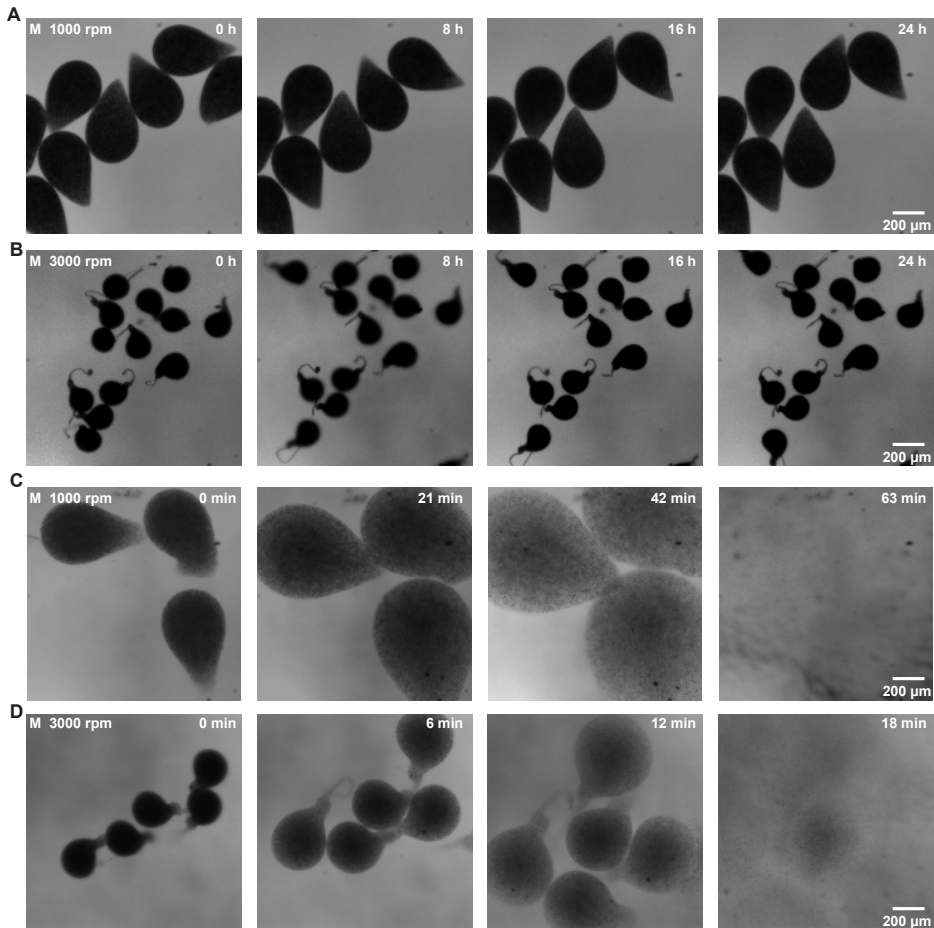


Figure 5.S13: Stability and degradation of magnetic alginate microrobots. Time-lapse micrographs show (A) teardrop-like microrobots in simulated gastric fluid (pH = 1.2), (B) tadpole-like microrobots in the same simulated gastric fluid, (C) teardrop-like microrobots in phosphate-buffer saline (PBS, pH = 7.4), and (D) tadpole-like microrobots in the same PBS.

## 5. *Magnetic Alginate Microrobots with Dual-Motion Patterns through Centrifugally Driven Flow Control*

---

### 5.6 Supplementary Tables

Table 5.S1: Yield per minute of magnetic alginate microrobots under different experimental conditions.

Nozzle diameters [ $\mu\text{m}$ ]	Revolution speeds [rpm]				
	1000	2000	3000	4000	5000
159	$\approx 5$	90-150	1000-1250	4200-5200	9000-12000
260	15-20	450-650	2550-2900	7200-9000	None
413	90-110	1250-2200	None	None	None

Table 5.S2: The comparison of magnetic microrobots inspired by sperm, fish, and tadpoles.

Inspired by	Fabrication methods	Step-out frequency [Hz]	Maximum velocity [ $\mu\text{m}$ ]	Types of motion	Locomotion efficiency [body lengths/s]	Reference
Tadpole	Centrifugally driven flow	4-5	346	Stick-slip	0.42	This chapter
		5	110.4	Swimming	0.13	
	Magnetically assisted in situ polymerization	3-5	5.9	Swimming	0.18-0.20	[279]
	Melt electrospinning writing	Unspecified	340.4	Stick-slip	1.23	[308]
Sperm	Photolithography + lift-off	45	158	Swimming	0.49	[43]
	Electrospinning	2	18.9	Swimming	0.05	[309]
	Vortex turbulence-assisted microfluidic	1	8.8	Swimming	0.07-0.11	[280]
	Electrostatic self-assembly + biotemplate	8	6.8	Swimming	0.10	[110]
	Electrodeposition technique + biotemplate	20	3	Swimming	0.25	[244]
Fish	Electrodeposition technique + sputter	11	30.9	Swimming	6.44	[81]
	Mold thermoforming	45	1200	Swinging at liquid surface	1.41	[310]

## 5.7 Supplementary Movies

### **Movie 5-S1. Rolling motion of the teardrop-like microrobot, stick-slip motion, and swimming motion of the tadpole-like microrobots**

This video showcases the rolling motion of a teardrop-like microrobot in a rotating magnetic field about  $y$  axis at a frequency of 3 Hz, the stick-slip motion of a tadpole-like microrobot in an oscillating magnetic field along  $y$  axis at the same frequency within  $YOZ$  plane, and the swimming motion in an oscillating magnetic field along  $y$  axis at a frequency of 2 Hz in  $XOY$  plane.

### **Movie 5-S2. Dual-motion patterns in different environments**

This video demonstrates two distinct motion capabilities of our proposed microrobots as they overcome obstacles and navigate within a vertically constrained channel. We evaluate the teardrop-like microrobot's rolling motion and the tadpole-like microrobot's stick-slip motion in these different environments.

### **Movie 5-S3. Ultrasound imaging of single and two teardrop-like microrobots' rolling motions**

This video shows the ultrasound imaging of rolling teardrop-like microrobots under a rotating permanent magnet. The ultrasound probe is employed to scan the cross-section of the microrobot within a water tank. The ultrasound system is configured in B-mode to display a sequence of rapidly acquired images at a frame rate of 32 frames per second. The gain of the ultrasound system is consistently set to 56%, and the ultrasound waves' frequency is maintained at 14 MHz for all trials.

### **Movie 5-S4. Ultrasound imaging of multiple teardrop-like microrobots' degradation**

This sped-up video shows the ultrasound imaging of teardrop-like microrobots as they degraded in phosphate-buffer saline (PBS, pH = 7.4). The complete degradation process spans approximately 20 min.

# 6

## Conclusions

This doctoral thesis focuses on the fabrication, modeling, and actuation of soft bioinspired microrobots. **Chapter 1** outlines the evolution of microrobots and explains the rationale behind bioinspired microrobots. **Chapter 2** presents an overview of soft bioinspired microrobots, elaborating on their design principles, energy sources, and biomedical applications. The following chapters present studies on both biological organisms and synthetic microrobots. **Chapter 3** establishes a theoretical framework to study the flagellar propulsion of natural sperm cells under external disturbances. This study provides valuable insights into enhancing the adaptability of soft bioinspired microrobots to intricate environments. The capacity of these microrobots to overcome disturbance forces is limited by their locomotion capability, which is directly related to the step-out frequency. Following this, **Chapter 4** theoretically and experimentally studies the step-out frequency of electrospun sperm-like microrobots by combining the established model for magnetism and the elasto-hydrodynamic model developed in the previous chapter. To facilitate the practical deployment of soft microrobotic systems, **Chapter 5** introduces a novel and facile fabrication method to create magnetic alginate microrobots, including teardrop-shaped and tadpole-shaped designs. This chapter demonstrates fine control over the shapes and dimensions of these microrobots and showcases their dual-motion patterns, ultrasound imaging capabilities, and biodegradability. These findings highlight the potential of our proposed microrobots to be integrated into microrobotic systems intended for biomedical applications. Finally, **Chapter 6** summarizes the research findings on biological

## 6. Conclusions

---

organisms and synthetic microrobots from this doctoral study, and offers insights into the future development of soft bioinspired microrobots, with the anticipation of advancing them toward clinical trials.

### 6.1 Biological Organisms

Sperm cells are able to move forward by undulating their soft and flexible flagellum. This characteristic captivates the interest of both biologists and engineers, leading to the invention of soft bioinspired microrobots. Before creating these microrobots, it is imperative to understand the locomotion mechanism and adaptability of sperm cells in complex environments. In **Chapter 3**, the elasto-hydrodynamic model is developed to study the interactions of sperm cells with an external force. To validate the proposed model, we design the experiments on the flagellar propulsion of collinear bundles. These bundles consist of two sperm cells in opposite orientations via the head-to-head attachment. In this configuration, one cell, with its head oriented opposite to the direction of the bundle's movement, exerts a time-periodic force on the other cell. This disturbance force arises from the steric and adhesive interactions at the head-to-head attachment. Although the formation of the collinear bundle is not observed during our experiments, our proposed model indicates that two cells will assemble into such a collinear bundle when the steric interaction dominates. By analyzing the flagellar propulsion of each cell within the collinear bundle, we find that they display wave patterns with smaller mean flagellar curvature and bending amplitude compared to free sperm cells. Our proposed model offers a numerical analysis of the flagellar propulsion of sperm cells during cell-to-cell interaction, which qualitatively aligns with our experimental findings. This model also complements the conclusions drawn from these findings. Specifically, when the initial phase of the propagating wave exceeds  $90^\circ$ , the mean flagellar curvature decreases, yet the bending amplitude increases upon forming the collinear bundle. The model also explores the impact of the flagellum's elastic sliding resistance, despite the difficulty of controlling this variable in the biological organisms. This study provides valuable insights into the flagellar propulsion of sperm cells in response to external interactions. These insights are crucial for advancing the design and fabrication of soft bioinspired microrobots in scenarios of complex environments.

## 6.2 Synthetic Microrobots

The ability to move in low-Reynold-numbers regimes necessitates breaking the time-reversible constraint of Stokes flows. Sperm cells achieve propulsion through their soft and flexible flagellum, which operates via the orchestrated actions of nexin links and dynein motors within the flagellar microtubule. These components work in synergy to undulate the flagellum, thus propelling the cell forward. To replicate this flagellar propulsion in synthetic microrobots, the selection of soft materials is critical. In **Chapter 4**, we investigate the flagellar propulsion of sperm-like microrobots constructed from polystyrene, and in **Chapter 5**, we test the locomotion efficiency of tadpole-like microrobots made from sodium alginate. When a magnetic torque is applied to the head of these microrobots, the oscillation in the head leads to tail deformation, thereby mimicking the flagellar undulation of sperm cells to achieve propulsion.

External magnetic fields provide the power sources for soft bioinspired microrobots. They are the most promising actuation method for *in vivo* application of microrobots due to their real-time properties, nontoxic, and deep penetration. Magnetic dipole moments are induced in the magnetic microrobots when exposed to external magnetic fields. The resulting magnetic torque influences the locomotion performance of the microrobots. **Chapter 4** explores the step-out frequencies of electrospun sperm-like microrobots. We modify the elasto-hydrodynamic model developed in sperm cells by including this magnetic torque. In this chapter, we propose an analytic model for determining the step-out frequency of magnetically actuated sperm-like microrobots. The proposed model enhances our understanding of the relationship between the step-out frequency and various factors, such as the microrobot's geometry, magnetization, wave patterns, and the viscosity of the surrounding medium. The magnetically actuated sperm-like microrobots are fabricated using electrospinning and ultrasonic cutting methods. Subsequently, we assess their swimming performance in an oscillating magnetic field. The experimental results not only validate the accuracy of our proposed analytic model for the step-out frequency but also reveal the independence of wave patterns from the actuation frequency of the oscillating field, in contrast to sperm cells. This distinct behavior allows our analytic model to accurately predict the step-out frequency of the sperm-like microrobot by evaluating the observed wave patterns at any

## 6. Conclusions

---

frequency below the step-out threshold. By accurately predicting the step-out frequency, the proposed model lays a foundation for enhancing the locomotion capability of soft bioinspired microrobots.

The efficient locomotion of soft microrobots enables them to perform biomedical tasks at specific locations. However, the costly and tedious fabrication methods limit their widespread applications. In **Chapter 5**, we propose a novel and facile method to fabricate magnetic alginate microrobots, including teardrop and tadpole designs, in a controllable manner. This fabrication method is based on centrifugally driven flow, which can be controlled by adjusting the nozzle size and revolution speed. Our simulation indicates that the variation in the extruded flow velocity allows for the tailored design of the microrobots' shapes. The dimensions of the microrobots are quantified by an analytic equation, which has been validated against experimental measurements. Based on the morphology of the alginate microrobots, the teardrop-like and the tadpole-like designs are intended to exhibit rolling and stick-slip motion, respectively. Although the rolling motion is more efficient, it has a limitation in passing through a vertically constrained channel, as it exhibits a full rotation. On the contrary, the stick-slip motion does not undergo an entire rotation, enabling the tadpole-like microrobots to pass through the vertically constrained channel. The dual-motion capability of magnetic alginate microrobots verifies their locomotion capabilities and demonstrates their potential to perform different tasks. Last, ultrasound imaging can show the potential of our proposed microrobots in clinical trials, as they can be monitored by clinical medical imaging equipment. These demonstrations substantiate the feasibility of our microrobots as viable candidates for microrobotic systems intended for biomedical applications.

6

### 6.3 Outlook

This doctoral thesis outlines fabrication, actuation, and modeling for soft bioinspired microrobots. These findings enhance our understanding of soft bioinspired microrobots and facilitate the “fantastic voyage” of microrobots. Before these microrobots can be applied to the human body, it is essential to address several challenges. Future research should focus on three main areas: designing soft bioinspired microrobots with stimuli-responsive capability, optimizing actuation, and addressing challenges for

---

clinical translation (Figure 6.1). In the following sections, I will elaborate on these perspectives and share my humble insights into each aspect.

### 6.3.1 Stimuli-Responsive Capability

Soft bioinspired microrobots are designed to mimic the behavioral sophistication of microorganisms or cells, primarily on their locomotion. These biological organisms provide an effective means for achieving movement in low Reynolds-number fluids, where reciprocal propulsion schemes are ineffective. The replication of organisms' structure and locomotion has been a central area of investigation over the past few decades. However, mere imitation can not fulfill the demands of microrobots with complex functionalities. Sperm-like or tadpole-like microrobots may share morphological similarities with their biological counterparts, but they lack functional capabilities inherent to these microorganisms or cells. These capabilities allow biological organisms to respond to environmental stimuli, which guides their navigation. As a result, biological organisms serve as attractive natural templates for designing advanced microrobotic systems. For example, *Magnetococcus marinus* MC-1 cells utilize geomagnetic-assisted aerotaxis to navigate toward low-oxygen regions in the oxic-anoxic transition zone. This capability has inspired researchers to engineer these bacteria to transport drug-loaded nanoliposomes into hypoxic tumor areas, showcasing an efficient method for targeted drug delivery [157]. Likewise, chemotaxis and thermotaxis of sperm cells enable them to find the oocyte for fertilization. By modifying sperm cells and leveraging their natural chemotaxis, sperm microrobots can navigate toward human ovarian cancer cells in vitro [109].

To replicate the stimuli-responsive capability in synthetic microrobots, it is essential to integrate advanced sensors into their design. Antibodies are considered ideal sensors because they specifically bind to antigens, offering high selectivity and sensitivity for target detection. Enzymes are another promising sensor by acting as biological catalysts with high specificity. Additionally, functional nucleic acids, such as DNA/RNA and nucleic acid enzymes, provide alternatives to antibodies by binding to a specific target. Beyond these biological recognition elements, polymers or supramolecules can be synthesized to respond to environmental changes, such as pH, temperature, and chemicals. With these sensors integrated, synthetic microrobots can be directed toward a target location that emits a stimulus. For

## 6. Conclusions

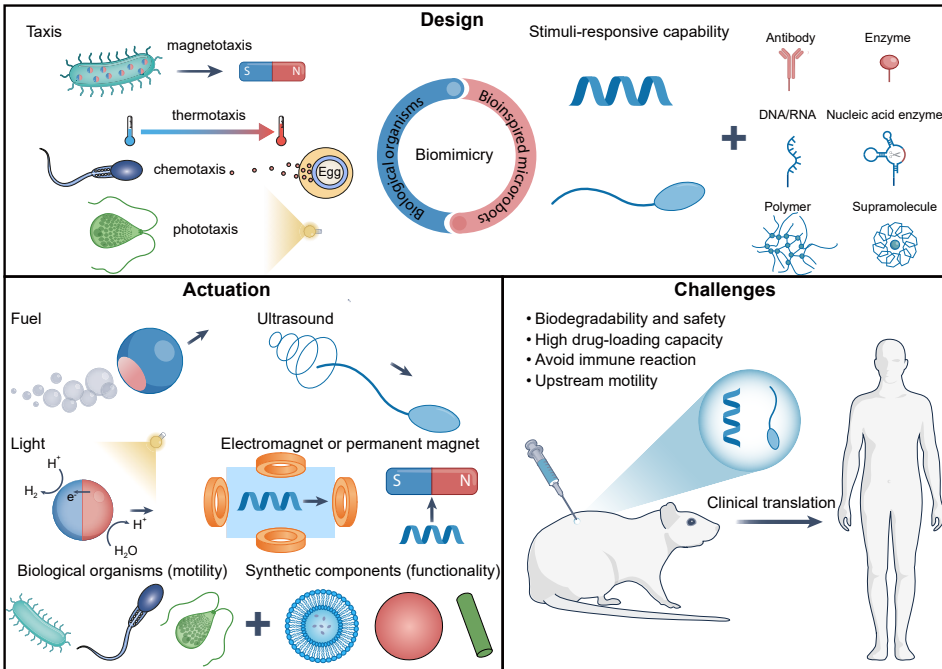


Figure 6.1: Future considerations for design, actuation, and clinical challenges of bioinspired microrobots. Top depicts the navigational strategies of biological organisms, including magnetotaxis, thermotaxis, chemotaxis, and phototaxis. These strategies enable organisms to navigate and adapt effectively to complex environments. To replicate these capabilities, synthetic microrobots can be designed with advanced sensors that respond to environmental stimuli. Bottom left illustrates and compares the actuation mechanisms of fuel-driven, externally powered, and biohybrid microrobots. This comparison aims to identify the optimal actuation method that maximizes the locomotion efficiency of bioinspired microrobots while ensuring their safe operation within the human body. Bottom right outlines the challenges associated with the clinical translation of bioinspired microrobots, with the goal of facilitating the transition from animal studies to human applications.

instance, external magnetic fields guide these microrobots over long distances and allow them to approach their target quickly. Once in proximity, their stimuli-responsive capability takes over the navigation, facilitating their accumulation at the target site. By developing synthetic microrobots that mimic the taxis of biological organisms, researchers can enhance their targeting efficiency within the human body. This improvement in synthetic

---

microrobots offers promising potential for disease treatment and diagnostics.

### 6.3.2 Optimizing Actuation

Synthetic microrobots can be categorized as fuel-driven and externally powered types according to their power sources. Fuel-driven microrobots achieve propulsion by catalyzing fuels such as hydrogen peroxide, urea, and glucose. This catalytic reaction produces bubbles or facilitates self-phoresis, enabling the movement of the microrobots. However, fuel-driven microrobots face limitations in controllability and lifespan. In contrast, externally powered microrobots utilize external energy sources, including ultrasound, light, and magnetic fields, to achieve propulsion. These actuation methods offer enhanced control and extended operational duration over the fuel-driven microrobots. High-frequency sound waves can actuate microrobots owing to the pressure exerted by acoustic radiation. However, its application within the human body is constrained by limited penetration depth. Light-powered microrobots utilize photoactive materials, where photogenerated carriers catalyze photochemical reactions, to generate bubble propulsion or self-phoresis. The primary challenge of light actuation is the attenuation of light intensity with depth and the inefficient self-phoresis observed in bodily fluids with high ion strength. Magnetic actuation stands out from these actuation manners because of its excellent permeability within the human body. Magnetic actuation systems can be divided into permanent magnets and electromagnets. Each type of these systems has unique challenges. Permanent magnet systems are often preferred in medical applications due to their large operational workspace, yet they cannot be turned off during surgical procedures, which can lead to unintended actuation and collisions. Electromagnet-based systems operate on the basic principle of converting electrical current into a magnetic field. The magnetic field can be turned off by ceasing the current supply. However, when used in deep areas of the body, the magnetic field strength falls off rapidly with distance from the source, increasing the control complexity of microrobots.

Given the various challenges experienced by fuel-driven and externally powered microrobots, researchers are increasingly exploring biohybrid microrobots as a promising alternative. The biohybrid microrobots are com-

## 6. Conclusions

---

posed of biological and synthetic components. Common choices for the biological constituents include sperm cells, bacteria, and algae [311]. Since the power for movement is provided by these biological components, the biohybrid microrobots can achieve long-term locomotion. Moreover, the taxis of the biological components allow them to respond to versatile environments and extreme conditions. The integration of synthetic components can offer the biohybrid microrobots unique characteristics, such as magnetic maneuverability, drug loading and controlled release, fluorescence imaging, and photothermal therapy. The development of biohybrid microrobots is still in its infancy, further in-depth research is essential to explore their potential for widespread use in biomedical applications [312].

### 6.3.3 Challenges for Clinical Translation

Most efforts have been devoted to proof-of-concept studies of microrobots, for instance, developing new fabrication methods, proposing advanced control algorithms, and introducing microrobots with innovative designs. Although these studies are necessary for the early-stage development of microrobots, the ultimate goal is to bring them to clinical trials. To achieve this goal, research on microrobots should focus on addressing practical challenges in clinical settings.

Given that microrobots should be safely removed from the human body after performing biomedical tasks, developing microrobots with biodegradable and biocompatible materials is necessary. This prevents the accumulation of microrobots in the body and reduces the risk of embolisms. As a multidisciplinary field, we can leverage mature technologies from various domains to develop microrobots. For instance, integrating commercially available materials approved by the Food and Drug Administration into microrobotic systems can ensure not only biodegradability but also biocompatibility and safety. By utilizing these well-established technologies, the translation of microrobots from laboratory research to clinical applications can be significantly accelerated.

Additionally, microrobots should be tailored to address limitations in conventional treatment methods. Traditional therapies often rely on passive diffusion and blood circulation for drug delivery, thus limiting the amount of drug-carrying nanoparticles that reach tumor lesions (only  $\approx 0.7\%$  of nanoparticles reach the tumors via the systemic intravenous injection).

tion ). In contrast, drug-carrying microrobots can be controlled to reach tumor lesions under external fields, enhancing the targeting efficiency of drugs. Numerous studies on drug delivery using microrobots have been conducted both *in vivo* and *in vitro* to demonstrate their feasibility in treatment. By enhancing drug targeting efficiency, microrobots can increase the success rate of treating tumor cells while mitigating side effects on healthy cells, leading to more effective and safer cancer therapies. However, the size of microrobots may limit the volume of drugs they can carry. The influence of the microrobot's size and geometry on the overall effectiveness of cancer treatment needs further investigation.

Another challenge in the clinical translation arises after microrobots are injected into the human body. Typically, intravenous injection is the preferred method for administering these microrobots systemically. However, once microrobots enter the blood vessels, the immune systems immediately detect and clear them, rendering them ineffective for biomedical applications. Moreover, high blood flow, ranging from 0.5-400 mm/s, poses significant resistance to the navigation of these microrobots. Currently, the maximum flow velocity that existing microrobots can overcome is only 100 mm/s, which is insufficient for navigating larger blood vessels such aorta and arteriole [313]. Therefore, the future development of microrobots should address the challenges posed by fast blood flow and the immune system within the human body.

In summary, the successful clinical translation of microrobots must overcome several critical challenges. These include ensuring the microrobot's safety and biodegradability in the body, enhancing the targeting efficiency of drug delivery, and addressing the physiological obstacles posed by fast blood flow and the immune system. Furthermore, the development of medical microrobots needs to incorporate insights from clinicians, as their expertise can guide the customization of microrobots to meet the specific demands of surgical procedures. By tackling technical challenges and clinical needs, the medical applications of microrobots as envisioned in science fiction movies will come into reality.



## Bibliography

- [1] R. P. Feynman, “There’s plenty of room at the bottom,” *Journal of Microelectromechanical Systems*, vol. 1, no. 1, pp. 60–66, 1992.
- [2] S. David and R. Fleischer, “Fantastic voyage,” 20th Century Fox, 1966.
- [3] M. Finnell and J. Dante, “Innerspace,” Amblin Entertainment, 1987.
- [4] S. DiMaio, M. Hanuschik, and U. Kreaden, “The da vinci surgical system,” in *Surgical Robotics: Systems Applications and Visions*. Boston, MA: Springer US, 2011, pp. 199–217.
- [5] B. J. Nelson, I. K. Kaliakatsos, and J. J. Abbott, “Microrobots for minimally invasive medicine,” *Annual Review of Biomedical Engineering*, vol. 12, no. 1, pp. 55–85, 2010.
- [6] V. Iacovacci, E. Diller, D. Ahmed, and A. Menciassi, “Medical microrobots,” *Annual Review of Biomedical Engineering*, vol. 26, pp. 561–591, 2024.
- [7] A. Kheyrradini Mousavi and Z. C. Leseman, “Basic mems actuators,” in *Encyclopedia of Nanotechnology*. Springer Netherlands, 2012, pp. 173–185.
- [8] K. B. Yesin, K. Vollmers, and B. J. Nelson, “Modeling and control of untethered biomicrobots in a fluidic environment using electromagnetic fields,” *The International Journal of Robotics Research*, vol. 25, no. 5-6, pp. 527–536, 2006.
- [9] Z. Nagy, O. Ergeneman, J. J. Abbott, M. Hutter, A. M. Hirt, and B. J. Nelson, “Modeling assembled-mems microrobots for wireless magnetic control,” in *2008 IEEE International Conference on Robotics and Automation*, 2008, pp. 874–879.
- [10] J. J. Abbott, Z. Nagy, F. Beyeler, and B. J. Nelson, “Robotics in the small, part i: Microbotics,” *IEEE Robotics & Automation Magazine*, vol. 14, no. 2, pp. 92–103, 2007.

- [11] M. Wautelet, “Scaling laws in the macro-, micro- and nanoworlds,” *European Journal of Physics*, vol. 22, no. 6, pp. 601, 2001.
- [12] I. S. M. Khalil, A. Klingner, and S. Misra, *Mathematical modeling of swimming soft microrobots*. Academic Press, 2021.
- [13] E. M. Purcell, “Life at low Reynolds number,” *American Journal of Physics*, vol. 45, no. 1, pp. 3–11, 1977.
- [14] C. Chen, S. Ding, and J. Wang, “Materials consideration for the design, fabrication and operation of microscale robots,” *Nature Reviews Materials*, vol. 9, no. 3, pp. 159–172, 2024.
- [15] J. J. Abbott, K. E. Peyer, M. C. Lagomarsino, L. Zhang, L. Dong, I. K. Kaliakatsos, and B. J. Nelson, “How should microrobots swim?” *The International Journal of Robotics Research*, vol. 28, no. 11-12, pp. 1434–1447, 2009.
- [16] E. Lauga, *The Fluid Dynamics of Cell Motility*. Cambridge University Press, 2020.
- [17] R. Pramanik, R. W. C. P. Verstappen, and P. R. Onck, “Nature-inspired miniaturized magnetic soft robotic swimmers,” *Applied Physics Reviews*, vol. 11, no. 2, pp. 021312, 2024.
- [18] N. Wadhwa and H. C. Berg, “Bacterial motility: machinery and mechanisms,” *Nature Reviews Microbiology*, vol. 20, no. 3, pp. 161–173, 2022.
- [19] R. E. Goldstein, “Green algae as model organisms for biological fluid dynamics,” *Annual Review of Fluid Mechanics*, vol. 47, no. Volume 47, 2015, pp. 343–375, 2015.
- [20] E. Gaffney, H. Gadêlha, D. Smith, J. Blake, and J. Kirkman-Brown, “Mammalian sperm motility: Observation and theory,” *Annual Review of Fluid Mechanics*, vol. 43, pp. 501–528, 2011.
- [21] L. Zhang, J. J. Abbott, L. Dong, B. E. Kratochvil, D. Bell, and B. J. Nelson, “Artificial bacterial flagella: Fabrication and magnetic control,” *Applied Physics Letters*, vol. 94, no. 6, pp. 064107, 2009.

- 
- [22] K. Han, C. W. Shields IV, and O. D. Velev, "Engineering of self-propelling microbots and microdevices powered by magnetic and electric fields," *Advanced Functional Materials*, vol. 28, no. 25, pp. 1705953, 2018.
- [23] F. Qiu, L. Zhang, K. E. Peyer, M. Casarosa, A. Franco-Obregón, H. Choi, and B. J. Nelson, "Noncytotoxic artificial bacterial flagella fabricated from biocompatible ormocomp and iron coating," *Journal of Materials Chemistry B*, vol. 2, no. 4, pp. 357–362, 2014.
- [24] J. Li, S. Sattayasamitsathit, R. Dong, W. Gao, R. Tam, X. Feng, S. Ai, and J. Wang, "Template electrosynthesis of tailored-made helical nanoswimmers," *Nanoscale*, vol. 6, no. 16, pp. 9415–9420, 2014.
- [25] Y. Yu, L. Shang, W. Gao, Z. Zhao, H. Wang, and Y. Zhao, "Microfluidic lithography of bioinspired helical micromotors," *Angewandte Chemie International Edition*, vol. 56, no. 40, pp. 12 127–12 131, 2017.
- [26] X. Yan, Q. Zhou, M. Vincent, Y. Deng, J. Yu, J. Xu, T. Xu, T. Tang, L. Bian, Y.-X. J. Wang, K. Kostarelos, and L. Zhang, "Multifunctional biohybrid magnetite microrobots for imaging-guided therapy," *Science Robotics*, vol. 2, no. 12, pp. eaaq1155, 2017.
- [27] A. Ghosh and P. Fischer, "Controlled propulsion of artificial magnetic nanostructured propellers," *Nano Letters*, vol. 9, no. 6, pp. 2243–2245, 2009.
- [28] D. Walker, B. T. Käsdorf, H.-H. Jeong, O. Lieleg, and P. Fischer, "Enzymatically active biomimetic micropropellers for the penetration of mucin gels," *Science Advances*, vol. 1, no. 11, pp. e1500501, 2015.
- [29] S. Tottori, L. Zhang, F. Qiu, K. K. Krawczyk, A. Franco-Obregón, and B. J. Nelson, "Magnetic helical micromachines: Fabrication, controlled swimming, and cargo transport," *Advanced Materials*, vol. 24, no. 6, pp. 811–816, 2012.
- [30] M. Medina-Sánchez, L. Schwarz, A. K. Meyer, F. Hebenstreit, and O. G. Schmidt, "Cellular cargo delivery: Toward assisted fertilization
-

- by sperm-carrying micromotors,” *Nano Letters*, vol. 16, no. 1, pp. 555–561, 2016.
- [31] M. A. Zeeshan, R. Grisch, E. Pellicer, K. M. Sivaraman, K. E. Peyer, J. Sort, B. Özkale, M. S. Sakar, B. J. Nelson, and S. Pané, “Hybrid helical magnetic microrobots obtained by 3d template-assisted electrodeposition,” *Small*, vol. 10, no. 7, pp. 1284–1288, 2014.
- [32] W. Gao, X. Feng, A. Pei, C. R. Kane, R. Tam, C. Hennessy, and J. Wang, “Bioinspired helical microswimmers based on vascular plants,” *Nano Letters*, vol. 14, no. 1, pp. 305–310, 2014.
- [33] V. de la Asunción-Nadal, C. Franco, A. Veciana, S. Ning, A. Terzopoulou, S. Sevim, X.-Z. Chen, D. Gong, J. Cai, P. D. Wendel-Garcia, B. Jurado-Sánchez, A. Escarpa, J. Puigmartí-Luis, and S. Pané, “Mosbots: Magnetically driven biotemplated mos2-based microrobots for biomedical applications,” *Small*, vol. 18, no. 33, pp. 2203821, 2022.
- [34] T.-Y. Huang, M. S. Sakar, A. Mao, A. J. Petruska, F. Qiu, X.-B. Chen, S. Kennedy, D. Mooney, and B. J. Nelson, “3d printed microtransporters: Compound micromachines for spatiotemporally controlled delivery of therapeutic agents,” *Advanced Materials*, vol. 27, no. 42, pp. 6644–6650, 2015.
- [35] X. Yan, Q. Zhou, J. Yu, T. Xu, Y. Deng, T. Tang, Q. Feng, L. Bian, Y. Zhang, A. Ferreira, and L. Zhang, “Magnetite nanostructured porous hollow helical microswimmers for targeted delivery,” *Advanced Functional Materials*, vol. 25, no. 33, pp. 5333–5342, 2015.
- [36] H. Lee, D.-i. Kim, S.-h. Kwon, and S. Park, “Magnetically actuated drug delivery helical microrobot with magnetic nanoparticle retrieval ability,” *ACS Applied Materials & Interfaces*, vol. 13, no. 17, pp. 19 633–19 647, 2021.
- [37] F. Qiu, S. Fujita, R. Mhanna, L. Zhang, B. R. Simona, and B. J. Nelson, “Magnetic helical microswimmers functionalized with lipoplexes for targeted gene delivery,” *Advanced Functional Materials*, vol. 25, no. 11, pp. 1666–1671, 2015.

- [38] Y. Dong, L. Wang, Z. Zhang, F. Ji, T. K. Chan, H. Yang, C. P. Chan, Z. Yang, Z. Chen, W. T. Chang, J. Y. K. Chan, J. J. Y. Sung, and L. Zhang, "Endoscope-assisted magnetic helical micromachine delivery for biofilm eradication in tympanostomy tube," *Science Advances*, vol. 8, no. 40, pp. eabq8573, 2022.
- [39] D. Gong, B. Li, N. Celi, J. Cai, and D. Zhang, "Efficient removal of pb(ii) from aqueous systems using spirulina-based biohybrid magnetic helical microrobots," *ACS Applied Materials & Interfaces*, vol. 13, no. 44, pp. 53 131–53 142, 2021.
- [40] Z. Ren, R. Zhang, R. H. Soon, Z. Liu, W. Hu, P. R. Onck, and M. Sitti, "Soft-bodied adaptive multimodal locomotion strategies in fluid-filled confined spaces," *Science Advances*, vol. 7, no. 27, pp. eabh2022, 2021.
- [41] S. Zhang, X. Hu, M. Li, U. Bozuyuk, R. Zhang, E. Suadiye, J. Han, F. Wang, P. Onck, and M. Sitti, "3d-printed micrometer-scale wireless magnetic cilia with metachronal programmability," *Science Advances*, vol. 9, no. 12, pp. eadf9462, 2023.
- [42] R. Dreyfus, J. Baudry, M. L. Roper, M. Fermigier, H. A. Stone, and J. Bibette, "Microscopic artificial swimmers," *Nature*, vol. 437, no. 7060, pp. 862–865, 2005.
- [43] I. S. M. Khalil, H. C. Dijkslag, L. Abelmann, and S. Misra, "Magne-toSperm: A microrobot that navigates using weak magnetic fields," *Applied Physics Letters*, vol. 104, no. 22, pp. 223701, 2014.
- [44] B. J. Williams, S. V. Anand, J. Rajagopalan, and M. T. A. Saif, "A self-propelled biohybrid swimmer at low reynolds number," *Nature Communications*, vol. 5, no. 1, pp. 3081, 2014.
- [45] L. Liu, M. Liu, Y. Su, Y. Dong, W. Zhou, L. Zhang, H. Zhang, B. Dong, and L. Chi, "Tadpole-like artificial micromotor," *Nanoscale*, vol. 7, no. 6, pp. 2276–2280, 2015.
- [46] I. S. M. Khalil, A. Fatih Tabak, A. Klingner, and M. Sitti, "Magnetic propulsion of robotic sperms at low-Reynolds number," *Applied Physics Letters*, vol. 109, no. 3, pp. 033701, 2016.

- [47] J. García-Torres, C. Calero, F. Sagués, I. Pagonabarraga, and P. Tierno, “Magnetically tunable bidirectional locomotion of a self-assembled nanorod-sphere propeller,” *Nature Communications*, vol. 9, no. 1, pp. 1663, 2018.
- [48] C. Calero, J. García-Torres, A. Ortiz-Ambriz, F. Sagués, I. Pagonabarraga, and P. Tierno, “Direct measurement of lighthill’s energetic efficiency of a minimal magnetic microswimmer,” *Nanoscale*, vol. 11, no. 40, pp. 18 723–18 729, 2019.
- [49] N. Celi, D. Gong, and J. Cai, “Artificial flexible sperm-like nanorobot based on self-assembly and its bidirectional propulsion in precessing magnetic fields,” *Scientific Reports*, vol. 11, no. 1, pp. 21728, 2021.
- [50] W. Gao, S. Sattayasamitsathit, K. M. Manesh, D. Weihs, and J. Wang, “Magnetically powered flexible metal nanowire motors,” *Journal of the American Chemical Society*, vol. 132, no. 41, pp. 14 403–14 405, 2010.
- [51] J. van der Mijle Meijer, I. Mulder, E. Ligtenberg, H. Liefers, V. Magdanz, and I. Khalil, “Controlled locomotion of ironsperm clusters: Evaluating maneuverability with x-ray-guided magnetic fields,” in *IEEE RAS EMBS 10th International Conference on Biomedical Robotics and Biomechatronics*, Heidelberg, Germany, 2024, pp. 883–888.
- [52] J. Amend, N. Cheng, S. Fakhouri, and B. Culley, “Soft robotics commercialization: Jamming grippers from research to product,” *Soft Robotics*, vol. 3, no. 4, pp. 213–222, 2016.
- [53] G. Li, X. Chen, F. Zhou, Y. Liang, Y. Xiao, X. Cao, Z. Zhang, M. Zhang, B. Wu, S. Yin, Y. Xu, H. Fan, Z. Chen, W. Song, W. Yang, B. Pan, J. Hou, W. Zou, S. He, X. Yang, G. Mao, Z. Jia, H. Zhou, T. Li, S. Qu, Z. Xu, Z. Huang, Y. Luo, T. Xie, J. Gu, S. Zhu, and W. Yang, “Self-powered soft robot in the mariana trench,” *Nature*, vol. 591, no. 7848, pp. 66–71, 2021.
- [54] K. C. Galloway, K. P. Becker, B. Phillips, J. Kirby, S. Licht, D. Tchernov, R. J. Wood, and D. F. Gruber, “Soft robotic grippers for

- 
- biological sampling on deep reefs,” *Soft Robotics*, vol. 3, no. 1, pp. 23–33, 2016.
- [55] Y. Kim, E. Genevriere, P. Harker, J. Choe, M. Balicki, R. W. Regenhardt, J. E. Vranic, A. A. Dmytriw, A. B. Patel, and X. Zhao, “Telerobotic neurovascular interventions with magnetic manipulation,” *Science Robotics*, vol. 7, no. 65, pp. eabg9907, 2022.
- [56] W. Hu, G. Z. Lum, M. Mastrangeli, and M. Sitti, “Small-scale soft-bodied robot with multimodal locomotion,” *Nature*, vol. 554, no. 7690, pp. 81–85, 2018.
- [57] M. Sun, C. Tian, L. Mao, X. Meng, X. Shen, B. Hao, X. Wang, H. Xie, and L. Zhang, “Reconfigurable magnetic slime robot: deformation, adaptability, and multifunction,” *Advanced Functional Materials*, vol. 32, no. 26, pp. 2112508, 2022.
- [58] S. Palagi, A. G. Mark, S. Y. Reigh, K. Melde, T. Qiu, H. Zeng, C. Parmeggiani, D. Martella, A. Sanchez-Castillo, N. Kapernaum, F. Giesselmann, D. S. Wiersma, E. Lauga, and P. Fischer, “Structured light enables biomimetic swimming and versatile locomotion of photoresponsive soft microrobots,” *Nature Materials*, vol. 15, no. 6, pp. 647–653, 2016.
- [59] S.-J. Park, M. Gazzola, K. S. Park, S. Park, V. Di Santo, E. L. Blevins, J. U. Lind, P. H. Campbell, S. Dauth, A. K. Capulli, F. S. Pasqualini, S. Ahn, A. Cho, H. Yuan, B. M. Maoz, R. Vijaykumar, J.-W. Choi, K. Deisseroth, G. V. Lauder, L. Mahadevan, and K. K. Parker, “Phototactic guidance of a tissue-engineered soft-robotic ray,” *Science*, vol. 353, no. 6295, pp. 158–162, 2016.
- [60] N. Kellaris, V. Gopaluni Venkata, G. M. Smith, S. K. Mitchell, and C. Keplinger, “Peano-hassel actuators: Muscle-mimetic, electrohydraulic transducers that linearly contract on activation,” *Science Robotics*, vol. 3, no. 14, pp. eaar3276, 2018.
- [61] E. Acome, S. K. Mitchell, T. Morrissey, M. Emmett, C. Benjamin, M. King, M. Radakovitz, and C. Keplinger, “Hydraulically amplified self-healing electrostatic actuators with muscle-like performance,” *Science*, vol. 359, no. 6371, pp. 61–65, 2018.
-

- [62] A. G. Athanassiadis, Z. Ma, N. Moreno-Gomez, K. Melde, E. Choi, R. Goyal, and P. Fischer, “Ultrasound-responsive systems as components for smart materials,” *Chemical Reviews*, vol. 122, no. 5, pp. 5165–5208, 2021.
- [63] J. Li, C. C. Mayorga-Martinez, C.-D. Ohl, and M. Pumera, “Ultrasound-propelled micro-and nanorobots,” *Advanced Functional Materials*, vol. 32, no. 5, pp. 2102265, 2022.
- [64] E. Lauga and T. R. Powers, “The hydrodynamics of swimming microorganisms,” *Reports on Progress in Physics*, vol. 72, no. 9, pp. 096601, 2009.
- [65] E. H. Harris, “Chlamydomonas as a model organism,” *Annual Review of Plant Biology*, vol. 52, no. 1, pp. 363–406, 2001.
- [66] Y. Kim, H. Yuk, R. Zhao, S. A. Chester, and X. Zhao, “Printing ferromagnetic domains for untethered fast-transforming soft materials,” *Nature*, vol. 558, no. 7709, pp. 274–279, 2018.
- [67] S. R. Dabbagh, M. R. Sarabi, M. T. Birtek, S. Seyfi, M. Sitti, and S. Tasoglu, “3d-printed microrobots from design to translation,” *Nature Communications*, vol. 13, no. 1, pp. 5875, 2022.
- [68] M. Wehner, R. L. Truby, D. J. Fitzgerald, B. Mosadegh, G. M. Whitesides, J. A. Lewis, and R. J. Wood, “An integrated design and fabrication strategy for entirely soft, autonomous robots,” *Nature*, vol. 536, no. 7617, pp. 451–455, 2016.
- [69] R. F. Shepherd, F. Ilievski, W. Choi, S. A. Morin, A. A. Stokes, A. D. Mazzeo, X. Chen, M. Wang, and G. M. Whitesides, “Multigait soft robot,” *Proceedings of the National Academy of Sciences*, vol. 108, no. 51, pp. 20 400–20 403, 2011.
- [70] Z. Zheng, H. Wang, S. O. Demir, Q. Huang, T. Fukuda, and M. Sitti, “Programmable aniso-electrodeposited modular hydrogel microrobots,” *Science Advances*, vol. 8, no. 50, pp. eade6135, 2022.
- [71] V. Magdanz, J. Gebauer, D. Mahdy, J. Simmchen, and I. S. M. Khalil, “Sperm-templated magnetic microrobots,” in *International*

- Conference on Manipulation, Automation and Robotics at Small Scales (MARSS)*. Helsinki, Finland: IEEE, 2019, pp. 1–6.
- [72] Y. Dong, L. Wang, N. Xia, Z. Yang, C. Zhang, C. Pan, D. Jin, J. Zhang, C. Majidi, and L. Zhang, “Untethered small-scale magnetic soft robot with programmable magnetization and integrated multi-functional modules,” *Science Advances*, vol. 8, no. 25, pp. eabn8932, 2022.
- [73] V. Magdanz, S. Sanchez, and O. G. Schmidt, “Development of a sperm-flagella driven micro-bio-robot,” *Advanced Materials*, vol. 25, no. 45, pp. 6581–6588, 2013.
- [74] B. Behkam and M. Sitti, “Bacterial flagella-based propulsion and on/off motion control of microscale objects,” *Applied Physics Letters*, vol. 90, no. 2, pp. 023902, 2007.
- [75] F. Zhang, Z. Li, L. Yin, Q. Zhang, N. Askarinam, R. Mundaca-Uribe, F. Tehrani, E. Karshalev, W. Gao, L. Zhang, and J. Wang, “Ace2 receptor-modified algae-based microrobot for removal of sars-cov-2 in wastewater,” *Journal of the American Chemical Society*, vol. 143, no. 31, pp. 12 194–12 201, 2021.
- [76] S. Palagi and P. Fischer, “Bioinspired microrobots,” *Nature Reviews Materials*, vol. 3, no. 6, pp. 113–124, 2018.
- [77] L. Ricotti, B. Trimmer, A. W. Feinberg, R. Raman, K. K. Parker, R. Bashir, M. Sitti, S. Martel, P. Dario, and A. Menciassi, “Biohybrid actuators for robotics: A review of devices actuated by living cells,” *Science Robotics*, vol. 2, no. 12, pp. eaaq0495, 2017.
- [78] E. Gultepe, S. Yamanaka, K. E. Laffin, S. Kadam, Y. Shim, A. V. Olaru, B. Limketkai, M. A. Khashab, A. N. Kalloo, and D. H. Gracias, “Biologic tissue sampling with untethered microgrippers,” *Gastroenterology*, vol. 144, no. 4, pp. 691–693, 2013.
- [79] K. Malachowski, M. Jamal, Q. Jin, B. Polat, C. J. Morris, and D. H. Gracias, “Self-folding single cell grippers,” *Nano Letters*, vol. 14, no. 7, pp. 4164–4170, 2014.
-

- [80] J. S. Randhawa, T. G. Leong, N. Bassik, B. R. Benson, M. T. Jochmans, and D. H. Gracias, "Pick-and-place using chemically actuated microgrippers," *Journal of the American Chemical Society*, vol. 130, no. 51, pp. 17 238–17 239, 2008.
- [81] T. Li, J. Li, H. Zhang, X. Chang, W. Song, Y. Hu, G. Shao, E. Sandraz, G. Zhang, L. Li, and J. Wang, "Magnetically propelled fish-like nanoswimmers," *Small*, vol. 12, no. 44, pp. 6098–6105, 2016.
- [82] T. G. Leong, C. L. Randall, B. R. Benson, N. Bassik, G. M. Stern, and D. H. Gracias, "Tetherless thermobiochemically actuated microgrippers," *Proceedings of the National Academy of Sciences*, vol. 106, no. 3, pp. 703–708, 2009.
- [83] N. Bassik, A. Brafman, A. M. Zarafshar, M. Jamal, D. Luvsanjav, F. M. Selaru, and D. H. Gracias, "Enzymatically triggered actuation of miniaturized tools," *Journal of the American Chemical Society*, vol. 132, no. 46, pp. 16 314–16 317, 2010.
- [84] S. Fusco, M. S. Sakar, S. Kennedy, C. Peters, R. Bottani, F. Starsich, A. Mao, G. A. Sotiriou, S. Pané, S. E. Pratsinis, D. Mooney, and B. J. Nelson, "An integrated microrobotic platform for on-demand, targeted therapeutic interventions," *Advanced Materials*, vol. 26, no. 6, pp. 952–957, 2014.
- [85] C. Yoon, R. Xiao, J. Park, J. Cha, T. D. Nguyen, and D. H. Gracias, "Functional stimuli responsive hydrogel devices by self-folding," *Smart Materials and Structures*, vol. 23, no. 9, pp. 094008, 2014.
- [86] J. C. Breger, C. Yoon, R. Xiao, H. R. Kwag, M. O. Wang, J. P. Fisher, T. D. Nguyen, and D. H. Gracias, "Self-folding thermo-magnetically responsive soft microgrippers," *ACS Applied Materials & Interfaces*, vol. 7, no. 5, pp. 3398–3405, 2015.
- [87] T. Mirkovic, M. L. Foo, A. C. Arsenault, S. Fournier-Bidoz, N. S. Zacharia, and G. A. Ozin, "Hinged nanorods made using a chemical approach to flexible nanostructures," *Nature Nanotechnology*, vol. 2, no. 9, pp. 565–569, 2007.

- [88] W. Gao, K. M. Manesh, J. Hua, S. Sattayasamitsathit, and J. Wang, “Hybrid nanomotor: A catalytically/magnetically powered adaptive nanowire swimmer,” *Small*, vol. 7, no. 14, pp. 2047–2051, 2011.
- [89] W. F. Paxton, K. C. Kistler, C. C. Olmeda, A. Sen, S. K. St. Angelo, Y. Cao, T. E. Mallouk, P. E. Lammert, and V. H. Crespi, “Catalytic nanomotors: autonomous movement of striped nanorods,” *Journal of the American Chemical Society*, vol. 126, no. 41, pp. 13 424–13 431, 2004.
- [90] B. Jang, E. Gutman, N. Stucki, B. F. Seitz, P. D. Wendel-García, T. Newton, J. Pokki, O. Ergeneman, S. Pané, Y. Or, and B. J. Nelson, “Undulatory locomotion of magnetic multilink nanoswimmers,” *Nano Letters*, vol. 15, no. 7, pp. 4829–4833, 2015.
- [91] D. Ahmed, T. Baasch, B. Jang, S. Pane, J. Dual, and B. J. Nelson, “Artificial swimmers propelled by acoustically activated flagella,” *Nano Letters*, vol. 16, no. 8, pp. 4968–4974, 2016.
- [92] J. Gray, “Studies in animal locomotion: I. the movement of fish with special reference to the eel,” *Journal of Experimental Biology*, vol. 10, no. 1, pp. 88–104, 1933.
- [93] X. Hu, I. C. Yasa, Z. Ren, S. R. Goudu, H. Ceylan, W. Hu, and M. Sitti, “Magnetic soft micromachines made of linked microactuator networks,” *Science Advances*, vol. 7, no. 23, pp. eabe8436, 2021.
- [94] T. Li, J. Li, K. I. Morozov, Z. Wu, T. Xu, I. Rozen, A. M. Leshansky, L. Li, and J. Wang, “Highly efficient freestyle magnetic nanoswimmer,” *Nano Letters*, vol. 17, no. 8, pp. 5092–5098, 2017.
- [95] S. S. Suarez and A. Pacey, “Sperm transport in the female reproductive tract,” *Human Reproduction Update*, vol. 12, no. 1, pp. 23–37, 2006.
- [96] S. Mohanty, U. Siciliani de Cumis, M. Solsona, and S. Misra, “Bi-directional transportation of micro-agents induced by symmetry-broken acoustic streaming,” *AIP Advances*, vol. 9, no. 3, pp. 035352, 2019.

- [97] M. Kaynak, A. Ozcelik, A. Nourhani, P. E. Lammert, V. H. Crespi, and T. J. Huang, “Acoustic actuation of bioinspired microswimmers,” *Lab on a Chip*, vol. 17, no. 3, pp. 395–400, 2017.
- [98] J. Xue, T. Wu, Y. Dai, and Y. Xia, “Electrospinning and electrospun nanofibers: Methods, materials, and applications,” *Chemical Reviews*, vol. 119, no. 8, pp. 5298–5415, 2019.
- [99] M. M. Stanton, J. Simmchen, X. Ma, A. Miguel-López, and S. Sánchez, “Biohybrid janus motors driven by escherichia coli,” *Advanced Materials Interfaces*, vol. 3, no. 2, pp. 1500505, 2016.
- [100] D. B. Weibel, P. Garstecki, D. Ryan, W. R. DiLuzio, M. Mayer, J. E. Seto, and G. M. Whitesides, “Microoxen: Microorganisms to move microscale loads,” *Proceedings of the National Academy of Sciences*, vol. 102, no. 34, pp. 11 963–11 967, 2005.
- [101] V. Magdanz, M. Medina-Sánchez, L. Schwarz, H. Xu, J. Elgeti, and O. G. Schmidt, “Spermatozoa as functional components of robotic microswimmers,” *Advanced Materials*, vol. 29, no. 24, pp. 1606301, 2017.
- [102] O. G. Schmidt and K. Eberl, “Thin solid films roll up into nanotubes,” *Nature*, vol. 410, no. 6825, pp. 168–168, 2001.
- [103] I. S. M. Khalil, V. Magdanz, S. Sanchez, O. G. Schmidt, and S. Misra, “Biocompatible, accurate, and fully autonomous: a sperm-driven micro-bio-robot,” *Journal of Micro-Bio Robotics*, vol. 9, no. 3, pp. 79–86, 2014.
- [104] V. Magdanz, M. Guix, F. Hebenstreit, and O. G. Schmidt, “Dynamic polymeric microtubes for the remote-controlled capture, guidance, and release of sperm cells,” *Advanced Materials*, vol. 28, no. 21, pp. 4084–4089, 2016.
- [105] H. Xu, M. Medina-Sánchez, and O. G. Schmidt, “Magnetic micromotors for multiple motile sperm cells capture, transport, and enzymatic release,” *Angewandte Chemie International Edition*, vol. 59, no. 35, pp. 15 029–15 037, 2020.

- 
- [106] G. Huszar, C. C. Ozenci, S. Cayli, Z. Zavaczki, E. Hansch, and L. Vigue, “Hyaluronic acid binding by human sperm indicates cellular maturity, viability, and unreacted acrosomal status,” *Fertility and Sterility*, vol. 79, pp. 1616–1624, 2003.
- [107] C. Ridzewski, M. Li, B. Dong, and V. Magdanz, “Gelatin microcartridges for onboard activation and antioxidant protection of sperm,” *ACS Applied Bio Materials*, vol. 3, no. 3, pp. 1616–1627, 2020.
- [108] F. Rajabasadi, S. Moreno, K. Fichna, A. Aziz, D. Appelhans, O. G. Schmidt, and M. Medina-Sánchez, “Multifunctional 4d-printed sperm-hybrid microcarriers for assisted reproduction,” *Advanced Materials*, vol. 34, no. 50, pp. 2204257, 2022.
- [109] C. Chen, X. Chang, P. Angsantikul, J. Li, B. Esteban-Fernández de Ávila, E. Karshalev, W. Liu, F. Mou, S. He, R. Castillo, Y. Liang, J. Guan, L. Zhang, and J. Wang, “Chemotactic guidance of synthetic organic/inorganic payloads functionalized sperm micromotors,” *Advanced Biosystems*, vol. 2, no. 1, pp. 1700160, 2018.
- [110] V. Magdanz, I. S. M. Khalil, J. Simmchen, G. P. Furtado, S. Mohanty, J. Gebauer, H. Xu, A. Klingner, A. Aziz, M. Medina-Sánchez, O. G. Schmidt, and S. Misra, “Ironsperm: Sperm-templated soft magnetic microrobots,” *Science Advances*, vol. 6, no. 28, pp. eaba5855, 2020.
- [111] I. S. M. Khalil, V. Magdanz, J. Simmchen, A. Klingner, and S. Misra, “Resemblance between motile and magnetically actuated sperm cells,” *Applied Physics Letters*, vol. 116, no. 6, pp. 063702, 2020.
- [112] K. I. Middelhoek, V. Magdanz, L. Abelman, and I. S. M. Khalil, “Drug-loaded ironsperm clusters: modeling, wireless actuation, and ultrasound imaging,” *Biomedical Materials*, vol. 17, no. 6, pp. 065001, 2022.
- [113] Y. Alapan, O. Yasa, B. Yigit, I. C. Yasa, P. Erkoç, and M. Sitti, “Microrobotics and microorganisms: Biohybrid autonomous cellular robots,” *Annual Review of Control, Robotics, and Autonomous Systems*, vol. 2, pp. 205–230, 2019.
-

- [114] E. Lauga, “Bacterial hydrodynamics,” *Annual Review of Fluid Mechanics*, vol. 48, pp. 105–130, 2016.
- [115] R. W. Carlsen, M. R. Edwards, J. Zhuang, C. Pacoret, and M. Sitti, “Magnetic steering control of multi-cellular bio-hybrid microswimmers,” *Lab on a Chip*, vol. 14, no. 19, pp. 3850–3859, 2014.
- [116] J. Zhuang, R. Wright Carlsen, and M. Sitti, “ph-taxis of biohybrid microsystems,” *Scientific Reports*, vol. 5, no. 1, pp. 11403, 2015.
- [117] D. Kim, A. Liu, E. Diller, and M. Sitti, “Chemotactic steering of bacteria propelled microbeads,” *Biomedical Microdevices*, vol. 14, no. 6, pp. 1009–1017, 2012.
- [118] E. Steager, C.-B. Kim, J. Patel, S. Bith, C. Naik, L. Reber, and M. J. Kim, “Control of microfabricated structures powered by flagellated bacteria using phototaxis,” *Applied Physics Letters*, vol. 90, no. 26, pp. 263901, 2007.
- [119] H. C. Berg and D. A. Brown, “Chemotaxis in escherichia coli analysed by three-dimensional tracking,” *Nature*, vol. 239, pp. 500–504, 1972.
- [120] M. M. Stanton, B.-W. Park, A. Miguel-López, X. Ma, M. Sitti, and S. Sánchez, “Biohybrid microtube swimmers driven by single captured bacteria,” *Small*, vol. 13, no. 19, pp. 1603679, 2017.
- [121] Y. Alapan, O. Yasa, O. Schauer, J. Giltinan, A. F. Tabak, V. Sourjik, and M. Sitti, “Soft erythrocyte-based bacterial microswimmers for cargo delivery,” *Science Robotics*, vol. 3, no. 17, pp. eaar4423, 2018.
- [122] M. B. Akolpoglu, Y. Alapan, N. O. Dogan, S. F. Baltaci, O. Yasa, G. Aybar Tural, and M. Sitti, “Magnetically steerable bacterial microrobots moving in 3d biological matrices for stimuli-responsive cargo delivery,” *Science Advances*, vol. 8, no. 28, pp. eabo6163, 2022.
- [123] C. T. Lefèvre and D. A. Bazylinski, “Ecology, diversity, and evolution of magnetotactic bacteria,” *Microbiology and Molecular Biology Reviews*, vol. 77, no. 3, pp. 497–526, 2013.
- [124] S. Martel, M. Mohammadi, O. Felfoul, Z. Lu, and P. Pouponneau, “Flagellated magnetotactic bacteria as controlled mri-trackable

- propulsion and steering systems for medical nanorobots operating in the human microvasculature,” *The International Journal of Robotics Research*, vol. 28, no. 4, pp. 571–582, 2009.
- [125] S. Martel and M. Mohammadi, “Using a swarm of self-propelled natural microrobots in the form of flagellated bacteria to perform complex micro-assembly tasks,” in *Proceedings of the IEEE International Conference on Robotics and Automation (ICRA)*. Anchorage, AK: IEEE, 2010, pp. 500–505.
- [126] D. De Lanauze, O. Felfoul, J.-P. Turcot, M. Mohammadi, and S. Martel, “Three-dimensional remote aggregation and steering of magnetotactic bacteria microrobots for drug delivery applications,” *The International Journal of Robotics Research*, vol. 33, no. 3, pp. 359–374, 2014.
- [127] I. S. M. Khalil, M. P. Pichel, L. Abelmann, and S. Misra, “Closed-loop control of magnetotactic bacteria,” *The International Journal of Robotics Research*, vol. 32, no. 6, pp. 637–649, 2013.
- [128] T. Gwisai, N. Mirkhani, M. G. Christiansen, T. T. Nguyen, V. Ling, and S. Schuerle, “Magnetic torque-driven living microrobots for increased tumor infiltration,” *Science Robotics*, vol. 7, no. 71, pp. eabo0665, 2022.
- [129] G. Santomauro, A. V. Singh, B.-W. Park, M. Mohammadrahimi, P. Erkoc, E. Goering, G. Schütz, M. Sitti, and J. Bill, “Incorporation of terbium into a microalga leads to magnetotactic swimmers,” *Advanced Biosystems*, vol. 2, no. 12, pp. 1800039, 2018.
- [130] S. Xie, N. Jiao, S. Tung, and L. Liu, “Controlled regular locomotion of algae cell microrobots,” *Biomedical Microdevices*, vol. 18, no. 3, pp. 1–9, 2016.
- [131] M. B. Akolpoglu, N. O. Dogan, U. Bozuyuk, H. Ceylan, S. Kizilel, and M. Sitti, “High-yield production of biohybrid microalgae for on-demand cargo delivery,” *Advanced Science*, vol. 7, no. 16, pp. 2001256, 2020.

- [132] Z. Yang and L. Zhang, “Magnetic actuation systems for miniature robots: A review,” *Advanced Intelligent Systems*, vol. 2, no. 9, pp. 2000082, 2020.
- [133] B. J. Nelson, S. Gervasoni, P. W. Chiu, L. Zhang, and A. Zemmar, “Magnetically actuated medical robots: an in vivo perspective,” *Proceedings of the IEEE*, vol. 110, no. 7, pp. 1028–1037, 2022.
- [134] J. Li, X. Li, T. Luo, R. Wang, C. Liu, S. Chen, D. Li, J. Yue, S.-h. Cheng, and D. Sun, “Development of a magnetic microrobot for carrying and delivering targeted cells,” *Science Robotics*, vol. 3, no. 19, pp. eaat8829, 2018.
- [135] X.-Z. Chen, B. Jang, D. Ahmed, C. Hu, C. De Marco, M. Hoop, F. Mushtaq, B. J. Nelson, and S. Pané, “Small-scale machines driven by external power sources,” *Advanced Materials*, vol. 30, no. 15, pp. 1705061, 2018.
- [136] K. E. Peyer, L. Zhang, and B. J. Nelson, “Bio-inspired magnetic swimming microrobots for biomedical applications,” *Nanoscale*, vol. 5, no. 4, pp. 1259–1272, 2013.
- [137] S. Mohanty, I. S. M. Khalil, and S. Misra, “Contactless acoustic micro/nano manipulation: a paradigm for next generation applications in life sciences,” *Proceedings of the Royal Society A*, vol. 476, no. 2243, pp. 20200621, 2020.
- [138] H. Ceylan, J. Giltinan, K. Kozielski, and M. Sitti, “Mobile microrobots for bioengineering applications,” *Lab on a Chip*, vol. 17, no. 10, pp. 1705–1724, 2017.
- [139] M. L. Palmeri, A. C. Sharma, R. R. Bouchard, R. W. Nightingale, and K. R. Nightingale, “A finite-element method model of soft tissue response to impulsive acoustic radiation force,” *IEEE Transactions on Ultrasonics, Ferroelectrics, and Frequency Control*, vol. 52, no. 10, pp. 1699–1712, 2005.
- [140] T. Xu, L.-P. Xu, and X. Zhang, “Ultrasound propulsion of micro-/nanomotors,” *Applied Materials Today*, vol. 9, pp. 493–503, 2017.

- 
- [141] N. Riley, “Steady streaming,” *Annual Review of Fluid Mechanics*, vol. 33, pp. 43, 2001.
- [142] N. Nama, P.-H. Huang, T. J. Huang, and F. Costanzo, “Investigation of acoustic streaming patterns around oscillating sharp edges,” *Lab on a Chip*, vol. 14, no. 15, pp. 2824–2836, 2014.
- [143] D. Ahmed, X. Mao, J. Shi, B. K. Juluri, and T. J. Huang, “A millisecond micromixer via single-bubble-based acoustic streaming,” *Lab on a Chip*, vol. 9, no. 18, pp. 2738–2741, 2009.
- [144] M. Sitti and D. S. Wiersma, “Pros and cons: Magnetic versus optical microrobots,” *Advanced Materials*, vol. 32, no. 20, pp. 1906766, 2020.
- [145] X. Pang, J.-a. Lv, C. Zhu, L. Qin, and Y. Yu, “Photodeformable azobenzene-containing liquid crystal polymers and soft actuators,” *Advanced Materials*, vol. 31, no. 52, pp. 1904224, 2019.
- [146] K. Foster and R. Smyth, “Light antennas in phototactic algae,” *Microbiological Reviews*, vol. 44, no. 4, pp. 572–630, 1980.
- [147] J. Gray and G. J. Hancock, “The Propulsion of Sea-Urchin Spermatozoa,” *Journal of Experimental Biology*, vol. 32, no. 4, pp. 802–814, 1955.
- [148] H. C. Berg, *E. coli in Motion*. Springer, 2004.
- [149] H. C. Berg, “The rotary motor of bacterial flagella,” *Annual Review Biochemistry*, vol. 72, no. 1, pp. 19–54, 2003.
- [150] R. Coy and H. Gadêlha, “The counterbend dynamics of cross-linked filament bundles and flagella,” *Journal of The Royal Society Interface*, vol. 14, no. 130, pp. 20170065, 2017.
- [151] R. Cortez, “The method of regularized stokeslets,” *SIAM Journal on Scientific Computing*, vol. 23, no. 4, pp. 1204–1225, 2001.
- [152] Y. Sowa and R. M. Berry, “Bacterial flagellar motor,” *Quarterly Reviews of Biophysics*, vol. 41, no. 2, pp. 103–132, 2008.
-

- [153] S. Wilhelm, A. J. Tavares, Q. Dai, S. Ohta, J. Audet, H. F. Dvorak, and W. C. Chan, “Analysis of nanoparticle delivery to tumours,” *Nature Reviews Materials*, vol. 1, no. 5, pp. 1–12, 2016.
- [154] W. Gao, D. Kagan, O. S. Pak, C. Clawson, S. Campuzano, E. Chuluun-Erdene, E. Shipton, E. E. Fullerton, L. Zhang, E. Lauga, and J. Wang, “Cargo-towing fuel-free magnetic nanoswimmers for targeted drug delivery,” *Small*, vol. 8, no. 3, pp. 460–467, 2012.
- [155] H. Xu, M. Medina-Sánchez, V. Magdanz, L. Schwarz, F. Hebenstreit, and O. G. Schmidt, “Sperm-hybrid micromotor for targeted drug delivery,” *ACS Nano*, vol. 12, no. 1, pp. 327–337, 2018.
- [156] H. Xu, M. Medina-Sánchez, W. Zhang, M. P. Seaton, D. R. Brisson, R. J. Edmondson, S. S. Taylor, L. Nelson, K. Zeng, S. Bagley, C. Ribeiro, L. P. Restrepo, E. Lucena, C. K. Schmidt, and O. G. Schmidt, “Human sperm-bots for patient-representative 3d ovarian cancer cell treatment,” *Nanoscale*, vol. 12, no. 39, pp. 20 467–20 481, 2020.
- [157] O. Felfoul, M. Mohammadi, S. Taherkhani, D. De Lanauze, Y. Zhong Xu, D. Loghin, S. Essa, S. Jancik, D. Houle, M. Lafleur, L. Gaboury, M. Tabrizian, N. Kaou, M. Atkin, T. Vuong, G. Batist, N. Beauchemin, D. Radzioch, and S. Martel, “Magneto-aerotactic bacteria deliver drug-containing nanoliposomes to tumour hypoxic regions,” *Nature Nanotechnology*, vol. 11, no. 11, pp. 941–947, 2016.
- [158] B.-W. Park, J. Zhuang, O. Yasa, and M. Sitti, “Multifunctional bacteria-driven microswimmers for targeted active drug delivery,” *ACS Nano*, vol. 11, no. 9, pp. 8910–8923, 2017.
- [159] J. Zhuang, B.-W. Park, and M. Sitti, “Propulsion and chemotaxis in bacteria-driven microswimmers,” *Advanced Science*, vol. 4, no. 9, pp. 1700109, 2017.
- [160] N. Buss, O. Yasa, Y. Alapan, M. B. Akolpoglu, and M. Sitti, “Nanoerythroosome-functionalized biohybrid microswimmers,” *APL Bioengineering*, vol. 4, no. 2, pp. 026103, 2020.

- [161] R. Bos, H. C. Van der Mei, and H. J. Busscher, “Physico-chemistry of initial microbial adhesive interactions—its mechanisms and methods for study,” *FEMS Microbiology Reviews*, vol. 23, no. 2, pp. 179–230, 1999.
- [162] S.-Y. Cheng, S. Heilman, M. Wasserman, S. Archer, M. L. Shuler, and M. Wu, “A hydrogel-based microfluidic device for the studies of directed cell migration,” *Lab on a Chip*, vol. 7, no. 6, pp. 763–769, 2007.
- [163] M. R. Edwards, R. Wright Carlsen, and M. Sitti, “Near and far-wall effects on the three-dimensional motion of bacteria-driven microbeads,” *Applied Physics Letters*, vol. 102, no. 14, pp. 143701, 2013.
- [164] S. Uthaman, S. Zheng, J. Han, Y. J. Choi, S. Cho, V. D. Nguyen, J.-O. Park, S.-H. Park, J.-J. Min, S. Park, and I.-K. Park, “Preparation of engineered salmonella typhimurium-driven hyaluronic-acid-based microbeads with both chemotactic and biological targeting towards breast cancer cells for enhanced anticancer therapy,” *Advanced Healthcare Materials*, vol. 5, no. 2, pp. 288–295, 2016.
- [165] R. Fernandes, M. Zuniga, F. R. Sassine, M. Karakoy, and D. H. Gracias, “Enabling cargo-carrying bacteria via surface attachment and triggered release,” *Small*, vol. 7, no. 5, pp. 588–592, 2011.
- [166] O. Yasa, P. Erkoc, Y. Alapan, and M. Sitti, “Microalga-powered microswimmers toward active cargo delivery,” *Advanced Materials*, vol. 30, no. 45, pp. 1804130, 2018.
- [167] F. Zhang, Z. Li, Y. Duan, H. Luan, L. Yin, Z. Guo, C. Chen, M. Xu, W. Gao, R. H. Fang, L. Zhang, and J. Wang, “Extremophile-based biohybrid micromotors for biomedical operations in harsh acidic environments,” *Science Advances*, vol. 8, no. 51, pp. eade6455, 2022.
- [168] F. Zhang, Z. Li, Y. Duan, A. Abbas, R. Mundaca-Uribe, L. Yin, H. Luan, W. Gao, R. H. Fang, L. Zhang, and J. Wang, “Gastrointestinal tract drug delivery using algae motors embedded in a degradable capsule,” *Science Robotics*, vol. 7, no. 70, pp. eabo4160, 2022.

- [169] Z. Wu, J. Troll, H.-H. Jeong, Q. Wei, M. Stang, F. Ziemssen, Z. Wang, M. Dong, S. Schnichels, T. Qiu, and P. Fischer, “A swarm of slippery micropellers penetrates the vitreous body of the eye,” *Science Advances*, vol. 4, no. 11, pp. eaat4388, 2018.
- [170] M. Sun, K. F. Chan, Z. Zhang, L. Wang, Q. Wang, S. Yang, S. M. Chan, P. W. Y. Chiu, J. J. Y. Sung, and L. Zhang, “Magnetic microswarm and fluoroscopy-guided platform for biofilm eradication in biliary stents,” *Advanced Materials*, vol. 34, no. 34, pp. 2201888, 2022.
- [171] B. Wang, K. F. Chan, K. Yuan, Q. Wang, X. Xia, L. Yang, H. Ko, Y.-X. J. Wang, J. J. Y. Sung, P. W. Y. Chiu, and L. Zhang, “Endoscopy-assisted magnetic navigation of biohybrid soft microrobots with rapid endoluminal delivery and imaging,” *Science Robotics*, vol. 6, no. 52, pp. eabd2813, 2021.
- [172] E. Gultepe, J. S. Randhawa, S. Kadam, S. Yamanaka, F. M. Selaru, E. J. Shin, A. N. Kalloo, and D. H. Gracias, “Biopsy with thermally-responsive untethered microtools,” *Advanced Materials*, vol. 25, no. 4, pp. 514–519, 2013.
- [173] Q. Jin, Y. Yang, J. A. Jackson, C. Yoon, and D. H. Gracias, “Untethered single cell grippers for active biopsy,” *Nano Letters*, vol. 20, no. 7, pp. 5383–5390, 2020.
- [174] C. C. Mayorga-Martinez, J. Zelenka, J. Grmela, H. Michalkova, T. Ruml, J. Mareš, and M. Pumera, “Swarming aqua sperm micromotors for active bacterial biofilms removal in confined spaces,” *Advanced Science*, vol. 8, no. 19, pp. 2101301, 2021.
- [175] H.-C. Flemming and J. Wingender, “The biofilm matrix,” *Nature Reviews Microbiology*, vol. 8, no. 9, pp. 623–633, 2010.
- [176] Z. Zhang, L. Wang, T. K. Chan, Z. Chen, M. Ip, P. K. Chan, J. J. Sung, and L. Zhang, “Micro-/nanorobots in antimicrobial applications: Recent progress, challenges, and opportunities,” *Advanced Healthcare Materials*, vol. 11, no. 6, pp. 2101991, 2022.

- [177] M. M. Stanton, B.-W. Park, D. Vilela, K. Bente, D. Faivre, M. Sitti, and S. Sánchez, “Magnetotactic bacteria powered biohybrids target *e. coli* biofilms,” *ACS Nano*, vol. 11, no. 10, pp. 9968–9978, 2017.
- [178] I. S. Shchelik, J. V. Molino, and K. Gademann, “Biohybrid microswimmers against bacterial infections,” *Acta Biomaterialia*, vol. 136, pp. 99–110, 2021.
- [179] F. Zhang, J. Zhuang, Z. Li, H. Gong, B. E.-F. de Ávila, Y. Duan, Q. Zhang, J. Zhou, L. Yin, E. Karshalev, W. Gao, V. Nizet, R. H. Fang, L. Zhang, and J. Wang, “Nanoparticle-modified microrobots for in vivo antibiotic delivery to treat acute bacterial pneumonia,” *Nature Materials*, vol. 21, no. 11, pp. 1324–1332, 2022.
- [180] Z. Wang, A. Klingner, V. Magdanz, M. W. Hoppenreijs, S. Misra, and I. S. M. Khalil, “Flagellar propulsion of sperm cells against a time-periodic interaction force,” *Advanced Biology*, vol. 7, no. 1, pp. 2200210, 2023.
- [181] V. M. Kadiri, C. Bussi, A. W. Holle, K. Son, H. Kwon, G. Schütz, M. G. Gutierrez, and P. Fischer, “Biocompatible magnetic micro- and nanodevices: fabrication of fept nanopropellers and cell transfection,” *Advanced Materials*, vol. 32, no. 25, pp. 2001114, 2020.
- [182] T.-Y. Huang, H. Gu, and B. J. Nelson, “Increasingly intelligent micromachines,” *Annual Review of Control, Robotics, and Autonomous Systems*, vol. 5, pp. 279–310, 2022.
- [183] S. Tenzer, D. Docter, J. Kuharev, A. Musyanovych, V. Fetz, R. Hecht, F. Schlenk, D. Fischer, K. Kiouptsi, C. Reinhardt, K. Landfester, H. Schild, M. Maskos, S. K. Knauer, and R. H. Stauber, “Rapid formation of plasma protein corona critically affects nanoparticle pathophysiology,” *Nature Nanotechnology*, vol. 8, no. 10, pp. 772–781, 2013.
- [184] A. Aziz, S. Pane, V. Iacovacci, N. Koukourakis, J. Czarske, A. Men-ciassi, M. Medina-Sánchez, and O. G. Schmidt, “Medical imaging of microrobots: Toward in vivo applications,” *ACS Nano*, vol. 14, no. 9, pp. 10 865–10 893, 2020.

- [185] R. Kamiya and S. Asakura, "Helical transformations of salmonella flagella in vitro," *Journal of Molecular Biology*, vol. 106, no. 1, pp. 167–186, 1976.
- [186] R. Kamiya and S. Asakura, "Flagellar transformations at alkaline ph," *Journal of Molecular Biology*, vol. 108, no. 2, pp. 513–518, 1976.
- [187] H. Hotani, "Micro-video study of moving bacterial flagellar filaments ii. polymorphic transition in alcohol," *Biosystems*, vol. 12, no. 3-4, pp. 325–330, 1980.
- [188] K. Shimada, R. Kamiya, and S. Asakura, "Left-handed to right-handed helix conversion in salmonella flagella," *Nature*, vol. 254, no. 5498, pp. 332–334, 1975.
- [189] V. Kantsler, J. Dunkel, M. Blayney, and R. E. Goldstein, "Rheotaxis facilitates upstream navigation of mammalian sperm cells," *Elife*, vol. 3, pp. e02403, 2014.
- [190] E. Hasegawa, R. Kamiya, and S. Asakura, "Thermal transition in helical forms of salmonella flagella," *Journal of Molecular Biology*, vol. 160, no. 4, pp. 609–621, 1982.
- [191] N. C. Darnton and H. C. Berg, "Force-extension measurements on bacterial flagella: triggering polymorphic transformations," *Biophysical Journal*, vol. 92, no. 6, pp. 2230–2236, 2007.
- [192] H. Hotani, "Micro-video study of moving bacterial flagellar filaments: Iii. cyclic transformation induced by mechanical force," *Journal of Molecular Biology*, vol. 156, no. 4, pp. 791–806, 1982.
- [193] R. M. Macnab and M. K. Ornston, "Normal-to-curly flagellar transitions and their role in bacterial tumbling. stabilization of an alternative quaternary structure by mechanical force," *Journal of Molecular Biology*, vol. 112, no. 1, pp. 1–30, 1977.
- [194] S. H. Larsen, R. W. Reader, E. N. Kort, W.-W. Tso, and J. Adler, "Change in direction of flagellar rotation is the basis of the chemotactic response in escherichia coli," *Nature*, vol. 249, no. 5452, pp. 74–77, 1974.

- [195] L. Turner, W. S. Ryu, and H. C. Berg, “Real-time imaging of fluorescent flagellar filaments,” *Journal of Bacteriology*, vol. 182, no. 10, pp. 2793–2801, 2000.
- [196] G. Langousis and K. L. Hill, “Motility and more: the flagellum of trypanosoma brucei,” *Nature Review Microbiology*, vol. 12, no. 7, pp. 505–518, 2014.
- [197] M. E. Teves, F. Barbano, H. A. Guidobaldi, R. Sanchez, W. Miska, and L. C. Giojalas, “Progesterone at the picomolar range is a chemoattractant for mammalian spermatozoa,” *Fertility and Sterility*, vol. 86, no. 3, pp. 745–749, 2006.
- [198] K. Miki and D. E. Clapham, “Rheotaxis guides mammalian sperm,” *Current Biology*, vol. 23, no. 6, pp. 443–452, 2013.
- [199] S. Boryshpolets, S. Pérez-Cerezales, and M. Eisenbach, “Behavioral mechanism of human sperm in thermotaxis: a role for hyperactivation,” *Human Reproduction*, vol. 30, no. 4, pp. 884–892, 2015.
- [200] A. Bahat, I. Tur-Kaspa, A. Gakamsky, L. C. Giojalas, H. Breitbart, and M. Eisenbach, “Thermotaxis of mammalian sperm cells: a potential navigation mechanism in the female genital tract,” *Nature Medicine*, vol. 9, no. 2, pp. 149–150, 2003.
- [201] J. Elgeti, U. B. Kaupp, and G. Gompper, “Hydrodynamics of sperm cells near surfaces,” *Biophysical Journal*, vol. 99, no. 4, pp. 1018–1026, 2010.
- [202] V. F. Geyer, F. Jülicher, J. Howard, and B. M. Friedrich, “Cell-body rocking is a dominant mechanism for flagellar synchronization in a swimming alga,” *Proceedings of the National Academy of Sciences*, vol. 110, no. 45, pp. 18 058–18 063, 2013.
- [203] A. Hilfinger, A. K. Chattopadhyay, and F. Jülicher, “Nonlinear dynamics of cilia and flagella,” *Physical Review E*, vol. 79, no. 5, pp. 051918, 2009.
- [204] B. J. Walker, K. Ishimoto, and E. A. Gaffney, “Efficient simulation of filament elasto-hydrodynamics in three dimensions,” *Physical Review Fluids*, vol. 5, no. 12, pp. 123103, 2020.

- [205] C. M. Cox, M. E. Thoma, N. Tchangelova, G. Mburu, M. J. Bornstein, C. L. Johnson, and J. Kiarie, “Infertility prevalence and the methods of estimation from 1990 to 2021: a systematic review and meta-analysis,” *Human Reproduction Open*, vol. 2022, no. 4, pp. hoac051, 2022.
- [206] D. J. Pearce, L. Hoogerbrugge, K. A. Hook, H. S. Fisher, and L. Giomi, “Cellular geometry controls the efficiency of motile sperm aggregates,” *Journal of the Royal Society Interface*, vol. 15, no. 148, pp. 20180702, 2018.
- [207] D. Miller and H. Burkin, “Gamete adhesion molecules.” *Reproduction Supplement*, vol. 58, pp. 147–158, 2001.
- [208] B. Nixon, H. Ecroyd, J.-L. Dacheux, F. Dacheux, V. Labas, S. D. Johnston, and R. C. Jones, “Formation and dissociation of sperm bundles in monotremes,” *Biology of Reproduction*, vol. 95, no. 4, pp. 91–1, 2016.
- [209] D. M. Higginson and S. Pitnick, “Evolution of intra-ejaculate sperm interactions: do sperm cooperate?” *Biological Reviews*, vol. 86, no. 1, pp. 249–270, 2011.
- [210] C. J. Brokaw, “Bend propagation by a sliding filament model for flagella,” *Journal of Experimental Biology*, vol. 55, no. 2, pp. 289–304, 1971.
- [211] H. Gadêlha, E. A. Gaffney, and A. Goriely, “The counterbend phenomenon in flagellar axonemes and cross-linked filament bundles,” *Proceedings of the National Academy of Sciences*, vol. 110, no. 30, pp. 12 180–12 185, 2013.
- [212] J. Elgeti and G. Gompper, “Microswimmers near surfaces,” *The European Physical Journal Special Topics*, vol. 225, no. 11, pp. 2333–2352, 2016.
- [213] S. Camalet and F. Jülicher, “Generic aspects of axonemal beating,” *New Journal of Physics*, vol. 2, no. 1, pp. 24, 2000.

- 
- [214] K. Inaba, “Sperm flagella: comparative and phylogenetic perspectives of protein components,” *Molecular Human Reproduction*, vol. 17, no. 8, pp. 524–538, 2011.
- [215] B. M. Friedrich, I. H. Riedel-Kruse, J. Howard, and F. Jülicher, “High-precision tracking of sperm swimming fine structure provides strong test of resistive force theory,” *Journal of Experimental Biology*, vol. 213, no. 8, pp. 1226–1234, 2010.
- [216] F. Striggow, M. Medina-Sánchez, G. K. Auernhammer, V. Magdanz, B. M. Friedrich, and O. G. Schmidt, “Sperm-driven micromotors moving in oviduct fluid and viscoelastic media,” *Small*, vol. 16, no. 24, pp. 2000213, 2020.
- [217] R. Rikmenspoel, “The tail movement of bull spermatozoa: observations and model calculations,” *Biophysical Journal*, vol. 5, no. 4, pp. 365–392, 1965.
- [218] J. M. S. Dias, D. Estima, H. Punte, A. Klingner, L. Marques, V. Magdanz, and I. S. M. Khalil, “Modeling and characterization of the passive bending stiffness of nanoparticle-coated sperm cells using magnetic excitation,” *Advanced Theory and Simulations*, vol. 5, no. 3, pp. 2100438, 2022.
- [219] C. Brokaw, “Bending moments in free-swimming flagella,” *Journal of Experimental Biology*, vol. 53, no. 2, pp. 445–464, 1970.
- [220] R. Lefebvre and S. S. Suarez, “Effect of capacitation on bull sperm binding to homologous oviductal epithelium,” *Biology of Reproduction*, vol. 54, no. 3, pp. 575–582, 1996.
- [221] S. Suarez and H.-C. Ho, “Hyperactivated motility in sperm,” *Reproduction in Domestic Animals*, vol. 38, no. 2, pp. 119–124, 2003.
- [222] J. Zhang, Z. Ren, W. Hu, R. H. Soon, I. C. Yasa, Z. Liu, and M. Sitti, “Voxelated three-dimensional miniature magnetic soft machines via multimaterial heterogeneous assembly,” *Science Robotics*, vol. 6, no. 53, pp. eabf0112, 2021.
- [223] J. Zhang, Y. Guo, W. Hu, and M. Sitti, “Wirelessly actuated thermo- and magneto-responsive soft bimorph materials with programmable
-

- shape-morphing,” *Advanced Materials*, vol. 33, no. 30, pp. 2100336, 2021.
- [224] S. Martel, “Swimming microorganisms acting as nanorobots versus artificial nanorobotic agents: A perspective view from an historical retrospective on the future of medical nanorobotics in the largest known three-dimensional biomicrofluidic networks,” *Biomicrofluidics*, vol. 10, no. 2, pp. 021301, 2016.
- [225] H. Hagiwara, N. Ohwada, T. Aoki, T. Suzuki, and K. Takata, “The primary cilia of secretory cells in the human oviduct mucosa,” *Medical Molecular Morphology*, vol. 41, no. 4, pp. 193–198, 2008.
- [226] A. Farahnaky, Z. Allahdad, M. Aminlari, M. Majzoobi, H. Askari, and R. Ramezani, “Rheological behaviour of dextran sulfate solutions,” *International Journal of Food Engineering*, vol. 8, no. 3, 2012.
- [227] C. Brennen and H. Winet, “Fluid mechanics of propulsion by cilia and flagella,” *Annual Review of Fluid Mechanics*, vol. 9, no. 1, pp. 339–398, 1977.
- [228] V. Magdanz, J. Vivaldi, S. Mohanty, A. Klingner, M. Vendittelli, J. Simmchen, S. Misra, and I. S. M. Khalil, “Impact of segmented magnetization on the flagellar propulsion of sperm-templated micro-robots,” *Advanced Science*, vol. 8, no. 8, pp. 2004037, 2021.
- [229] R. Dong, Q. Zhang, W. Gao, A. Pei, and B. Ren, “Highly efficient light-driven tio<sub>2</sub>-au janus micromotors,” *ACS Nano*, vol. 10, no. 1, pp. 839–844, 2016.
- [230] K. Kim, X. Xu, J. Guo, and D. L. Fan, “Ultrahigh-speed rotating nanoelectromechanical system devices assembled from nanoscale building blocks,” *Nature Communications*, vol. 5, no. 1, pp. 3632, 2014.
- [231] W. Wang, L. A. Castro, M. Hoyos, and T. E. Mallouk, “Autonomous motion of metallic microrods propelled by ultrasound,” *ACS Nano*, vol. 6, no. 7, pp. 6122–6132, 2012.
- [232] M. Xuan, Z. Wu, J. Shao, L. Dai, T. Si, and Q. He, “Near infrared light-powered janus mesoporous silica nanoparticle motors,” *Journal*

- 
- of the American Chemical Society*, vol. 138, no. 20, pp. 6492–6497, 2016.
- [233] S. Li, D. Liu, Y. Hu, Z. Su, X. Zhang, R. Guo, D. Li, and Y. Lu, “Soft magnetic microrobot doped with porous silica for stability-enhanced multimodal locomotion in a nonideal environment,” *ACS Applied Materials & Interfaces*, vol. 14, no. 8, pp. 10 856–10 874, 2022.
- [234] D. Gong, N. Celi, D. Zhang, and J. Cai, “Magnetic biohybrid micro-robot multimers based on chlorella cells for enhanced targeted drug delivery,” *ACS Applied Materials & Interfaces*, vol. 14, no. 5, pp. 6320–6330, 2022.
- [235] J. Jiang, F. Wang, W. Huang, J. Sun, Y. Ye, J. Ou, M. Liu, J. Gao, S. Wang, D. Fu, B. Chen, L. Liu, F. Peng, and Y. Tu, “Mobile mechanical signal generator for macrophage polarization,” *Exploration*, vol. 3, no. 2, pp. 20220147, 2023.
- [236] Z. Wang, A. Klingner, V. Magdanz, S. Misra, and I. S. M. Khalil, “Soft bio-microrobots: Toward biomedical applications,” *Advanced Intelligent Systems*, vol. 6, no. 2, pp. 2300093, 2024.
- [237] R. Nauber, S. R. Goudu, M. Goeckenjan, M. Bornhäuser, C. Ribeiro, and M. Medina-Sánchez, “Medical microrobots in reproductive medicine from the bench to the clinic,” *Nature Communications*, vol. 14, no. 1, pp. 728, 2023.
- [238] J. Jiang, Z. Yang, A. Ferreira, and L. Zhang, “Control and autonomy of microrobots: Recent progress and perspective,” *Advanced Intelligent Systems*, vol. 4, no. 5, pp. 2100279, 2022.
- [239] L. Yang and L. Zhang, “Motion control in magnetic microrobotics: From individual and multiple robots to swarms,” *Annual Review of Control, Robotics, and Autonomous Systems*, vol. 4, pp. 509–534, 2021.
- [240] A. W. Mahoney, N. D. Nelson, K. E. Peyer, B. J. Nelson, and J. J. Abbott, “Behavior of rotating magnetic microrobots above the step-out frequency with application to control of multi-microrobot systems,” *Applied Physics Letters*, vol. 104, no. 14, pp. 144101, 2014.
-

- [241] X. Wang, C. Hu, L. Schurz, C. De Marco, X. Chen, S. Pané, and B. J. Nelson, “Surface-chemistry-mediated control of individual magnetic helical microswimmers in a swarm,” *ACS Nano*, vol. 12, no. 6, pp. 6210–6217, 2018.
- [242] H.-W. Huang, F. E. Uslu, P. Katsamba, E. Lauga, M. S. Sakar, and B. J. Nelson, “Adaptive locomotion of artificial microswimmers,” *Science Advances*, vol. 5, no. 1, pp. eaau1532, 2019.
- [243] J. Tang, L. W. Rogowski, X. Zhang, and M. J. Kim, “Flagellar nanorobot with kinetic behavior investigation and 3d motion,” *Nanoscale*, vol. 12, no. 22, pp. 12 154–12 164, 2020.
- [244] N. Celi, J. Cai, H. Sun, L. Feng, D. Zhang, and D. Gong, “Biohybrid flexible sperm-like microrobot for targeted chemo-photothermal therapy,” *ACS Applied Materials & Interfaces*, vol. 16, no. 19, pp. 24 341–24 350, 2024.
- [245] W. Liu, Z. Xu, L. Sun, P. Guo, C. Zeng, C. Wang, and L. Zhang, “Polymerization-induced phase separation fabrication: A versatile microfluidic technique to prepare microfibers with various cross sectional shapes and structures,” *Chemical Engineering Journal*, vol. 315, pp. 25–34, 2017.
- [246] M. Yamada, S. Sugaya, Y. Naganuma, and M. Seki, “Microfluidic synthesis of chemically and physically anisotropic hydrogel microfibers for guided cell growth and networking,” *Soft Matter*, vol. 8, no. 11, pp. 3122–3130, 2012.
- [247] R. Grande, E. Trovatti, A. J. F. Carvalho, and A. Gandini, “Continuous microfiber drawing by interfacial charge complexation between anionic cellulose nanofibers and cationic chitosan,” *Journal of Materials Chemistry A*, vol. 5, no. 25, pp. 13 098–13 103, 2017.
- [248] S. Aldana, F. Vereda, R. Hidalgo-Alvarez, and J. de Vicente, “Facile synthesis of magnetic agarose microfibers by directed self-assembly in w/o emulsions,” *Polymer*, vol. 93, pp. 61–64, 2016.
- [249] A. J. Robinson, A. Pérez-Nava, S. C. Ali, J. B. González-Campos, J. L. Holloway, and E. M. Cosgriff-Hernandez, “Comparative analysis

- 
- of fiber alignment methods in electrospinning,” *Matter*, vol. 4, no. 3, pp. 821–844, 2021.
- [250] A. T. Chwang and T. Y.-T. Wu, “Hydromechanics of low-reynolds-number flow. part 2. singularity method for stokes flows,” *Journal of Fluid Mechanics*, vol. 67, no. 4, pp. 787–815, 1975.
- [251] C. H. Wiggins and R. E. Goldstein, “Flexive and propulsive dynamics of elastica at low reynolds number,” *Physical Review Letters*, vol. 80, no. 17, pp. 3879–3882, 1998.
- [252] E. Lauga, “Floppy swimming: Viscous locomotion of actuated elastica,” *Physical Review E*, vol. 75, no. 4, pp. 041916, 2007.
- [253] J. J. Abbott, O. Erogeneman, M. P. Kummer, A. M. Hirt, and B. J. Nelson, “Modeling magnetic torque and force for controlled manipulation of soft-magnetic bodies,” *IEEE Transactions on Robotics*, vol. 23, no. 6, pp. 1247–1252, 2007.
- [254] H. Gadêlha, “On the optimal shape of magnetic swimmers,” *Regular and Chaotic Dynamics*, vol. 18, no. 1, pp. 75–84, 2013.
- [255] D. Oriola, H. Gadêlha, and J. Casademunt, “Nonlinear amplitude dynamics in flagellar beating,” *Royal Society Open Science*, vol. 4, no. 3, pp. 160698, 2017.
- [256] C. J. Brokaw, “Effects of Increased Viscosity on the Movements of Some Invertebrate Spermatozoa\*,” *Journal of Experimental Biology*, vol. 45, no. 1, pp. 113–139, 1966.
- [257] D. J. Smith, E. A. Gaffney, H. Gadêlha, N. Kapur, and J. C. Kirkman-Brown, “Bend propagation in the flagella of migrating human sperm, and its modulation by viscosity,” *Cell Motility*, vol. 66, no. 4, pp. 220–236, 2009.
- [258] G. Saggiorato, L. Alvarez, J. F. Jikeli, U. B. Kaupp, G. Gompper, and J. Elgeti, “Human sperm steer with second harmonics of the flagellar beat,” *Nature Communications*, vol. 8, no. 1, pp. 1415, 2017.
- [259] J. F. Jikeli, L. Alvarez, B. M. Friedrich, L. G. Wilson, R. Pascal, R. Colin, M. Pichlo, A. Rennhack, C. Brenker, and U. B. Kaupp,
-

- “Sperm navigation along helical paths in 3d chemoattractant landscapes,” *Nature Communications*, vol. 6, no. 1, pp. 7985, 2015.
- [260] C. Xu and J. Prince, “Snakes, shapes, and gradient vector flow,” *IEEE Transactions on Image Processing*, vol. 7, no. 3, pp. 359–369, 1998.
- [261] R. Ahmad, A. J. Bae, Y.-J. Su, S. G. Pozveh, E. Bodenschatz, A. Pumir, and A. Gholami, “Bio-hybrid micro-swimmers propelled by flagella isolated from *c. reinhardtii*,” *Soft Matter*, vol. 18, no. 25, pp. 4767–4777, 2022.
- [262] B. J. Nelson and S. Pané, “Delivering drugs with microrobots,” *Science*, vol. 382, no. 6675, pp. 1120–1122, 2023.
- [263] X. Peng, M. Urso, M. Kolackova, D. Huska, and M. Pumera, “Bio-hybrid magnetically driven microrobots for sustainable removal of micro/nanoplastics from the aquatic environment,” *Advanced Functional Materials*, vol. 34, no. 3, pp. 2307477, 2024.
- [264] C. C. Mayorga-Martinez, M. Fojtů, J. Vyskočil, N.-J. Cho, and M. Pumera, “Pollen-based magnetic microrobots are mediated by electrostatic forces to attract, manipulate, and kill cancer cells,” *Advanced Functional Materials*, vol. 32, no. 46, pp. 2207272, 2022.
- [265] S. Xu, J. Liu, C. Yang, X. Wu, and T. Xu, “A learning-based stable servo control strategy using broad learning system applied for micro-robotic control,” *IEEE Transactions on Cybernetics*, vol. 52, no. 12, pp. 13 727–13 737, 2022.
- [266] S. Zhong, Y. Hou, Q. Shi, Y. Li, H.-W. Huang, Q. Huang, T. Fukuda, and H. Wang, “Spatial constraint-based navigation and emergency replanning adaptive control for magnetic helical microrobots in dynamic environments,” *IEEE Transactions on Automation Science and Engineering*, vol. 21, no. 4, pp. 7180–7189, 2024.
- [267] H. Wang, S. Zhong, Z. Zheng, Q. Shi, T. Sun, Q. Huang, and T. Fukuda, “Data-driven parallel adaptive control for magnetic helical microrobots with derivative structure in uncertain environments,” *IEEE Transactions on Systems, Man, and Cybernetics: Systems*, vol. 54, no. 7, pp. 4139–4150, 2024.

- [268] Y. Liu, H. Chen, Q. Zou, X. Du, Y. Wang, and J. Yu, “Automatic navigation of microswarms for dynamic obstacle avoidance,” *IEEE Transactions on Robotics*, vol. 39, no. 4, pp. 2770–2785, 2023.
- [269] R. K. Harrison, “Phase ii and phase iii failures: 2013–2015,” *Nature Reviews Drug Discovery*, vol. 15, no. 12, pp. 817–818, 2016.
- [270] J. Aparicio-Blanco, N. Vishwakarma, C.-M. Lehr, C. A. Prestidge, N. Thomas, R. J. Roberts, C. R. Thorn, and A. Melero, “Antibiotic resistance and tolerance: What can drug delivery do against this global threat?” *Drug Delivery and Translational Research*, vol. 14, no. 6, pp. 1725–1734, 2024.
- [271] S. Senapati, A. K. Mahanta, S. Kumar, and P. Maiti, “Controlled drug delivery vehicles for cancer treatment and their performance,” *Signal Transduction and Targeted Therapy*, vol. 3, no. 1, pp. 7, 2018.
- [272] U. Bozuyuk, P. Wrede, E. Yildiz, and M. Sitti, “Roadmap for clinical translation of mobile microrobotics,” *Advanced Materials*, vol. 36, no. 23, pp. 2311462, 2024.
- [273] H. Wang and M. Pumera, “Fabrication of micro/nanoscale motors,” *Chemical Reviews*, vol. 115, no. 16, pp. 8704–8735, 2015.
- [274] Z. Wang, A. Klingner, V. Magdanz, S. Misra, and I. S. M. Khalil, “Soft bio-microrobots: Toward biomedical applications,” *Advanced Intelligent Systems*, vol. 6, no. 2, pp. 2300093, 2024.
- [275] C. Huang, Z. Lai, L. Zhang, X. Wu, and T. Xu, “A magnetically controlled soft miniature robotic fish with a flexible skeleton inspired by zebrafish,” *Bioinspiration & Biomimetics*, vol. 16, no. 6, pp. 065004, 2021.
- [276] J. Leclerc, H. Zhao, D. Bao, and A. T. Becker, “In vitro design investigation of a rotating helical magnetic swimmer for combined 3-d navigation and blood clot removal,” *IEEE Transactions on Robotics*, vol. 36, no. 3, pp. 975–982, 2020.
- [277] H.-W. Huang, M. S. Sakar, A. J. Petruska, S. Pané, and B. J. Nelson, “Soft micromachines with programmable motility and morphology,” *Nature Communications*, vol. 7, no. 1, pp. 12263, 2016.
-

- [278] C. Xin, D. Jin, Y. Hu, L. Yang, R. Li, L. Wang, Z. Ren, D. Wang, S. Ji, K. Hu, D. Pan, H. Wu, W. Zhu, Z. Shen, Y. Wang, J. Li, L. Zhang, D. Wu, and J. Chu, “Environmentally adaptive shape-morphing microrobots for localized cancer cell treatment,” *ACS Nano*, vol. 15, no. 11, pp. 18 048–18 059, 2021.
- [279] M. You, F. Mou, K. Wang, and J. Guan, “Tadpole-like flexible microswimmers with the head and tail both magnetic,” *ACS Applied Materials & Interfaces*, vol. 15, no. 34, pp. 40 855–40 863, 2023.
- [280] R. Tan, X. Yang, H. Lu, and Y. Shen, “One-step formation of polymorphous sperm-like microswimmers by vortex turbulence-assisted microfluidics,” *Nature Communications*, vol. 15, no. 1, pp. 4761, 2024.
- [281] G. Velve-Casquillas, M. Le Berre, M. Piel, and P. T. Tran, “Microfluidic tools for cell biological research,” *Nano Today*, vol. 5, no. 1, pp. 28–47, 2010.
- [282] E. Livak-Dahl, I. Sinn, and M. Burns, “Microfluidic chemical analysis systems,” *Annual Review of Chemical and Biomolecular Engineering*, vol. 2, no. 1, pp. 325–353, 2011.
- [283] P. Yager, T. Edwards, E. Fu, K. Helton, K. Nelson, M. R. Tam, and B. H. Weigl, “Microfluidic diagnostic technologies for global public health,” *Nature*, vol. 442, no. 7101, pp. 412–418, 2006.
- [284] S. Bahrami, N. Baheiraei, M. Najafi-Ashtiani, S. Nour, and M. Razavi, “Chapter 9 - microfluidic devices in tissue engineering,” in *Biomedical Applications of Microfluidic Devices*. Academic Press, 2021, pp. 209–233.
- [285] K. Y. Lee and D. J. Mooney, “Alginate: Properties and biomedical applications,” *Progress in Polymer Science*, vol. 37, no. 1, pp. 106–126, 2012.
- [286] S. Groß, V. Reichelt, and A. Reusken, “A finite element based level set method for two-phase incompressible flows,” *Computing and Visualization in Science*, vol. 9, no. 4, pp. 239–257, 2006.

- 
- [287] W. Doherty, T. N. Phillips, and Z. Xie, “A stabilised finite element framework for viscoelastic multiphase flows using a conservative level-set method,” *Journal of Computational Physics*, vol. 477, pp. 111936, 2023.
- [288] G.-H. Cottet, E. Maitre, and T. Milcent, *Level Set Methods for Fluid-Structure Interaction*. Springer Nature, 2022.
- [289] J. A. Sethian and P. Smereka, “Level set methods for fluid interfaces,” *Annual Review of Fluid Mechanics*, vol. 35, no. 1, pp. 341–372, 2003.
- [290] E. Olsson and G. Kreiss, “A conservative level set method for two phase flow,” *Journal of Computational Physics*, vol. 210, no. 1, pp. 225–246, 2005.
- [291] A. S. Utada, E. Lorenceau, D. R. Link, P. D. Kaplan, H. A. Stone, and D. A. Weitz, “Monodisperse double emulsions generated from a microcapillary device,” *Science*, vol. 308, no. 5721, pp. 537–541, 2005.
- [292] S. Haeberle, L. Naegele, R. Burger, F. v. Stetten, R. Zengerle, and J. Ducree, “Alginate bead fabrication and encapsulation of living cells under centrifugally induced artificial gravity conditions,” *Journal of Microencapsulation*, vol. 25, no. 4, pp. 267–274, 2008.
- [293] W.-Z. Fang, S. Ham, R. Qiao, and W.-Q. Tao, “Magnetic actuation of surface walkers: The effects of confinement and inertia,” *Langmuir*, vol. 36, no. 25, pp. 7046–7055, 2020.
- [294] P. Tierno, R. Golestanian, I. Pagonabarraga, and F. Sagués, “Controlled swimming in confined fluids of magnetically actuated colloidal rotors,” *Physical Review Letters*, vol. 101, no. 21, pp. 218304, 2008.
- [295] G. Kaklamani, D. Cheneler, L. M. Grover, M. J. Adams, and J. Bowen, “Mechanical properties of alginate hydrogels manufactured using external gelation,” *Journal of the Mechanical Behavior of Biomedical Materials*, vol. 36, pp. 135–142, 2014.
- [296] C. Pawashe, S. Floyd, and M. Sitti, “Dynamic Modeling of Stick Slip Motion in an Untethered Magnetic Micro-Robot,” in *Robotics: Science and Systems IV*. The MIT Press, 2009, pp. 286–293.
-

- [297] B. Wang, Q. Wang, K. F. Chan, Z. Ning, Q. Wang, F. Ji, H. Yang, S. Jiang, Z. Zhang, B. Y. M. Ip, H. Ko, J. P. W. Chung, M. Qiu, J. Han, P. W. Y. Chiu, J. J. Y. Sung, S. Du, T. W. H. Leung, S. C. H. Yu, and L. Zhang, “tpa-anchored nanorobots for in vivo arterial recanalization at submillimeter-scale segments,” *Science Advances*, vol. 10, no. 5, pp. eadk8970, 2024.
- [298] H. Zhang, Z. Li, C. Gao, X. Fan, Y. Pang, T. Li, Z. Wu, H. Xie, and Q. He, “Dual-responsive biohybrid neutroblots for active target delivery,” *Science Robotics*, vol. 6, no. 52, pp. eaaz9519, 2021.
- [299] B. Wang, Y. Zhang, and L. Zhang, “Recent progress on micro- and nano-robots: towards in vivo tracking and localization,” *Quantitative Imaging in Medicine and Surgery*, vol. 8, no. 5, 2018.
- [300] H. Zhou, C. C. Mayorga-Martinez, S. Pané, L. Zhang, and M. Pumera, “Magnetically driven micro and nanorobots,” *Chemical Reviews*, vol. 121, no. 8, pp. 4999–5041, 2021.
- [301] Y. Kim, E. Genevriere, P. Harker, J. Choe, M. Balicki, R. W. Regenhardt, J. E. Vranic, A. A. Dmytriw, A. B. Patel, and X. Zhao, “Telerobotic neurovascular interventions with magnetic manipulation,” *Science Robotics*, vol. 7, no. 65, pp. eabg9907, 2022.
- [302] L. Su, D. Jin, Y. Wang, Q. Wang, C. Pan, S. Jiang, H. Yang, Z. Yang, X. Wang, N. Xia, K. F. Chan, P. W. Y. Chiu, J. J.-Y. Sung, and L. Zhang, “Modularized microrobot with lock-and-detachable modules for targeted cell delivery in bile duct,” *Science Advances*, vol. 9, no. 50, pp. eadj0883, 2023.
- [303] D. Jin, Q. Wang, K. F. Chan, N. Xia, H. Yang, Q. Wang, S. C. H. Yu, and L. Zhang, “Swarming self-adhesive microgels enabled aneurysm on-demand embolization in physiological blood flow,” *Science Advances*, vol. 9, no. 19, pp. eadf9278, 2023.
- [304] C. Li, S. Misra, and I. S. M. Khalil, “Closed-loop control characterization of untethered small-scale helical device in physiological fluid with dynamic flow rates,” *Advanced Intelligent Systems*, vol. 5, no. 5, pp. 2200322, 2023.

- [305] S. Bajpai and S. Sharma, “Investigation of swelling/degradation behaviour of alginate beads crosslinked with  $Ca^{2+}$  and  $Ba^{2+}$  ions,” *Reactive and Functional Polymers*, vol. 59, no. 2, pp. 129–140, 2004.
- [306] R. Mundaca-Urbe, N. Askarinam, R. H. Fang, L. Zhang, and J. Wang, “Towards multifunctional robotic pills,” *Nature Biomedical Engineering*, vol. 8, no. 11, pp. 1334–1346, 2023.
- [307] A. W. Adamson and A. P. Gast, *Physical Chemistry of Surfaces*, 6th ed. John Wiley and Sons, 1997.
- [308] Y. Su, T. Qiu, W. Song, X. Han, M. Sun, Z. Wang, H. Xie, M. Dong, and M. Chen, “Melt electrospinning writing of magnetic micro-robots,” *Advanced Science*, vol. 8, no. 3, pp. 2003177, 2021.
- [309] I. S. M. Khalil, A. F. Tabak, M. Abou Seif, A. Klingner, and M. Sitti, “Controllable switching between planar and helical flagellar swimming of a soft robotic sperm,” *PLoS One*, vol. 13, no. 11, pp. e0206456, 2018.
- [310] L. Wang, M. Zhao, Y. He, S. Ding, and L. Sun, “Fish-like magnetic microrobots for microparts transporting at liquid surfaces,” *Soft Matter*, vol. 19, no. 16, pp. 2883–2890, 2023.
- [311] L. Schwarz, M. Medina-Sánchez, and O. G. Schmidt, “Hybrid biomi-cromotors,” *Applied Physics Reviews*, vol. 4, no. 3, pp. 031301, 2017.
- [312] F. Zhang, Z. Li, C. Chen, H. Luan, R. H. Fang, L. Zhang, and J. Wang, “Biohybrid microalgae robots: Design, fabrication, materials, and applications,” *Advanced Materials*, vol. 36, no. 3, pp. 2303714, 2024.
- [313] U. Bozuyuk, H. Ozturk, and M. Sitti, “Microrobotic locomotion in blood vessels: A computational study on the performance of surface microrollers in the cardiovascular system,” *Advanced Intelligent Systems*, vol. 5, no. 9, pp. 2300099, 2023.



## Acknowledgements

As I write this acknowledgment, it dawns on me that my Ph.D. journey is reaching its destination. This moment feels just as challenging as finishing a research project, as my gratitude and emotions are too deep to be expressed in just a few hundred words. After rigorous training in scientific writing, logic, coherence, flow, and clarity often dominate my thoughts. I hope my supervisors will be gentle with their comments on this section, as I attempt to articulate what truly lies within my heart. Reflecting on the past three and a half years, I am always reminded of the happiness, excitement, and frustration that have defined my Ph.D. journey. Every memory is an important part of the tapestry of my life, and I am immensely grateful to those who have supported me along this incredible journey.

First, I extend my heartfelt gratitude to my doctoral promoter, **Prof. Sarthak Misra** for accepting me as your Ph.D. student. When I recall our first interview in 2019, I still remember your warmth and enthusiasm. I have to admit that it was a challenging time, and just two months later, the COVID-19 pandemic hit China. Despite these obstacles, we collaborated on the research proposal for the CSC Scholarship and achieved success together. Our biweekly meetings have been an invaluable experience for me, shaping my scientific writing and critical thinking skills. I owe a great debt of gratitude to **Dr. Islam S. M. Khalil**. This thesis would not have been possible without your unwavering support and mentorship. The significant progress and insightful discussions during our weekly meetings stand as a testament to your exceptional guidance. You have influenced my research perspective and refined my writing abilities. Your expertise, insightful feedback, and encouragement have been invaluable in fostering my growth as a scholar. In addition, I express my deepest appreciation to **Chinese Scholarship Council** for funding my studies and supporting my life in Groningen.

Next, I am grateful to my collaborators for their invaluable assistance and fruitful discussions throughout the research projects. Without their contribution, I would not have been able to complete this Ph.D. thesis. **Dr. Anke Klingner**, you have always been my first point of contact whenever I encounter difficulties in mathematics and physics. **Dr. Veronika Mag-**

**danz**, thank you for providing the videos of sperm cells. If it weren't for your help, I would have had no idea how to conduct these experiments. **Dr. Wenjian Li** and **Prof. Yutao Pei**, I sincerely appreciate your assistance in SEM characterization and constructive feedback. Your support has been invaluable for my work.

I also would like to acknowledge the members of my reading committee, **Prof. U Kei Cheang** from Southern University of Science and Technology, **Prof. Romana Schirhagl** from University of Groningen and University Medical Center Groningen, **Prof. Patrick R. Onck** from University of Groningen. Your expertise and critical evaluations have enriched my work immensely, ensuring the quality and depth of my research. Additionally, I extend my thanks to **Dr. Patrick van Rijn**, **Dr. Ali Sadeghi**, and **Dr. M-Ali Shahbazi** for accepting my invitation to join my Ph.D. examination committee without hesitation.

Being part of the Surgical Robotics Lab (SRL) has been a joy. My dear colleagues at UMCG-SRL, I spent the majority of my Ph.D. journey working alongside you. **Zhengya Zhang**, our restaurant adventures in Groningen, and conversations on everything from research to politics were highlights. **Yiyang Li**, thank you for your guidance on supermarkets and housing when I was a newcomer in Groningen. **Chuang Li**, I cherish the time we spent playing football together on weekends. Despite my lack of skill, it's been a fantastic way to stay active and bond over our shared passion for the sport. We often share our thoughts on tactics and players from various football clubs. I appreciate that we share a similar attitude toward matches, which makes our discussions all the more enjoyable, although we are fans of rival teams. **Chen Wang** and **Yiling Zhang**, your kindness as a couple has left a lasting impression. The memories we created together in Spain and Germany are ones I will always treasure. **Chen Wang**, I enjoy the competition and friendship that we build in ping-pong, pooling, and padel. Engaging in these sports relaxes me the most each week. **Kaixuan Zhang**, as my office mate, our discussions about research and life have been enlightening. Your patience, carefulness, and rigor have taught me much. **Zhuoyue Wang**, you are the true pooling champion. The times I've managed to beat you can be counted on one hand. I must admit that I've made progress in pooling after countless losses. Your skills have certainly pushed me to improve! **Adriana Vasi**, it was a pleasure to know you during your internship at SRL. Your warmth and communication

brought a delightful atmosphere to our lab. I wish you all the best on your doctoral journey.

A special thanks goes to my colleagues at UMCG-BBT. **Fenghua Zhao**, you were my first Chinese friend outside the SRL. Our conversations were always a joy. **Sidi Liu**, the memories of our travels to Paris and Ghent are ones that I hold dear. **Rui Shi** and **Renfei Wu**, we share many wonderful memories playing ping-pong and padel together. Those moments added so much joy to my time here! **Dayuan Wang**, it was an honor to be your paranymph at your Ph.D. defense. **Guang Yang**, your kindness resonated with me, even though our time together was limited. **Henk**, I remember our conversations during the Ph.D. defenses of your students. We often discussed global issues and politics, and I truly appreciated knowing your opinions. **Kaiqi Wu**, thank you for helping me find consumable products and facilities in our department. **Hélder** and **Ali**, our Friday ping-pong sessions pushed me to improve and brought much enjoyment. I also thank every member of BBT (formerly known BME), including **Henny**, **Inge**, **Prashant**, **Theo**, **Brandon**, **Jelmer**, **Wytse**, **Ina**, **Sonya**, **Willy**, **Joop**, **Reinier**, **Willem**, **Hans**, **Marja**, and **Jelly**. Your unwavering support has been key to the smooth progression of my research. A special mention **Ed** here. Whenever I encounter difficulties, you are always there to lend a helping hand, and I also appreciate your assistance in translating the Dutch Summary of my thesis. I would also like to acknowledge my other colleagues: **Arturo Elías Llumbet**, **Thamir Hamoh**, **Han Gao**, **Tianqi Feng**, **Adi Mohan**, **Yuewen Zhu**, **Jiachen Li**, **Huijie Han**, **Torben van der Boon**, **Runrun Li**, **Yue Zhang**, **Siyu Fan**, **Ruichen Zhang**, **Yanjing Ji**, **Yunlong Cao**, **Jie Gao**, **Renata Maia**, **Ke Ren**, **Lei Li**, and **Xiangpan Kong**. Thank you all for your company and support! Apologies if I missed anyone.

To the dear UT-SRL gang, it has been a privilege to constitute the SRL with you. Thank you, **Jeanine**, for expertly coordinating our meetings between me and my supervisors. **Michiel Richter**, thank you for your invaluable assistance in measuring magnetization. **Theodosia Lourdes Thomas**, I truly enjoyed our trip to “De Hoge Veluwe National Park” together. It was a wonderful experience, filled with beautiful scenery and memorable moments. **Juan Julian Jesus Huaroto Sevilla**, thank you for sharing your two-photon microscopy techniques with me. It’s exciting to see you developing new imaging methods in our lab! **Yu-Hsiang Lin**,

every time we discuss research, it's clear how passionate you are about your work, and that enthusiasm is truly inspiring. **Mert Kaya**, I appreciate you generously teaching me electrospinning and sharing your protocols. You are a kind person, and I wish you all the best in the future. **Mina M. M. Farag**, thank you for showing me around Hengelo and for discovering the Dutch restaurant with the delicious Chow Mian. Also, I would like to thank other members or alumni of the SRL, including **Venkat Kalpathy Venkiteswaran**, **Christoff M. Heunis**, **Jakub Sikorski**, **Luigi Capuano**, **Hugo Daguerre**, **Franco Pinan Basualdo**, **T. Hellebore Fass**, **Fouzia Khan**, **Amin Lotfiani**, **Rob Struik**, **Alaaeldine Sadek**, **Yuxin Jin**, **Fragkiskos Furlas**, **Antonio Lobosco**, **Lukas Masjosthusmann**, and **Simon Frieler**. It is my honor to meet you and work with you.

**Jiaxin**(家昕) and **Qing**(青), growing up together with you has been a true blessing. You have treated and protected me like brothers. While I may be ahead of you in terms of education, you both excel far beyond me when it comes to family. I wish you all the best in this next stage of your life. **Huayi**(华溢) and **Lijun**(力钧), you are my best friends since high school. It's a pity we can no longer reunite as a trio due to misunderstandings. I cherish the friendship we share and hope it lasts a lifetime.

Last but not least, I would like to express my deep appreciation to my family. Dear Mom and Dad, I know you are proud of me, and I feel incredibly lucky to have you as my parents. You have always respected my choices and never placed pressure on me; instead, you have given me your endless trust and support. I feel guilty for not being able to spend more time with you since high school. As your only child, I realize that I should be working to support and take responsibility for our family at this stage of life. I dedicate my doctoral thesis to my loving family, who have always stood by me and believed in me.

## About the author

Zihan Wang was born on 23<sup>th</sup> July 1998 in Hubei province, China. He graduated with his undergraduate degree in Mechanical and Electrical Engineering from Wuhan University of Technology, Wuhan, Hubei Province, China 2018. In the same year, he embarked on his master's studies through a joint program between Harbin Institute of Technology and Southern University of Science and Technology. He obtained his master's degree in 2020. During his master, his research interests include the fabrication and control of magnetically actuated helical microrobots.



In March 2021, he began his doctoral studies in the Surgical Robotics Laboratory at the Department of Biomaterials and Biomedical Technology (previously known as the Department of Biomedical Engineering), University of Groningen and University Medical Center Groningen, Groningen, the Netherlands, under the supervision of Prof. Dr. Sarthak Misra and Dr. Islam S. M. Khalil. His doctoral research centered on the fabrication, elasto-hydrodynamics, modeling, and biomedical applications of magnetically-actuated biohybrid microrobots.